

INFORMATION TO USERS

This manuscript has been reproduced from the microfilm master. UMI films the text directly from the original or copy submitted. Thus, some thesis and dissertation copies are in typewriter face, while others may be from any type of computer printer.

The quality of this reproduction is dependent upon the quality of the copy submitted. Broken or indistinct print, colored or poor quality illustrations and photographs, print bleedthrough, substandard margins, and improper alignment can adversely affect reproduction.

In the unlikely event that the author did not send UMI a complete manuscript and there are missing pages, these will be noted. Also, if unauthorized copyright material had to be removed, a note will indicate the deletion.

Oversize materials (e.g., maps, drawings, charts) are reproduced by sectioning the original, beginning at the upper left-hand corner and continuing from left to right in equal sections with small overlaps.

**ProQuest Information and Learning
300 North Zeeb Road, Ann Arbor, MI 48106-1346 USA
800-521-0600**

UMI[®]

**WETTABILITY MODIFICATION OF POLYSILICON FOR
STICTION REDUCTION IN SILICON BASED MICRO-
ELECTROMECHANICAL STRUCTURES**

by

Angeles Marcia Almanza-Workman

Copyright © Angeles Marcia Almanza-Workman 2002

**A Dissertation Submitted to the Faculty of the
DEPARTMENT OF MATERIALS SCIENCE AND ENGINEERING
In Partial Fulfillment of the Requirements
For the Degree of
DOCTOR OF PHILOSOPHY
In the Graduate College
THE UNIVERSITY OF ARIZONA**

2002

UMI Number: 3073184

Copyright 2002 by
Almanza-Workman, Angeles Marcia

All rights reserved.

UMI[®]

UMI Microform 3073184

Copyright 2003 by ProQuest Information and Learning Company.
All rights reserved. This microform edition is protected against
unauthorized copying under Title 17, United States Code.

ProQuest Information and Learning Company
300 North Zeeb Road
P.O. Box 1346
Ann Arbor, MI 48106-1346

THE UNIVERSITY OF ARIZONA &
GRADUATE COLLEGE

As members of the Final Examination Committee, we certify that we have read the dissertation prepared by Angeles Marcia Almanza-Workman entitled Wettability Modification of Polysilicon for Stiction Reduction in Silicon Based Micro-Electromechanical Structures

and recommend that it be accepted as fulfilling the dissertation requirement for the Degree of Doctor of Philosophy

S.R.

Srini Raghavan

12/12/02

Date

P. Peymier

Pierre A. Peymier

12/12/02

Date

William G. Davenport

William G. Davenport

12/12/02

Date

David J. Monk

David J. Monk

12/12/02

Date

Date

Final approval and acceptance of this dissertation is contingent upon the candidate's submission of the final copy of the dissertation to the Graduate College.

I hereby certify that I have read this dissertation prepared under my direction and recommend that it be accepted as fulfilling the dissertation requirement.

S.R.

Dissertation Director Srini Raghavan

12/12/02

Date

STATEMENT BY AUTHOR

This dissertation has been submitted in partial fulfillment of requirements for an advanced degree at The University of Arizona and is deposited in the University Library to be made available to borrowers under rules of the Library.

Brief quotations from this dissertation are allowable without special permission, provided that accurate acknowledgment of source is made. Requests for permission for extended quotation from or reproduction of this manuscript in whole or in part may be granted by the copyright holder.

SIGNED _____

A handwritten signature in black ink, appearing to be "M. J. ...", written over a horizontal line.

ACKNOWLEDGEMENTS

I would like to thank to my advisor, Dr. Srin Raghavan, and co-advisor, Dr. Pierre Deymier, whose support, guidance and encouragement have made it possible to complete this work. I would also like to thank Dr. David Monk, Dr. Slobodan Petrovic, Dr. Bishnu Gogoi and Dr. Ray Roop from Sensor Products Division at Motorola and Dr. Andy Hooper from Motorola Labs for their technical assistance. Thanks also goes to Dr. William G. Davenport for his academic advise.

Special thanks go to Richard Workman and Srin Manne for AFM interpretation, Bert Vermeire for EIS analysis and Dr. Roger Sperline for ATR-FTIR guidance.

I am thankful for all my co-workers in Dr. Raghavan's group. Special thanks go to Wayne Huang, Vivek Kapila and undergraduate students L. Morgan Hart and Kim M. Leung.

This project was funded by National Science Foundation through the GOALI program under Grant No 9905957; this financial support is gratefully acknowledged.

I would like to take this opportunity to thank my parents, Rafael Almanza and Marcia Gollas, and my brother, Rafael Almanza, for their guidance, care, love and support. Finally, I want to thank my husband, Richard Workman for his endless love, encouragement, help and patience.

I dedicate this dissertation to my son, Alexander, and husband who have given me a lot of joy at the end of this study.

TABLE OF CONTENTS

LIST OF ILLUSTRATIONS.....	8
LIST OF TABLES.....	16
ABSTRACT	18
CHAPTER 1. INTRODUCTION.....	20
CHAPTER 2. BACKGROUND.....	23
2.1 Micro-electromechanical systems.....	23
2.1.1 Stiction in micro-electromechanical systems	27
2.1.1.1 Causes of stiction	29
2.1.1.1.1 Solid bridging	29
2.1.1.1.2 Capillary forces.....	30
2.1.1.1.3 Hydrogen bridging.....	32
2.1.1.1.4 Van der Waals forces.....	32
2.1.1.1.5 Electrostatic forces.....	32
2.1.1.2 Preventing stiction	35
2.2 Self-assembled monolayers and Langmuir-Blodgett films	45
2.2.1 Langmuir isotherms	47
2.2.2 Langmuir-Blodgett films	49
2.2.3 Self-assembled monolayers	50
2.2.3.1 Transition Temperature.....	52
2.2.3.2 Defects in self-assembled monolayers.....	57
2.3 Chemistry of organosilanes	59
2.3.1 Hydrolysis and condensation.....	59
2.3.1.1 Effect of pH	61
2.3.2 Deposition of organosilane coatings from organic media	68
2.3.3 Deposition of organosilane coatings from aqueous media	71
CHAPTER 3. EXPERIMENTAL MATERIALS AND METHODS.....	75
3.1 Materials	75
3.1.1 Silicon and polysilicon wafers.....	75
3.1.2 Water dispersible silanes	75
3.1.2.1 Siliclad [®]	76
3.1.2.2 Glassclad [®] 18.....	76
3.1.2.3 DuPont TLF-8291	77
3.1.2.4 Cationic alkoxysilanes	77

TABLE OF CONTENTS - Continued

3.1.3 Surfactants	80
3.2 Methods	82
3.2.1 Cleaning and pre-oxidation of silicon and polysilicon samples	82
3.2.2 Preparation of silane dispersions	83
3.2.3 Coating deposition	83
3.2.3.1 Dip coating.....	83
3.2.3.2 Langmuir-Blodgett films	85
3.3 Characterization techniques.....	89
3.3.1 Zeta potential measurements	89
3.3.2 Wettability evaluation.....	91
3.3.2.1 Static contact angle measurements	91
3.3.2.2 Dynamic contact angle measurements.....	94
3.3.3 Determination of critical micelle concentration	98
3.3.4 Viscosity measurements	100
3.3.5 Spectroscopic ellipsometry	103
3.3.6 Nulling ellipsometry	103
3.3.7 Atomic force microscopy.....	105
3.3.7.1 Tapping mode	105
3.3.7.2 Contact and soft contact mode.....	105
3.3.8 Electrochemical impedance spectroscopy	108
3.3.9 Attenuated total reflection Fourier transform-Infrared spectroscopy (ATR- FTIR)	110
3.3.9.1 Polarized ATR-FTIR	113
CHAPTER 4. RESULTS AND DISCUSSION.....	118
4.1 Characterization of polysilicon and oxides.....	118
4.1.1 Roughness and grain size.....	118
4.1.2 Zeta potential	120
4.2 Coatings deposited onto polysilicon	123
4.2.1 System 1: Siliclad [®] without surfactant	123
4.2.1.1 Wettability of Siliclad [®] coatings.....	123
4.2.1.2 Stability of Siliclad [®] coatings.....	133
4.2.1.3 Surface coverage and molecular orientation of Siliclad coatings.....	136
4.2.1.4 Zeta Potential measurements on Siliclad [®] coatings.....	143
4.2.1.5 Langmuir-Blodgett film deposition of Siliclad [®] coatings	145
4.2.1.6 Stability of Siliclad [®] aqueous dispersions	147
4.2.2 System 2: Siliclad [®] with surfactant	152
4.2.3 System 3: Glassclad [®] 18.....	171

TABLE OF CONTENTS - Continued

4.2.4 System 4: Dupont TLF-8291	171
4.2.5 System 5: Cationic alkoxysilanes	175
4.2.5.1 Octadecyl cationic alkoxysilane (DMOAP)	177
4.2.5.1.1 Effect of temperature and humidity on coating hydrophobicity	188
4.2.5.2 Didecyl cationic alkoxysilane (DIDAP)	191
4.3 Coatings deposited onto single crystal silicon	194
4.3.1 Layer thickness	195
4.3.1.1 Nulling ellipsometry	195
4.3.1.2 Spectroscopic ellipsometry	198
4.3.2 Wettability	209
4.3.3 Uniformity	211
4.3.3.1 Removal of excess DMOAP	216
4.3.4 Porosity	218
4.4 DMOAP coatings deposited onto mica	227
4.5 Optimization of dip coating conditions using design of experiments	233
4.6 Anti-stiction properties of DMOAP coatings	244
CHAPTER 5. CONCLUSIONS AND SUGGESTIONS FOR FUTURE RESEARCH.....	
5.1 Conclusions.....	253
5.2 Suggestions for future research.....	256
APPENDIX: GLOSSARY OF STATISTICAL TERMS.....	
REFERENCES	265

LIST OF ILLUSTRATIONS

Figure 2.1:	Lateral accelerometer in (a) planar view and (b) SEM photograph of a surface micromachined accelerometer (fabricated by Motorola, reproduced with permission from David Monk).....	24
Figure 2.2:	Schematics of basic steps employed in a surface micromachining fabrication process	26
Figure 2.3:	Comparison of a fully released cantilever structure (a) and a structure with vertical stiction (b)	28
Figure 2.4:	SEM photograph of vertical stiction (courtesy of Gary O'Brien, University of Michigan).....	28
Figure 2.5:	Water contact angles and corresponding droplet shape on (a) hydrophilic oxide and (b) hydrophobic surfaces. Underneath the hydrophilic beam, the concave meniscus creates a capillary force which acts to bring the cantilever beam into contact with the substrate. No such attractive capillary force exists underneath the hydrophobic beam; the meniscus maintains a convex curvature.	31
Figure 2.6:	Variations of capillary, van der Waals and electrostatic forces per unit area with the surface separation distance for smooth surfaces	34
Figure 2.7:	Schematic of a cantilever beam array of different lengths with single and doubly clamped beams. ⁽¹⁸⁾	40
Figure 2.8:	A cantilever beam of length l , width w and thickness t , anchored at a gap spacing g . The beam adheres to the substrate at a distance x from the anchor, which is called "stiction length".....	40
Figure 2.9:	Approaches to prepare crystalline organic thin films ⁽⁴⁰⁾	46
Figure 2.10:	Surface pressure versus area isotherm	48
Figure 2.11:	Preparation of self-assembled monolayers. The pre-oxidized silicon substrate is immersed into a solution of the desired organosilane. Initial adsorption is fast (seconds); then organization of the molecules occurs. A schematic of a fully assembled SAM is shown to the right.....	51

LIST OF ILLUSTRATIONS - Continued

Figure 2.12: Typical phase diagram of a Langmuir monolayer of insoluble surfactants spread at the air-water interface. Solid lines denote the isotherms and the coexistence curves are denoted by dashed lines. ⁽⁵⁹⁾	54
Figure 2.13: A schematic of formation of alkyltrichlorosilane SAM coatings depending on adsorption temperature. ⁽⁶³⁾	56
Figure 2.14: Schematic representation of defects in organosilane films	58
Figure 2.15: Reaction and bonding mechanism of alkoxysilanes ⁽⁷³⁾	60
Figure 2.16: Acid-catalyzed alkoxysilane hydrolysis.....	63
Figure 2.17: Base-catalyzed alkoxysilane hydrolysis.....	63
Figure 2.18: Acid-catalyzed alkoxysilane condensation	64
Figure 2.19: Base-catalyzed alkoxysilane condensation	64
Figure 2.20: pH dependence of alkoxysilanes hydrolysis and condensation ⁽⁸¹⁾	66
Figure 2.21: Effect of pH on alkoxysilane hydrolysis ⁽⁷³⁾	67
Figure 2.22: Silanization reaction in the presence of adsorbed water	70
Figure 2.23: Possible products of the reaction of alkyltrialkoxysilanes in the aqueous phase and at the solution/substrate interface.....	72
Figure 2.24: Aggregates of water dispersible silanes	74
Figure 3.1: Adsorption of Cationic Silanes onto pre-oxidized polysilicon.....	79
Figure 3.2: Schematic of the orientation of DMOAP ⁽⁹⁶⁾	79
Figure 3.3: Schematic diagram of a DCA system used for dip coating. surface tension and dynamic contact angle measurements.....	84
Figure 3.4: Monolayer reorganization after an imposed compression or expansion..	86
Figure 3.5: Deposition of a Langmuir-Blodgett film onto a hydrophilic substrate	88
Figure 3.6: A schematic sketch of the steaming potential cell	90
Figure 3.7: Environmental chamber setup for humid environments	92

LIST OF ILLUSTRATIONS - Continued

Figure 3.8:	Heating and cooling ramp times for environmental chamber	93
Figure 3.9:	Force balance during the measurements of surface tension and contact angle. 1) Plate in air prior to contact with liquid. 2) plate just at the liquid-air interface and 3) plate immersed in the liquid	95
Figure 3.10:	Dynamic contact angle hysteresis loop formed using the Wilhelmy plate technique. (a) $\theta_{advancing} < 90^\circ$ and (b) $\theta_{advancing} > 90^\circ$	96
Figure 3.11:	Critical Micelle Concentration	99
Figure 3.12:	Viscometers used for silane dispersion stability measurements: (a) Ostwald viscometer; (b) Ubbelohde	102
Figure 3.13:	Optical Model of silane coatings deposited onto thin chemical oxide covering a silicon wafer	104
Figure 3.14:	Schematic of the technique for imaging surface aggregates by AFM (Courtesy of Srin Manne, Department of Physics, University of Arizona)	107
Figure 3.15:	Lateral and top view of the fluid cell: 1) cantilever, 2) O-ring and 3) laser beam ⁽¹¹⁰⁾	107
Figure 3.16:	A schematic sketch of the cell used for the electrochemical characterization of coated and uncoated silicon surfaces in HF solutions	109
Figure 3.17:	ATR-FTIR liquid flow cell	111
Figure 3.18:	Schematic diagram of axes and an adsorbed silane molecule on a pre-oxidized surface	114
Figure 4.1:	AFM image of undoped polysilicon deposited on (a) the polished side and (b) on the backside of the wafer	119
Figure 4.2:	Electrokinetic measurements on undoped and phosphorous doped polysilicon subjected to different wet oxidation treatments in 10^{-3} M KNO_3 solution	121
Figure 4.3:	Zeta potential as a function of pH for undoped polysilicon subjected to SCI pre-oxidation treatment at different concentrations of indifferent electrolytes	122

LIST OF ILLUSTRATIONS - Continued

Figure 4.4:	DI water contact angles on coatings deposited from an aqueous medium containing 3% reactive silane at different pH values.....	124
Figure 4.5:	DI water contact angles on coatings deposited from Siliclad [®] aqueous dispersions containing 3% reactive silane as a function of deposition temperature.....	125
Figure 4.6:	DI water contact angles on coatings deposited from aqueous silane dispersions containing different amounts of reactive silane onto undoped and P doped polysilicon	127
Figure 4.7:	Effect of temperature and substrate roughness on hydrophobicity of coatings (coatings deposited from 5% reactive silane dispersions) [OTS data from ref. ⁽¹²²⁾].....	128
Figure 4.8:	Hydrophobicity of coatings cured at low temperature (90°C) as a function of curing time (dashed line is for a coating cured at 250° for 5 min)	130
Figure 4.9:	Thermal stability of Siliclad [®] coatings deposited onto polysilicon in air and nitrogen environments.....	134
Figure 4.10:	Stability of coated and uncoated samples in (a) air and (b) DI water	135
Figure 4.11:	ATR-FTIR spectra of Siliclad [®] at different adsorption times.....	137
Figure 4.12:	Effect of immersion time in a 0.5% reactive silane dispersion.....	138
Figure 4.13:	ATR-FTIR spectra obtained using polarized IR beam on a coating deposited from 0.5% reactive silane dispersion. a) 90° b) 0°	140
Figure 4.14:	Zeta potential of coated and uncoated pre-oxidized polysilicon as a function of pH	144
Figure 4.15:	Surface pressure-area isotherm for Siliclad [®] spread on water. Contact angles and adsorption densities of coatings formed at different surface pressures and cured at 200°C for 5 min	146
Figure 4.16:	Viscosity of Silane Dispersions and Water Contact Angles on Coated surfaces as a function of dispersion age.....	148
Figure 4.17:	Dispersion stability as a function of pH.....	150

LIST OF ILLUSTRATIONS - Continued

Figure 4.18: Dispersion stability as a function of reactive silane concentration at pH=4.....	151
Figure 4.19: (a) Stability of silane dispersions and (b) coating hydrophobicity as a function of Empigen BAC surfactant concentration.....	153
Figure 4.20: Stability of 3% reactive silane dispersions containing different cationic surfactants (Note: surfactant concentration was 20 times the critical micelle concentration).....	154
Figure 4.21: Stability of silane dispersions containing the same molar concentration of surfactant and silane (0.05 M).....	156
Figure 4.22: (a) DTAB adsorption isotherm onto pre-oxidized silicon at pH of 4 and (b) amount of surfactant remaining as a function of rinsing time.....	159
Figure 4.23: DI water advancing contact angles of cured and uncured coatings and adsorption density of rinsed coated samples formed from a 3% reactive silane dispersion containing different amounts of surfactant.....	160
Figure 4.24: Viscosity of silane dispersions containing CTAB and water advancing contact angles on coated surfaces as a function of dispersion age.....	162
Figure 4.25: ATR-FTIR spectra of 3% reactive silane (a) without surfactant as a function of dispersion age and (b) with and without surfactant aged for 4 hours.....	164
Figure 4.26: Kinetics of condensation for dispersions containing 3% reactive silane with and without surfactant.....	165
Figure 4.27: Mechanism model of surfactant/silane aggregation and adsorption onto pre-oxidized silicon at a pH of 4.....	167
Figure 4.28: Zeta potential of pre-oxidized polysilicon as a function of pH and DTAB concentration.....	169
Figure 4.29: DTAB adsorption density as a function of pH.....	170
Figure 4.30: DI water contact angles on coatings deposited from Glassclad [®] 18 dispersions containing different amounts of reactive silane.....	172
Figure 4.31: DI water contact angles on coatings deposited from Dupont TLF-8291 dispersions containing different amounts of reactive silane.....	173

LIST OF ILLUSTRATIONS - Continued

Figure 4.32: Force versus immersion depth curves for Dupont TLF-8291 and Siliclad [®] coated polysilicon samples	174
Figure 4.33: Surface Tension of DI water as a function of DMOAP and DIDAP concentration	176
Figure 4.34: DI water contact angles on coatings deposited from DMOAP aqueous silane dispersions as a function of (a) reactive silane, (b) pH and (c) temperature.....	179
Figure 4.35: Π -A isotherms of DMOAP monolayers on DI water subphase at different temperatures	181
Figure 4.36: Effect of curing under nitrogen environment on hydrophobicity of DMOAP coatings (coatings deposited from 0.01% reactive silane dispersions at 40°C)	185
Figure 4.37: Viscosity of a DMOAP dispersion containing 3% reactive silane and water contact angles on coated surfaces deposited at room temperature (~22°C) as a function of dispersion age.....	187
Figure 4.38: DI water contact angles on coatings deposited from DIDAP aqueous dispersions containing 0.1% reactive silane at pH value of ~5.2 as a function of deposition temperature	192
Figure 4.39: Π -A isotherms of DIDAP monolayers on DI water subphase at different temperatures	193
Figure 4.40: Molecular modeling of cationic alkoxy silanes using HyperChem v.3.0 software	197
Figure 4.41: Delta and Psi values for uncoated and coated samples	199
Figure 4.42: Regions on a wafer used to determine thickness uniformity by a dip coating process	203
Figure 4.43: Thickness uniformity of coatings deposited from dispersions containing 0.1% DMOAP at withdrawal speed of (a) 40 $\mu\text{m}/\text{sec}$ and (b) 400 $\mu\text{m}/\text{sec}$	204
Figure 4.44: Thickness uniformity of coatings deposited from a dispersion containing 0.1% DIDAP at withdrawal speed of 40 $\mu\text{m}/\text{sec}$ and different delay times.....	205

LIST OF ILLUSTRATIONS - Continued

Figure 4.45: Thickness uniformity of coatings deposited from Siliclad [®] dispersions .	207
Figure 4.46: Thickness uniformity of (a) DMOAP/Siliclad [®] and (b) DIDAP/Siliclad [®] double coating systems	208
Figure 4.47: AFM images, of a 1 μ m x 1 μ m region, showing Siliclad [®] coatings on single crystal silicon substrates (Height profiles in the lower part of the image were measured along the horizontal white lines. The pore height profiles were measured along the dotted lines).....	212
Figure 4.48: AFM image (1 μ m x 1 μ m) of DMOAP coating. (Height profiles in the lower part of the image were measured along the horizontal white lines. Pore height profiles were measured along the dotted lines).....	214
Figure 4.49: AFM image (1 μ m x 1 μ m) of a DMOAP/Siliclad [®] coating. (Height profiles in the lower part of the image were measured along the horizontal white lines. Pore height profiles were measured along the dotted lines).....	215
Figure 4.50: Tapping-mode AFM height images, of a 5 μ m x 5 μ m area, showing DMOAP coatings on single crystal silicon substrates: (a) without rinsing, (b) rinsed with DI water for 5 min, (c) immersed in DI water for 20 min and (d) rinsed with 0.1 M acetic acid (z range = 5 nm)	217
Figure 4.51: Equivalent circuit used for the interpretation of impedance spectra obtained for (a) uncoated and (b) coated silicon/solution interface in 100:1 HF.....	219
Figure 4.52: Nyquist plots for Siliclad [®] coated silicon samples in 100:1 HF.....	221
Figure 4.53: Nyquist plots for DMOAP and DIDAP coated silicon samples in 100:1 HF.....	221
Figure 4.54: Nyquist plots for single and double DMOAP-Siliclad [®] coatings on silicon samples in 100:1 HF.....	226
Figure 4.55: Nyquist plots for single and double DIDAP-Siliclad [®] coatings on silicon samples in 100:1 HF.....	226
Figure 4.56: Tip displacement versus tip-mica sample separation curve for DI water and a 0.0035% reactive silane DMOAP dispersion	228

LIST OF ILLUSTRATIONS - Continued

Figure 4.57: <i>In-situ</i> deflection-mode AFM images, of a 3.5 μm x 3.5 μm region, showing DMOAP aggregates on mica as a function of exposure time at $\sim 22^\circ\text{C}$	230
Figure 4.58: Tip displacement versus tip-sample separation profiles for DMOAP dispersions containing different amounts of reactive silane on mica	232
Figure 4.59: Deflection mode AFM images, of a 10 μm x 10 μm region, showing DMOAP aggregates on mica as a function of reactive silane concentration	232
Figure 4.60: Factors and levels used for the optimization of coating deposition by the two-level factorial design	235
Figure 4.61: Design-Expert software general sequence of analysis	237
Figure 4.62: Half normal probability plot for the effects of advancing and receding contact angles of DMOAP and DIDAP coatings with power transformation (A: Withdrawal Speed and B: Delay time).....	239
Figure 4.63: Effect of withdrawal speed and delay time on the hydrophobicity of DMOAP and DIDAP coatings	242
Figure 4.64: Schematic of GOB devices	245
Figure 4.65: Optical microscopy stiction focal plane identification.....	246
Figure 4.66: Effect of surface treatment on stiction	250
Figure 4.67: Stiction on 120 μm x 3 μm com-like beam arrays by different treatments	252

LIST OF TABLES

Table 2.1:	Summary of the release and SAM-coating process for polysilicon microstructures ⁽³⁾	37
Table 2.2:	Physical property data of various coatings ⁽³¹⁾	38
Table 2.3:	Comparison between different anti-stiction techniques	41
Table 3.1:	Cationic surfactants used to stabilize Siliclad [®] dispersions.....	81
Table 3.2:	Oxidation pre-treatments for silicon and polysilicon samples	82
Table 3.3:	Experimental techniques used to characterize the substrate, silane dispersions, coatings and anti-stiction properties of the films.	117
Table 4.1:	DI water dynamic contact angles on coatings deposited onto chemical oxides formed on polysilicon by different treatments	132
Table 4.2:	Effect of type of acid used for pH adjustment on contact angle	132
Table 4.3:	Linear dichroic ratio and chain orientation for silane adsorbed on single crystal silicon. Refractive indexes used for the calculations were $n_{\text{silicon}}=3.42$, $n_{\text{water}}=1.42$ and $n_{\text{SAM}}=1.5$	142
Table 4.4:	DI water contact angles on DMOAP LB films deposited at different surface pressures	182
Table 4.5:	Thermal stability of DMOAP coatings under different conditions.....	190
Table 4.6:	DI water contact angles on DIDAP LB films deposited at different surface pressures	194
Table 4.7:	Ellipsometric thicknesses of Siliclad coatings deposited at different exposure times in a dispersion containing 3% reactive silane	195
Table 4.8:	Ellipsometric thicknesses of Siliclad coatings deposited from dispersions containing different amounts of silanes	196
Table 4.9:	Film thicknesses determined by Ellipsometry	200
Table 4.10:	DI water contact angles on coated single crystal silicon.....	209

LIST OF TABLES - *Continued*

Table 4.11: Parameters obtained from the fitting of the EIS data to equivalent circuits	223
Table 4.12: Important factors for dip coating of organosilanes	233
Table 4.13: Table of experiments generated by Design Expert software (ver. 6.0.7)..	234
Table 4.14: Statistics from ANOVA analysis	240
Table 4.15: Optimum conditions to deposit hydrophobic coatings onto polysilicon...	243
Table 4.16: Sequence of processing steps used for release GOB devices	248
Table 5.1: Comparison of coating processes.....	255

ABSTRACT

Surface micromachining using deposited polysilicon films is a technology that is widely used for the fabrication of micro-electromechanical structures. One of the biggest yield and reliability problems in the fabrication of such structures is “*stiction*” or adhesion to the substrate. This may occur during the *drying* step that is required after wet processing and/or during *use* of a device. Deposition of self-assembled monolayer coatings is one of the most successful approaches to chemical modification of silicon surfaces to reduce stiction. This approach involves making the surfaces of pre-oxidized polysilicon highly hydrophobic.⁽¹⁻³⁾ As a result, microstructures come out of the final water rinse extremely dry without being broken or adhered to the substrate. Available technology requires that these coatings are applied from *organic media*. However, increasing pressure on semiconductor companies to reduce the generation of organic wastes has sparked interest in the feasibility of applying these coatings from *aqueous media*. The objective of this research was to develop the chemistry and techniques for the application of hydrophobic coatings on polysilicon from aqueous media.

The results obtained from three commercially available water dispersible silanes and cationic alkoxysilanes are discussed. Key experimental variables that were investigated are concentration of reactive silane, type of oxidation pretreatment of polysilicon, pH and temperature of the silane dispersion and curing temperature of the coating. The stability of the dispersions was characterized by viscosity measurements. The formation and quality of the films were studied using atomic force microscopy

(AFM), ellipsometry, dynamic contact angle measurements and electrochemical impedance spectroscopy (EIS). The coatings showed contact angles greater than 100° . It was found using AFM that the structure of these films is a continuous film with some particulates attributed to bulk polymerization of the precursor molecule in water. EIS results indicated that the coatings had low porosity as well as high charge transfer resistance across the silicon/HF interface. Ellipsometric analysis showed that thickness of these coatings is roughly a (statistical) monolayer. The stability improvement of the dispersions by the addition of quaternary ammonium cationic surfactants is also discussed.

CHAPTER 1

INTRODUCTION

Surface micromachining of micro-electromechanical systems (MEMS) using deposited polysilicon films is a technology that is widely used for the fabrication of microsensors and microactuators. The microstructures are released by removing the surrounding sacrificial oxide layers in a liquid-phase HF or buffered HF etch, followed by rinsing and drying. Surface machined microstructures have lateral dimensions of 50-500 μm , with thickness of 0.1-2.4 μm and are offset 0.1-2 μm from the substrate. Given their large surface area-to-volume ratio, these microstructures are particularly vulnerable to “stiction” or adhesion to the substrate and to adjacent microstructures during the release process or during use.

In a conventional drying process, liquid is removed by evaporation and capillary forces that arise as a result of the surface tension of the liquid-vapor interface cause stiction. A number of methods have been investigated to reduce or prevent stiction and they are based on reduction of surface tension or increase of contact angle. One technique is to carry out the drying at elevated temperatures to exploit the fact that surface tension of water and solvents decreases on increasing the temperature.⁽⁴⁾ Another method uses supercritical drying process,^(5,6) where the liquid is transferred to vapor via the supercritical phase and hence there are no capillary forces to contend with. Carbon dioxide has been the material of choice for supercritical drying because of its low critical temperature and pressure ($T_c=31.1^\circ\text{C}$, $P_c=72.8\text{ atm}$).

Deposition of self-assembled monolayer (SAM) coatings is one of the most successful approaches to wettability modification of silicon surfaces in order to reduce adhesion in microstructures.. This approach involves making the surfaces of pre-oxidized silicon and polysilicon hydrophobic, through the formation of SAM films.⁽¹⁻³⁾ By making the surface hydrophobic, the capillary attraction that collapses the microstructure when the surfaces are hydrophilic is greatly reduced. As a result, microstructures come out of the final water rinse extremely dry without being broken or adhered to the substrate. Extensive studies of SAMs of alkylchlorosilanes (RSiCl_3), alkylsiloxanes ($\text{RSi}(\text{OR}')_3$) and alkylaminosilanes ($\text{RSi}(\text{NR}'_2)_3$) deposited from organic media onto silicon oxide surfaces have been reported.⁽⁷⁾

High quality SAMs of alkyltrichlorosilane derivatives are not easy to form, mainly because of the need to carefully control the amount of water in the liquid medium used for deposition.⁽⁸⁻¹⁰⁾ While incomplete monolayers are formed in the absence of water, excess water results in polymerization in the solution and polysiloxane deposition on the surface.⁽¹¹⁾ As a result, the solvents used for SAM coating with RSiCl_3 precursors must be highly anhydrous. For example, for octadecyltrichlorosilane (OTS) coatings, an alkane is used with 30 vol.% of a cosolvent such as carbon tetrachloride (CCl_4) or chloroform (CHCl_3).⁽¹²⁾ The CCl_4 is believed to help in dehydrating the structures prior to film formation, solvate OTS head group in the solvent mixture and rinse away excess OTS molecules, which may be physisorbed to the surface.

Available technology requires that these coatings are applied from organic media. However, increasing concerns regarding the use of organic solvents in work places and

the generation of organic wastes has sparked interest in the feasibility of applying highly hydrophobic coatings from predominantly aqueous media. The objective of this research was to develop the chemistry and techniques for the application of hydrophobic coatings on polysilicon MEMS based structures from aqueous media. In particular, the use of water dispersible silanes in forming hydrophobic coatings was investigated. Key experimental variables that were studied are the concentration of reactive silane, type of oxidation pretreatment of polysilicon substrates, pH and temperature of the silane dispersion and curing temperature of the coating. The formation and quality of the coatings was studied using dynamic contact angle measurements, atomic force microscopy, ellipsometry, attenuated total reflection Fourier transform-infrared spectroscopy and electrochemical impedance spectroscopy. The stability of aqueous dispersions was evaluated by viscosity measurements. The ability of the coatings to prevent stiction was investigated with simple test structures.

CHAPTER 2

BACKGROUND

2.1 Micro-electromechanical systems

Micro-electromechanical systems (MEMS) are microscale devices, with feature sizes of the order of tens of micrometers. Silicon micromachines are built in the same fashion as silicon integrated circuit (IC). Starting with a silicon wafer, materials such as polysilicon, silicon nitride, silicon dioxide and gold are deposited and patterned in a sequence of steps, thereby producing a complicated three-dimensional structure. However, unlike an IC, the device is released at the concluding processing step by etching away material surrounding the device, leaving sections free to move. Silicon MEMS process technology can be divided primarily into bulk micromachining and surface micromachining.

Bulk micromachining is a subtractive process that involves the removal of material to form holes, grooves, membranes and complex 3-D structures. *Surface micromachining* is a process for making micromechanical structures from deposited thin films. By selectively removing sacrificial layers from a stack of patterned thin films, micromechanical structures such as bearings, gears and suspended plates can be formed. This process is the primary technology for silicon micro-electromechanical systems (MEMS) and is widely used in the manufacturing of crash-detection accelerometers (Figure 2.1) and digital micromirror devices.⁽¹³⁾

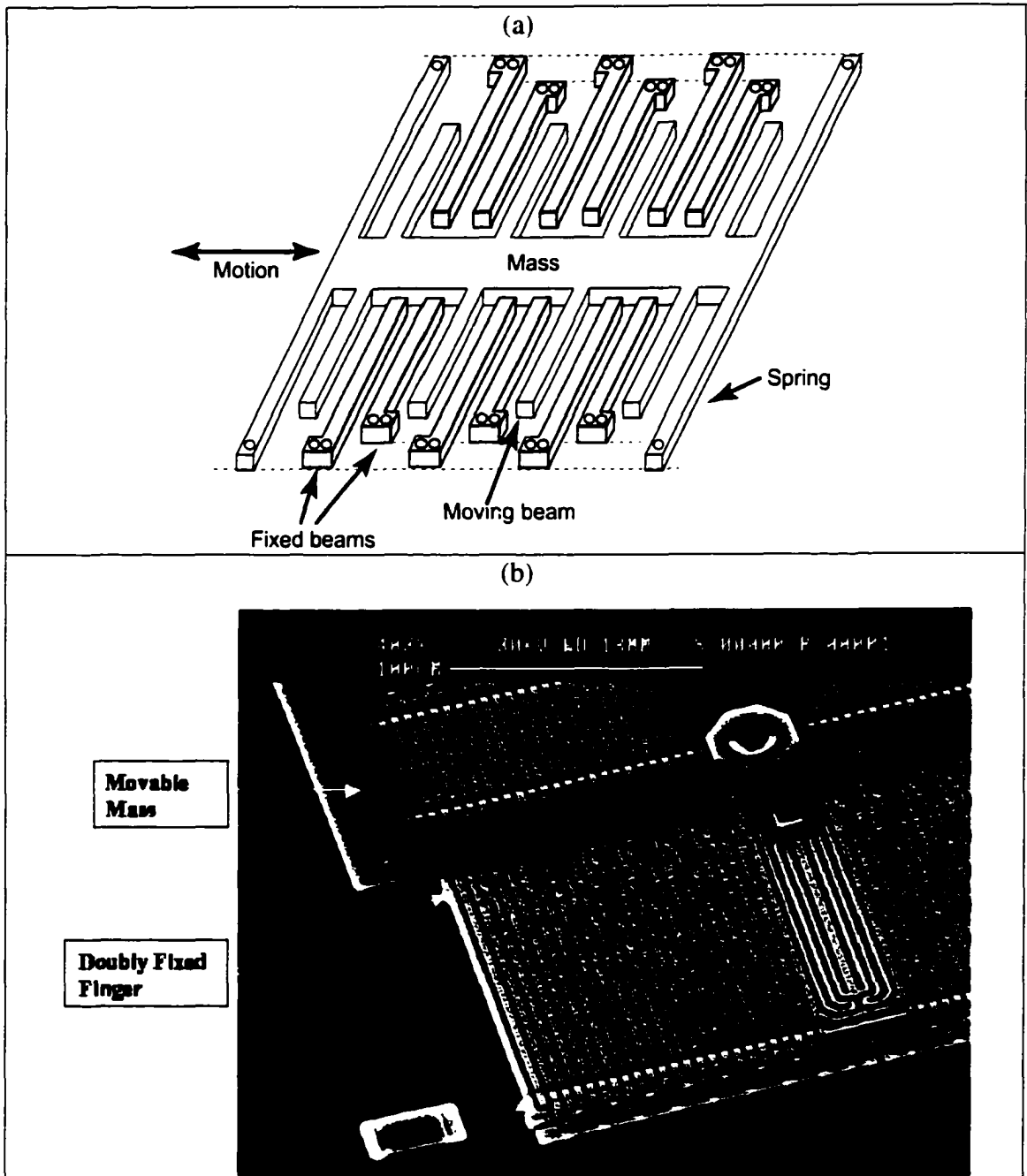


Figure 2.1: Lateral accelerometer in (a) planar view and (b) SEM photograph of a surface micromachined accelerometer (fabricated by Motorola, reproduced with permission from David Monk)

Figure 2.2 illustrates the basic steps involved in a surface micromachining process. First, the substrate is typically coated with an isolation layer (Figure 2.2(a)) that protects it during subsequent etching steps. A sacrificial layer (SiO_2) is then deposited on a silicon substrate. The anchor region, whose purpose is to anchor the polysilicon beams to the substrate, is defined by an opening in the sacrificial layer (Figure 2.2(b)). A polysilicon thin film is then deposited and etched to form the required structures (Figure 2.2(c)). Finally, the microstructures are released by removing the surrounding sacrificial oxide layers in a liquid-phase etch which uses HF based solutions, followed by rinsing with deionized water and drying (Figure 2.2d). Subsequent processing does not remove but may modify the composition of the surface layer. For example, treatment with a peroxide solution after water rinsing results in a thin chemical oxide layer with hydroxyl (-OH) surface termination. The technique can be extended to make multiple layer microstructures.

Polysilicon is used as a structural material in surface micromachined structures for the following primary reasons: (1) it has good mechanical properties, comparable to single crystal silicon; (2) it is compatible with standard IC processing and its processing technology has been developed by the IC industry; (3) it is resistant to HF, so that silicon dioxide can be used as a sacrificial layer. Polysilicon is commonly deposited by low-pressure chemical vapor deposition (LPCVD). The isolation layer is typically silicon nitride. The sacrificial layer can be an oxide film or phosphosilicate glass (PSG). PSG layers under the polysilicon can also be used as a phosphorus doping source for polysilicon.

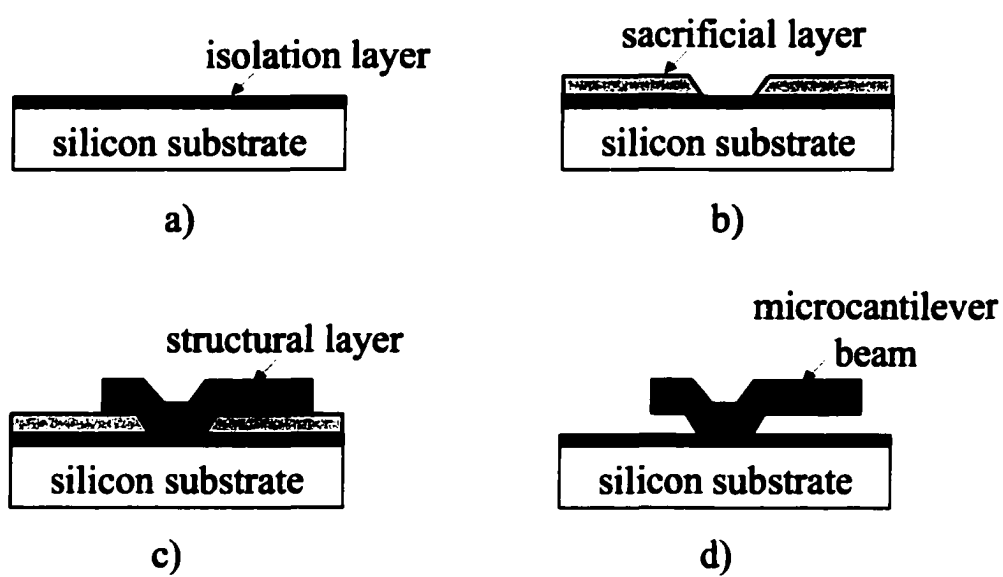


Figure 2.2: Schematics of basic steps employed in a surface micromachining fabrication process

2.1.1 Stiction in micro-electromechanical systems

Surface microstructures typically have lateral dimensions of 50-500 μm , with thicknesses of 0.1-2.5 μm and are offset 0.1-2 μm from the substrate. Because of the large surface area-to-volume ratio, these structures are particularly vulnerable to adhesion to the substrate (Figure 2.3) or adjacent microstructures either during the drying step that is required after the etching of sacrificial oxide to release the structures (release stiction) or when parts come into direct contact due to out-of-range inputs or mechanical instabilities during their operational life-time (in-use stiction).⁽¹³⁾

Stiction is a term that has been used to describe adhesion which occurs in the structures due to capillary, van der Waals, hydrogen bridging and electrostatic attractions.^(2,14,15) During drying, surface tension from the liquid-vapor interface causes a downward force on the structural layer. If the layer touches the substrate, it is prone to stick onto the surface (Figure 2.4).⁽¹⁶⁾ Unless very thick or short structures and large gap spacing are used, it is not possible to avoid contact during drying. Structures that stick can sometimes be released by using the Lorentz interaction between a current and an external magnetic field that generates an upward force of sufficient magnitude to overcome the adhesion force.⁽¹⁷⁾

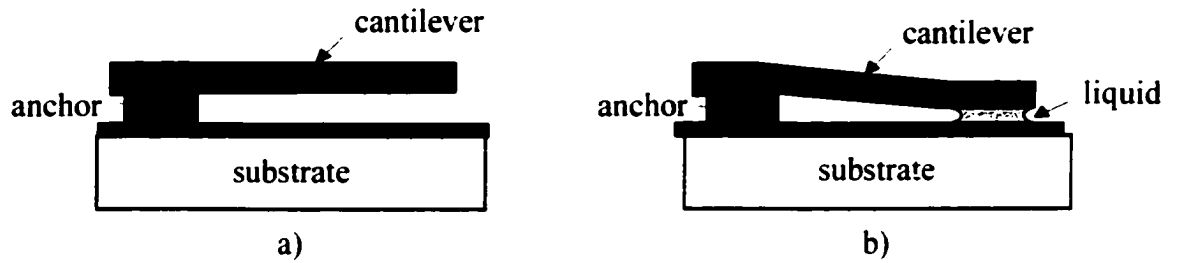


Figure 2.3: Comparison of a fully released cantilever structure (a) and a structure with vertical stiction (b)



Figure 2.4: SEM photograph of vertical stiction (courtesy of Gary O'Brien, University of Michigan)

2.1.1.1 Causes of stiction

The causes of microdynamic structure stiction have been considered similar to those of particle adhesion under similar wet processing and drying conditions.¹⁴⁾ Solid bridging, capillary forces, hydrogen bonding, van der Waals forces and electrostatic forces have been identified^(14,15,18-20) as being responsible for adhesion or stiction of microstructures.

2.1.1.1.1 Solid bridging

During rinsing of the solvents to remove residual etchant and etch byproducts, deposition of impurities dissolved in the solvent (usually deionized water or alcohol) at interfacial gaps may lead to permanent surface adhesion. This phenomenon is termed solid bridging.¹⁴⁾ Since the concentration of impurities increases with the progression of the drying process, it may exceed the solubility limit before the completion of liquid evaporation resulting in residue precipitation. There are three possible origins of precipitates: (i) impurities present in the solvent prior its use, (ii) products of the HF release-etch that may not be readily removed by rinsing and (iii) material dissolved in the water during rinsing. The adhesive strength resulting from solid bridging is difficult to estimate because of the variability in the deposition process and density of deposited material, but tends to be large.

2.1.1.1.2 Capillary forces

The formation of liquid menisci at micromachined interfaces (liquid bridging) can be encountered at the final stage of the release-etch drying process and during the use of the device due to the condensation of vapors from the environment. If the contact angle (θ) between liquid and solid is less than 90° (Figure 2.5), the liquid meniscus underneath the microstructures creates a pressure, called Laplace pressure (ΔP_{la}):⁽²¹⁾

$$\Delta P_{la} = \gamma_{la} \left(\frac{1}{r_1} + \frac{1}{r_2} \right) \quad (2.1)$$

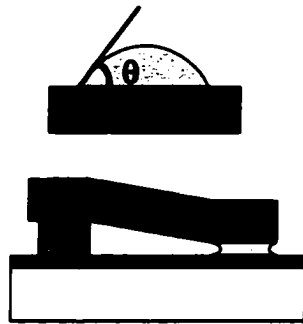
In the above equation, the liquid-air surface tension is denoted γ_{la} and r_1 and r_2 are the two radii of curvature of the liquid surface. Since in micromechanical structures lateral dimensions are often much larger than the vertical spacings, $r_2 \gg r_1$ and $r_1 = -\frac{g}{2 \cos \theta}$, the

total capillary pressure force is:

$$F_{cp} = -A \Delta P_{la} = -\frac{2\gamma_{la}(\cos \theta)A}{g} \quad (2.2)$$

where A is the wetted area, θ is the contact angle of the liquid on the solid surface and g is the separation between the two surfaces. Note that a positive force corresponds to a negative Laplace pressure. The pressure inside the liquid is lower than outside and the plates are pushed together by pressure forces when $\theta < 90^\circ$. The capillary force becomes zero at $\theta = 90^\circ$ and becomes negative for $\theta > 90^\circ$. Therefore, hydrophobic surfaces in liquid do not experience capillary attraction.

(a) hydrophilic surface



(b) hydrophobic surface

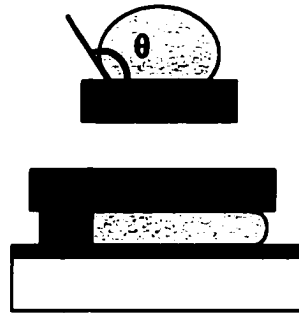


Figure 2.5: Water contact angles and corresponding droplet shape on (a) hydrophilic oxide and (b) hydrophobic surfaces. Underneath the hydrophilic beam, the concave meniscus creates a capillary force which acts to bring the cantilever beam into contact with the substrate. No such attractive capillary force exists underneath the hydrophobic beam; the meniscus maintains a convex curvature.

2.1.1.1.3 Hydrogen bridging

Hydrophilic silicon surfaces, under atmospheric conditions after drying and temperatures below 200°C, contain adsorbed water layers. When two of these hydrated surfaces are brought into close contact, hydrogen bonds may form between oxygen and the hydrogen atoms of the adsorbed water layers. The strength of most hydrogen bonds lies between 10 and 40 kJ/mol, yielding adhesion energies in the range of 90-350 mJ/m².⁽²²⁾

2.1.1.1.4 Van der Waals forces

This force is present in all materials and results from the interaction between the instantaneous dipole moments of atoms. Such forces are always present to some degree, but can be reduced by using surface layers having lower surface energy, such as hydrocarbon or fluorocarbon monolayers. The Van der Waals force between two flat and smooth surfaces is:

$$F_{vdw} = -\frac{HA}{2\pi g^2} \quad (2.3)$$

where H is the Hamaker constant (1.7 eV for Si/Si and 0.34 eV for SiO₂/SiO₂ in air) and A is the shared area of the two surfaces having a separation distance of "g".

2.1.1.1.5 Electrostatic forces

Electrostatic attractive forces under dry conditions may arise because of electrostatic charging or differences in the work functions of opposed surfaces. The former can result from kV-range potentials generated on wafer surfaces as a result of

etching, rinsing and drying. Charge trapping in the silicon nitride and oxide insulators may occur momentarily during processing. However, this non-equilibrium condition should relax with time, or upon contact between conducting surfaces.^(14,20) Neglecting the internal space charge regions, the electrostatic force acting between two flat surfaces with potential difference U separated by an air gap “ g ” with permittivity ϵ_0 is:

$$F_{el} = -\frac{\epsilon_0 U^2 A}{2g^2} \quad (2.4)$$

The effects of capillary, van der Waals and electrostatic attractive forces acting on two perfectly flat and parallel surfaces are compared in Figure 2.6. For capillary force, a contact angle of 0° and 85° is assumed. For electrostatic attraction, a 1 V potential difference is assumed since the work function difference for silicon yields at most 1 V potential difference in equilibrium. All forces increase by several orders of magnitude as the interfacial gap decreases, with the capillary force exhibiting the strongest attraction at all distances. The capillary force decreases with an increase in contact angle. The van der Waals and electrostatic forces become significant when the two surfaces are near contact. Therefore all of these forces must be manipulated to reduce adhesion. An effective treatment for these microstructures must provide a hydrophobic surface in order to avoid the formation of water layers on the surface, thereby eliminating capillary forces. The removal of the hydrophilic hydroxyl groups from the surface will also eliminate the possibility for hydrogen bonding as the two surfaces come into contact. To minimize electrostatic attraction, the two surfaces should be conductive, allowing charge dissipation to occur effectively.

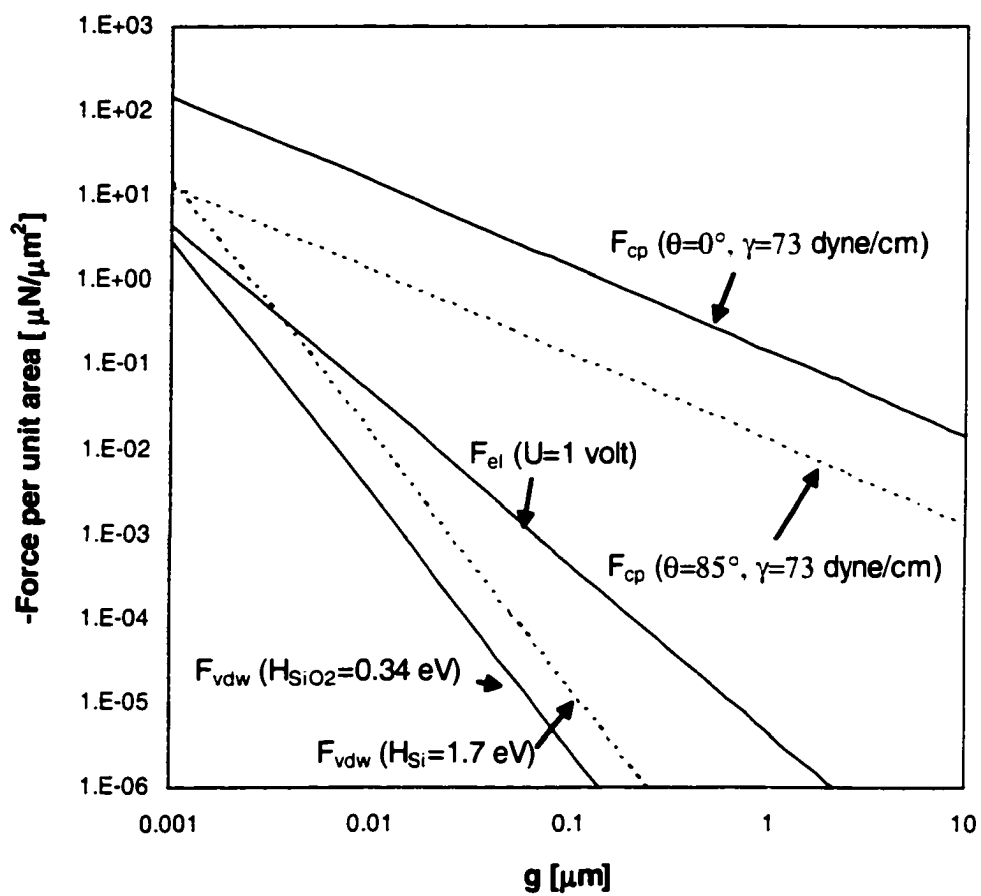


Figure 2.6: Variations of capillary, van der Waals and electrostatic forces per unit area with the surface separation distance for smooth surfaces

2.1.1.2 Preventing stiction

A number of methods have been investigated to reduce or prevent stiction. One technique consists on reducing the actual area of contact between the structure and underlying substrate and this has been done through the creation of surface roughness or the formation of microscale bumps on the surface.^(23,24) Matsumoto *et al.* carried out silicon anodization to roughened the silicon surface causing hillocks of a few tens of nanometer in height and a few hundreds of nanometer in diameter, so that water contact angle was increased over 100°. ⁽¹⁸⁾ Abe *et al.* have attempted to carry out the drying at elevated temperatures by exploiting the fact that surface tension of water and solvents decreases with increasing temperature.⁽⁴⁾ Fedder and Howe used breakable tethers to hold the device in place temporarily during sacrificial layer etching and drying. These tethers could be broken or melted following release, and stiction was never encountered.⁽²⁵⁾

The use of gas phase HF to totally eliminate liquid from the sacrificial etch process has also been investigated,⁽²⁶⁻²⁸⁾ Some of the drawbacks of this process are precipitation of etching byproducts on the surface, condensation of water on the etch surface that can induce stiction, usage of strong corrosive and toxic gases during etching, and protection of metal interconnects and pads is required during the release of the structures.. Lee *et al.*⁽²⁸⁾ were able to reduce water condensation by using anhydrous HF/CH₃OH mixture under low pressure.

The simplest approach to reduce capillary attraction is to use a rinse solution that exhibits a lower surface tension force during drying. Iso-propanol (IPA), methanol or

other low surface tension solutions, like n-hexane,⁽²⁹⁾ have been used during drying. But, it is not feasible to eliminate this problem with this approach because the surface tension force induced of even low surface tension solutions, like alcohols, is still high enough to cause release stiction.

Capillary forces can be avoided by using a supercritical drying process. In the ordinary drying process, liquid evaporates and capillary forces arise as a result of the surface tension of the liquid-vapor interface. In the supercritical drying process,^(5,6) liquid is transferred to vapor via the supercritical phase and hence there are no capillary forces to contend with. Carbon dioxide has been the material of choice for supercritical drying because of its low critical temperature and pressure ($T_c = 31.1^\circ\text{C}$, $P_c = 72.8\text{ atm}$).

A very effective method to reduce or prevent stiction is to make polysilicon surfaces hydrophobic (water contact angles higher than 110°) through the formation of self-assembled monolayers (SAM) using octadecyltrichlorosilane (OTS) precursor molecules dissolved in anhydrous organic solvents.^(1-3,30) Self-assembled monolayers are systems where a monolayer coating is formed spontaneously by the immersion of an appropriate substrate into a solution of the active precursor in an organic solvent. By making the surface hydrophobic, the capillary attraction that collapses the microstructure when the surfaces are hydrophilic is greatly reduced. As a result, microstructures come out of the final water rinse extremely dry without being broken or adhered to the substrate.

A typical sequence of steps used in the formation of SAM coatings is shown in Table 2.1. As may be discerned from this table, the process requires the use of several

organic solvents and results in organic and aqueous wastes. It would be highly desirable to develop a coating technique that is almost organic solvent free.

Table 2.1: Summary of the release and SAM-coating process for polysilicon microstructures⁽³⁾

1. Sacrificial Layer Etch	- Dilute HF (5:1 v/v H ₂ O)
2. Surface Oxidation	- H ₂ O rinse - H ₂ O ₂ soak - H ₂ O rinse
3. SAM Formation	- IPA rinse - Iso-octane rinse - OTS solution in 4:1 hexadecane:CCl ₄ or hexadecane:CHCl ₃ - Iso-octane rinse
4. Rinse and Dry	- IPA rinse - H ₂ O rinse - pull structures directly from water

Coatings that are useful in reducing stiction in micromechanical structures must meet several criteria. These coatings must be hydrophobic, with water contact angles greater than 110°. In addition, the coating must be conformal enough to cover the underside of the microstructure and thick enough to withstand vaporization, friction and wear. Furthermore, the coating must be durable and able to withstand humid

environments for many years without losing its hydrophobic properties. Finally, it must be compatible with the surface microstructure fabrication and release process and with the “back-end” processes of wafer dicing, die attachment, and final hermetic encapsulation.⁽¹³⁾ A major consideration is the temperature encountered during die attachment and hermetic encapsulation, which can be in the range of 350-525°C. Hence, the anti-stiction coating must also be capable of withstanding higher temperatures. The organic hydrophobic coatings of relevance to MEMS are octadecyltrichlorosilane (OTS), 1H, 1H, 2H, 2H-perfluorodecyl-trichlorosilane (FDTS), dichlodimethylsilane (DDMS) and Octadecene.⁽³¹⁾ Some of the properties for these coatings are listed in Table 2.2

Table 2.2: Physical property data of various coatings⁽³¹⁾

Surface Treatment	Contact Angle		Work of adhesion [mJ/m ²]	Coefficient of static friction	Thermal stability in air	Particulate formation
	Water	Hexadecane				
OTS ⁽³²⁾	110°	38°	0.012	0.07	225°C	High
FDTS ^(2,33)	115°	68°	0.005	0.10	400°C	Very high
DDMS ⁽³²⁾	103°	38°	0.045	0.28	400°C	Low
Octadecene ⁽³⁴⁾	104°	35°	0.009	0.05	200°C	Negligible
Oxide	0-30°	0-20°	20	1.1	---	---

In-use stiction depends greatly on the environment the devices are subject to, such as relative humidity (RH).⁽³⁵⁾ Water may eventually penetrate hermetically sealed devices and if the operating temperature of the device drops, RH levels can increase towards 100% because of the exponential dependence of RH on water content. Packaging

engineers are most often concerned with in-use stiction because of the potential reliability problems that it can cause; however, a phenomenon similar to release stiction can be a problem if devices are exposed to liquids during assembly – particularly during the wafer sawing operation. A technique to eliminate the possibility of encountering the structure is by the use of a hermetic seal around the microstructure. An example of this is the Motorola accelerometer, which uses a glass frit wafer bond that hermetically seals the microstructure from the environment, to eliminate the possibility of moisture from affecting the device. Table 2.3 summarizes the different anti-stiction techniques that have been reported in the literature. Most of these existing techniques present disadvantages and limitations.

The performance of surface modifications is often evaluated by a parameter called *detachment length*.⁽²²⁾ Cantilever beam arrays (Figure 2.7) are used to determine this length, where an array of micromachined polysilicon or silicon beams anchored to the substrate with different lengths parallel to the substrate is fabricated. The anchors can be made of silicon oxide or polysilicon. The length at which the beams exhibit a transition from adhered to free standing is identified as detachment length (l_d). Ideally, this length should be as large as possible. Figure 2.8 shows a cross section of a cantilever beam of length “ l ”, thickness “ t ” and width “ w ”, anchored at a initial gap spacing “ g ”. The beam attaches to the substrate at a distance “ x ” from the anchor.

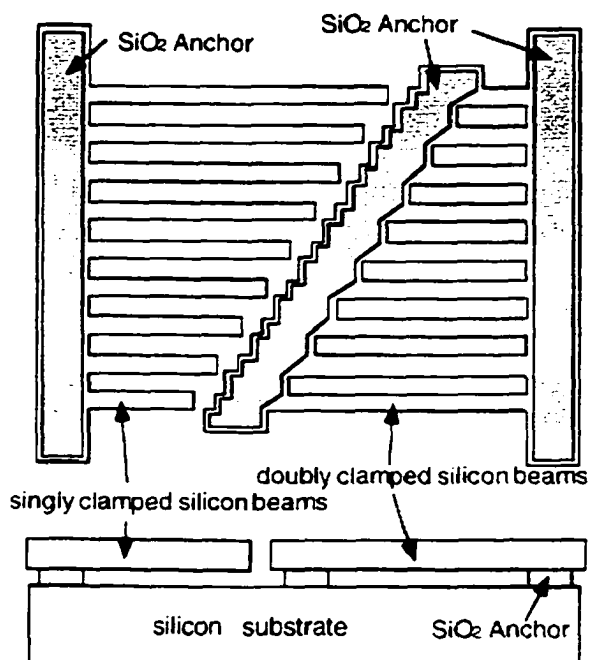


Figure 2.7: Schematic of a cantilever beam array of different lengths with single and doubly clamped beams⁽¹⁵⁾

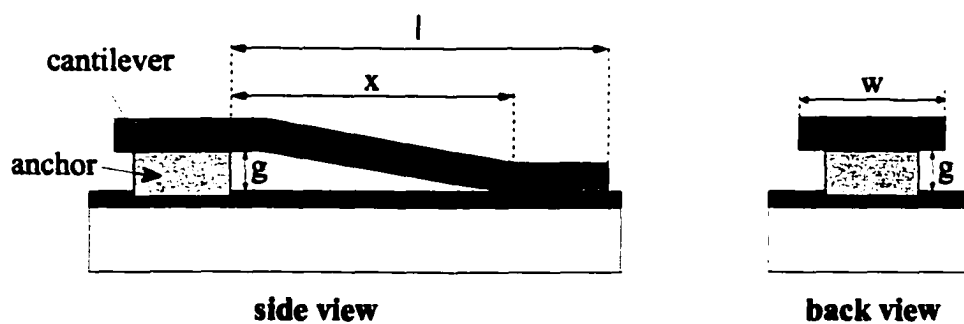


Figure 2.8: A cantilever beam of length l , width w and thickness t , anchored at a gap spacing g . The beam adheres to the substrate at a distance x from the anchor, which is called "stiction length"

Table 2.3: Comparison between different anti-stiction techniques

Technique	Stiction preventing	Advantages	Disadvantages	Beam release/Surface Treatment	Water Contact Angle [deg]	Cantilever Beam Array Dimensions (CBA)	Detachment length (μm)
Supercritical CO_2 drying ^(5,6)	release	<ul style="list-style-type: none"> - low surface tension - virtually inert - non-flammable - non corrosive - readily available - high purity grades - low viscosity - low critical pressure - low critical temperature 	<ul style="list-style-type: none"> - complicated setup - equipment operates wafer by wafer - CO_2 is only a liquid at pressures greater than 900 psi 	<ul style="list-style-type: none"> • HF etch • H_2O rinse • MeOH or acetone rinse, soak • Supercritical CO_2 dry 		t: 2.25 μm g: 2 μm w: 10 μm and 20 μm l: 10 to 100 μm in 2 μm increments; 100 to 500 μm in 5 μm increments	850 ⁽⁵⁾ >500 ⁽⁶⁾
HF treatment	release	- simple	- Surface reoxidizes during drying	<ul style="list-style-type: none"> • HF etch • H_2O rinse • 4:1 MeOH:H_2O rinse, soak • MeOH soak • Supercritical CO_2 dry 	86	t: 2.2 μm g: 2 μm w: 10 μm l: 50 to 60 μm in 10 μm increments; 260 to 1000 μm in 20 μm increments	520 ^(3,13)
NH_4F treatment ⁽³⁶⁾	release		- Surface reoxidizes during drying	<ul style="list-style-type: none"> • HF etch • NH_4F etch • H_2O rinse • MeOH:Water rinse • MeOH soak 	97	t: 2.1 μm g: 2.5 μm w: 40 μm l: 10 to 300 μm in 1 μm	>300 ^(1,36)

Table 2.3 - Continued

				<ul style="list-style-type: none"> • Supercritical CO₂ dry 		increments	
Dry release with HF-vapor phase ⁽²⁸⁾	release	<ul style="list-style-type: none"> - no liquid involved - excellent results 	- complicated setup	<ul style="list-style-type: none"> • HF/MeOH vapor etching 			
Thin oxide passivation (H ₂ O ₂)	release		- Surfaces are hydrophilic	<ul style="list-style-type: none"> • HF etch • H₂O rinse • H₂O₂ soak • H₂O rinse • MeOH rinse, soak • Supercritical CO₂ dry 	0-30	t: 2.2 μm g: 2 μm w: 10 μm l: 50 to 60 μm in 10 μm increments; 260 to 1000 μm in 20 μm increments	117 ⁽¹¹⁾
Surface Roughening	release and in-use	- reduce real contact area					300 ⁽²⁴⁾
Pinpoint Polysilicon Bumps ⁽⁷⁾	release and in-use	<ul style="list-style-type: none"> - reduce contact area to dimensions smaller than the resolution of the photolithography used - pull-down force is reduced 					

Table 2.3 - Continued

<p>Polymeric sacrificial supports⁽³⁸⁾</p>	<p>release</p>	<ul style="list-style-type: none"> - prevent structure contact by employing polymeric spacers under the structural layer that are etched away in a dry plasma system 	<ul style="list-style-type: none"> - this process can only be used with low temperature processing 				
<p>Fluorocarbon coating formed by plasma polymerization^(22,39)</p>	<p>release and in-use</p>	<ul style="list-style-type: none"> - low friction and wear 	<ul style="list-style-type: none"> - the highly directional ion impingement coupled with the short diffusion length of the plasma, results in a mostly line of sight growth 				
<p>Self-Assembled Monolayers</p>	<p>release and in-use</p>	<ul style="list-style-type: none"> - extremely hydrophobic surfaces - low surface energy - long term passivation - no capillary forces - densely packed structure - very low work of adhesion values 	<ul style="list-style-type: none"> - coatings are applied using organic solvents - OTS-based SAM has a marked reduction in contact angle in air at 150°C - Chlorine in OTS may cause corrosion of aluminum 	<ul style="list-style-type: none"> • HF etch • H₂O rinse • H₂O₂ soak • FDTS or OTS (organic media) SAM formation. Coating time: 10-15 min. • Propanol rinse • H₂O rinse 	<p>FDTS: 115 OTS: 112</p>	<p>t: 2.2 μm g: 2 μm w: 10 μm l: 50 to 60 μm in 10 μm increments; 260 to 1000 μm in 20 μm increments</p>	<ul style="list-style-type: none"> - surface roughness of 12 nm: OTS: 950⁽⁴⁰⁾ FDTS: 1000⁽⁴⁰⁾ - surface roughness of 3 nm: OTS: 550⁽⁴⁰⁾ FDTS: 780⁽⁴⁰⁾

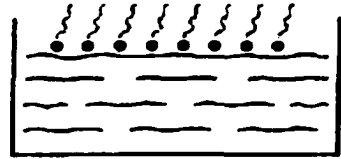
Table 2.3 - Continued

			metal interconnect lines				
Alkene based monolayers (14)	release and in-use			<ul style="list-style-type: none"> • HF etch • H₂O rinse • HF etch • IPA rinse • 1 octadecene treatment at 180°C. Coating time: 30 min. • Petroleum ether rinse • IPA rinse • H₂O rinse 	104	t: 2.5 μm g: 2 μm w: 20μm l: 150 to 1700 μm in 50 μm increments	820
Dichloromet hylsilane (DDMS) ⁽¹²⁾	release and in-use			<ul style="list-style-type: none"> • HF etch • H₂O rinse • 30% H₂O₂ (90°C/15min) soak • H₂O rinse • IPA rinse • DDMS (organic media for 1 hour) coating formation • IPA rinse • H₂O rinse (Lab Conditions: 20°C and 50% RH) 	103	t: 2.5 μm g: 2 μm w: 20μm l: 150 to 1700 μm in 50 μm increments	540

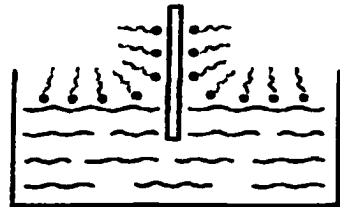
2.2 Self-assembled monolayers and Langmuir-Blodgett films

Figure 2.9 schematically shows the most common methods to prepare crystalline organic thin films.^(40,41) Monolayers formed by a substance that is insoluble in the liquid subphase are called *Langmuir layers*, whereas those formed by substances soluble in the bulk but adsorbed preferentially at the interface are known as *Gibbs layers*. Langmuir films consist of amphiphilic molecules spread on a liquid surface. The hydrophilic headgroup has an affinity to the water while the hydrophobic endgroup sticks out on the other side. Langmuir layers transferred to solid substrates are known as *Langmuir-Blodgett (LB) layers*. These films are typically weakly bound to the substrate. Multilayers can be prepared by repeated (periodic) dipping of the substrate in appropriate solutions. *Self-Assembled Monolayers (SAMs)* grown from solution or from the gas-phase, represent another class of organic thin films. SAMs are ordered molecular assemblies formed spontaneously by chemisorption of molecules with suitable anchor groups on a solid surface. They have a stable, homogeneous, oriented, and well ordered molecular structure.

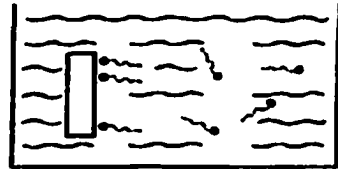
- Langmuir Films
amphiphilic molecules
at liquid/gas interface



- Langmuir-Blodgett Films
Langmuir films
transferred onto solid substrate



- Self-Assembled Monolayers
grown from solution



- Self-Assembled Monolayers
grown from vapor

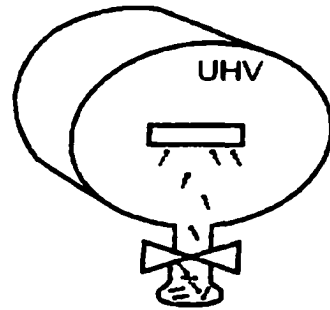


Figure 2.9: Approaches to prepare crystalline organic thin films⁴⁰⁾

2.2.1 Langmuir isotherms

Many amphiphilic molecules that are nearly insoluble in water can form a monolayer at the air-water interface. The area available to each molecule (A) can be decreased by imposing an external surface pressure (Π), which lowers the normal air-water surface tension γ_0 to γ ($\Pi = \gamma_0 - \gamma$). Measurements of Π versus A at constant temperature (Figure 2.10) are known as isotherms. At large surface areas per molecule, monolayers are *gaseous*, where the hydrophobic portions of the molecule make significant contact with the water surface but little contact with each other. As the monolayer is compressed into the *liquid-expanded* (LE) phase, the hydrophobic parts of the molecules come into contact with each other and lift from the water surface but remain largely disordered and fluid. Further compression leads to a first order transition to the *liquid-condensed* (LC) phase, where the molecules exhibit long range order, are less compressible, and less fluid than in the LE phase. A kink in the isotherm at higher Π marks the transformation to a better ordered *solid* (S) phase, in which the hydrocarbons chains are oriented vertically and packed together. The film is relatively incompressible. If the slope of the isotherm for this region is extrapolated to the abscissa, this area (a_0) corresponds to the molecular cross-section when the molecules are oriented perpendicular to the surface.^(42,43)

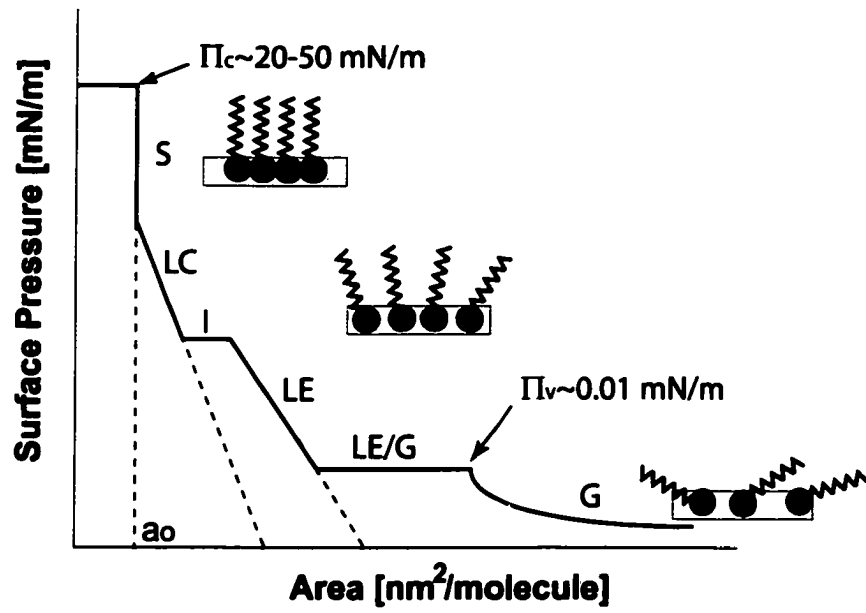


Figure 2.10: Surface pressure versus area isotherm

Eventually, the surface pressure reaches a limiting value beyond which the monolayer can not be compressed further. Such pressure is known as the *collapse pressure* and depends on the nature of the substance, temperature, rate of compression and previous history of the film itself. At these limiting conditions, a flat monolayer is similar mechanically to a plate under compression; as the pressure is increased past the limiting value, the plate can (i) fracture and break, (ii) buckle at constant area, or (iii) lose material (and hence interfacial area) depending on the elastic and solubility properties of the monolayer.⁽⁴⁴⁻⁴⁷⁾

It is important to study the pressure-area isotherm of the monolayer as a prerequisite to the determination of dipping conditions. From the isotherm, information can be obtained as to the way in which the molecules pack at the interface and the stability of the compressed layer at high pressures.

2.2.2 Langmuir-Blodgett films

The transfer of Langmuir films from the air-liquid surface to a solid substrate is known as *Langmuir-Blodgett (LB)* deposition. The film is transferred to the solid as it is passed vertically through the liquid interface. The LB method for organic film deposition has the advantage of preparing highly ordered densely packed and defect-free thin molecular films. However, its application in manufacturing is limited. The quality and stability of LB films are mainly affected by the properties of monolayers on the sub-phase and by the transfer condition from liquid to the solid support. The surface pressure

of the monolayer under which the transfer is carried out and the transfer rate are very important in controlling the arrangement and orientation of the molecules on a solid support.

2.2.3 Self-assembled monolayers

Self-assembled monolayers (SAMs) are ordered molecular assemblies that are formed spontaneously by the adsorption of a precursor with a specific affinity of its headgroup to the substrate. Figure 2.11 shows a schematic outline of the SAM preparation procedure, as well as, the constituents of a SAM-molecule (headgroup, chain or backbone, endgroup). The ease of preparation and the low costs of solution deposition are one important reason for the popularity of SAMs. The substrate simply has to be dipped into the corresponding solution for a certain period of time, and the monolayer will assemble. Successful self-assembly requires a relatively strong bond between the substrate and an atom or moiety in the molecule, and an additional lateral interaction between molecules in the monolayer.

SAMs on metals and oxides are created by the adsorption of long-chain acids, alkythiols, alkyltrichlorosilanes or alkoxy silanes. SAMs of alkylchlorosilanes (RSiCl_3), alkylsiloxanes ($\text{RSiO}_x(\text{OH})_y$) and alkylaminosilanes have been deposited onto silicon oxide surfaces.⁽⁷⁾ The primary advantage of a thin-film SAM over an LB film is its stability, due to the strong chemical bonds with the surface.

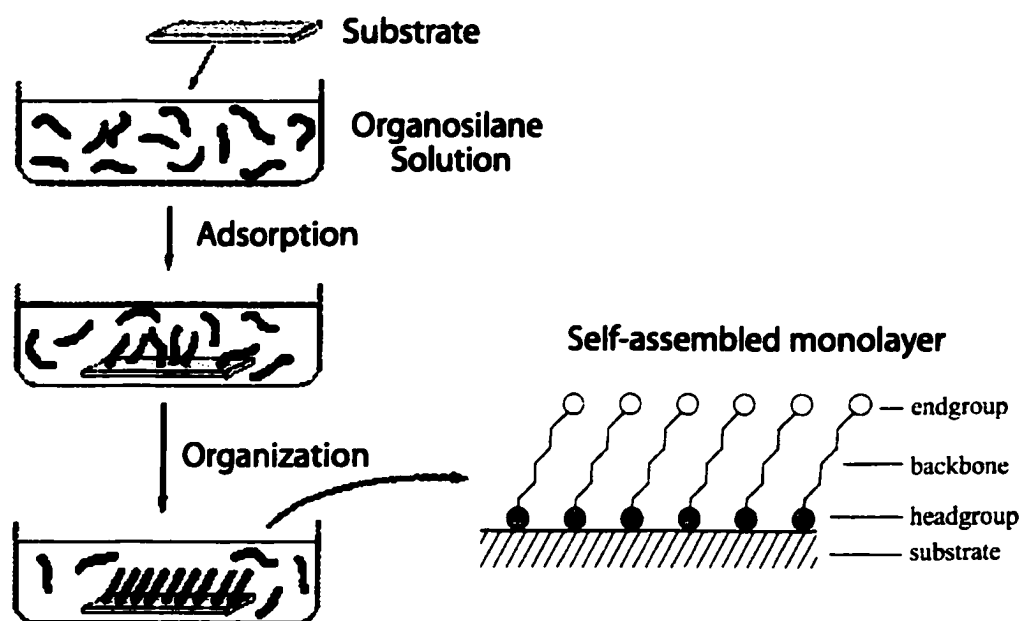


Figure 2.11: Preparation of self-assembled monolayers. The pre-oxidized silicon substrate is immersed into a solution of the desired organosilane. Initial adsorption is fast (seconds); then organization of the molecules occurs. A schematic of a fully assembled SAM is shown to the right

The structure of alkylchlorosilanes SAMs on pre-oxidized silicon has been studied extensively.^(8,10,48-53) AFM studies⁽⁵⁴⁻⁵⁸⁾ have shown the formation of both a dense organized assembly with vertically aligned hydrocarbon chains and domains with disordered molecules that have not self-assembled. The relative proportions of the different phases depend on water concentration, solution age, temperature, silane concentration, exposure or reaction time and substrate pretreatment. The presence of large particulates that are up to several microns in diameter has been observed on OTS coatings prepared at 50% relative humidity and 20°C.⁽³²⁾

2.2.3.1 Transition Temperature

Several authors^(56,59-63) have reported the existence of a transition temperature (T_c) for the formation of well organized monolayers of *n*-alkyltrichlorosilanes on oxidized silicon. When silanization is performed below T_c , monolayers of high quality are obtained. In contrast, when prepared above T_c , the films exhibit monotonically decreasing coverage with increasing temperature as the alkyl chains increasingly assume higher conformational disorder.

Brzoska *et al.*⁽⁵⁹⁾ studied the influence of the temperature of reaction during silanization over an extended range of temperature (-1 to 60°C), and for *n*-alkyltrichlorosilanes of different lengths ($n=10$ to 22). They determined the value of T_c through critical surface tension values derived from contact angle data of three different alkanes (*n*-octane, nonane and decane) on the coated surfaces. The transition temperature values were linear as a function of chain length, with a T_c shift of $3.5 \pm 0.5^\circ\text{C}$ per

additional methylene (-CH₂-) group in the grafted chain. The critical temperature for octadecyltrichlorosilane was ~28°C. This temperature is in excellent agreement with the value obtained using contact angle measurements, nulling ellipsometry and infrared spectroscopy by Parikh *et al.*⁽¹²⁾

The critical temperature for ordering of the alkyl chains has been interpreted in terms of the two-dimensional phase diagram from Langmuir monolayers of long chain fatty acids at the air-water interface.^(56,59,64) Figure 2.12 shows a schematic surface pressure versus area per molecule diagram which allows the various thermodynamic states of the monolayer to be distinguished. At high temperature, the monolayer state can change from gas (G) to liquid expanded (LE) and finally to liquid condensed (LC) physical states as the monolayer surface density (i.e. decreasing the area per molecule A) is increased, whereas at low temperature the G phase is directly followed by the LC phase. There is a well-defined temperature T_0 , called the triple point, which separates the high-temperature and low-temperature behaviors. Kellner *et al.*⁽⁶⁵⁾ determined that T_0 is a function of alkyl chain length n and that it increases linearly by roughly 10°C for each additional methylene group. Above T_0 , the coexistence of two successive regions (G/LE and LE/LC) is observed upon increasing the surface density. Below T_0 , the coexistence of only one region (LC/G) in the phase diagram is observed.

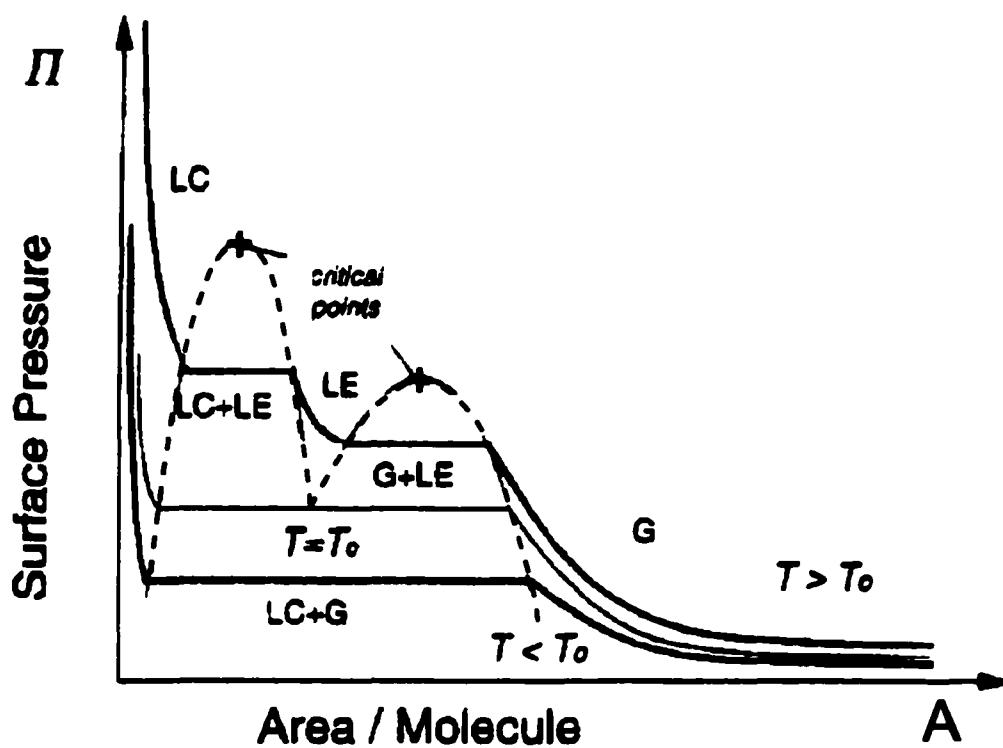


Figure 2.12: Typical phase diagram of a Langmuir monolayer of insoluble surfactants spread at the air-water interface. Solid lines denote the isotherms and the coexistence curves are denoted by dashed lines⁽⁵⁹⁾

Carraro *et al.*⁽⁵⁶⁾ determined using atomic force microscopy on OTS films that T_c is not the counterpart of the triple point temperature T_o in the Langmuir films. For $T < T_o$, self-assembly proceeds initially by island growth only, the substrate between islands remaining essentially unfilled; such a growth pattern is characteristic of a Langmuir film nucleates liquid-condensed (LC) domains coexisting with the gas phase below the triple point. For $T > T_o$, island growth occurs more slowly, while the substrate between islands is gradually filled in with OTS molecules. This growth regime is attributed to nucleation of LC domains coexisting with a liquid-expanded phase. This mechanism operates only up to a characteristic temperature T_c , above which no island nucleation occurs but homogeneous growth of a disordered monolayer takes place instead.

A schematic illustration of monolayer formation at different adsorption temperatures is shown in Figure 2.13.⁽⁶³⁾ Upon first contact of the substrate with the silane solution, only a few molecules adsorb and the monolayer is in its gaseous state. At longer times, the surface coverage eventually reaches the point where a coexistence phase exists. At low temperature, the coexistence is between LC and G phases, and LC domains of close-packed chains are formed. Further adsorption takes place into the gaseous portion of the monolayer, and the process repeats itself until the whole monolayer is in the LC state. At high temperature (above T_o), the coexistence is first between the LE and the G phase, and the monolayer goes through a homogeneous LE state. This state, made of disorganized aliphatic chains, but at the same time considerably denser than the gaseous phase, opposes a strong barrier to further adsorption. It is then possible that the monolayer is unable to reach its densest LC state, resulting in poor layer quality.

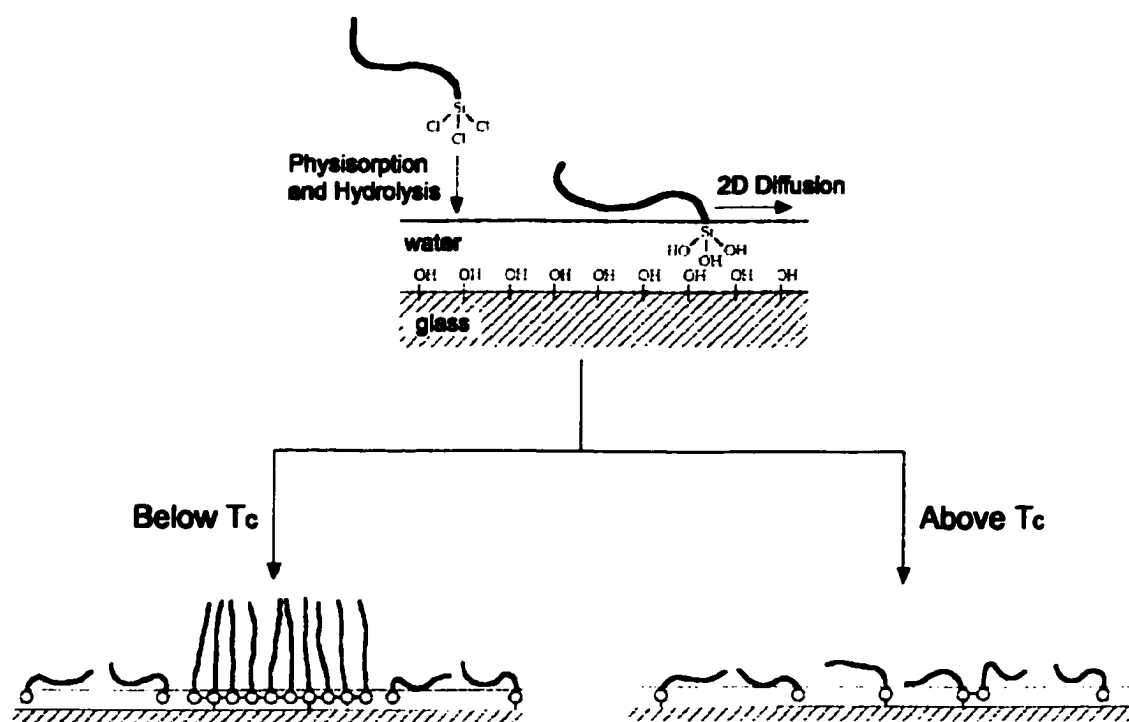
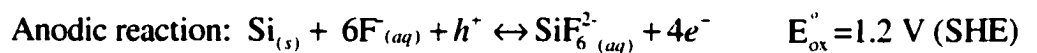


Figure 2.13: A schematic of formation of alkyldichlorosilane SAM coatings depending on adsorption temperature⁽⁶³⁾

2.2.3.2 Defects in self-assembled monolayers

Structural defects⁽⁶⁶⁻⁶⁸⁾ that have been identified to exist on alkyl mercaptane and n-alkanethiol SAMs deposited on gold (Figure 2.14) are: (i) *pinholes or pores* where no molecules are adsorbed onto the surface, (ii) “*lying-down*” molecules near these pinholes that in fact cover the defects and (iii) *collapsed sites* where differently tilted molecules at the boundaries of differently oriented domains give rise to a thin layer. These defects have been characterized through their impact on electron-transfer reactions, which can be studied using electrochemical impedance spectroscopy in aqueous chloride solutions. The largest electron-transfer rate constants were exhibited at sites with pores, somewhat smaller rate constants were found at the “collapsed” sites, and the smallest values were obtained for well-oriented monolayers. Defect free coatings have the advantage of exhibiting very large energy barriers to carrier tunneling that makes them exceptional insulators for nanoscale devices.⁽⁶⁹⁾

In the case of coatings formed on oxidized silicon, hydrofluoric acid solutions can be effectively used to probe liquid penetration into the coatings. Hydrofluoric acid solutions upon penetration through the coating attack the oxide layer and thereby promote charge transfer reactions at the Si/HF solution interface in the absence of dissolved oxygen. The corresponding charge transfer reactions are^(70,71):



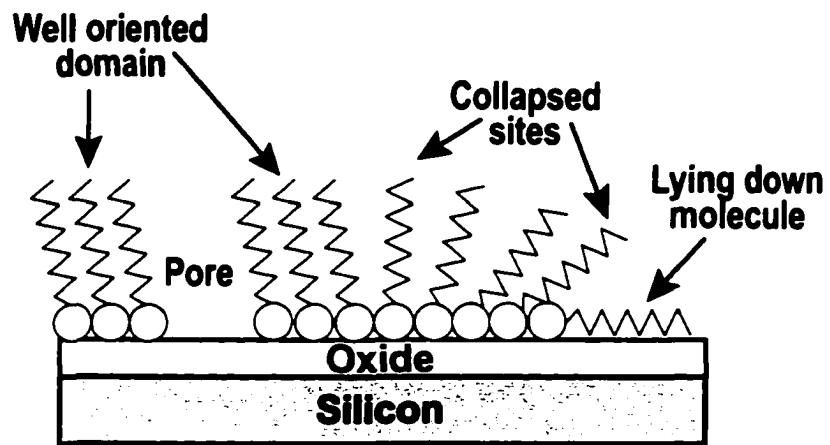


Figure 2.14: Schematic representation of defects in organosilane films

2.3 Chemistry of organosilanes

2.3.1 Hydrolysis and condensation

Trifunctional organosilanes, such as trichlorosilanes (RSiCl_3) and trialkoxysilanes (RSi(OR)_3), are preferred in surface modification reactions because they form networks, cross-linking on the surface. These organosilanes hydrolyze in water to give the corresponding silanols, which ultimately condense to siloxanes. Both reaction rates are strongly dependent on pH, silane concentration, water and solvent content, but under optimum conditions the hydrolysis is relatively fast (minutes), while the condensation reaction is much slower (several hours).⁽⁷²⁾ A simplified view of the reactions is shown in Figure 2.15.⁽⁷³⁾ The hydrolysis reaction, through the addition of water, replaces alkoxide groups (OR') with hydroxyl groups (OH). The silanol-containing species (Si-OH) are highly reactive intermediates which are responsible for siloxane bond (Si-O-Si) formation plus water as a by-product. When the trialkoxysilanes encounter an existing inorganic oxide surface, the polymerization process can be intercepted by the Si-OH groups at the interface, first by hydrogen bonding and then, upon curing, a permanent bond can be formed.

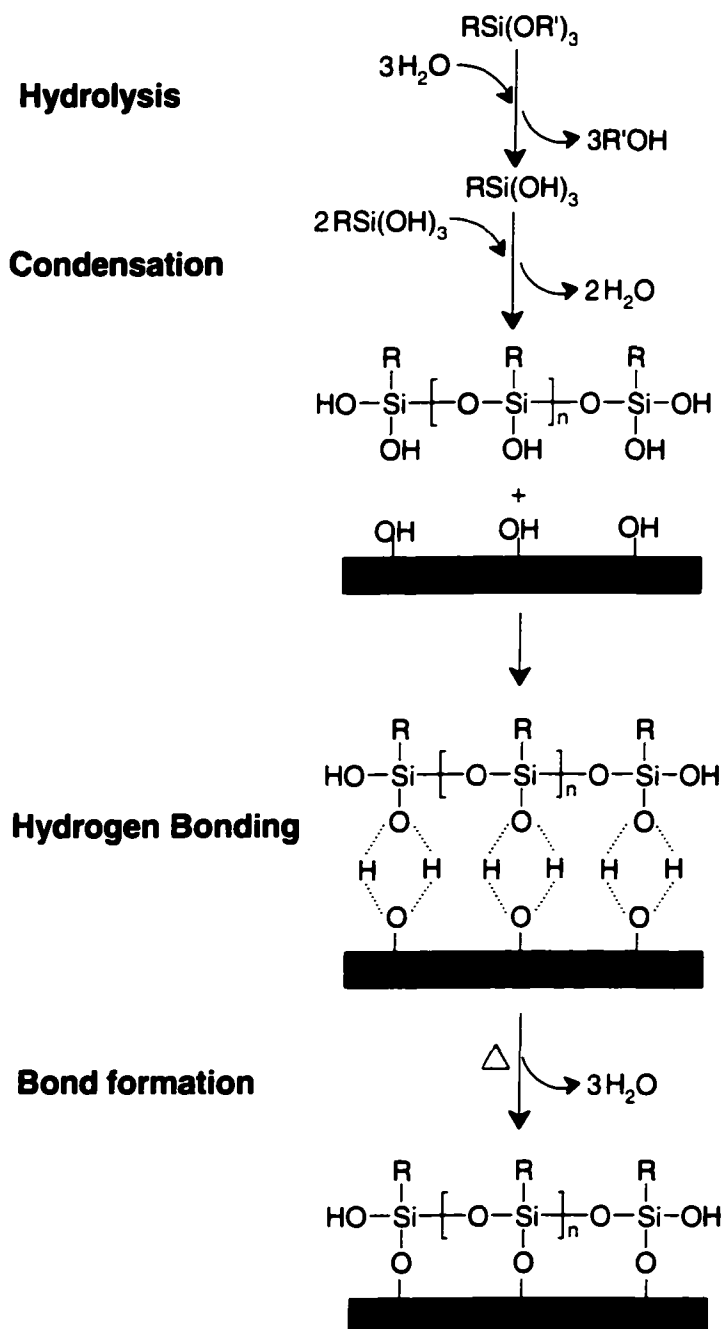


Figure 2.15: Reaction and bonding mechanism of alkoxy silanes⁽⁷³⁾

Although hydrolysis can occur without addition of external catalysts, it is most rapid and complete when they are employed. Mineral acids (HCl) and ammonia are the most commonly used, however, other catalysts are acetic acid, potassium hydroxide (KOH), amines, potassium fluoride (KF) and hydrofluoric acid (HF).⁽⁷⁴⁾ Additionally, it has been observed that the rate and extent of the hydrolysis reaction is most influenced by the strength and concentration of the acid- or base catalyst.

The relative rate of hydrolysis for halogen substituted silanes is $I > Br > Cl > F$.⁽⁷⁵⁾ The byproduct of hydrolysis is the hydrohalic acid. Alkoxysilanes are less reactive because they generate no acid on hydrolysis. The rates of hydrolysis of the alkoxy groups can also be affected by steric effects. For example, increasing the chain length of the alkoxy group and increasing the number of alkoxy substitutions will decrease the rate of hydrolysis:⁽⁷³⁾



2.3.1.1 Effect of pH

Alkoxysilanes undergo hydrolysis and condensation under both base- and acid-catalyzed conditions, but occurs only very slowly at neutral pH value. *Acid-catalyzed hydrolysis* (Figure 2.16) involves a fast reversible protonation step, followed by an electrophilic attack by water. This results in the formation of a penta-coordinate transition state with significant S_N2 -type character.^(74,76) The transition state decays by displacement of an alcohol and inversion of the silicon tetrahedron.⁽⁷⁷⁾ The reaction rate is governed by the concentration of H^+ in solution. The lower the pH, the faster the reaction proceeds.

Base-catalyzed hydrolysis proceeds much more slowly than acid-catalyzed hydrolysis at an equivalent catalyst concentration.⁽⁷⁸⁾ Basic alkoxide oxygens tend to repel the nucleophile, OH⁻. However, once an initial hydrolysis has occurred, following reactions with each subsequent alkoxide group will be removed from the monomer more easily than the previous one.⁽⁷⁹⁾ Therefore, more highly hydrolyzed silicones are more prone to attack. Because this mechanism has a penta-coordinated silicon atom in the activated complex, hydrolysis of a polymer is more sterically hindered than the hydrolysis of a monomer. Thus, under basic conditions, it is likely that water dissociates to produce hydroxyl anions in a rapid first step. The hydroxyl anion then attacks the silicon atom. Again, an S_N2-type mechanism has been proposed in which the -OH displaces -OR. This is seen in Figure 2.17.

Acid-catalyzed condensation mechanism (Figure 2.18) involves protonated silanol species. Protonation of the silanol makes the silicon more electrophilic and thus susceptible to nucleophilic attack. The most basic silanol species (silanols contained in monomers or weakly branched oligomers) are the most likely to be protonated. Therefore, condensation reactions may occur preferentially between neutral species and protonated silanols situated on monomers, end groups of chains, etc.⁽⁷⁴⁾

The mechanism for the *base-catalyzed condensation* reaction involves the attack of a nucleophilic deprotonated silanol (SiO⁻) on a neutral silicate species (Figure 2.19).⁽⁸⁰⁾

Furthermore, it is generally believed that the base-catalyzed condensation mechanism is valid in the pH range of 3-12⁽⁷⁸⁾ and involves penta- or hexa-coordinated silicon intermediates or transition states, similar to that of a S_N2 type mechanism.⁽⁷⁴⁾

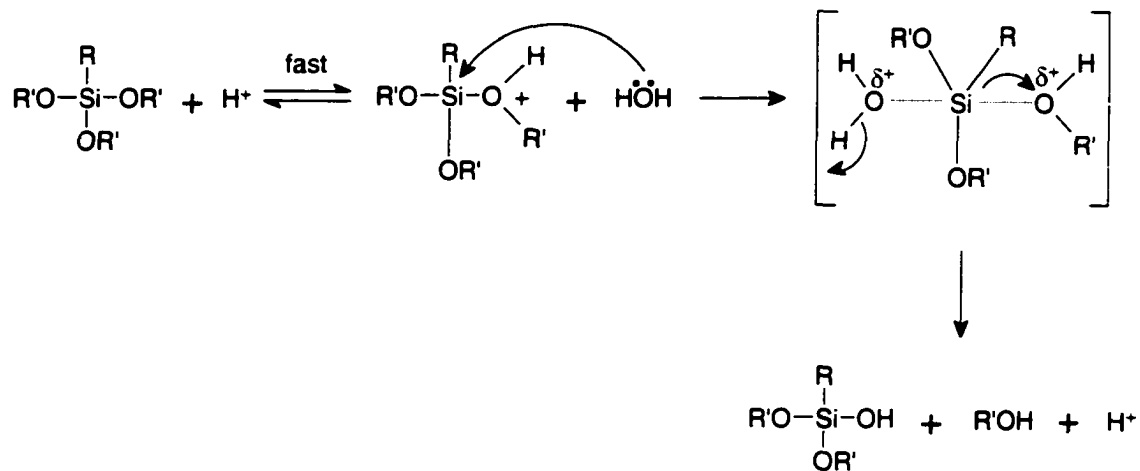


Figure 2.16: Acid-catalyzed alkoxy silane hydrolysis

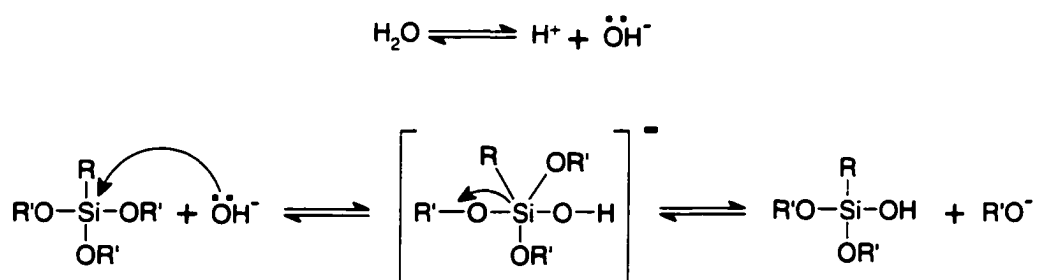


Figure 2.17: Base-catalyzed alkoxy silane hydrolysis

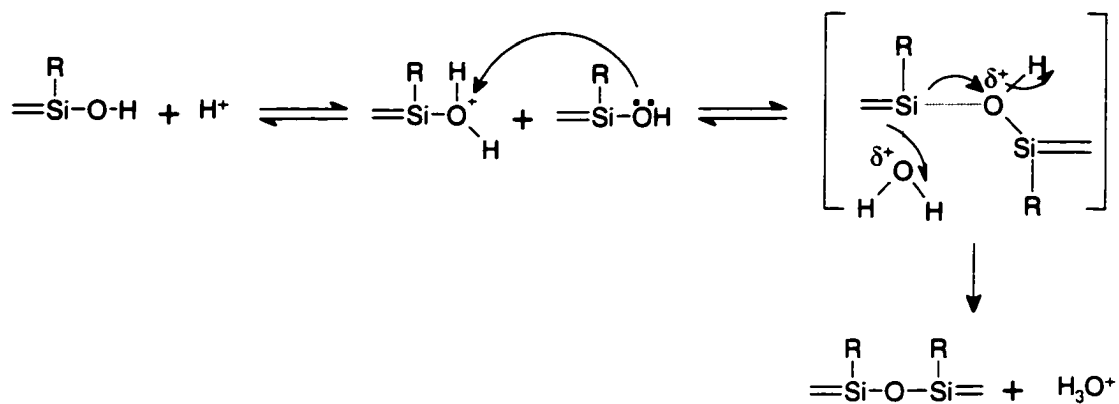


Figure 2.18: Acid-catalyzed alkoxy silane condensation



Figure 2.19: Base-catalyzed alkoxy silane condensation

It can be seen in Figure 2.20 how pH affects the rate of hydrolysis and condensation.⁽⁸¹⁾ The hydrolysis reaction proceeds under both acidic and basic conditions, but occurs only very slowly at neutrality (pH=7). The condensation reaction is fastest at a pH of about 5-6. The overall maximum reaction rate for hydrolysis and condensation occurs at a pH of 4.

Figure 2.21 shows the changes in silane condensation and polymerization under acid versus base condition. Under acidic conditions, the condensation reaction is the rate-limiting step. As a result, weakly branched polymeric networks are initially formed, which at high conversion more completely crosslink to give "crosslinked spaghetti". By contrast, under basic conditions, hydrolysis turns out to be the rate-limiting step. As a result, three-dimensional clusters are initially formed. Further condensation increases the size of the clusters, which then coalesce into a 3D web comprised of a linked network of dense particles.

Acidic catalysis is preferred to maximize the solution life of silanol species, because fast hydrolysis is followed by slow condensation. If base catalysis is used, condensation to siloxane may occur even before all the alkoxy groups are hydrolyzed, promoting gelation.⁽⁸²⁾

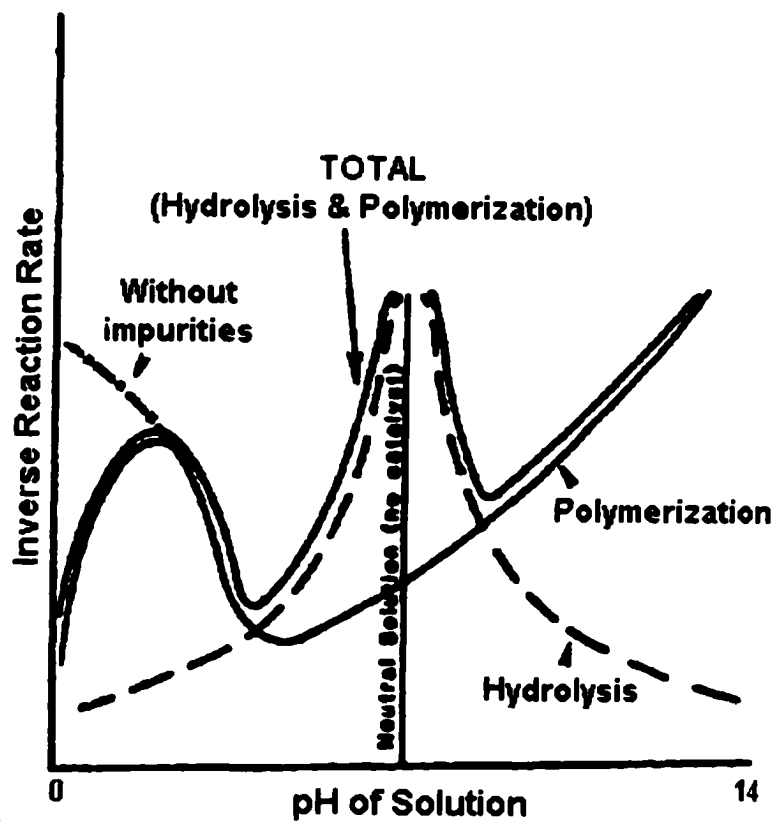


Figure 2.20: pH dependence of alkoxy silanes hydrolysis and condensation^(S1)

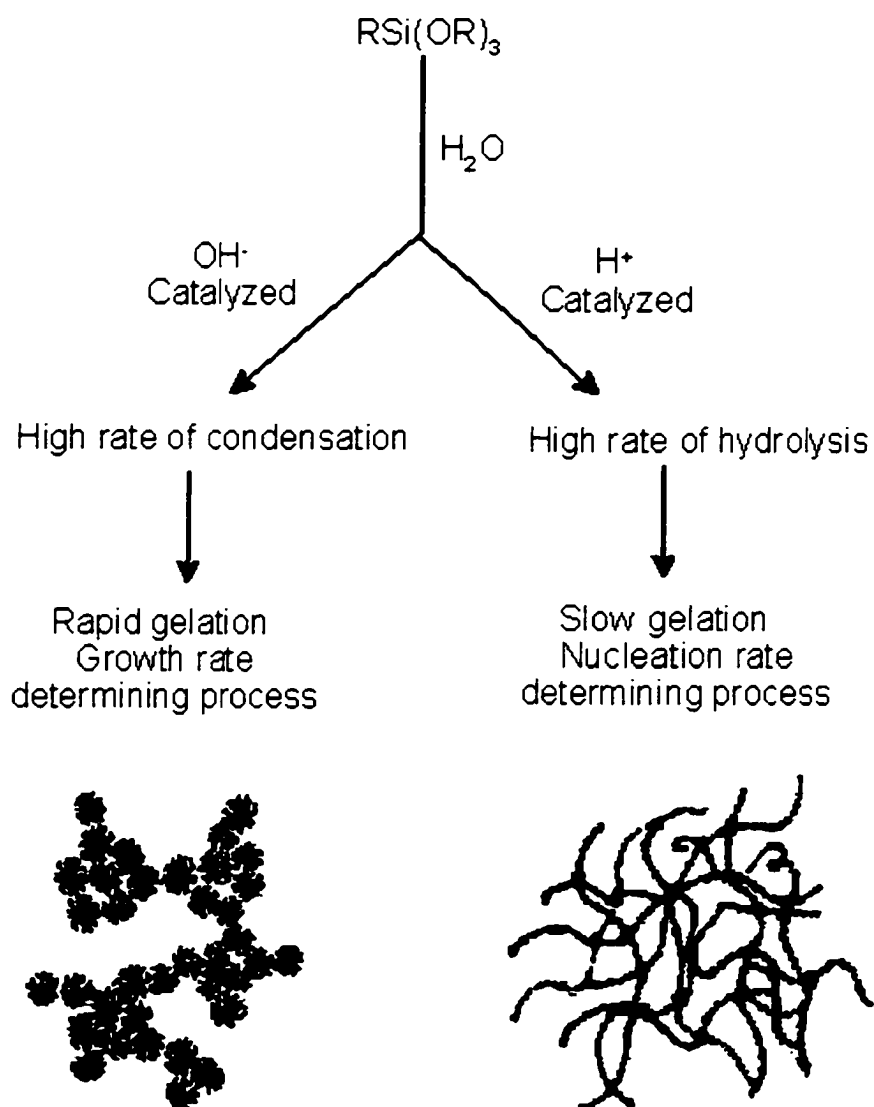


Figure 2.21: Effect of pH on alkoxy silane hydrolysis⁽⁷³⁾

2.3.2 Deposition of organosilane coatings from organic media

High quality SAMs of alkyltrichlorosilane derivatives are not easy to form, mainly because of the need to carefully control the amount of water in the liquid medium used for deposition.^(8-10,83) The presence of adsorbed water between the substrate and the organic layer has been reported^(11,34,55) to be necessary for optimum monolayer deposition. Insufficient water leads to an incomplete monolayer whereas a thick water layer gives rise to a polymerized silane layer which can sit on top of the surface water layer. In the case of octadecyltrichlorosilane (OTS) no reaction occurs in the absence of water or with a single water layer, because tightly bound water is not reactive enough to participate in the hydrolysis of chlorosilane groups. As a result, the solvents used for SAM coating with RSiCl_3 precursors must be as anhydrous as possible. Typically, for an octadecyltrichlorosilane (OTS) coating, an alkane is used with 30 vol.% of a co-solvent such as carbon tetrachloride (CCl_4) or chloroform (CHCl_3).⁽¹²⁾ CCl_4 is believed to help in dehydrating the structures prior to film formation, help solvate the OTS head group in the solvent mixture, and to rinse away excess OTS molecules which may be physisorbed to the surface. Often curing or baking of the coating in air at temperatures between 100 and 200°C is carried out to enhance the cross-linking process to produce a more densely packed and stable film. The curing completes the lateral condensation reaction between adjacent silane molecules to form a 2-dimensional cross-linked silane layer.⁽⁸⁴⁾

The mechanism of silanization in the presence of small amounts of water is summarized in Figure 2.22.⁽⁵⁹⁾ An initial water layer exists on the substrate onto which the organic molecules contained in the reactive solution gradually adsorb (stage 1).

Following physisorption, trichlorosilane head groups hydrolyze and form trisilanols (stage 2). The presence of a thin film of water permits the in-plane lateral mobility of the long chain silanes by Brownian motion in the water film. During the two-dimensional random walk, the species are captured by the surface silanol groups through covalent or hydrogen bondings (stage 3) or collide with others, to produce immobilized nuclei or mobile clusters.⁽⁶³⁾ Finally, intermolecular cross-linking by the silanol groups of the adsorbed molecules occurs. Stages 3 and 4 can be facilitated by moderate baking of the substrate, which helps the removal of the water layer.

The effect of curing after derivatization of silica gel with trifunctional silanes has been studied using NMR by Caravajal⁽⁸⁶⁾ and Vansant⁽⁸⁷⁾. They concluded that the curing process increases number of Si-O-Si bonds. The increase could be attributed either to surface Si-O-Si, or intermolecular Si-O-Si bond formation. A detailed study of the hydrolysis of trichlor-, dichloro- and mono-chloromethylsilanes on hydrated silica surface and the effect of curing in post-reaction treatment was done by Tripp and Hair.⁽⁸⁸⁾ Based on IR experiments they showed that: (1) at the gas-solid interface methylchlorosilanes are fully hydrolyzed to methylsilanols due to the surface water on the hydrated silica; (2) the percentage of the adsorbed methylsilanols condensing with the surface hydroxyl groups follows the order $(\text{CH}_3)_3\text{SiOH} > (\text{CH}_3)_2\text{Si}(\text{OH})_2 > \text{CH}_3\text{Si}(\text{OH})_3$; (3) for trihydroxy- and dihydroxy-dimethylsilanols the curing process mostly completes cross-linking, and also results in a few attachments to the surface through Si-O-Si_s bonds. In case of trimethylsilanol lateral polymerization is not possible, and the curing process mostly results in removal of physically adsorbed silanol species from the silica surface.

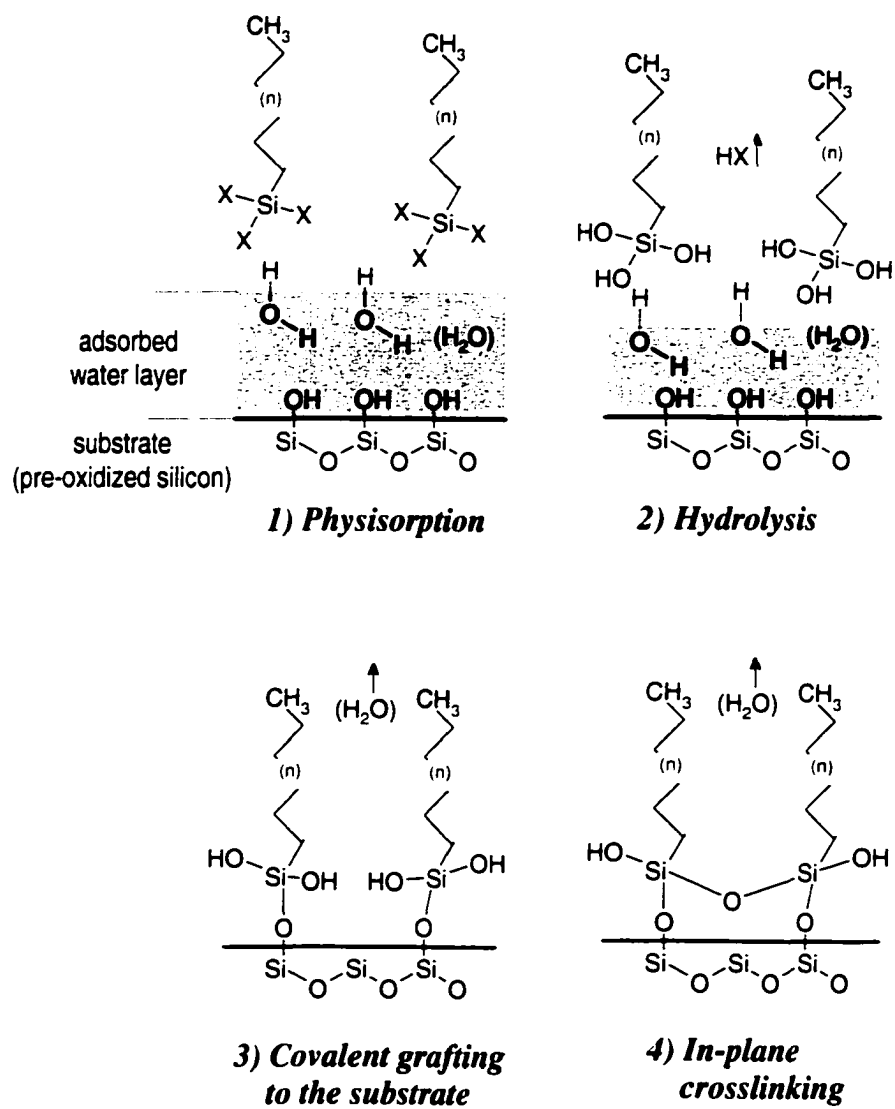


Figure 2.22: Silanization reaction in the presence of adsorbed water

2.3.3 Deposition of organosilane coatings from aqueous media

Self-assembled monolayer coverage (Figure 2.23(a))⁽⁶¹⁾ of the surface is not generally favored with water as the reaction solvent. Instead, the deposition of particulates may be formed due to vertical polycondensation of hydrolyzed silanes on the substrate (Figure 2.23(b)) or as a result of condensation reactions of the organosilanes in the aqueous phase that lead to the formation of grafted networks, which react with the existing pre-oxidized substrate (Figure 2.23(c)).^(59,90) The relative proportion of these aggregates depends on water concentration, solution age, chain length of silane molecules, temperature,^(12,60,64) silane concentration, exposure or reaction time, dispersion pH,⁽⁸¹⁾ substrate pretreatment⁽⁸⁾ and steric effects.^(56,91) The complexity of this chemistry is illustrated in Figure 2.23 As a result, the solvents used for SAM coating with RSiCl_3 precursors must be as anhydrous as possible. However, increasing concerns regarding the use of organic solvents in work places and the generation of organic wastes have sparked interest in the feasibility of applying highly hydrophobic coatings from aqueous base chemistries.

Some factors that enhance the stability of silanols in aqueous solutions are:⁽⁷³⁾ (i) neutral conditions, (ii) limited condensation; (iii) the presence of hydroxylic species and (iv) silanes forming stable zwitterions.

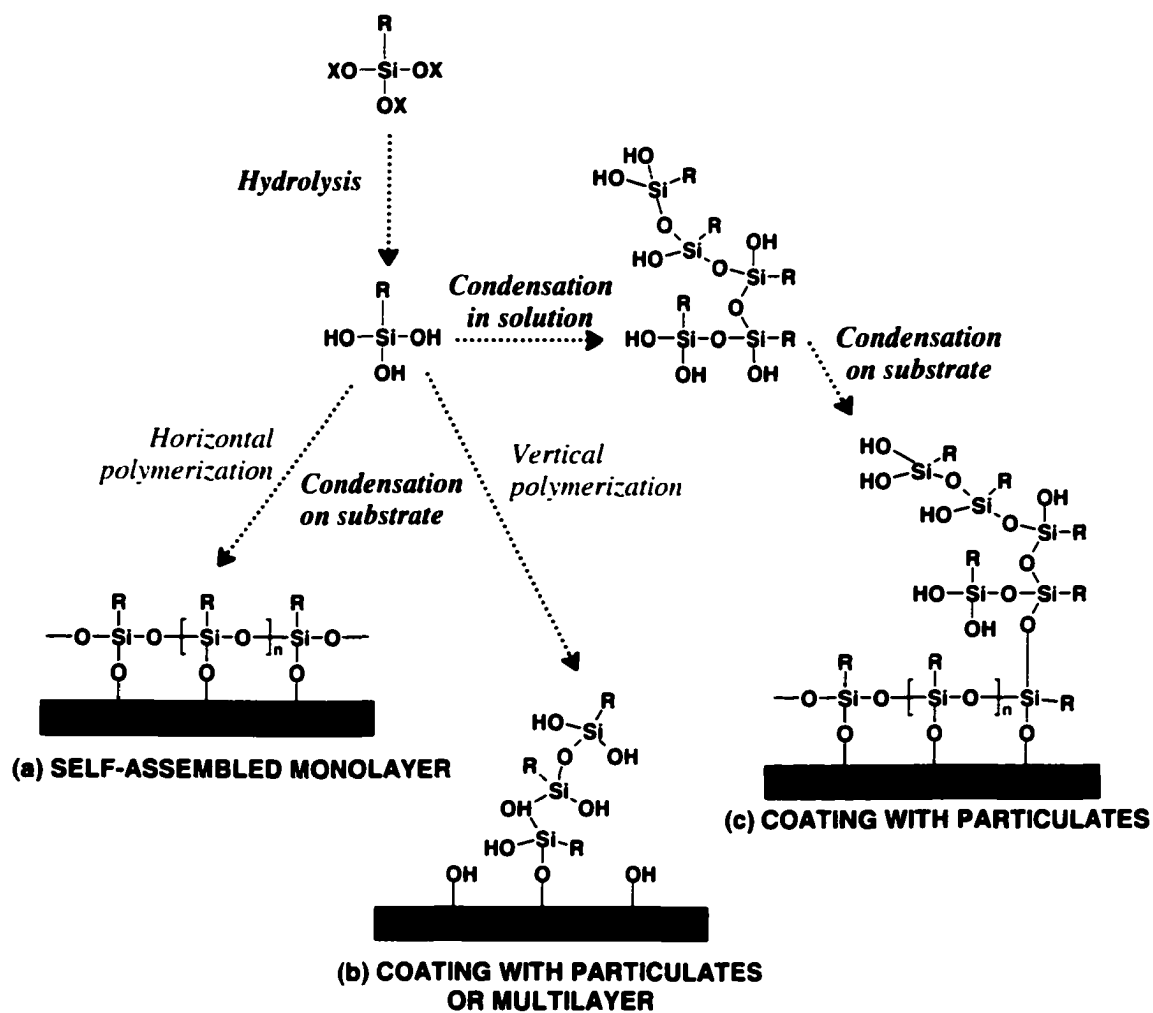


Figure 2.23: Possible products of the reaction of alkyltrialkoxysilanes in the aqueous phase and at the solution/substrate interface

Water dispersible silanes typically have a general structure of (PB)-(PL)-spacer-(O-X)₃, where PB is the hydrophobic alkyl group. PL is the hydrophilic head group, X is a proprietary “end blocker” and the spacer is a short (CH₂)_n group that gives flexibility to help alignment and assembly. In alcoholic solutions the –O-X groups are stable but in aqueous solutions they undergo hydrolysis and condensation at a rate dependent on the pH. Depending on the chain length of the alkyl group in R, the silane may form micelles in an aqueous solution with the core containing R-(CH₂)_n- (Figure 2.24).

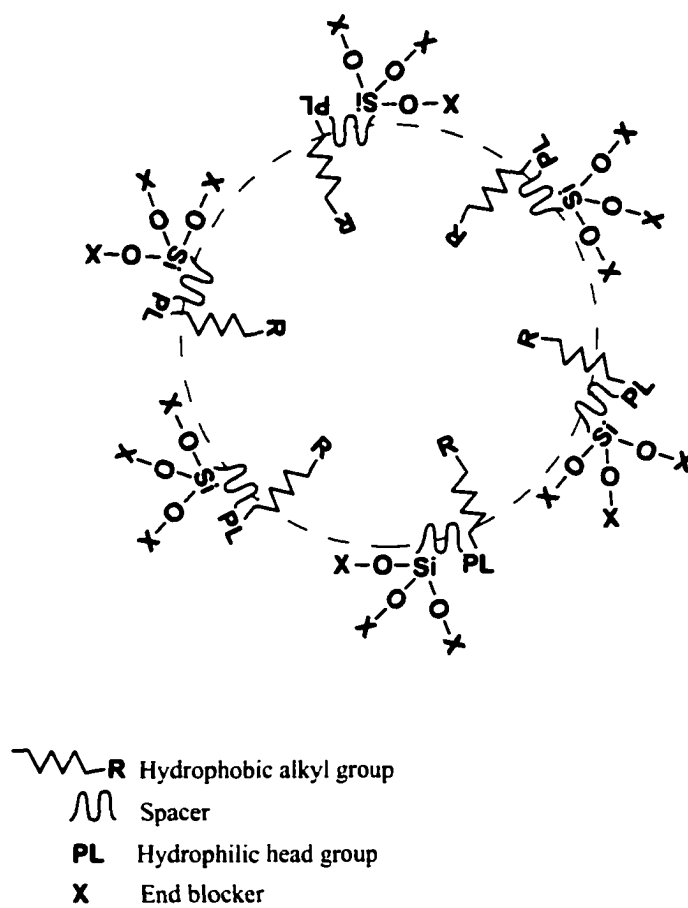


Figure 2.24: Aggregates of water dispersible silanes

CHAPTER 3

EXPERIMENTAL MATERIALS AND METHODS

3.1 Materials

3.1.1 Silicon and polysilicon wafers

The polysilicon samples used for experimental work were 2 μm thick LPCVD films deposited on top of Si wafers and were donated by Motorola, Inc. in Tempe, AZ. Phosphorous doping of the samples was achieved by depositing 2 μm PSG (6.5 wt % P) followed by annealing at 1015°C for 5 hours.

Two types of single crystal silicon (100) wafers were used: antimony doped n-type (0.02 $\Omega\text{-cm}$) cut into pieces of 1 cm x 1 cm for electrochemical impedance spectroscopy experiments and boron doped p-type (7-17 $\Omega\text{-cm}$) for ellipsometry, atomic force microscopy and contact angle measurements.

3.1.2 Water dispersible silanes

Four different commercially available water dispersible organosilane systems were characterized in this project. These were used as received and diluted with deionized (DI) water (resistivity 18 $\text{M}\Omega\text{-cm}$). The organosilanes are described in the following sections.

3.1.2.1 Siliclad[®]

Siliclad[®] is a commercially available, proprietary, water dispersible octadecylsilane based chemical. This organosilane, purchased from Gelest, Inc, is reported to contain the reactive silane at a concentration of 20% in a mixture of tertiary alcohols (2-methyl-2-butanol) and diacetone alcohol (4-hydroxy-4 methyl-2-pentanone). According to the manufacturer, this hydrolyzed silane has a molecular weight of 332.6 and can be used for coating glass from an aqueous solution containing 0.1-1 % reactive silane at a pH value of 4 to 5.

3.1.2.2 Glassclad[®]18

Glasscad[®]18, purchased from United Chemical Technologies, Inc., is a monomeric octadecylsilane derivative in a solution of 2-methyl-2-propanol and 4-hydroxy-4-methyl-2-pentanone that reacts with water to form a silanol-rich polymer and an alcohol. The silanol-rich pre-polymer is able to condense with available hydroxyl groups on the substrate to form a chemical bond. This organosilane is reported to have a general structure of $C_{18}H_{37}SiX_3$, where X is a proprietary hydrolyzeable leaving group. The formulation is reported to contain 20% of reactive silane.

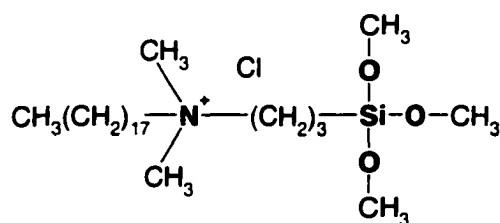
3.1.2.3 DuPont TLF-8291

DuPont TLF-8291 is an aqueous formulation containing 10% of an alkyltrialkoxysilane and a tetraalkylammonium chloride surfactant. TLF-8291 is reported to be very effective at low concentrations (1-5% product in water) and stable in the pH range of 3 to 11, though best performance can be achieved at $\text{pH} < 7$. According to the manufacturer, this aqueous hydrocarbon silane can provide excellent scratch protection and water repellency for glass, ceramics, porcelain and other nonporous glass-like surfaces. It can be applied by dipping, spraying, wiping or brushing.

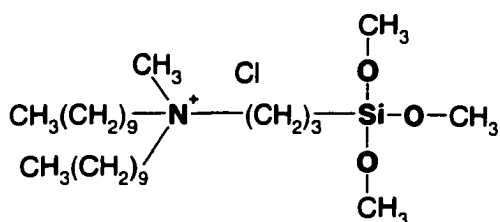
3.1.2.4 Cationic alkoxysilanes

The fourth chemical system consisted of cationic alkoxysilanes with two functional groups: one that allows physical adsorption and the other that promotes chemisorption onto silicon oxide in a specific pH range. The presence of a quaternary ammonium group also allows the silane to aggregate and disperse in the aqueous phase.

The cationic alkoxysilanes, purchased from Gelest, inc., chosen for detailed investigation are:



N,N-Dimethyl-N-octadecyl-3-aminopropyltrimethoxysilyl chloride (DMOAP)



N,N-didecyl-N-methyl-3-aminopropyltrimethoxysilyl chloride (DIDAP)

Cationic alkoxy silanes have been employed as lubricants, anti-static surface treatments, to impart antimicrobial properties,⁽⁹²⁾ for molecular imprinting in biosensors⁽⁹³⁾ and to promote homeotropic alignment (perpendicular to the surface) of nematic liquid crystals.^(94,95)

Kahn⁽⁹⁶⁾ used DMOAP molecules as coupling agents to generate chemically stable interfaces on a variety of conducting and insulating substrates to promote liquid crystal orientation. His deposition procedure was to dip the clean substrate in a dilute solution of the alkoxy silane (0.1%) and agitate at room temperature for 5 min. The substrate was then rinsed in deionized water to remove excess silane; excess water was then blown off with clean nitrogen. He reported that DMOAP coated surfaces consist mainly of octadecyl hydrocarbon chains oriented normal to the substrate (Figure 3.2), where liquid crystal molecules can align with their long axes parallel to DMOAP-coated substrates.

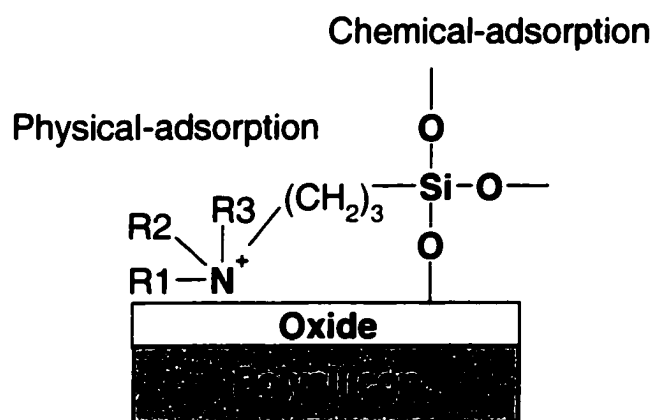


Figure 3.1: Adsorption of Cationic Silanes onto pre-oxidized polysilicon

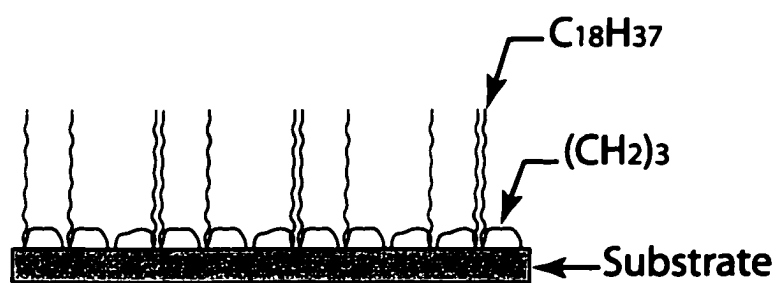


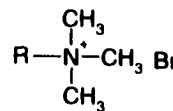
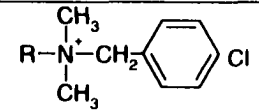
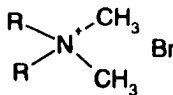
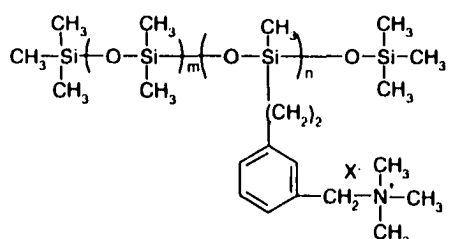
Figure 3.2: Schematic of the orientation of DMOAP⁽⁹⁶⁾

3.1.3 Surfactants

Cationic surfactants were used to improve the stability of Siliclad[®] dispersions because of their ability to interact with silicon dioxide over a wide solution pH range. Surfactants with different alkyl chain length and structure were chosen and are shown in Table 3.1. All surfactants were used as received. Some properties of these surfactants are also listed in the same table.

These surfactants aggregate to form micelles when the surfactant concentration is above their *critical micelle concentration* (CMC). In this arrangement, the polar headgroups are directed towards the water and the hydrophobic groups associate to form a hydrophobic core. The number of surfactant molecules in a micelle is referred as *aggregation number*. The temperature at which the aqueous solubility of the cationic surfactant equals the CMC is referred to as the *Krafft point*. Below the Krafft point, micelles do not form and the concentration of surfactant monomers in solution never exceeds the CMC.

Table 3.1: Cationic surfactants used to stabilize Siliclad[®] dispersions

Surfactant structure		Abbr.	R	Produced by (Purity)	Molecular Weight	CMC [mM]	Aggregation Number	Krafft Point [°C]
I. Alkyl Quaternaries	A. One tail-one head 	DTAB	C ₁₂ H ₂₅	Aldrich (99%)	308.35	16.01 ⁽⁹⁷⁾	48 ⁽⁹⁸⁾	<0 ⁽⁹⁹⁾
		TTAB	C ₁₄ H ₂₉	Fluka (98%)	336.41	3.56 ⁽¹⁰⁰⁾	58 ^(98,101)	
		CTAB	C ₁₆ H ₃₃	Aldrich (97.4%)	364.46	0.92 ⁽¹⁰²⁾	62 ⁽⁹⁸⁾	25 ⁽⁹⁹⁾
		OTAB	C ₁₈ H ₃₇	Aldrich (>97%)	392.5		N/A	35-37 ⁽⁹⁹⁾
		Empigen BAC	C ₁₂₋₁₆	Albright & Wilson (50%)	462.65	0.19*	N/A	N/A
	B. Two tails-one head 	DDAB	C ₁₂ H ₂₅	Aldrich (98%)	354	0.014 ⁽¹⁰³⁾	N/A	N/A
II. Silicone Alkyl Quaternary		Gelest QMS	-----	Gelest, Inc. (35-45%)	1800-2000	0.21*	N/A	N/A

*Determined experimentally using Wilhelmy plate technique
N/A not available

3.2 Methods

3.2.1 Cleaning and pre-oxidation of silicon and polysilicon samples

Prior to conducting any experiments, test samples were cleaned in 4:1 H₂SO₄ (98%):H₂O₂ (30%) solution at ~90°C for 15 minutes to remove organic contaminants, thoroughly rinsed in deionized (DI) water, then etched in 50:1 HF to remove the oxide film and finally dried using filtered nitrogen gas.

In order to immobilize the organosilane molecules through covalent bonding with the substrate, the presence of Si-OH groups on the substrate surface is necessary. Therefore, different oxidation pre-treatments were performed before deposition of silane coatings, as listed in Table 3.2.

Table 3.2: Oxidation pre-treatments for silicon and polysilicon samples

Oxidation Treatment	Chemistry	Oxidation Time	Oxidation Temperature
<i>SCI</i> 1:1:25 NH ₄ OH:H ₂ O ₂ :H ₂ O	1 part of 49% NH ₄ OH 1 part of 30% H ₂ O ₂ 25 parts of DI water	10 min	70°C
<i>Piranha</i> 1:4 H ₂ O ₂ :H ₂ SO ₄	1 part 30% H ₂ O ₂ 4 parts of 98% H ₂ SO ₄	15 min	80°C
<i>Peroxide</i> H ₂ O ₂	30% H ₂ O ₂	15 min	20°C

3.2.2 Preparation of silane dispersions

The as-received organosilanes were diluted in deionized (DI) water (resistivity of 18 M Ω -cm) before use. The pH value of the coating dispersion was adjusted with acetic acid, hydrochloric acid or potassium hydroxide.

For Siliclad[®] dispersions containing surfactants, the surfactant aqueous solution was prepared prior to the addition of organosilane. This was followed by the adjustment of pH with hydrochloric acid or potassium hydroxide. Samples were stirred for at least 10 minutes prior to viscosity measurements and coating deposition.

3.2.3 Coating deposition

3.2.3.1 Dip coating

Coatings were deposited on 1.5 cm x 1.5 cm samples, by immersing into and withdrawing from silane dispersions at controlled speeds using a dynamic contact angle analyzer (Cahn-DCA-312) shown in Figure 3.3. The immersion/withdrawal speed range of this instrument is 20-260 $\mu\text{m}/\text{sec}$. Delay times between immersion and withdrawal steps were necessary only for Siliclad[®] coatings. The film-covered substrates were thoroughly rinsed with DI water and finally blow-dried with nitrogen. Curing of Siliclad[®] coatings was done in a convection oven for 5 minutes at different predetermined temperatures. The deposition of coatings onto 4-inch single crystal wafers was done with a BAS XY recorder, setup only to move on the Y direction and controlled by an EG&G Parc Model 175 universal programmer to speeds of 40 $\mu\text{m}/\text{sec}$ to 4000 $\mu\text{m}/\text{sec}$.

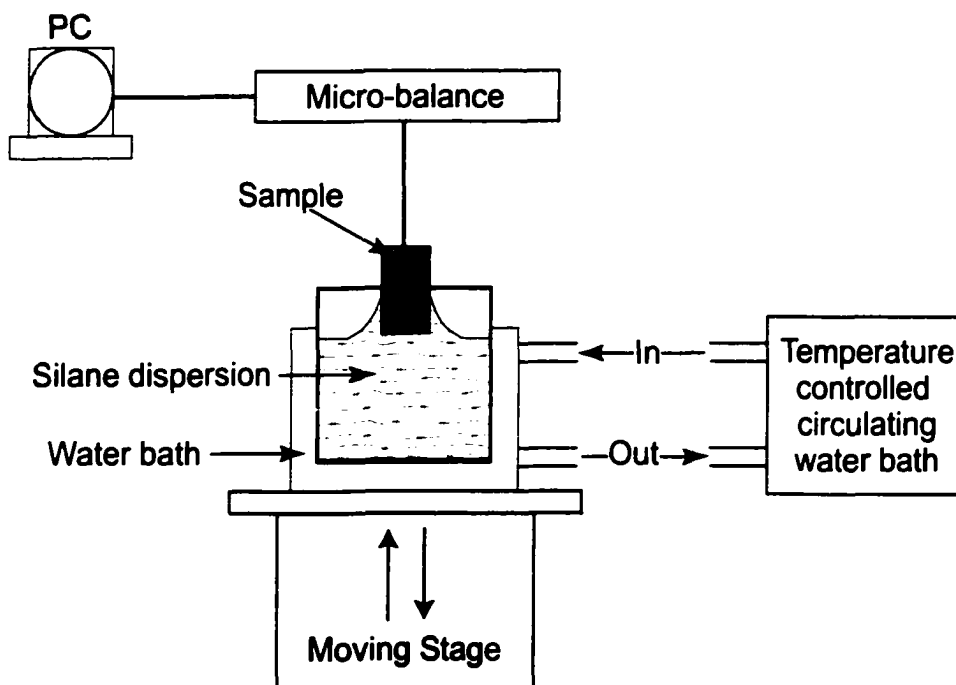


Figure 3.3: Schematic diagram of a DCA system used for dip coating, surface tension and dynamic contact angle measurements

3.2.3.2 Langmuir-Blodgett films

Pressure-area isotherm measurements of organosilane monolayers on water and transfer of such monolayers onto polysilicon substrates were carried out using a 30 cm × 20 cm × 1 cm polytetrafluorethylene Langmuir Blodgett Trough (Nima Technology Ltd., Model 611D). Data acquisition was achieved with a custom program written by Wayne Huang and the author of this dissertation in Microsoft Visual Basic.

The organosilane monolayer was spread on the surface of the aqueous sub-phase by dissolving the organosilane in high purity methanol and by depositing the solution drop by drop onto the water from a syringe held a few millimeters above the sub-phase. The solvent was allowed to evaporate for 1 hour. The characteristics of the organosilane monolayer on the water surface were studied by measuring the changes in surface tension upon compressing the monolayer at a rate of 0.5 cm²/sec (Figure 3.4). The reduction of surface tension (surface pressure) was measured by means of chromatographic paper Wilhelmy plates (1 cm × 2 cm × 0.015 cm) attached to a microbalance. Experiments with cationic alkoxy silanes were performed at different subphase temperatures. Quantitative values of areas per molecule were not calculated due to the uncertainties in the concentration and Siliclad[®] chemical structure of the as-received silanes.

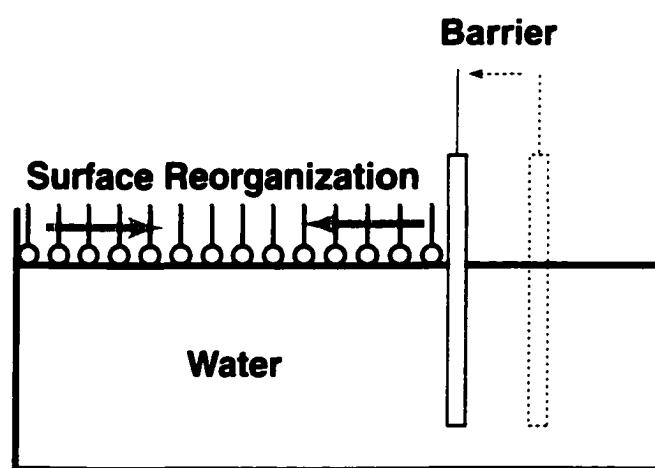


Figure 3.4: Monolayer reorganization after an imposed compression or expansion

In order to form a Langmuir-Blodgett film onto pre-oxidized polysilicon, the substrate was passed through a compressed monolayer at different predetermined pressures. Deposition onto these hydrophilic substrates occurred when the substrate made its first “up” pass through the water/air interface (Figure 3.5), as the direction of the meniscus favored the head group of the molecule to be attracted to the surface. The substrate had to be immersed in the aqueous subphase prior to spreading and compressing the organosilane monolayer to prevent the deposition of molecular film aggregates onto the substrate during the first “down” stroke.

In order to form a Langmuir-Blodgett film onto pre-oxidized polysilicon, the substrate was passed through a compressed monolayer at different predetermined pressures. Deposition onto these hydrophilic substrates occurred when the substrate made its first “up” pass through the water/air interface (Figure 3.5), as the direction of the meniscus favored the head group of the molecule to be attracted to the surface. The substrate had to be immersed in the aqueous subphase prior to spreading and compressing the organosilane monolayer to prevent the deposition of molecular film aggregates onto the substrate during the first “down” stroke.

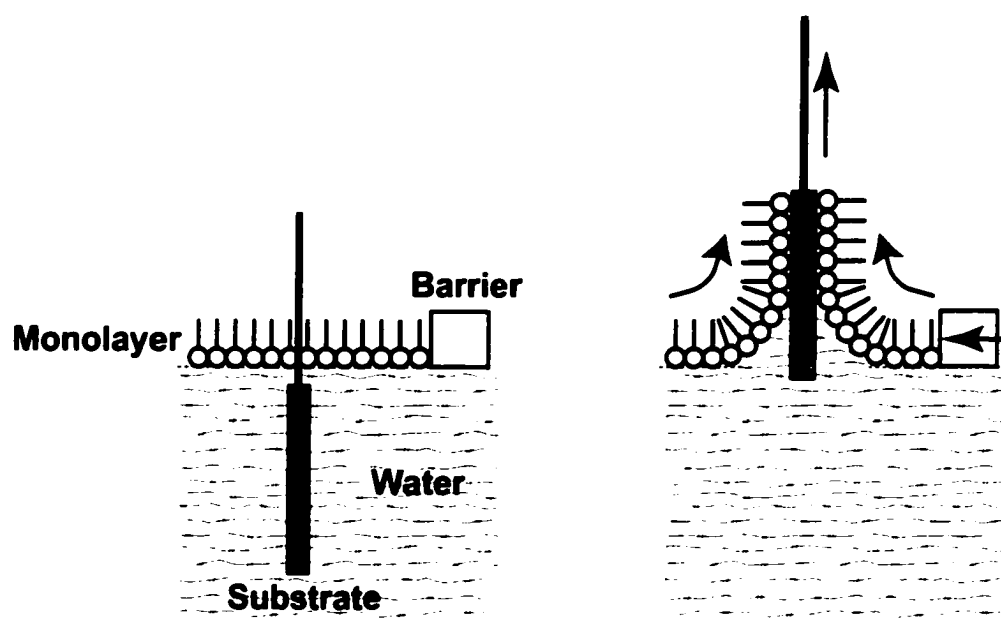


Figure 3.5: Deposition of a Langmuir-Blodgett film onto a hydrophilic substrate

3.3 Characterization techniques

3.3.1 Zeta potential measurements

Zeta potential measurements on polysilicon substrates subjected to different wet oxidation processes were carried out by a flat-plate streaming potential method (Figure 3.6) using a BI-EKA Electro Kinetic Analyzer. Polysilicon samples, cut into 7.3 cm x 1.6 cm and 7.4 x 1.95 cm, were separated by a 0.25 mm thick Teflon sheet. Solutions containing 0.001 M KNO₃, and adjusted to different pH values with KOH and HNO₃, were pumped through the channel at driving pressures of 0 to 250 mbar, in both flow directions. Platinized platinum electrodes⁽¹⁰⁴⁾ were inserted on both ends of the cell.

The zeta potential was calculated according to the method by Fairbrother and Mastin.⁽¹⁰⁵⁻¹⁰⁷⁾

$$\psi_{\xi} = \frac{\eta K_B \Delta E_{str}}{\varepsilon \varepsilon_0 \Delta P} \quad (3.1)$$

In the above equation, ΔE_{str} is the streaming potential measured across the capillary, ΔP is the pressure difference across the capillary responsible for the flow of electrolyte, ε is the dielectric constant of the solution, ε_0 is the permittivity of free space, η is the viscosity of the solution and K_B is the specific electrical conductivity of the solution. The slope $\frac{\Delta E_{str}}{\Delta P}$ can be obtained by the measurements of streaming potential at various flowing pressures. Surface conductance is generally neglected except in electrolytes of extremely low ionic strength, i.e. less than 10⁻⁴ M.

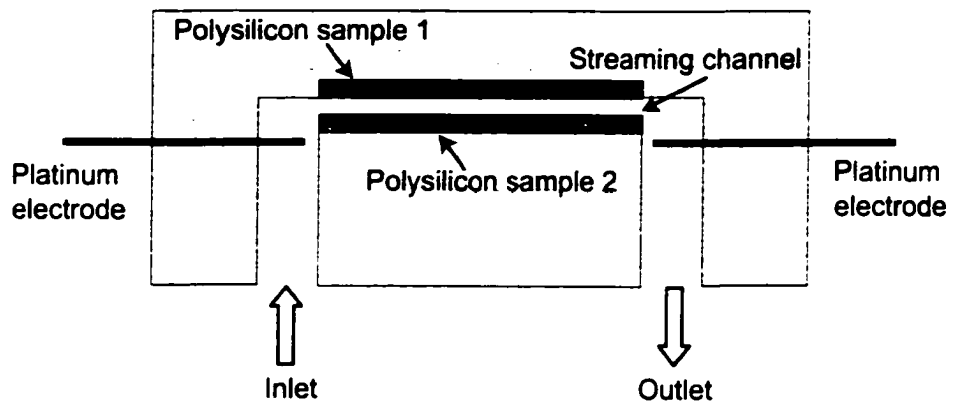


Figure 3.6: A schematic sketch of the streaming potential cell

3.3.2 Wettability evaluation

3.3.2.1 Static contact angle measurements

Static contact angles were measured using a Rame-Hart optical goniometer, model 100-00115. Droplets of 15, 20 and 25 μl were used in the measurements.

A Rame-Hart environmental chamber accessory (Figure 3.7) equipped with a temperature controller and external relative humidity/temperature transmitter (Omega HX93V) was used to study the thermal stability of coatings under nitrogen, compressed air and humid conditions. Temperatures up to 315°C were obtained by an integral electrical heater, while cooling of the chamber was produced by circulating a suitable coolant through the base of the chamber.

The relative humidity (RH) of the gas flowing to the inlet of the environmental chamber was increased by blowing dry nitrogen through a tube connected to a glass frit immersed in DI water. The DI water was kept at ambient temperature to prevent 100% RH or condensation in the environmental chamber.

Figure 3.8 shows the environmental chamber heating and cooling profiles. It may be noticed that heating occurs rapidly: a temperature of 300°C can be reached in 15 min. Cooling is improved by flowing water through the base of the chamber.

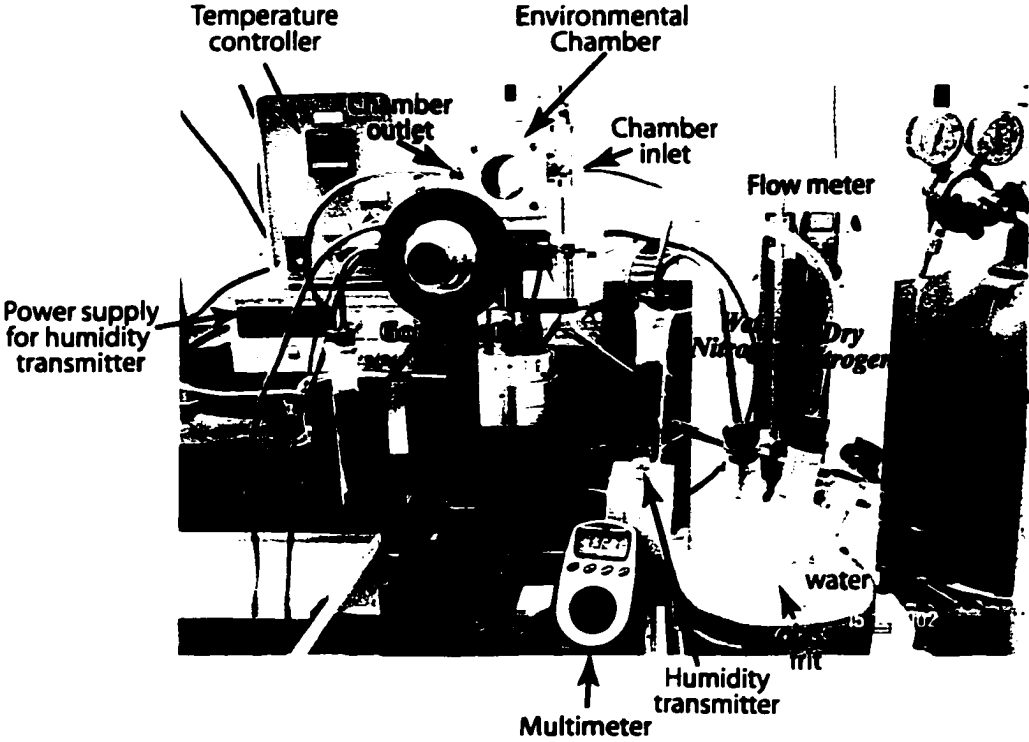


Figure 3.7: Environmental chamber setup for humid environments

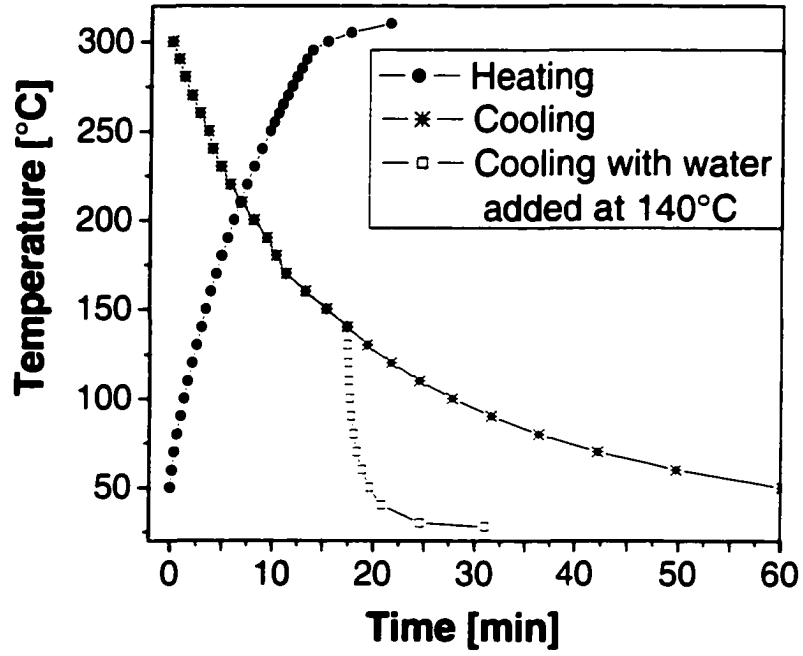


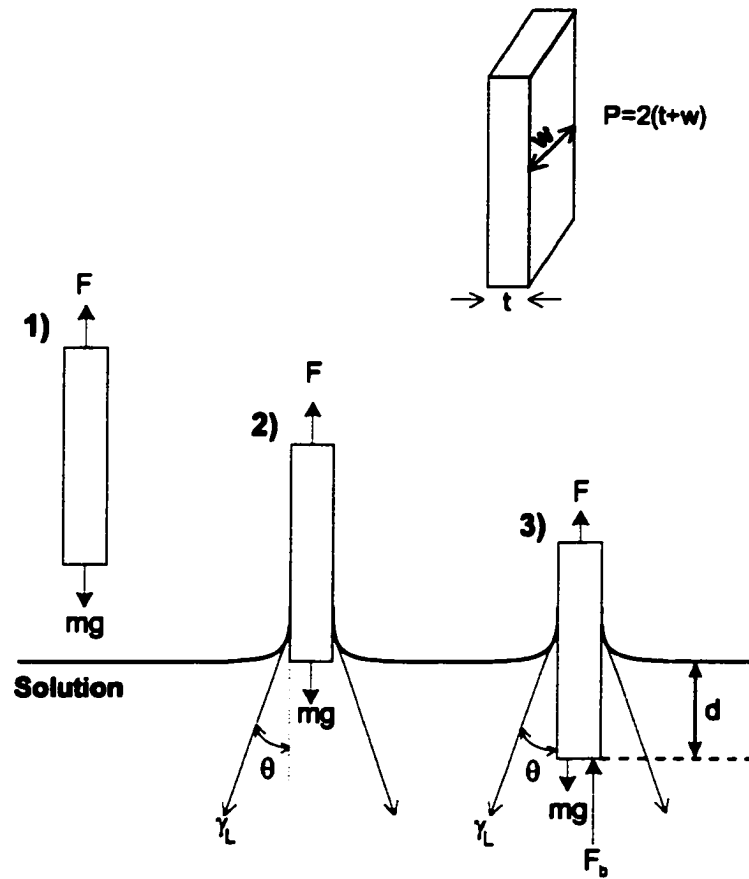
Figure 3.8: Heating and cooling ramp times for environmental chamber

3.3.2.2 Dynamic contact angle measurements

Hydrophobicity of coated samples was determined by measuring contact angles of deionized water immediately after film deposition with a Cahn DCA-312 dynamic contact angle analyzer (Figure 3.3) using the Wilhelmy plate technique (Figure 3.9).

In the dynamic contact angle measurement, the force as shown in Figure 3.9 exerted on a flat plate during immersion and withdrawal from a liquid at controlled speed is measured using a microbalance. Figure 3.10 illustrates the dynamic contact angle hysteresis loop formed during the experiment. As the sample enters the liquid surface, an abrupt change in force is detected due to the vertical component of the surface tension of liquid. As the sample continues to become immersed in the liquid, it provides a buoyancy force, which manifests itself as a straight line, and is used for the advancing angle measurement. After the appropriate immersion depth is reached, the direction is reversed and the sample is withdrawn from the liquid. If the advancing and receding lines are assumed to be straight and are extrapolated to the zero depth of immersion, the buoyancy force can be eliminated from the force balance.

Contact angles on the coated samples were measured immediately after film deposition at a sample immersion/emersion speed of 80 $\mu\text{m}/\text{sec}$. This allowed good repeatability of experimental results. Three-cycle immersion/emersion test was performed to verify that the coating was properly rinsed and that the coating was not perturbed by water penetration.



$$1) F = mg$$

$$2) F = mg + P\gamma_L \cos(\theta)$$

$$3) F = mg + P\gamma_L \cos(\theta) - F_b$$

F : total force, P : perimeter, t : thickness, w : width

m : mass of the sample, g : acceleration due to gravity,

γ_L : surface tension of the liquid, θ : contact angle,

F_b : buoyancy force = $\rho g A d$

ρ : liquid density, A : cross sectional area, d : immersion depth

Figure 3.9: Force balance during the measurements of surface tension and contact angle. 1) Plate in air prior to contact with liquid, 2) plate just at the liquid-air interface and 3) plate immersed in the liquid

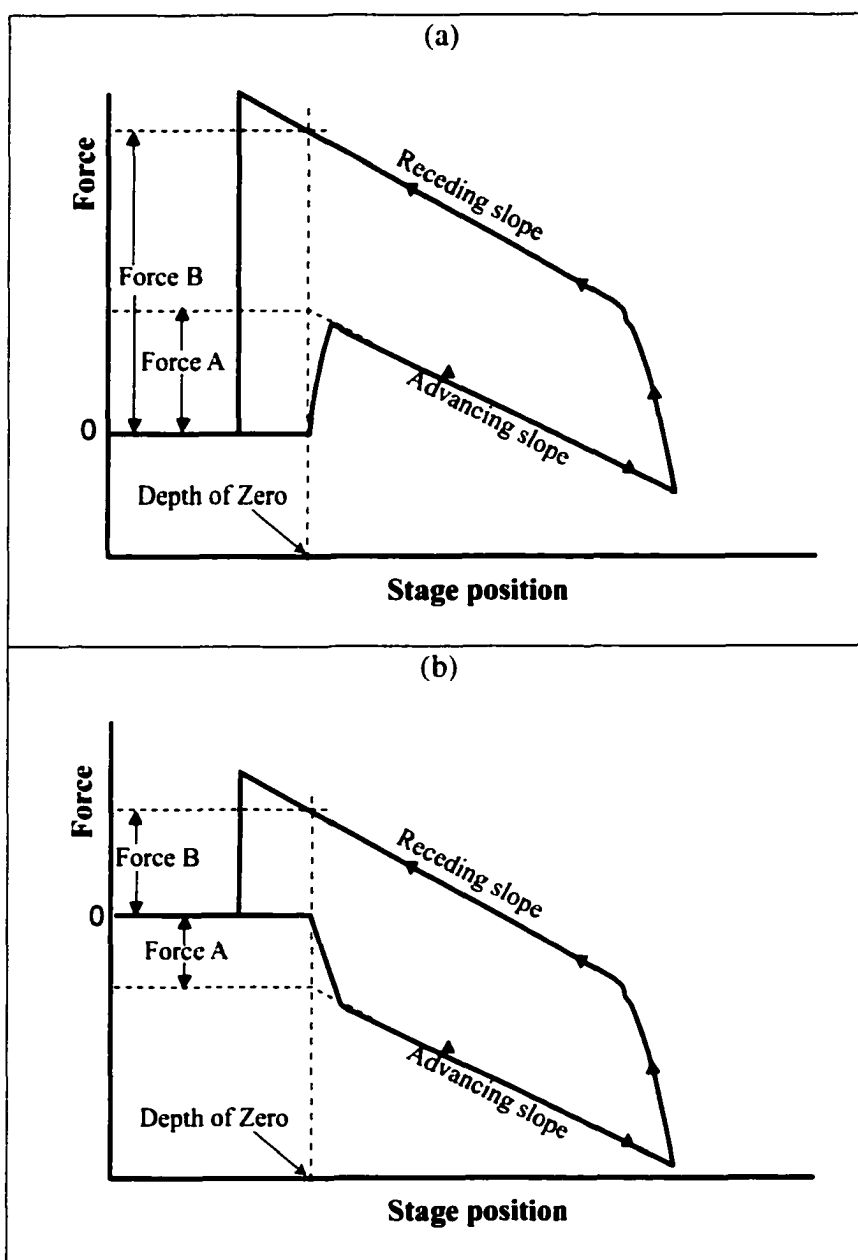


Figure 3.10: Dynamic contact angle hysteresis loop formed using the Wilhelmy plate technique. (a) $\theta_{advancing} < 90^\circ$ and (b) $\theta_{advancing} > 90^\circ$

For an ideally smooth and homogeneous surface, the contact angle of a liquid upon it should have only one equilibrium value. However, the advancing and receding contact angles are not always identical because of the heterogeneity and roughness of the solid surface. The difference between advancing θ_a and receding θ_r contact angles is referred to as the contact angle hysteresis, $\Delta\theta$.

$$\Delta\theta = \theta_a - \theta_r \quad (3.2)$$

This hysteresis is commonly observed during dynamic contact angle measurements and has been attributed to the heterogeneous nature of surfaces, such as (i) different chemical composition (ex.. chemical heterogeneity of polymer surfaces), (ii) different crystallographic faces (ex. during anisotropic etching of polysilicon using TMAH), (iii) existence of defects, (iv) solution impurities adsorbed on the surface (ex. contamination of foreign substances during manufacture of coatings), (v) rearrangement or alteration of the surface (i.e. molecular reorientation in a polar polymer surface under the influence of a liquid. As an example, hydroxyl groups in a polymer backbone chain are buried away from the air phase at a polymer-air interface, but when it is in contact with water, the hydroxyl groups turn over to form hydrogen bonds with water) and (vi) roughness on surfaces.

3.3.3 Determination of critical micelle concentration

Critical Micelle Concentration or CMC is the concentration at which micelles of surfactant begin to form in solution. For solutions of pure surfactants, surface tension decreases and becomes a constant at concentrations greater than the CMC (Figure 3.11). The critical micelle concentration of the surfactants and organosilanes in aqueous solutions was measured at room temperature ($\sim 22^{\circ}\text{C}$) using a CMC accessory for a Cahn DCA-312 Dynamic Contact Angle Analyzer. The accessory attaches to the DCA-312 instrument and performs computer-controlled dilution of a surfactant into a solvent, mixing the solution, and making surface tension measurements of the solutions using the Wilhelmy plate technique. The surface tension was measured after each addition of surfactant solution. The controlled dilution resulted in surface tension values as a function of surfactant concentration from which a value of the CMC of the surfactant-solvent system under study was obtained.

For CMC experiments a platinum plate (30 mm x 15 mm x 0.15 mm) was used, since it was completely wet by all solutions investigated. Before each experiment the platinum plate was cleaned in isopropanol and dried with a natural gas flame.

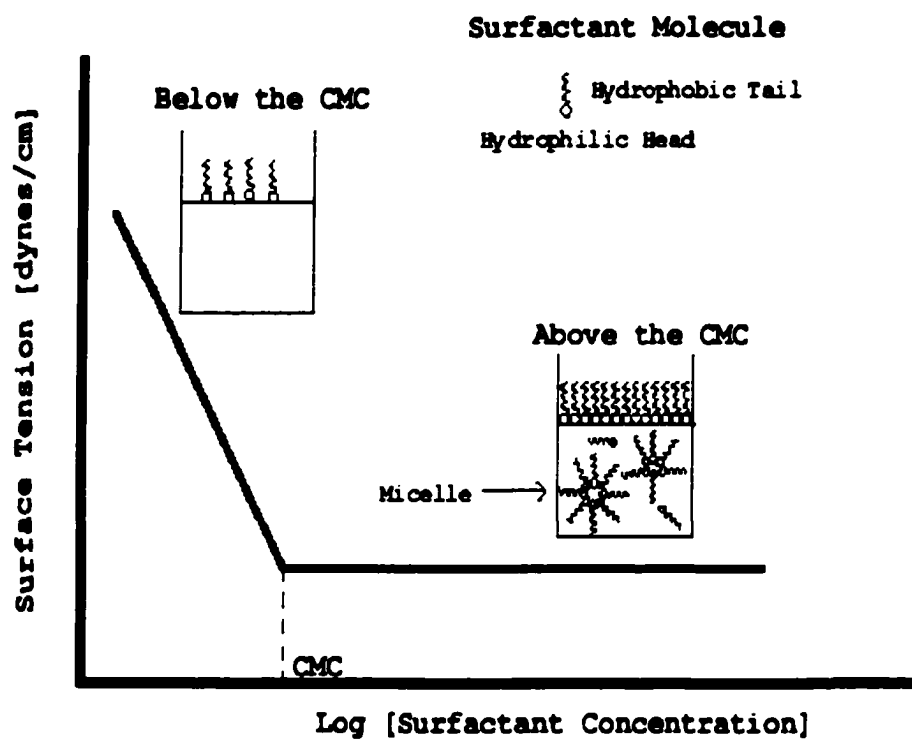


Figure 3.11: Critical Micelle Concentration

3.3.4 Viscosity measurements

The stability of silane dispersions was determined by viscosity measurements at 30°C as a function of the age of silane dispersions using a vertical Ostwald-type viscometer (2 to 10 Cst) and an Ubbelohde-type viscometer (7 to 35 Cst). (Figure 3.12). The viscosity of a fluid is simply a measure of its resistance to flow and as such reflects the frictional forces between the molecules. In the silane dispersions it was expected that these frictional forces increased with the size of the organosilane network formed in the bulk. The dispersions were kept in an oven at 30°C and taken out only when viscosity measurements were required.

In the Ostwald viscometer, a given volume of liquid was introduced into section B (see Figure 3.12) and was drawn up by suction into A until the liquid level was above the mark m_1 . The suction was released and the time required for the liquid level to fall from m_1 to m_2 was measured. The average driving force during the flow of this volume of liquid through the capillary tube is proportional to the average difference in heights of the liquids in tubes B and A. In order that this driving force is the same in all cases, it is essential that the same amount of liquid should always be introduced into tube B. This requirement that the same amount of liquid should always be used does not apply in the case of the Ubbelohde viscometer. Here, the liquid was introduced into B. With tube 3 closed, the liquid was drawn up by suction into A so that the liquid level was above mark

m_1 . The suction was released, tube 3 was opened to the air, bulb C filled with air and the time required for the liquid level to fall from m_1 to m_2 was measured. In this case, the driving force for flow through the capillary is independent of the level of the liquid in B, since the average height, h , is always the same. The gravity effect is compensated by the presence of the second arm of the capillary tube minimizing errors with temperature induced changes in density.

The viscosity was calculated in terms of the viscometer flow times:

$$\frac{\eta}{\eta_0} = \frac{t}{t_0} \quad (3.3)$$

where t and t_0 are the flow times of silane dispersion and water, η is the viscosity of the silane dispersion and η_0 is the viscosity of pure water.

The Ubbelohde and Ostwald viscometers calibration constants (k) reported by the manufacturer (Cannon Instrument Co.) were 0.01051 Cst/sec and 0.03249 Cst/sec, respectively. The kinematic viscosity value in centistokes was obtained by multiplying the efflux time (t) in seconds by the viscometer constant ($\eta=kt$).

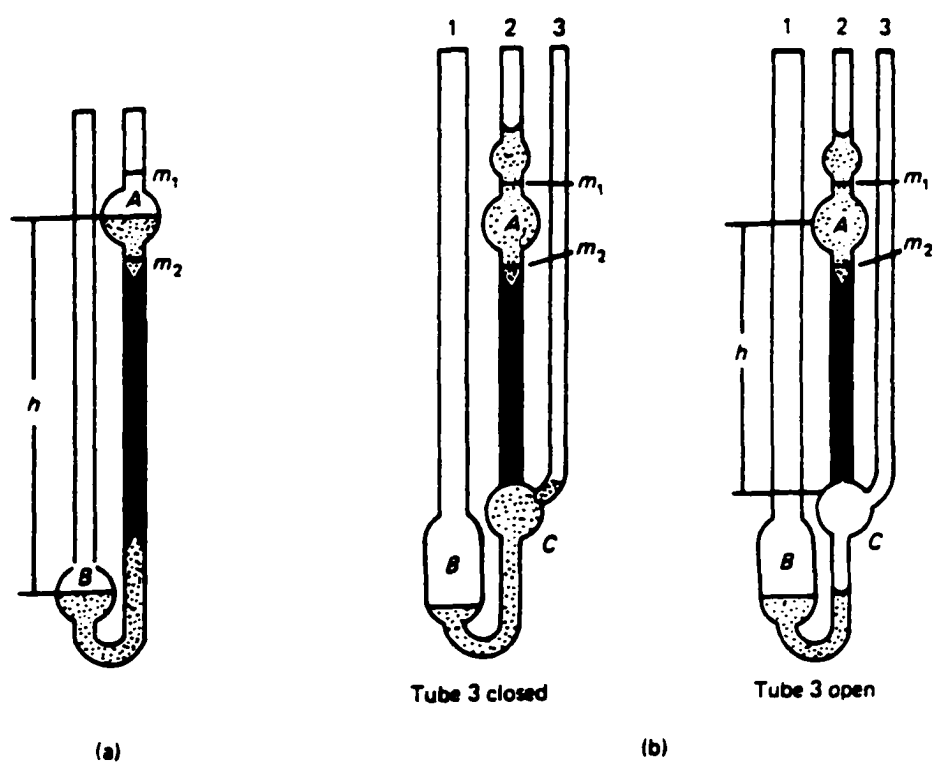


Figure 3.12: Viscometers used for silane dispersion stability measurements: (a) Ostwald viscometer; (b) Ubbelohde

3.3.5 Spectroscopic ellipsometry

Ellipsometric film thickness measurements were carried out using a variable angle spectroscopic ellipsometer (VASE) from J.A. Woollam Co. The ellipsometric parameters ψ (amplitude ratio) and Δ (phase change) were measured at 3 different incidence angles (70° , 75° and 80°) over the 2000-6000 Å wavelength range. The composite optical constants (n and k) of the silicon substrate with the thin oxide film were calculated and taken as baseline for thickness calculation of the organosilane films. Since optical constants of self-assembled monolayers were not available for the wavelength range used, it was assumed that the organic film had the same optical properties as silicon dioxide. Ellipsometric measurements were taken immediately before and after coating each sample.

3.3.6 Nulling ellipsometry

Coating thickness measurements were carried out on a Gaertner variable angle ellipsometer L116E with micro-spot optics (15 μm diameter), rotating analyzer and a He-Ne laser ($\lambda=632.8$ Å). An incidence angle of 70° was used for all the measurements. The ellipsometric angles (relative phase shift Δ and amplitude ratio Ψ) were converted into film thickness using instrument software for multilayers using a three-layer (air/monolayer/substrate) model. The optical constants used in the calculation are shown in Figure 3.13. Before each determination, the thickness of the chemical oxide was measured. The refractive index of the organosilane film was fixed at 1.5. Each sample was measured 3 times on 5 different spots.

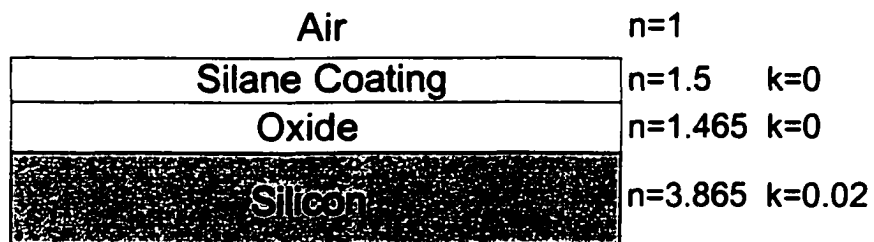


Figure 3.13: Optical Model of silane coatings deposited onto thin chemical oxide covering a silicon wafer

3.3.7 Atomic force microscopy

3.3.7.1 Tapping mode

AFM measurements on organosilane coatings were performed on a Dimension 3000 microscope system (Digital Instruments, Inc) and a TM Microscope Explorer AFM operated in tapping mode. Measurements were performed in air using commercial silicon cantilevers with spring constants of 20-100 N/m and resonance frequency of 300-350 KHz. Data analysis was performed with the Digital Instruments NanoScope III version 5.12r2 software and ThermoMicroscopes SPMLab NT ver. 5.01 software. The depth of pores and height of particulates on the coating were determined from cross-sectional profiles at several locations for each AFM image.

3.3.7.2 Contact and soft contact mode

The roughness of polysilicon samples was measured with a Dimension 3100 microscope system (Digital Instruments, Inc) operated in contact mode. AFM images were obtained by scanning the surface in air with a Si_3N_4 tip (nominal spring constant ~ 0.35 N/m). The root-mean-square surface roughness (R_{rms}) was measured within the region investigated and is defined as:

$$R_{\text{RMS}} = \sqrt{\frac{\sum_{i=1}^n (Z_i - \bar{Z})^2}{n}} \quad (3.4)$$

$$\bar{Z} = \frac{\sum_{i=1}^n Z_i}{n} \quad (3.5)$$

where Z_i is the height at point (x,y) , i is the number of measurement and n is the number of data points.

In-situ imaging of the solid-liquid interface of adsorbed silane onto mica was performed using repulsive stabilization forces^(108,109) between cationic alkoxy silane layers adsorbed to both the tip and sample using a Digital Instruments MultiMode AFM with a liquid cell. The technique for imaging interfacial aggregates is schematically illustrated in Figure 3.14. An aqueous solution containing the cationic alkoxy silane above its critical micelle concentration was injected into the fluid cell shown in Figure 3.15. Adsorption of the cationic organosilane on the sample and AFM tip charged both surfaces positively, setting up a pre-contact repulsive force in the “soft” contact region (Figure 3.14). The force set point was chosen in the soft contact region that allowed the adsorbate topography to be imaged while the tip was “flying” above the plane of hard contact.

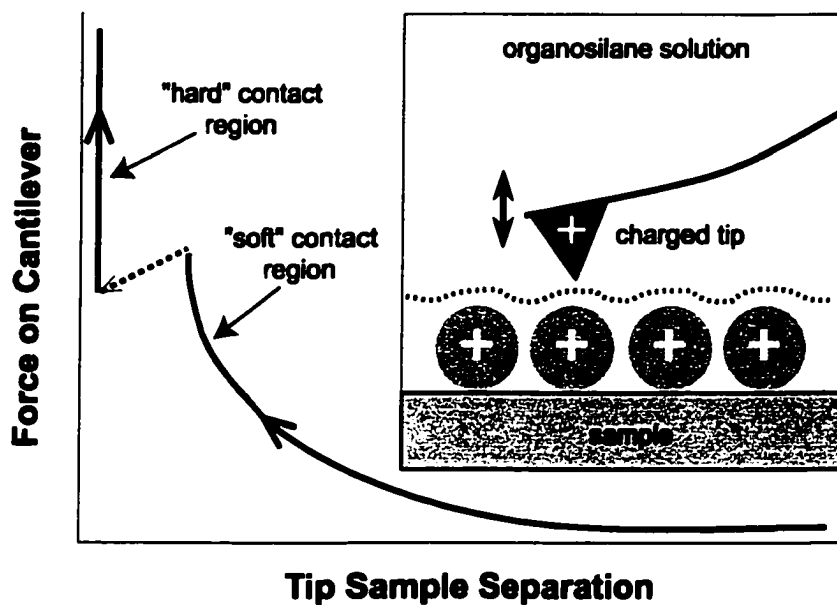


Figure 3.14: Schematic of the technique for imaging surface aggregates by AFM (Courtesy of Srin Manne, Department of Physics, University of Arizona)

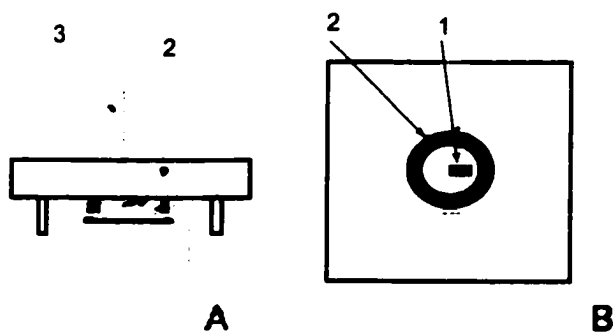


Figure 3.15: Lateral and top view of the fluid cell: 1) cantilever, 2) O-ring and 3) laser beam⁽¹¹⁰⁾

3.3.8 Electrochemical impedance spectroscopy

Electrochemical experiments were performed using a three-electrode cell made of Teflon with a polystyrene transparent cover (Figure 3.16). A calomel reference electrode was immersed in 4M KCl and isolated from the cell by a salt bridge made of Teflon capillary tube filled with KCl (3 M) gelled in agar. The counter electrode was a platinum spiral surrounded by a plastic tube to prevent hydrogen bubbles from disturbing the system. The working electrode was antimony doped single crystal silicon ($0.02 \Omega \text{ cm}$) with a sample area of 0.18 cm^2 as defined by a Viton[®] O-ring. The top of the cell was irradiated with an optical fiber lamp (30 watt) at its maximum intensity. Solutions were purged with nitrogen gas for a minimum of one hour before each electrochemical experiment and kept under a nitrogen atmosphere during the course of the experiment. All experiments were conducted using high purity (ppb grade) 100:1 HF (100 volumes H_2O , 1 volume 49% HF) to avoid formation of oxide at the bottom of the pores in the coating. The oxide on the backside was removed by gently rubbing the surface with a small cotton tip soaked in HF solution, followed by Ni printing to obtain ohmic contact. For coated samples, the reverse side was sanded with alumina paper to remove the coating prior to Ni printing.

Electrochemical measurements were carried out using an EG&G frequency response analyzer model 1025 connected to a Potentiostat/Galvanostat (EG&G model 283). The impedance data were automatically acquired using M398 electrochemical impedance software (EG&G). Electrochemical impedance spectroscopy (EIS) responses of uncoated and coated antimony doped single crystal silicon samples in 100:1 HF were

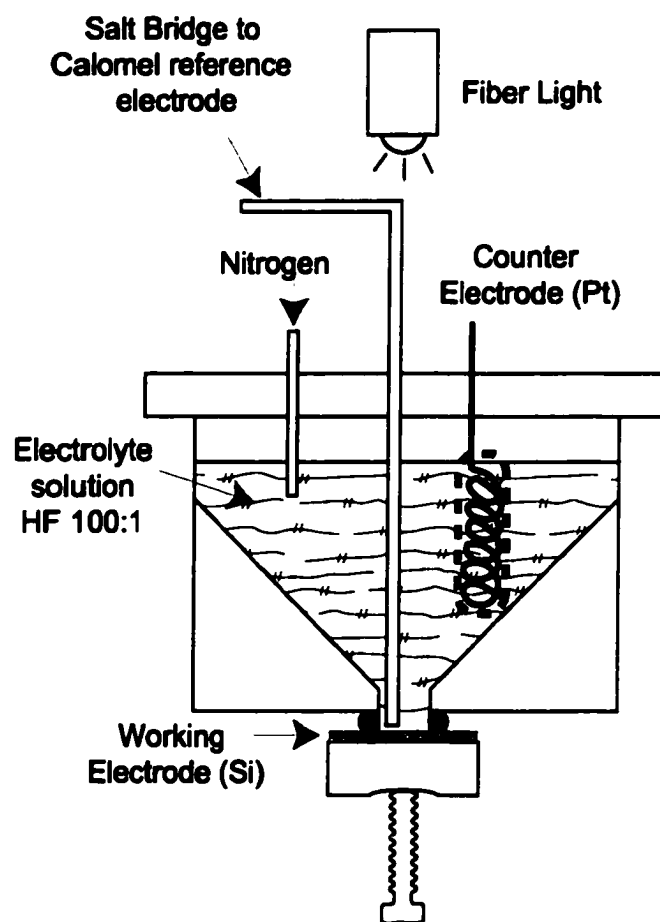


Figure 3.16: A schematic sketch of the cell used for the electrochemical characterization of coated and uncoated silicon surfaces in HF solutions

obtained by applying single 5 mV sine wave in the frequency range of 5×10^{-3} to 5×10^6 Hz with 5 points per decade. The silicon-coated electrode was held at the open circuit potential for all electrochemical impedance spectroscopy experiments to prevent any potential drift and possible voltage-dependent degradation of the coating. The impedance data were fitted to equivalent circuits using EQUIVCRT software (v 4.55), which uses a nonlinear least square fit (NLLSF) technique. The quality of the fit was evaluated from the chi-squared values.

3.3.9 Attenuated total reflection Fourier transform-Infrared spectroscopy (ATR-FTIR)

In-situ Attenuated Total Reflection Infrared Spectroscopy (ATR-FTIR) was used to follow the formation of silane coatings as a function of time. These measurements were carried out using a Perkin-Elmer Spectrum 2000 FTIR Spectrometer equipped with a mid-infrared DTGS (Deuterated TriGlycerine Sulfate) detector. Undoped single crystal silicon parallelogram plates ($50 \times 15 \times 0.5$ mm, transmission range: $8300\text{-}1500$ cm^{-1}), polished on both faces and beveled at 45° , were used as internal reflection elements (IRE). Up to 60 internal reflections on each face with IR beam incidence normal to the bevel face were achieved. Samples were positioned into a liquid flow cell (Figure 3.17) made from PTFE (Harrick Scientific model MEC-1T0). The cell was installed in a twin parallel mirror reflection attachment (Harrick Scientific Model TMP-F-PO5 45°). Flushing the spectrometer optics and sample compartment with ultra pure nitrogen gas minimized interference from atmospheric H_2O and CO_2 .

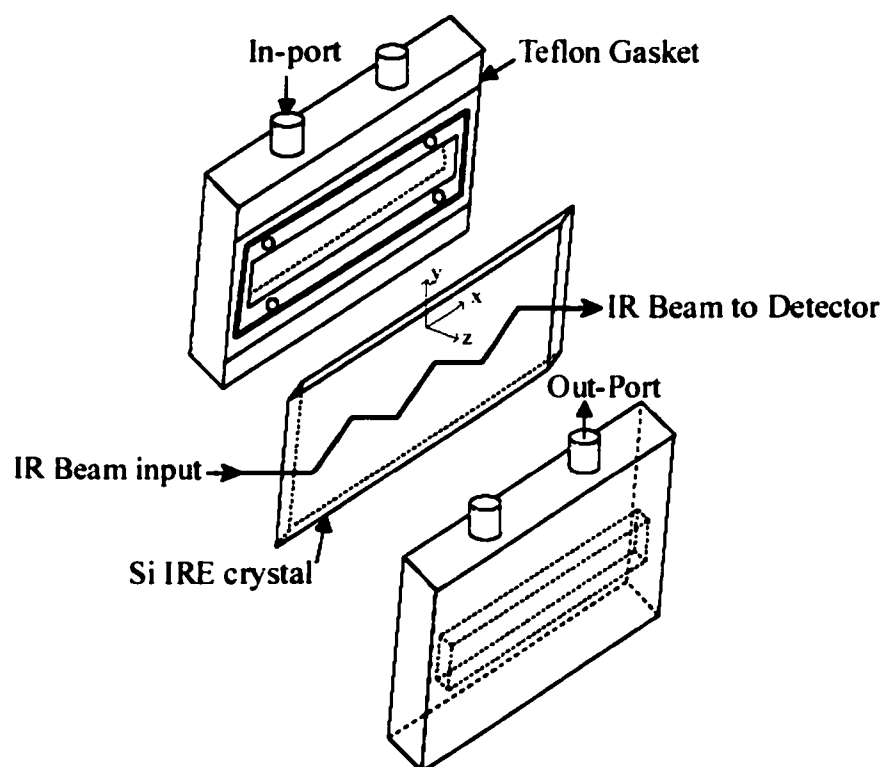


Figure 3.17: ATR-FTIR liquid flow cell

The silicon crystal was first subjected to a pre-oxidation treatment with 30% H₂O₂ at 30°C for 10 minutes and then mounted in the ATR flow cell. The cell was flushed with DI water and a background spectrum of the Si-water interface was taken. A dilute solution of water dispersible silane was then injected rapidly (~0.3 ml/sec) into the cell, followed by continuous pumping of the solution at a slower rate (0.2 ml/min). Spectra were recorded every minute during the 15 first minutes and then less frequently thereafter for a total time of 3 hours. The IR spectra were collected at 4 cm⁻¹ resolution and averaged over 5 to 15 individual scans.

In-situ condensation of Siliclad[®] in aqueous solutions was characterized by measuring the intensity of the Si-O-Si band near 1100 cm⁻¹ using the ATR-FTIR technique. A ZnSe IRE (50 × 10 × 2 mm, transmission range: 17000-720 cm⁻¹) was used for these measurements.⁽¹¹¹⁻¹¹³⁾ Prior to exposure to silane dispersions, the ZnSe crystal was rinsed with iso-propanol and cleaned in an UV/ozone photoreactor to remove organic contaminants. Dispersions were prepared by adding Siliclad[®] to DI water with or without surfactant, adjusted to pH of 4 with acetic acid and injected rapidly into the cell. Silane condensation was followed by acquiring spectra every minute during the 15 first minutes and then less frequently for a total time of 40 hours in the wavelength range of 1300-800 cm⁻¹.

3.3.9.1 Polarized ATR-FTIR

In-situ Attenuated Total Reflection Infrared Spectroscopy (ATR-FTIR) with polarized IR beams was used to investigate the average molecular chain orientation of adsorbed silane at the solid/liquid interface. The polarized IR beam was obtained using a gold wire grid polarizer. The background spectrum for the pre-oxidized-Si/water interface was taken with polarized (0° and 90°) and an unpolarized IR beam.

The organosilane coatings were formed by flowing silane solution through the fluid cell at 0.5 ml/min and the absorbance was monitored until equilibrium was reached. The sample was rinsed, cured and positioned into the flow cell. The spectrum of each sample/water interface was measured with 0° and 90° plane-polarized light.

The calculation of chain orientation using the linear dichroic ratio has been described in the literature.⁽¹¹⁴⁻¹¹⁷⁾ The linear dichroic ratio (LD) is defined as the ratio of the absorbances measured using perpendicular (A_L or at 90°) and parallel ($A_{||}$ or at 0°) polarized IR beams ($LD=A_L/A_{||}$). The technique is based on the principle that absorption of energy only occurs if there is an electric vector of the radiation parallel to the dipole moment change coupled with a vibration. The absorption intensity will depend on the angle between the transition moment of the CH_2 groups and the electric vector of the radiation. Figure 3.18 shows the relationship of the optical axes at the Si IRE surface with the axes of an adsorbed silane molecule. The x and z axes are in the plane of reflection of the polarized beam, while the y -axis is perpendicular to the plane. The z -axis is normal to the silicon surface.

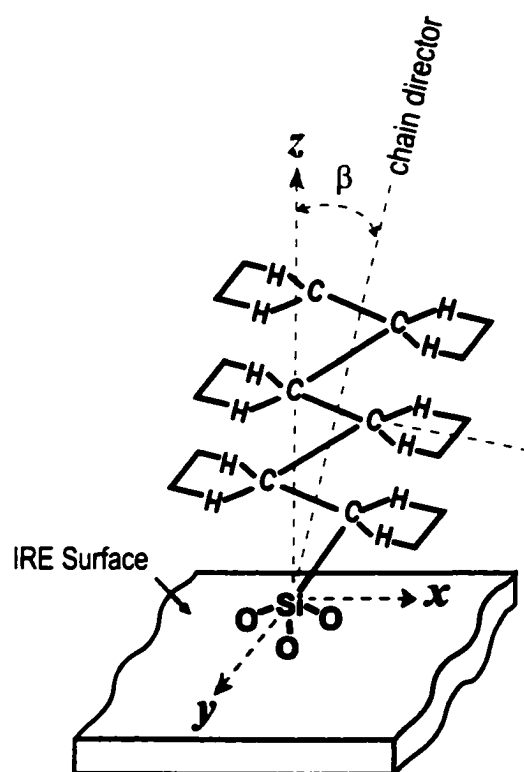


Figure 3.18: Schematic diagram of axes and an adsorbed silane molecule on a pre-oxidized surface

Two limiting cases can be used to deduce the orientation of adsorbed molecules:

Case 1: Chains oriented with the long molecular axis ("director") normal to the surface, all CH₂ stretching transition moments are parallel to the IRE surface:

$$LD_{\text{perpend}} = \frac{A_{\perp}}{A_{\parallel}} = \frac{E_{y_0}^2}{E_{x_0}^2} \quad (3.6)$$

Case 2: Completely random orientation of the chains:

$$LD_{\text{random}} = \frac{A_{\perp}}{A_{\parallel}} = \frac{E_{y_0}^2}{E_{x_0}^2 + E_{y_0}^2} \quad (3.7)$$

For the thin-film case, the unit electric field amplitudes that can interact with the sample are given by:^{114,117}

$$E_{y_0} = \frac{2(\cos \theta)}{(1 - n_{31}^2)^{1/2}} \quad (3.8)$$

$$E_{x_0} = \frac{2(\cos \theta)(\sin^2 \theta - n_{31}^2)^{1/2}}{(1 - n_{31}^2)^{1/2} \left[(1 + n_{31}^2) \sin^2 \theta - n_{31}^2 \right]^{1/2}} \quad (3.9)$$

$$E_{z_0} = \frac{2(\cos \theta \sin \theta) n_{32}^2}{(1 - n_{31}^2)^{1/2} \left[(1 + n_{31}^2) \sin^2 \theta - n_{31}^2 \right]^{1/2}} \quad (3.10)$$

where, E_{x_0} and E_{y_0} = amplitude of the electric field at the interface lying in the plane of the crystal surface

E_{z_0} = amplitude of the electric field perpendicular to the plane of the crystal surface

n_1 = refractive index of Si IRE

n_2 = refractive index of organosilane film

n_3 = refractive index of water

$n_{31}=n_3/n_1$

$n_{21}=n_2/n_1$

$n_{32}=n_3/n_2$

θ = incident angle of light= 44 degrees

The average tilt angle between the z-axis and the chain director (spatial chain orientation angle), β , can be calculated from values of measured linear dichroic ratio and calculated squared electric field amplitudes:⁽¹¹⁵⁾

$$\beta = \sin^{-1} \sqrt{\frac{2[E_{y_0}^2 - LD(E_{x_0}^2)]}{[2LD(E_{z_0}^2) + E_{y_0}^2 - LD(E_{x_0}^2)]}} \quad (3.11)$$

For the calculation of dichroic ratio, the individual CH stretching absorption sub-peaks were obtained by Gaussian curve fitting using Origin-peak fitting module v 6.1 to determine the spatial chain orientation.

In summary, Table 3.3 shows the techniques used in this research to characterize the substrate, silane aqueous dispersions, coatings and anti-stiction properties of the films.

Table 3.3: Experimental techniques used to characterize the substrate, silane dispersions, coatings and anti-stiction properties of the films

	EXPERIMENTAL TECHNIQUE	PROPERTY CHARACTERIZED
<i>Substrate Characterization</i>	Streaming Potential Measurements	<ul style="list-style-type: none"> • Electrokinetic characteristics of the surface oxide layer
	AFM	<ul style="list-style-type: none"> • Roughness
<i>Silane Dispersion Characterization</i>	Viscosity Measurements	<ul style="list-style-type: none"> • Silane dispersion stability
	Wilhelmy Plate Technique	<ul style="list-style-type: none"> • Silane dispersions surface tension • Critical Micelle Concentration of surfactants and silanes
	ATR-FTIR (ZnSe IRE)	<ul style="list-style-type: none"> • Hydrolysis and condensation of silanes
<i>Coating Characterization</i>	Wilhelmy Plate Technique	<ul style="list-style-type: none"> • Coating hydrophobicity
	ATR-FTIR (Silicon IRE)	<ul style="list-style-type: none"> • Coating and surfactant coverage • Average molecular chain orientation
	AFM	<ul style="list-style-type: none"> • Coating uniformity and topography • Coating structure
	EIS	<ul style="list-style-type: none"> • Coating porosity
	Ellipsometry	<ul style="list-style-type: none"> • Coating thickness
	Langmuir-Blodgett film transfer	<ul style="list-style-type: none"> • Quality of the films
	Langmuir-Blodgett isotherms	<ul style="list-style-type: none"> • Monolayer Π versus A isotherms
<i>Anti-Stiction Properties</i>	Optical microscopy and SEM	<ul style="list-style-type: none"> • Stiction or adhesion of cantilever beams to the substrate

CHAPTER 4

RESULTS AND DISCUSSION

4.1 Characterization of polysilicon and oxides

4.1.1 Roughness and grain size

The topography of polysilicon films deposited on both sides of the wafer was imaged by contact mode atomic force microscopy (Figure 4.1). Both sides of the wafer were characterized since deposition of organosilane coatings was done on both sides of the sample and the starting silicon substrates were polished only on the front side.

AFM results show that the as-deposited polysilicon is quite rough. The front side root-mean-square (R_{rms}) surface roughness was found to be ~ 43 nm over a $10\ \mu\text{m} \times 10\ \mu\text{m}$ and $40\ \mu\text{m} \times 40\ \mu\text{m}$ area. Figure 4.1(a) shows a representative $10\ \mu\text{m} \times 10\ \mu\text{m}$ scan of the front side polysilicon and a close-up $1\ \mu\text{m} \times 1\ \mu\text{m}$ area showing the grains. The unpolished back side (Figure 4.1(b)) had a similar roughness to the front side on a $10\ \mu\text{m} \times 10\ \mu\text{m}$ scale, however a $40\ \mu\text{m} \times 40\ \mu\text{m}$ scan had a much larger roughness of ~ 197 nm, revealing the larger scale coarseness of the surface.

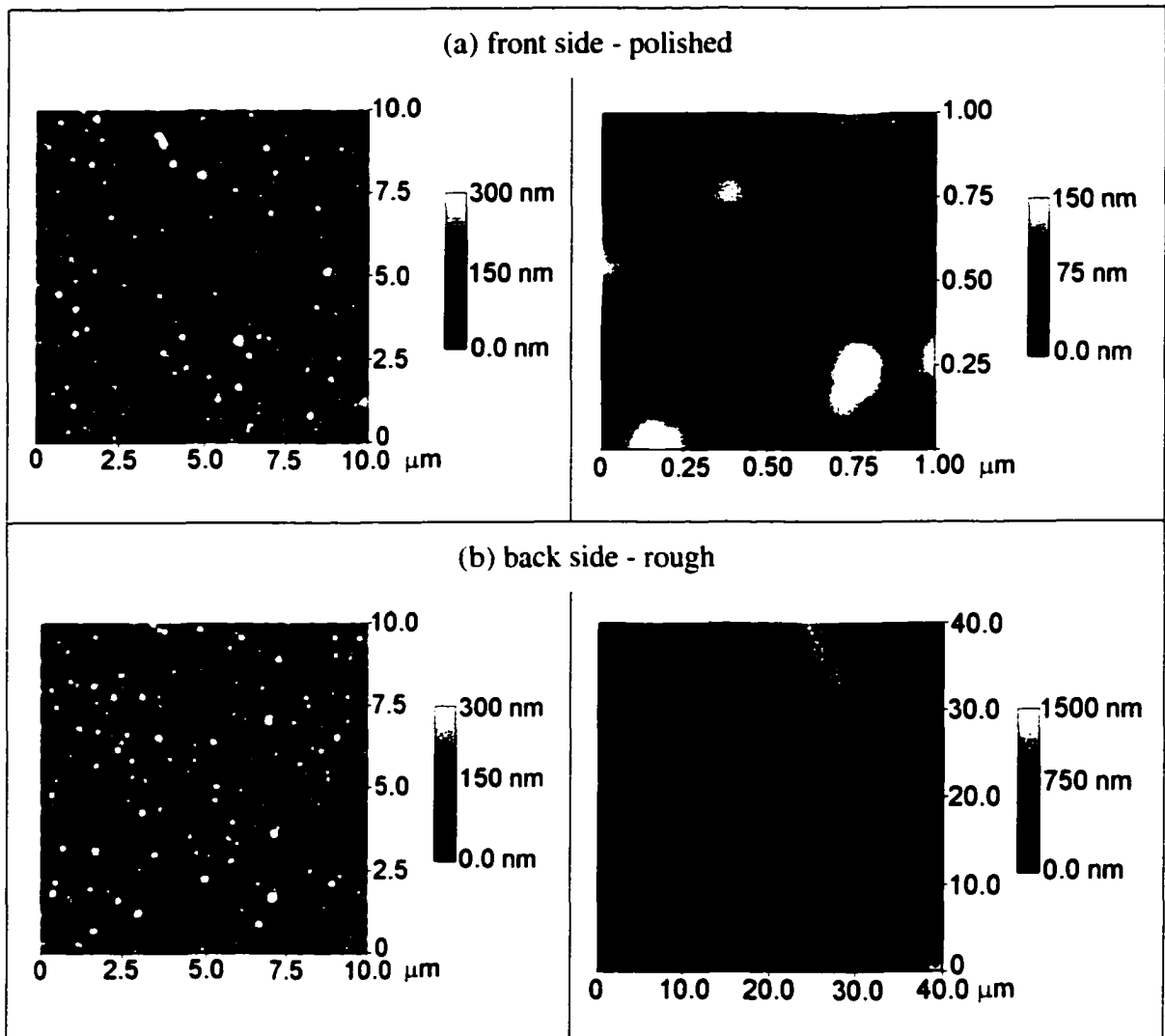
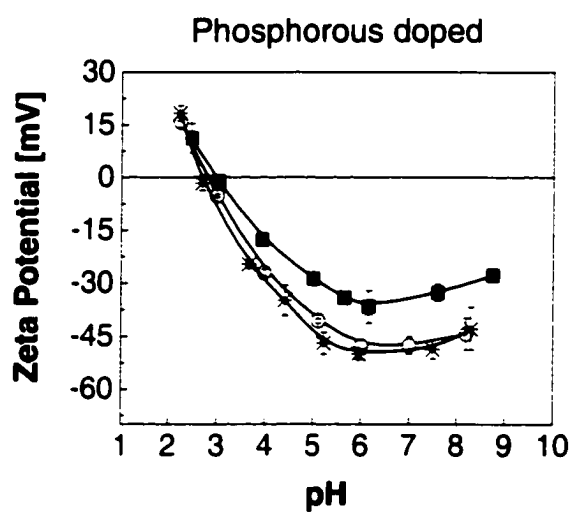
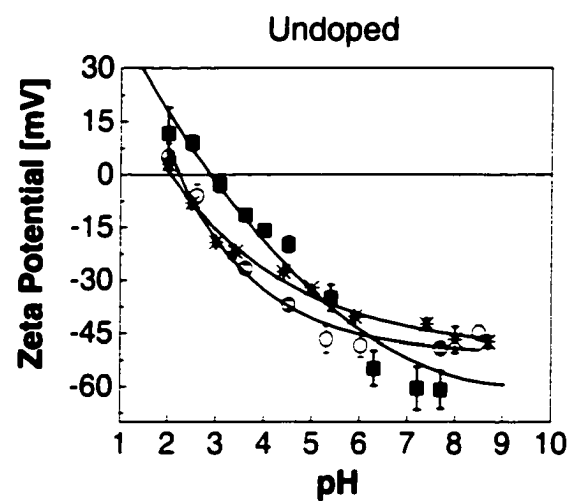


Figure 4.1: AFM image of undoped polysilicon deposited on (a) the polished side and (b) on the backside of the wafer

4.1.2 Zeta potential

Zeta potential (ZP) measurements on undoped and phosphorous doped polysilicon substrates subjected to different oxidation treatments were done to determine whether the electrokinetic properties were sensitive to the type of oxidation process (Figure 4.2). The point of zero zeta potential or iso-electric point (IEP) for all oxides was between 2 and 3; this is in agreement with values reported in literature for silicon oxides on single crystal silicon.⁽¹¹⁸⁻¹²⁰⁾ Interestingly, the type of surface oxidation treatment did not appear to have a significant influence on zeta potential values. The zeta potential data suggested that a pH value greater than 3 is suitable for the attachment of cationic surfactant molecules and any cationic moieties in the silane.

The zeta potential data obtained for SC1 treated sample at different concentrations of KNO_3 are shown in Figure 4.3. The ZP-pH curves intersect at a pH~2.3, confirming that the IEP indeed occurs at that pH value.



- | | |
|---|---|
| ✱ | 1:4 $\text{H}_2\text{O}_2:\text{H}_2\text{SO}_4$ 15 min @ 80°C |
| ○ | 1:1:25 $\text{NH}_4\text{OH}:\text{H}_2\text{O}_2:\text{H}_2\text{O}$ 10 min @ 70°C |
| ■ | 30% H_2O_2 15 min @ 20°C |

Figure 4.2: Electrokinetic measurements on undoped and phosphorous doped polysilicon subjected to different wet oxidation treatments in 10^{-3} M KNO_3 solution

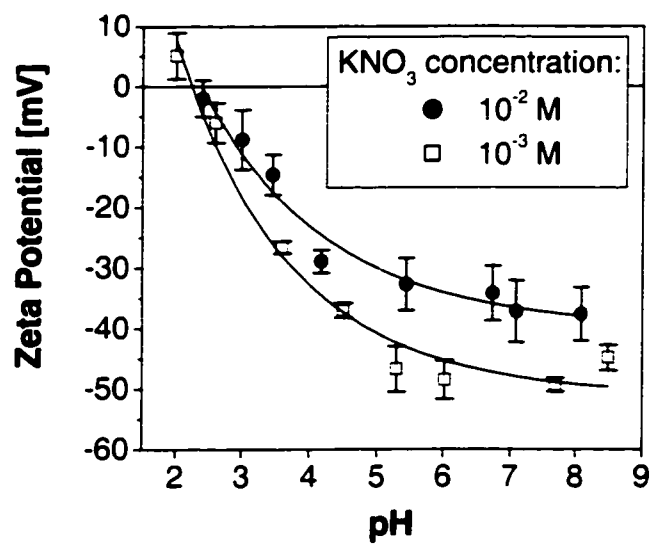


Figure 4.3: Zeta potential as a function of pH for undoped polysilicon subjected to SCI pre-oxidation treatment at different concentrations of indifferent electrolytes

4.2 Coatings deposited onto polysilicon

4.2.1 System 1: Siliclad[®] without surfactant

4.2.1.1 Wettability of Siliclad[®] coatings

Since the kinetics of hydrolysis and condensation of alkoxy silanes in water has been reported⁽¹²¹⁾ to be strongly dependent on pH, initial experiments were focused on applying the coatings from an aqueous dispersion containing 5% reactive silane without surfactant at different pH values. The pH was adjusted with hydrochloric acid and potassium hydroxide. It may be seen in Figure 4.4 that the hydrophobicity of the coatings exhibited a maximum when deposited at a pH of 4. It should be mentioned that at pH 6 the dispersion was hazy and at pH values above 7 the dispersion separated into two phases. In the pH range of 3 to 6 the silane dispersion was clear for almost one day. For optimal dispersion stability it is desirable to have fast hydrolysis and low condensation, which for Siliclad[®] appears to be around pH 4, and is similar to what has been reported in literature⁽⁷⁶⁾ for other alkyltrialkoxysilanes.

The effect of silanization temperature on the hydrophobic character of Siliclad[®] coatings from dispersions containing 3% reactive is shown in Figure 4.5. It appears that Siliclad[®] coatings are not sensitive to preparation temperature. This could be because the coating deposition occurs very rapidly, and/or the formation of different phases, which are characteristic of coatings prepared below the transition temperature (T_c), do not occur.

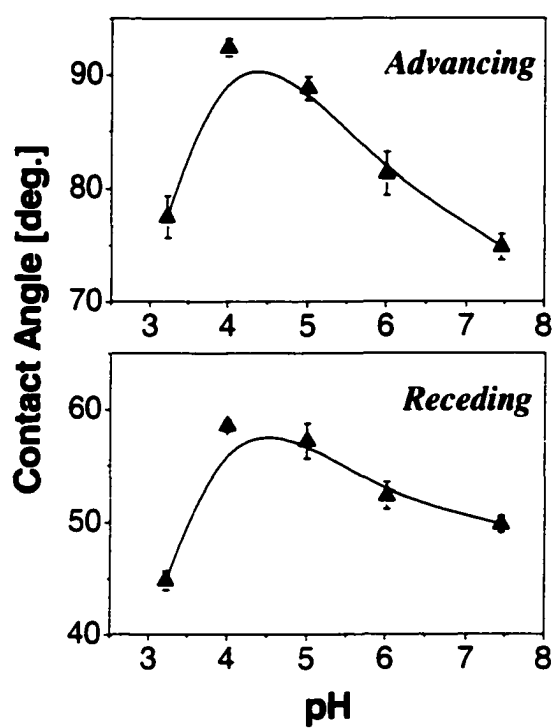


Figure 4.4: DI water contact angles on coatings deposited from an aqueous medium containing 3% reactive silane at different pH values

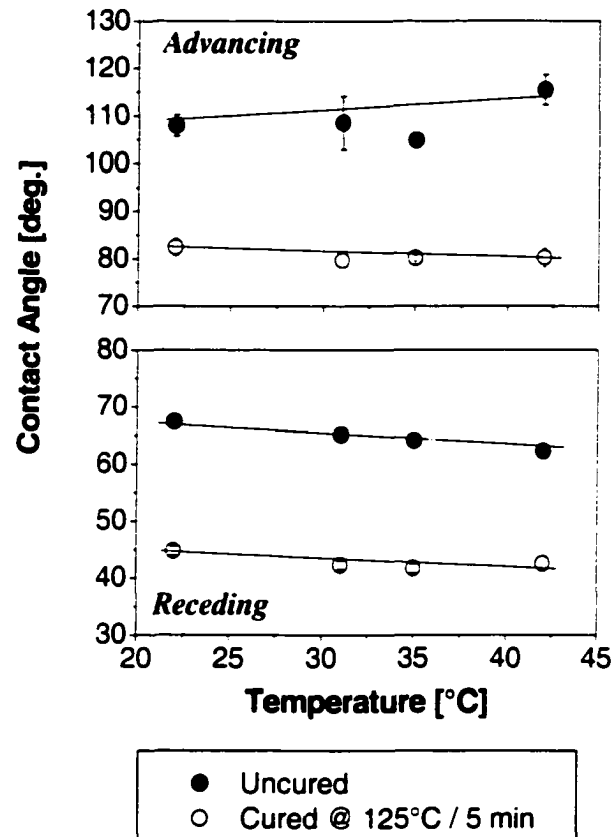
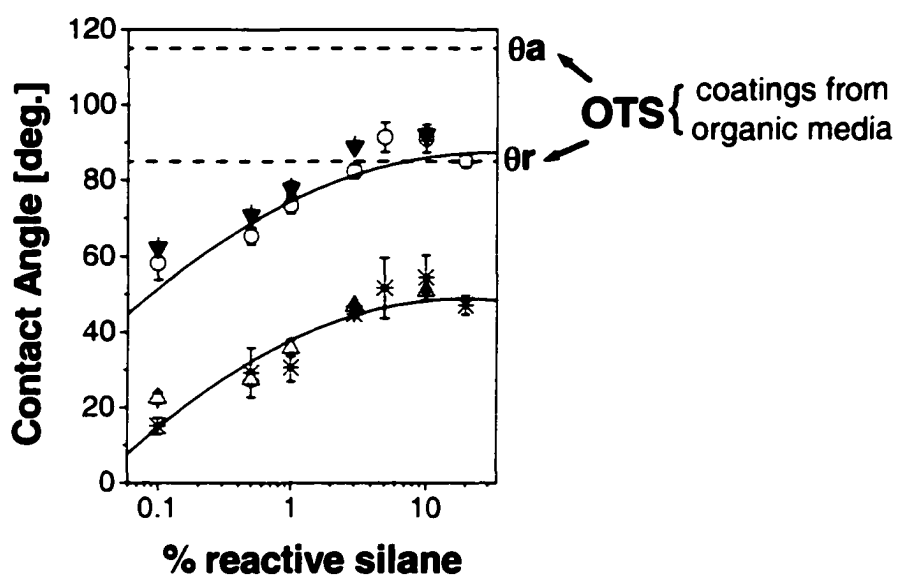


Figure 4.5: DI water contact angles on coatings deposited from Siliclad[®] aqueous dispersions containing 3% reactive silane as a function of deposition temperature

Water contact angles on undoped and phosphorous doped polysilicon samples coated by immersion in silane dispersions at pH 4 are displayed in Figure 4.6 as a function of reactive silane concentration. As may be seen from this figure, highly hydrophobic coatings, as determined by the value of the advancing (θ_{adv}) and receding (θ_{rec}) contact angles, are formed when the reactive silane concentration is higher than 3%. Phosphorous doping of the samples did not affect the hydrophobic character of the coatings. The contact angle values for coatings prepared from a dispersion containing 3% or more reactive silane are lower by $\sim 30^\circ$ than those for coatings formed from an organic solvent containing octadecyltrichlorosilane (OTS) ($\theta_{adv}=115^\circ$ and $\theta_{rec}=85^\circ$)^(1,22)

The next step in this research was to check whether drying/curing at elevated temperatures could improve the coating hydrophobicity. The effect of curing temperature in air on the hydrophobic character of the coatings deposited from a dispersion containing 5% reactive silane is shown in Figure 4.7. Both the advancing and receding contact angles increase with an increase in the curing temperature. For example, curing of the coatings at 250° increased the advancing contact angle from 90° to 120° and the receding angle from 60° to 85° . This increase could be as a result of improved packing of the film due to cross-linking of Si-OH groups in the silane molecules deposited on the surface. It has been reported that covalent attachment of hydrolyzed organosilanes with surface silanols can be facilitated by heating the silane solution to 70°C .⁽⁸⁹⁾ Interestingly, the contact angles obtained by curing the silane coatings at 250°C are equal to or slightly higher than the reported values for OTS coatings with and without curing.^(2,3,122)



Advancing: ○ undoped ▼ P doped
 Receding: * undoped △ P doped

Figure 4.6: DI water contact angles on coatings deposited from aqueous silane dispersions containing different amounts of reactive silane onto undoped and P doped polysilicon

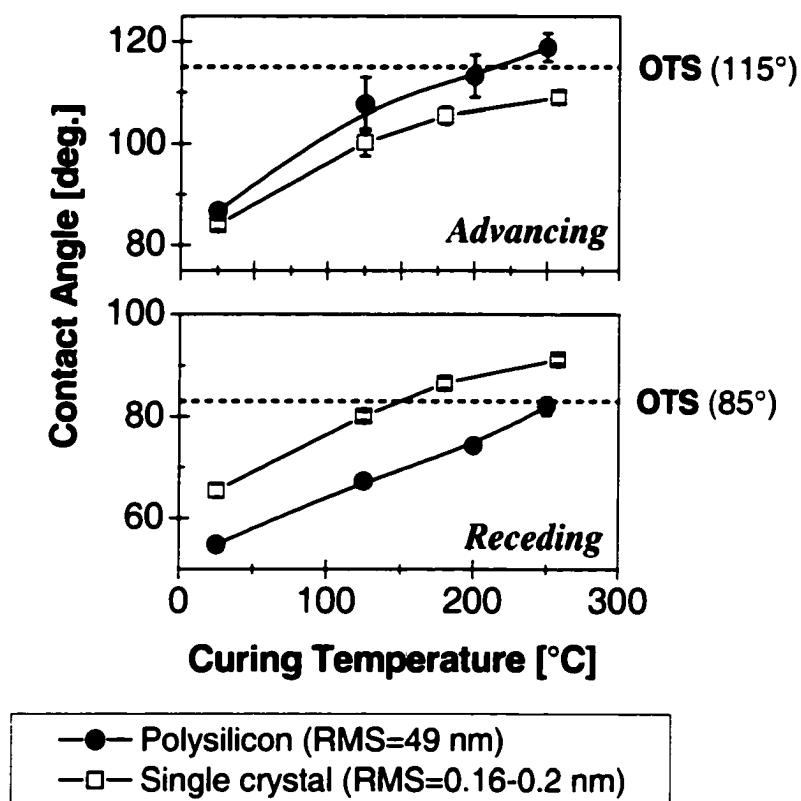


Figure 4.7: Effect of temperature and substrate roughness on hydrophobicity of coatings (coatings deposited from 5% reactive silane dispersions) [OTS data from ref.⁽¹²²⁾]

A preliminary study of the effect of surface roughness on the coating hydrophobicity was also investigated. For this purpose, coatings were also applied to smooth (RMS~0.2 nm) single crystal silicon samples pretreated in a 30% H₂O₂ solution. A comparison of advancing and receding water contact angle values obtained on a smooth single crystal surface and a rough polysilicon surface are also shown in Figure 4.7. The advancing angles of water on polysilicon are higher than that on single crystal silicon, while the reverse is true for receding angles. This can be explained using Wenzel's theory,⁽¹²³⁾ which relates the contact angle on a rough surface to that on a smooth surface through the a roughness factor ($r>1$):

$$r = \frac{\cos \theta_{\text{rough}}}{\cos \theta_{\text{smooth}}} \quad (4.1)$$

Contact angles less than 90° are decreased by roughness, while angles greater than 90° are increased by surface roughness.

Since both temperature and time are variables in a curing step, the possibility of curing at a lower temperature in an extended time period was investigated. The hydrophobicity of a coating deposited from a 3% reactive silane was evaluated as a function of curing time at 90°C. In may be seen in Figure 4.8 that the hydrophobicity achieved on coatings cured at 250°C for 5 min (indicated by a dashed line) is comparable to that obtained after curing the samples for 5 hours at 90°C.

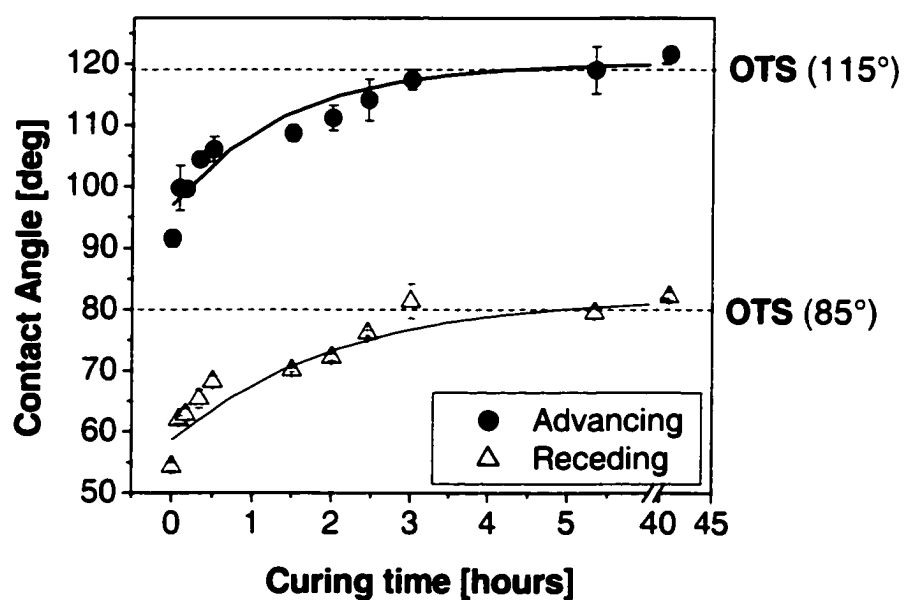


Figure 4.8: Hydrophobicity of coatings cured at low temperature (90°C) as a function of curing time (dashed line is for a coating cured at 250° for 5 min)

In order to immobilize the organic silane molecules on the substrate, a covalent bond between the silane molecules and Si-OH groups on the substrate surface is necessary. Since the nature and reactivity of Si-OH groups may depend on the oxidation treatment, investigations were carried out to determine the effect, if any, of the type of chemical oxidation treatment on the hydrophobicity of coatings. Table 4.1 shows that the quality of the coating is independent of the type of oxidation pretreatment. Interestingly, it was found that hydrophobic coatings could also be applied to freshly prepared hydrogen terminated surfaces. It is not clear at this point whether this is due to oxidation that may have occurred during the water rinsing step, physical adsorption of the silane onto bare polysilicon or chemisorption of the hydrolyzed silane on the hydrogen terminated surface. Even though the reaction of alcohols with hydrogen terminated silicon surfaces has been reported to occur in dry environments,⁽¹²⁴⁻¹²⁷⁾ no literature data exist that suggest such an interaction in an aqueous environment. If Siliclad[®] has a cationic group in its structure, then the negatively charged Si-H surface⁽¹¹⁸⁾ could induce the adsorption of the silane molecule to the substrate through electrostatic interactions. As will be shown later (Figure 4.10), the hydrogen-terminated surface requires many hours of immersion in water to be transformed to a hydrophilic state.

Table 4.1: DI water dynamic contact angles on coatings deposited onto chemical oxides formed on polysilicon by different treatments

Oxide	Without Coating		With Coating			
			Before curing		Cured @ 125°C, 5 min	
	Advancing	Receding	Advancing	Receding	Advancing	Receding
1:1:25 NH ₄ OH:H ₂ O ₂ : H ₂ O (10 min, 70°C)	15 ± 3	14 ± 1	91 ± 4	52 ± 8	108 ± 6	68 ± 1
1:4 H ₂ O ₂ :H ₂ SO ₄ (15 min, 80°C)	18 ± 2	17 ± 1	88 ± 2	50 ± 2	111 ± 5	64 ± 1
30% H ₂ O ₂ (15 min, 20°C)	13 ± 5	17 ± 1	87 ± 1	55 ± 1	108 ± 5	67 ± 2
50:1 HF (1 min)	90 ± 4	46 ± 3	93 ± 4	50 ± 1	110 ± 2	63 ± 1

In the experiments reported so far, the pH of the dispersions was adjusted with hydrochloric acid. Since it is well known that chloride may cause corrosion of aluminum metal interconnect lines, experiments were conducted to check whether the use of acetic acid for pH adjustment would affect the hydrophobicity of the coatings. It may be seen in Table 4.2 that the type of acid used had no significant effect on the hydrophobic character of the coatings.

Table 4.2: Effect of type of acid used for pH adjustment on contact angle

	UNCURED		CURED @ 250°C / 5 min	
	Advancing	Receding	Advancing	Receding
HCl	88° ± 2	50° ± 2	120° ± 2	82° ± 1
Acetic Acid	91° ± 1	53° ± 1	116° ± 4	83° ± 2

4.2.1.2 Stability of Siliclad[®] coatings

The thermal stability of Siliclad[®] coatings needs to be characterized, because most packaging processes involve steps at elevated temperatures. Figure 4.9 shows the DI water contact angles on polysilicon samples coated from 3% reactive silane dispersion at pH value of 4 as a function of annealing temperature. These samples were annealed in a nitrogen or room air environment. For the samples annealed in nitrogen, the contact angles remained constant up to 450°C. However, the film hydrophobicity is severely degraded when heated in air above 250°C. Considering the literature reports^(2,3) that OTS coatings deposited from organic media degrade when heated in air above 150°C and in nitrogen at 400°C, the aqueous silane system may offer some advantages for high temperature environments.

The effect of the presence of oxygen in air and in water on the hydrophobicity of the coatings was studied by aging coated and uncoated samples in laboratory air and by immersing samples in DI water. Bare polysilicon samples pretreated in HF were used as a baseline. It may be seen in Figure 4.10(b), that the advancing and receding water contact angles on hydrogen passivated polysilicon decreased rapidly, in a couple of hours, on exposure to water as a result of native oxide growth. The coated samples did not show any degradation for two months. This indicates that the coatings are stable for long periods of time under high humidity conditions. When exposed to laboratory air (Figure 4.10(a)), a bare polysilicon sample showed significant oxidation after a couple of days but the coated sample did not show any decrease in its hydrophobic nature in the same time frame.

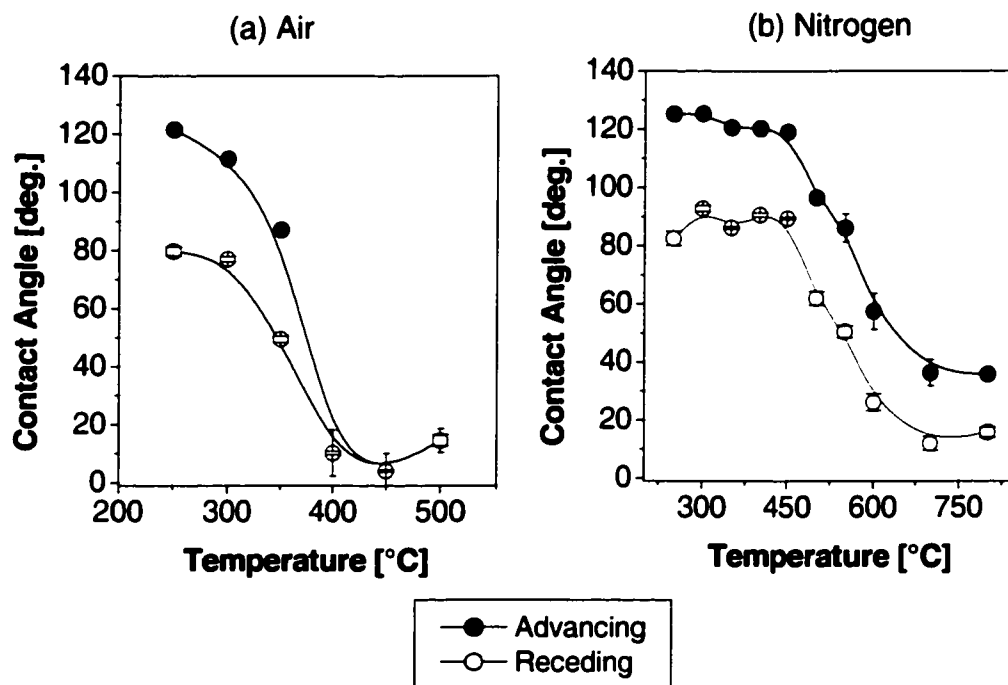


Figure 4.9: Thermal stability of Siliclad[®] coatings deposited onto polysilicon in air and nitrogen environments

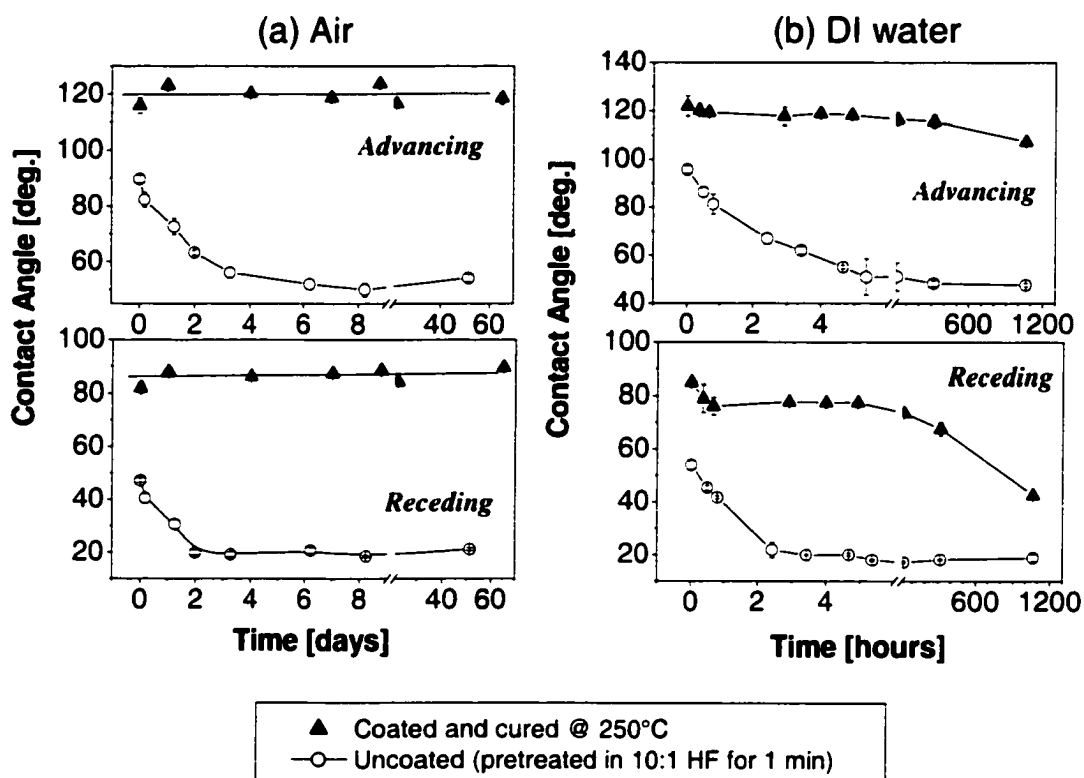


Figure 4.10: Stability of coated and uncoated samples in (a) air and (b) DI water

4.2.1.3 Surface coverage and molecular orientation of Siliclad coatings

Decreasing the reactive silane concentration in the coating solution is likely to enhance the bath life due to reduced bath cross-linking of hydrolyzed end groups of silane. Hence, the feasibility of applying the coatings from solutions containing 0.5% reactive silane was investigated as a function of immersion time. In these tests the coating formation was followed by measuring the absorbance due to the asymmetric $-\text{CH}_2$, symmetric $-\text{CH}_2$ and $-\text{CH}_3$ stretching vibrations in the $2800\text{-}3000\text{ cm}^{-1}$ region of the ATR-FTIR spectra. Figure 4.11 shows the spectra for a sample exposed for 1 and 60 min to a 0.05% reactive silane dispersion. It may be observed that the intensity of the peaks increased with exposure time as a result of increased adsorption of silane molecules to the substrate.

As shown in Figure 4.12, coating coverage increased rapidly during the first 10 minutes and slowed down perhaps due to silane adsorption onto empty spaces and/or reorientation of the molecules. In the same figure, contact angles on uncured coatings deposited at different immersion times are shown. It may be seen that a 10 minute immersion time in a silane dispersion containing 0.5% reactive silane yields coatings which are comparable to coatings deposited from a 3% reactive silane by the immersion/emersion technique done in ~ 2.5 min (Figure 4.6). This indicates that high coverage can be achieved by exposing the substrate to reactive silane dispersions of low concentration for longer periods of time.

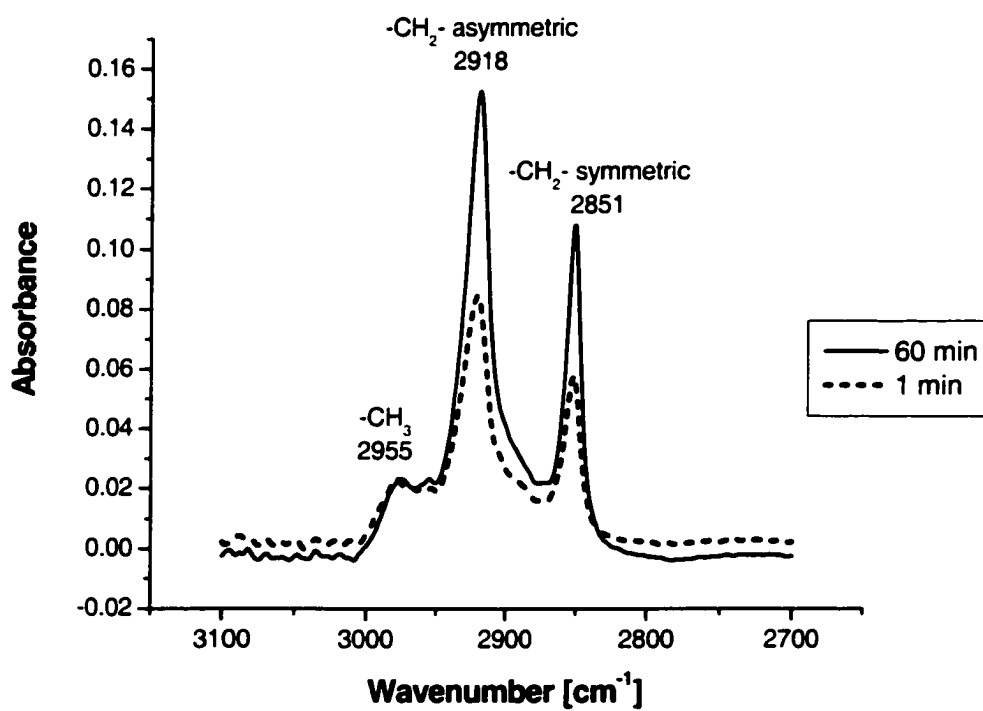


Figure 4.11: ATR-FTIR spectra of Siliclad[®] at different adsorption times

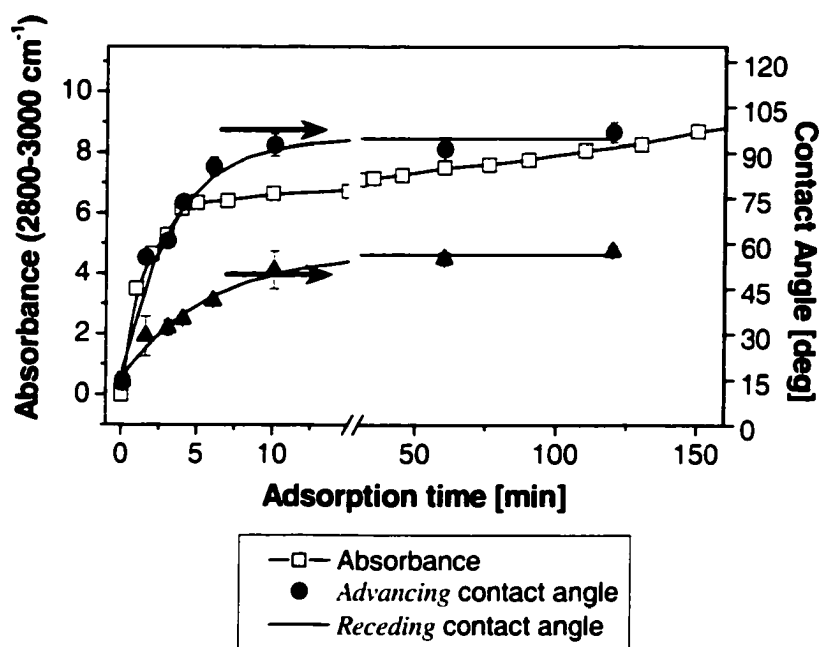


Figure 4.12: Effect of immersion time in a 0.5% reactive silane dispersion

The orientation of the molecules in the films formed by dip coating was investigated using plane and perpendicularly polarized infrared beams (Figure 3.18). The average tilt angle, β of the chain axis with respect to the substrate was calculated from the dichroic ratio (LD).

The ATR-FTIR spectra obtained using polarized (perpendicular and parallel) IR beams are shown in Figure 4.13(a) and (b) for a coating deposited from 0.5% reactive silane dispersion. Three major peaks were observed in the aliphatic stretching region (3100-2800 cm^{-1}), which were further resolved into 7 sub-peaks obtained by Gaussian curve fitting using Origin-peak fitting module v 6.1. The quality of the fit was evaluated from the chi-squared values, which were between 7.4×10^{-4} and 9.8×10^{-4} . The CH_2 stretching frequency bands in the aliphatic region were observed in the vicinity of 2918 cm^{-1} ($d^+(\pi)v_{as}(-\text{CH}_2-)$), 2852 cm^{-1} ($d^+(\pi)v_s(-\text{CH}_2-)$) and 2857 cm^{-1} ($\omega(\text{CH}_2)$). In addition, this region contained two broad bands near 2898 cm^{-1} and 2922 cm^{-1} , which are components of $d^+(\pi)$ and are in (weak) Fermi resonance with a combination of CH_2 bending vibrations. Other weak features were due to the terminal $-\text{CH}_3$ group such as 2953 cm^{-1} ($r_b^-v_{as}(\text{CH}_3)$) and 2962 ($r_a^-v_{as}(\text{CH}_3)$). Others⁽¹²⁸⁻¹³⁰⁾ have observed the same peaks in SAM coatings and surfactant systems.

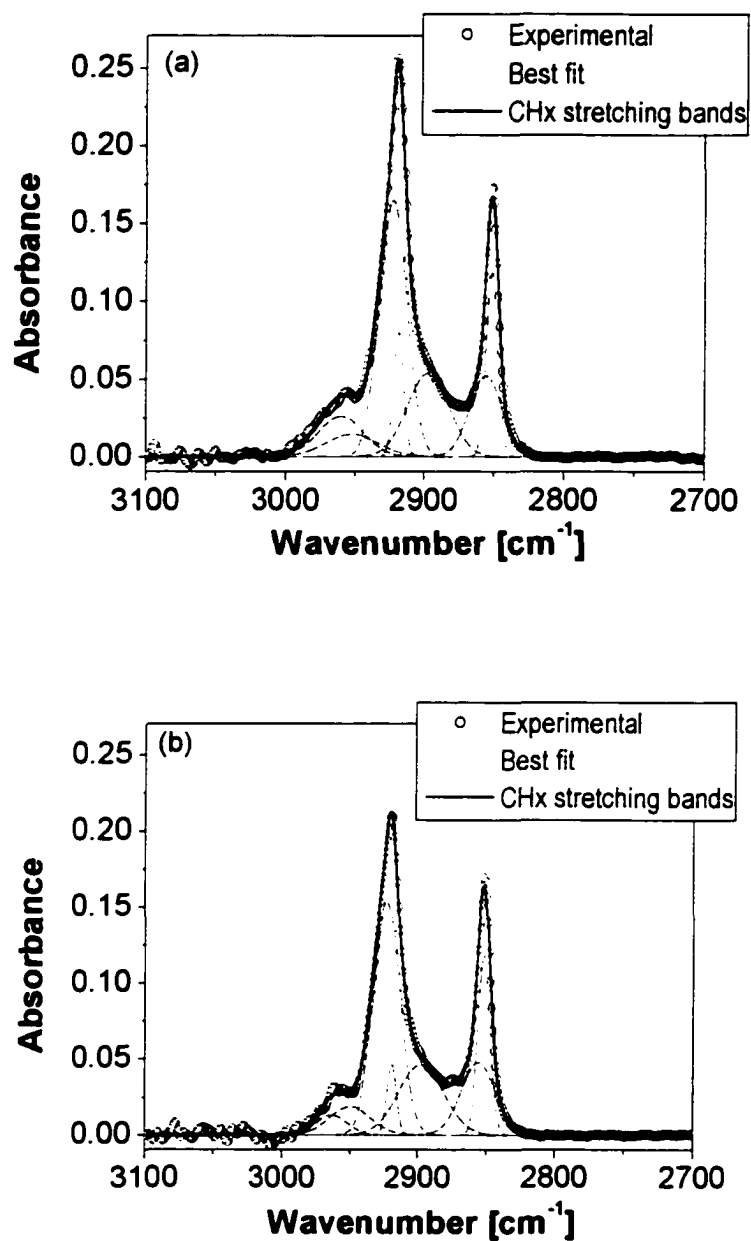


Figure 4.13: ATR-FTIR spectra obtained using polarized IR beam on a coating deposited from 0.5% reactive silane dispersion. a) 90° b) 0°

The linear dichroic ratio ($A_L/A_{||}$) was calculated for each of the $-CH_2$ sub-peaks and was used to calculate the tilt angle β (Table 4.3). The averaged linear dichroic ratios for the aliphatic region were 1.07, 1.05 and 1.01 for coatings deposited from 0.05%, 0.5% and 5% reactive silane dispersions. These values are higher than the calculated linear dichroic ratio for random orientation ($LD_{\text{random}}=0.49$) and less than the calculated linear dichroic ratio for perpendicular orientation ($LD_{\text{perpen}}=1.27$) given by equations (1) and (2). The spatial chain orientation angles (β) obtained from equation (6) for each of the sub peaks for coatings deposited from 0.05%, 0.5% and 5% are also presented in Table 4.3. The average chain orientation angles normal to the substrate were 6.5° , 7.2° and 9.2° , respectively. This indicates that the silane chains are slightly tilted. The small decrease in tilt angle β with decreasing concentration could be as a result of a decrease in particulate deposition on the coating.

The chain angles obtained for Siliclad[®] molecules are in agreement with what Allara⁽⁵⁰⁾ and Bierbaum⁽¹³¹⁾ found for octadecyltrichlorosilane (OTS) and octadecyltrimethoxysilane (OTMS) monolayers. They found that OTS is tilted at $10 \pm 2^\circ$ and that the adsorption mechanisms of trichlorosilane and trimethoxysilane groups were different, resulting in a higher tilt angle of the chains in OTMS SAMs.

Table 4.3: Linear dichroic ratio and chain orientation for silane adsorbed on single crystal silicon. Refractive indexes used for the calculations were $n_{\text{silicon}}=3.42$, $n_{\text{water}}=1.42$ and $n_{\text{SAM}}=1.5$.

Mode description of $-\text{CH}_2$ stretching	0.05%		
	Peak frequency center [cm^{-1}]	LD	β [deg.]
$d^-(\pi)v_{\text{as}}$	2919.7 ± 0.6	0.96	10.8
$d^+(\pi)v_{\text{s}}$	2851.4 ± 0.2	1.13	4.4
ω	2855.5 ± 0.1	1.02	8.3
$d_{\text{s}}^-(\text{CH}_2)$	2921.8 ± 0.2	1.21	1.9
$d_{\text{s}}^+(\text{FRC})$	2895.6 ± 0.6	1.06	6.9
Average		1.07 ± 0.1	6.5 ± 3.5
	0.5%		
$d^-(\pi)v_{\text{as}}$	2918.7 ± 0.5	1.19	2.4
$d^+(\pi)v_{\text{s}}$	2851.6 ± 0.3	0.93	12.2
ω	2856.0 ± 0.2	1.02	8.4
$d_{\text{s}}^-(\text{CH}_2)$	2921.1 ± 0.3	1.09	5.6
$d_{\text{s}}^+(\text{FRC})$	2897.5 ± 0.2	1.04	7.5
Average		1.05 ± 0.1	7.2 ± 3.6
	5%		
$d^-(\pi)v_{\text{as}}$	2918.8 ± 0.5	1.01	8.7
$d^+(\pi)v_{\text{s}}$	2851.7 ± 0.2	0.85	15.9
ω	2853.7 ± 0.5	1.10	5.5
$d_{\text{s}}^-(\text{CH}_2)$	2922.6 ± 0.1	0.99	9.6
$d_{\text{s}}^+(\text{FRC})$	2897.8 ± 0.5	1.08	6.1
Average		1.01 ± 0.1	9.2 ± 4.1

It is well established that the asymmetric CH_2 stretching frequency ($d^-(\pi) v_{\text{s}}(-\text{CH}_2-)$) is a reliable indicator of film quality for alkyl SAMs. It can vary from 2917 cm^{-1} for close-packed films to 2924 cm^{-1} for liquid-like films.⁽¹²⁾ This stretching frequency for Siliclad[®] coatings was around 2919 cm^{-1} , which indicates the formation of reasonably close-packed films.

4.2.1.4 Zeta Potential measurements on Siliclad[®] coatings

The zeta potential profiles of coated and uncoated polysilicon are displayed in Figure 4.14. The negative zeta potentials of the coated sample are lower than those of uncoated pre-oxidized polysilicon. This is attributable to the reduction of the number of silanol groups on the substrate, due to their consumption through covalent bonding of organosilane molecules with the substrate. The iso-electric point of the coated sample was estimated to be at pH 3.5-4.0. This is higher than the uncoated sample's IEP. The same behavior has been reported⁽¹³²⁾ for silicon oxide coated with octadecyltrimethoxysilane (OTMS) and fluoroalkylsilanes (FDTS). In fact, literature reports indicate that the surface chemical properties of OTMS and FDTS coated surfaces are similar to polyethylene and polytetrafluoroethylene plates.

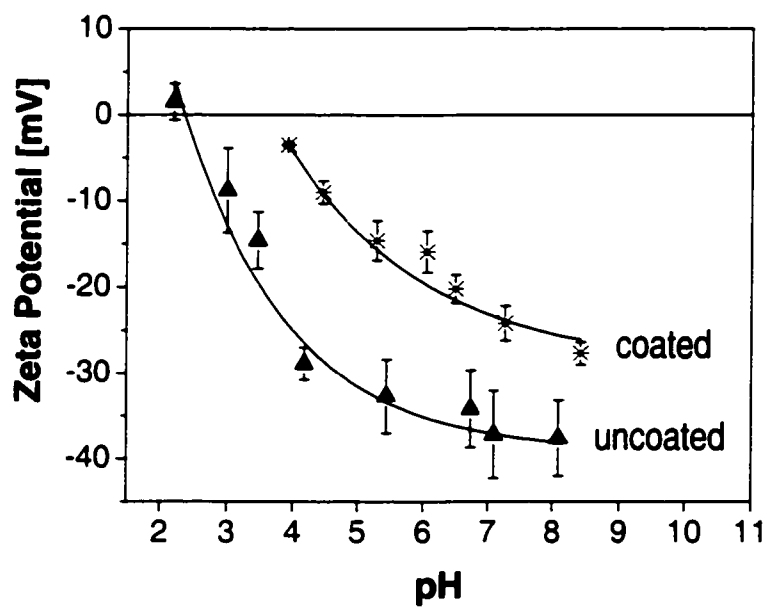


Figure 4.14: Zeta potential of coated and uncoated pre-oxidized polysilicon as a function of pH

4.2.1.5 Langmuir-Blodgett film deposition of Siliclad[®] coatings

Siliclad[®] coatings were prepared by the Langmuir-Blodgett method for organic film deposition, because it has the advantage of preparing highly ordered densely packed and defect-free thin molecular films. The hydrophobic character of these films was compared to those deposited by dip coating, which are described in section 4.2.1.1 of this dissertation. Figure 4.15 shows the surface-pressure-area (π -A) isotherm for Siliclad[®] spread on the surface of pure water at room temperature. Siliclad[®] molecules were spread by depositing drop by drop 550 μ L of a 0.04% reactive silane solution onto 400 ml of DI water. The isotherm exhibited a sharp rise in surface pressure when the film area was compressed to 250 cm^2 . The shape of the isotherm in the region of 0 to 34 dynes/cm indicates a liquid-condensed phase. It is not clear what the transition around 34 dynes/cm really means. The slope of the π -A isotherm did not change when the area was further decreased. Hence, it is unlikely that the small transition represents liquid-expanded to liquid-condensed phases.

Contact angles of water on the films deposited at different surface pressures are indicated in Figure 4.15. The adsorption density of Siliclad determined by ATR-FTIR measurements is also shown in the same figure. It appears that the films are rendered more hydrophobic if deposited at high surface pressures. Additionally, the adsorption density of Siliclad onto pre-oxidized silicon increases with an increase in surface pressure. However, the hydrophobicity of these coatings is similar to those deposited by dip

coating. It appears that there is no advantage in using the Langmuir-Blodgett technique to deposit coatings.

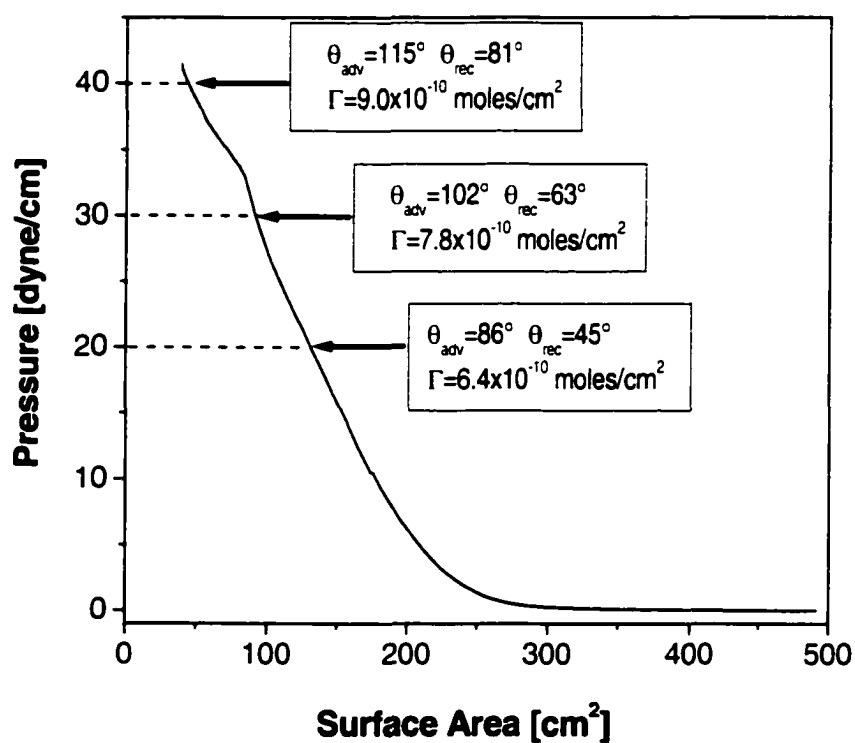


Figure 4.15: Surface pressure-area isotherm for Siliclad[®] spread on water. Contact angles and adsorption densities of coatings formed at different surface pressures and cured at 200°C for 5 min

4.2.1.6 Stability of Siliclad[®] aqueous dispersions

For efficient attachment to surfaces, water dispersible silanes need to be hydrolyzed but at the same time cross-linking between silane molecules in the bulk needs to be minimized. The attachment of bulk cross-linked silane oligomers would result in the build up of silane films, as shown in Figure 2.23(b) and (c). Aqueous silane dispersions containing 3% reactive silane at a pH value of 4 were not very stable, and turned cloudy and precipitated after standing for several days. The stability of silane dispersions was evaluated by measuring the viscosity at 30°C as a function of aging time (Figure 4.16). The viscosity increased slowly during the first few days and then increased rapidly. The stability limit was taken at the time when a rapid change in viscosity started to occur. This pattern of rapid increase in viscosity at the gel point is typical for thermosetting systems. It may be seen from Figure 4.16 that the hydrophobicity of the coatings decreased with the onset of rise in viscosity of the silane dispersion. After aging the dispersion for 4 days, curing at 125°C did not improve the hydrophobic character of the coatings.

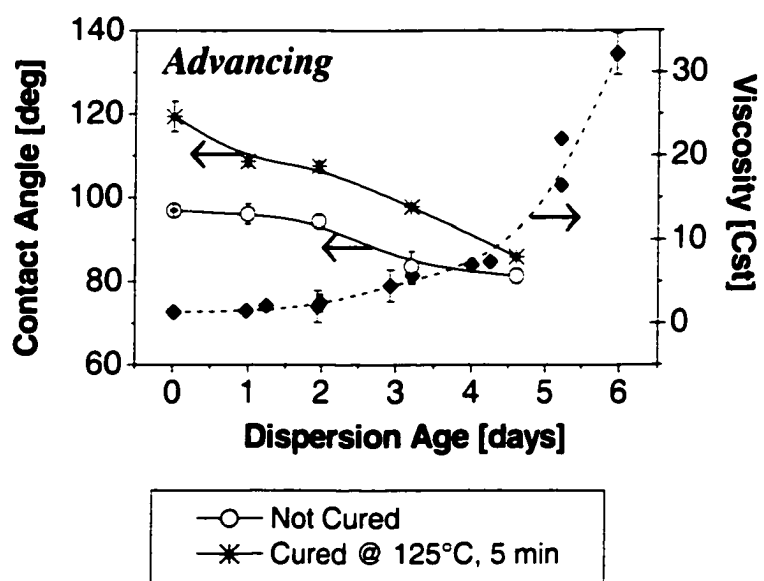


Figure 4.16: Viscosity of Silane Dispersions and Water Contact Angles on Coated surfaces as a function of dispersion age

The stability of fresh aqueous dispersions containing 3% reactive silane at different pH values was evaluated by measuring the increase in viscosity as a function of aging time (Figure 4.17(a)). The gel point was determined as the number of days it took for the viscosity to reach a value of ~3 cSt and is plotted in Figure 4.17(b) as a function of pH. The stability of Siliclad[®] dispersions exhibited a maximum around a pH of 4. This is similar to what has been reported in literature^(81,133) for other alkyltrialkoxysilanes. As discussed earlier (Figure 4.4), the highest hydrophobicity ($\theta_{adv} > 110^\circ$) was produced from dispersions adjusted to a pH of 4.

The amount of reactive silane in the aqueous phase (Figure 4.18) can also affect the relative rates of hydrolysis and condensation of silanes. The viscosity of dispersions containing 1% reactive silane at pH value of 4 reached a maximum after 15 days and no gelling was observed. However, precipitation of small particulates was observed at the bottom of the container. For a dispersion containing 3% reactive silane, the formation of a solid gel was observed after 4 days. The viscosity of dispersions containing less than 0.1% reactive silane did not change for more than one month, indicating that the formation of high molecular weight networks does not occur over a period of a month at very low Siliclad[®] concentrations.

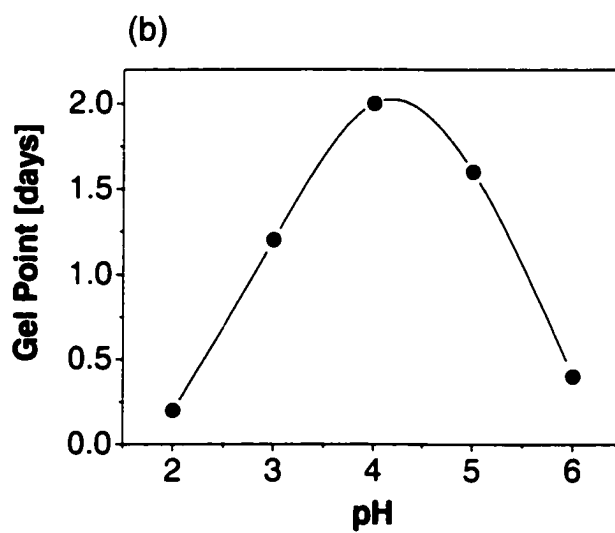
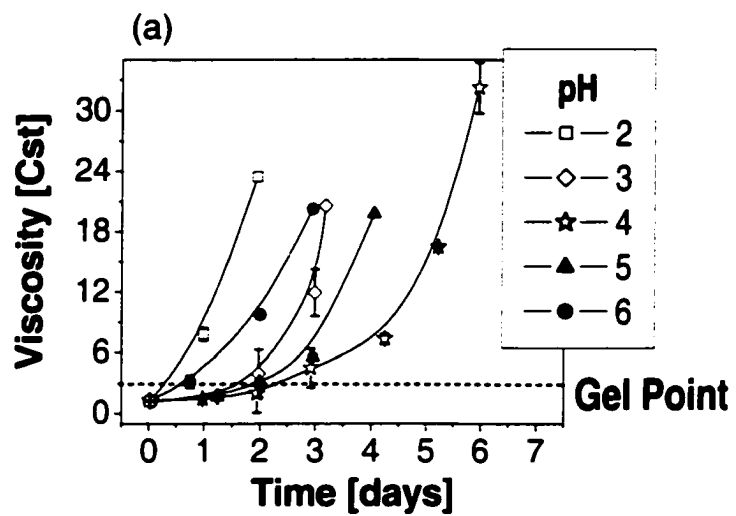


Figure 4.17: Dispersion stability as a function of pH

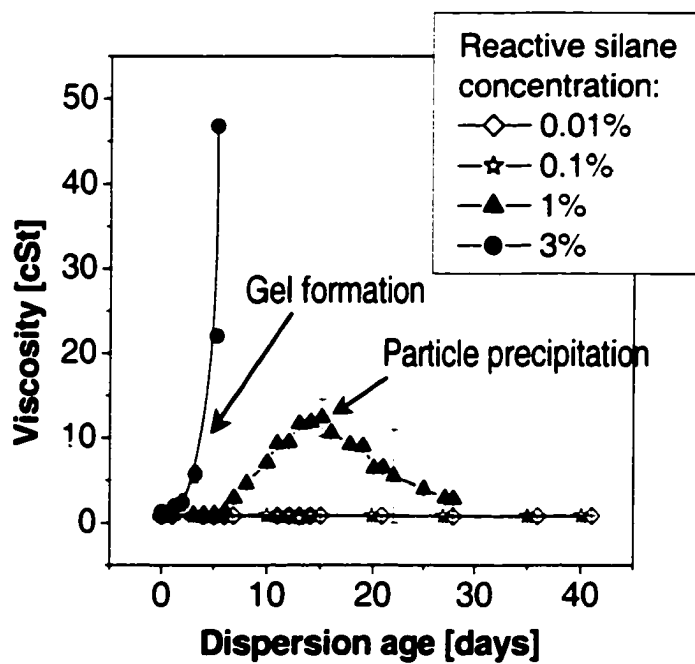


Figure 4.18: Dispersion stability as a function of reactive silane concentration at pH=4

4.2.2 System 2: Siliclad[®] with surfactant

For efficient attachment to surfaces, water dispersible silanes need to be hydrolyzed but at the same time cross-linking between silane molecules in the bulk needs to be minimized. A first set of experiments were conducted to check whether the addition of an alkyl dimethyl benzyl ammonium chloride (Empigen BAC) cationic surfactant can increase the stability of the silane dispersions and thereby improve coating bath life. As may be seen from Figure 4.19(a), the addition of this cationic surfactant, at a suitable concentration, can delay the onset of the rise in viscosity. The surfactant addition had no deleterious effect on the contact angle when the surfactant concentration was below 0.05 M (Figure 4.19(b)), but at higher concentrations the surfactant molecules prevented the silanes molecules from adsorbing onto the surface, which is reflected by the decrease of contact angles.

The addition of other cationic surfactants was also investigated. Initial experiments on the improvement on the stability of Siliclad[®] aqueous dispersions were focused on mixing the cationic surfactants at 20 times their critical micelle concentration (CMC) with 3% reactive silane adjusted to pH of 4. It may be seen in Figure 4.20 that the addition of dodecyltrimethylammonium bromide (DTAB) created a very stable silane dispersion, but the hydrophobicity of the coatings applied from this dispersion was very poor ($\theta_{adv}=60^\circ$ and $\theta_{red}=30^\circ$). This is most likely caused by the competitive adsorption of DTAB onto the polysilicon surface since the dispersion contains very high surfactant concentration (0.32 M) as compared to Siliclad[®] (0.05 M). No correlation between the surfactant structure and stability improvement was found.

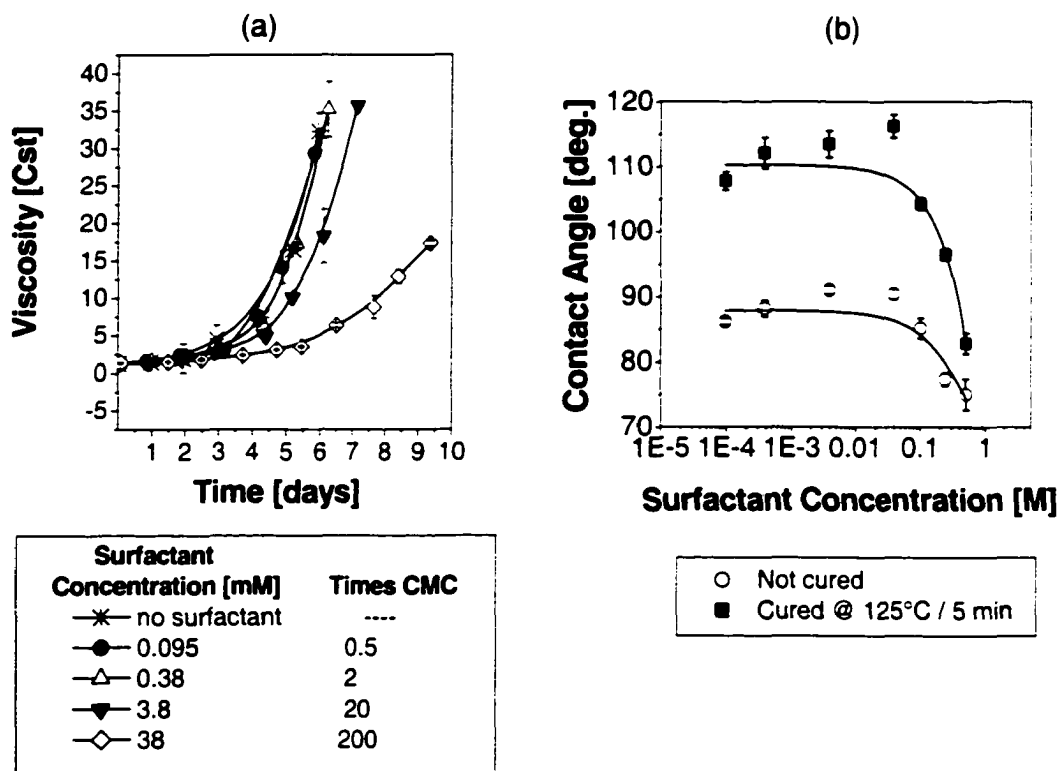


Figure 4.19: (a) Stability of silane dispersions and (b) coating hydrophobicity as a function of Empigen BAC surfactant concentration

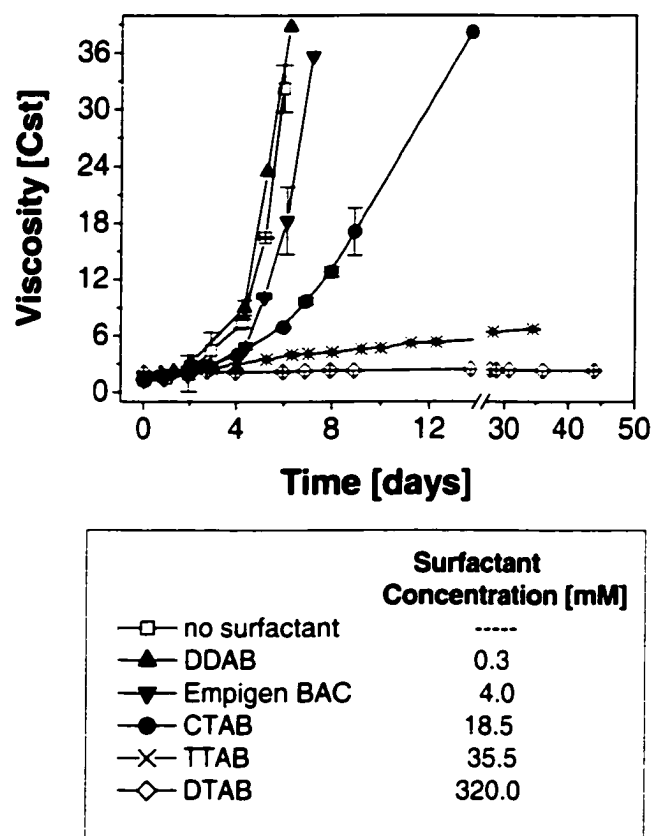


Figure 4.20: Stability of 3% reactive silane dispersions containing different cationic surfactants (Note: surfactant concentration was 20 times the critical micelle concentration)

In order to characterize the influence of the surfactant structure and chain length on the stability of aqueous silane dispersions, studies were focused on dispersions that contained the same molar concentration of surfactant and silane (0.05 M). Figure 4.21 shows that linear alkyl ammonium surfactants were the most effective in stabilizing the dispersions; this can be seen from the low and constant viscosity values even after 10 to 15 days. Cetyltrimethylammonium bromide (CTAB) was the most effective of all and prevented the viscosity from rising above 6 cSt in more than one month, whereas the silane dispersion without surfactant turned cloudy and reached a viscosity value of 40 cSt in less than 3 days. The stability of the silane dispersion increased by increasing the length of the hydrocarbon chain of the surfactant; this may be explained by the formation of micelles containing surfactant as well as hydrolyzed organosilane molecules. The longer the surfactant molecule, the higher the aggregation number (Table 3.1) and the lower the concentration at which aggregation is initiated: this may allow the formation of micelles at lower concentration with a greater number of organosilane and surfactant molecules in each micelle. The role of these mixed micelles in controlling interaction of silane with the surface hydroxyl groups will be addressed in a later section of this dissertation.

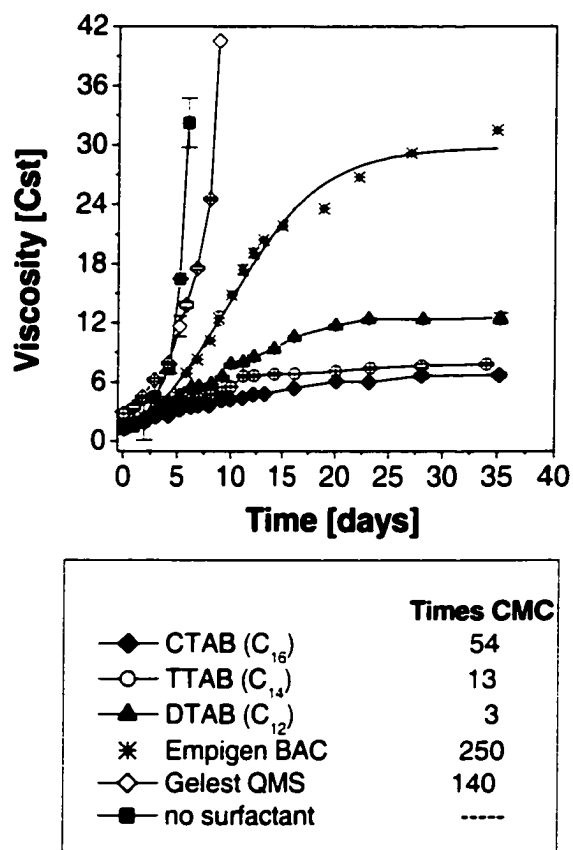


Figure 4.21: Stability of silane dispersions containing the same molar concentration of surfactant and silane (0.05 M)

The DTAB surfactant was chosen for an in depth study. ATR-FTIR measurements were carried out to determine the extent of DTAB adsorption onto pre-oxidized silicon. For these tests a DTAB concentration of 16 mM and a pH of 4 were chosen. After carrying out the adsorption for 1 hour the IRE crystal was rinsed with DI water. As may be noticed from Figure 4.22(a), DTAB exhibited rapid adsorption in the first 10 minutes and adsorbed slowly thereafter up to a value of 2.7×10^{-10} moles/cm². The desorption behavior of DTAB is shown in Figure 4.22(b) and is evident that most of the surfactant (2.45×10^{-10} moles/cm²) desorbed from the surface after rinsing with deionized water for 10 minutes.

The hydrophobicity of coatings deposited from Siliclad[®] dispersions containing 3% reactive silane and different amounts of DTAB, CTAB and Empigen BAC surfactant are shown in Figure 4.23(a). It is pertinent to mention that the samples were rinsed prior to contact angle measurements. Highly hydrophobic coatings were obtained when the surfactant concentration was below 0.05 M, what indicates that considerable amount of silane must adsorb at surfactant concentration < 0.5 M. Increasing surfactant level above this concentration decreased the contact angle. This suggests that the surfactant interferes with the interaction of silane with the surface. It is possible for DTAB molecules themselves to adsorb on silicon, however as shown in Figure 4.23(b), increasing the amount of DTAB adsorption actually makes polysilicon more hydrophilic.

ATR-FTIR measurements were also carried out to determine the adsorption of Siliclad[®] from dispersions containing 3% reactive silane and different amounts of DTAB. These data, obtained after a water rinse following the adsorption step, are shown in Figure 4.23(b). It should be mentioned that the adsorption density was calculated using the absorbance of the CH₂ and CH₃ region. Typically, this would represent the adsorption of both DTAB and Siliclad[®]. However, the rinsing step as shown in Figure 4.22(b)) would have removed most of the adsorbed DTAB. For coatings deposited from dispersions containing DTAB below its critical micelle concentration (CMC), the adsorption density was between 1.3×10^{-9} and 1.6×10^{-9} moles/cm². The adsorption density of Siliclad[®] decreased rapidly to values as low as 6×10^{-10} moles/cm² when the surfactant concentration increased above 0.5 M. It is reported in literature^(122,134,135) that one hydrolyzed OTS molecule occupies an area of 0.21 ± 0.03 nm². Using these values and assuming that hydrolyzed Siliclad[®] molecules behave as OTS, a monolayer of Siliclad[®] may be calculated to be in the range 6.9×10^{-10} to 9.2×10^{-10} moles/cm². Coatings deposited from silane dispersions containing small amounts of DTAB (below 0.01 M) appear to be thicker than a monolayer. AFM studies in section 4.3.3 of this dissertation will show that these coatings indeed contain particulates. As the surfactant concentration increased, the adsorption density decreased due to retarded condensation in solution that reduced the deposition of particulates on the substrate. For surfactant concentration greater than 0.05 M the formation of mixed DTAB-Siliclad[®] coating would be expected immediately after dip coating. Rinsing would effectively remove DTAB, resulting in disordered and porous coatings with poor hydrophobicity.

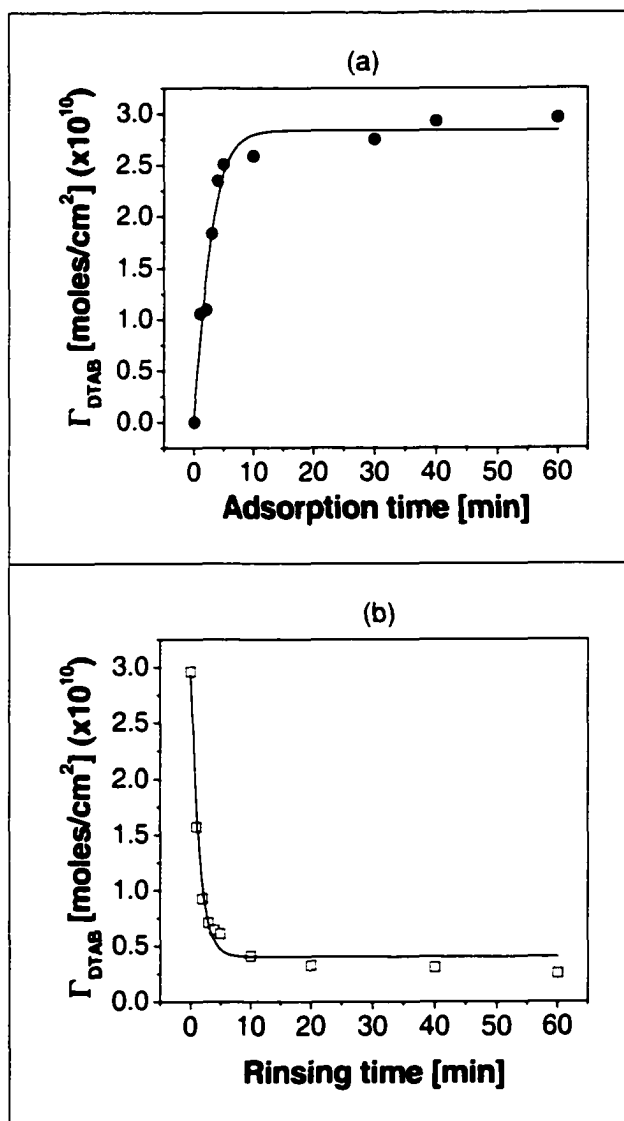


Figure 4.22: (a) DTAB adsorption isotherm onto pre-oxidized silicon at pH of 4 and (b) amount of surfactant remaining as a function of rinsing time

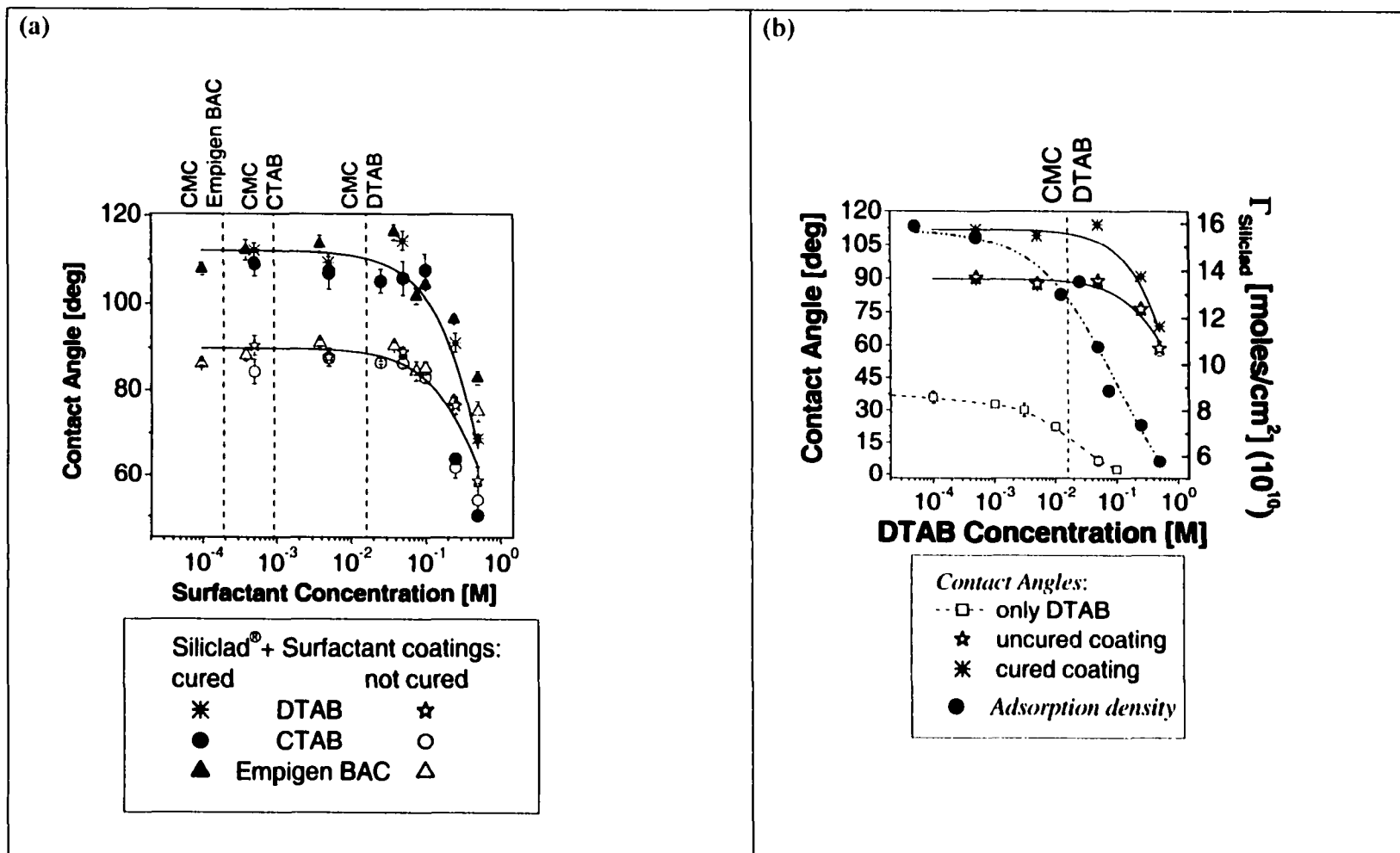


Figure 4.23: DI water advancing contact angles of cured and uncured coatings and adsorption density of rinsed coated samples formed from a 3% reactive silane dispersion containing different amounts of surfactant

The hydrophobicity of coatings deposited from dispersions with CTAB surfactant as a function of aging time is shown in Figure 4.24. The cured films formed from freshly prepared baths yield very hydrophobic films with advancing contact angles of 114° . The advancing contact angle for cured films decreased from 115° to 100° during the first five days of bath life and remained almost constant afterwards. This indicates that the surfactant reduced considerably the silanol cross-linking in the aqueous dispersion but did not eliminate it. In all cases curing improved the hydrophobicity of the coatings by at least 10° .

The role of cationic surfactants in retarding the condensation of silanes was investigated using ATR-FTIR technique with a ZnSe IRE. Figure 4.25(a) shows the evolution of ATR-FTIR spectra of a freshly prepared 3% reactive silane dispersion without surfactant as a function of dispersion age. Sharp bands due to SiO_x stretching modes appear in the region between $1100\text{-}900\text{ cm}^{-1}$.^(136,137) The bands in the range $980\text{-}890\text{ cm}^{-1}$ are associated with the Si-OH groups.⁽⁵¹⁾ The increase of the broad band centered at 1063 cm^{-1} , which can be attributed to asymmetrical stretching of the Si-O groups, is due to the covalent attachment with other organosilane molecules via Si-O-Si bonds. The presence of absorption bands at 1077 and 1048 cm^{-1} are due to the formation of longer alkylpolysiloxane chains that split the Si-O adsorption band into two or more overlapping components.⁽¹³⁸⁾ The number, positions, widths and intensities of these Si-O-Si bands have been established to depend on many structural parameters, such as extent

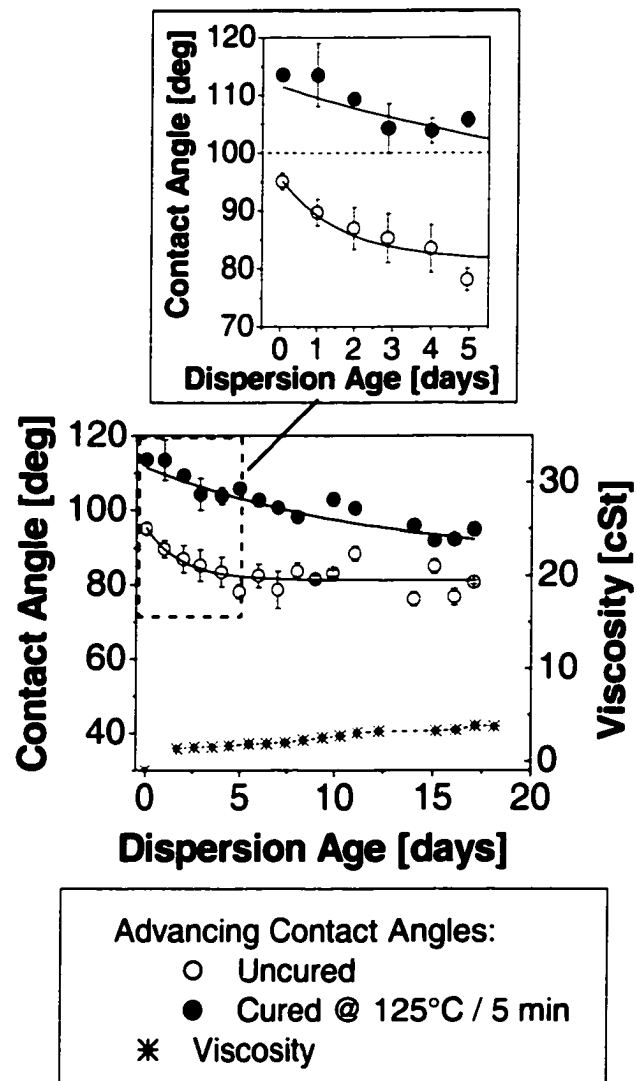


Figure 4.24: Viscosity of silane dispersions containing CTAB and water advancing contact angles on coated surfaces as a function of dispersion age

of polymerization, branching, presence and size of cyclic units, hydrogen bonding of unreacted silanols and nature of alkyl substituents on the silicon.⁽¹³⁹⁾ With increasing dispersion age, the intensity of the bands associated with Si-O-Si increased. It is interesting that the intensity of the Si-OH peaks is almost constant during the aging process; this perhaps indicates that the condensation of the Si-OH peaks to form Si-O-Si is much faster than the hydrolysis process which yields Si-OH groups.

Figure 4.25(b) shows the effect of DTAB and CTAB on the condensation of silanes in a dispersion aged for 4 hours. It should be easily discernible from this figure that the addition of surfactant decreases the intensity of the peak in the vicinity of 1063 cm^{-1} that is attributable to the Si-O-Si group. This clearly shows that cationic surfactants retard the condensation of silanes. Since the structure of Siliclad[®] molecules is unknown due to proprietary information from the company, it is difficult to establish the exact hydrolysis mechanism.

The kinetics of Siliclad[®] condensation from dispersions with and without surfactant was followed through the intensity of the peak at 1063 cm^{-1} ; this is shown in Figure 4.26 as a function of dispersion age. In the systems containing surfactant, the height of the 1063 cm^{-1} peak increased less rapidly with time when DTAB or CTAB is present. At a given dispersion age, CTAB appears to be more effective than DTAB in retarding the formation of organosilane networks.

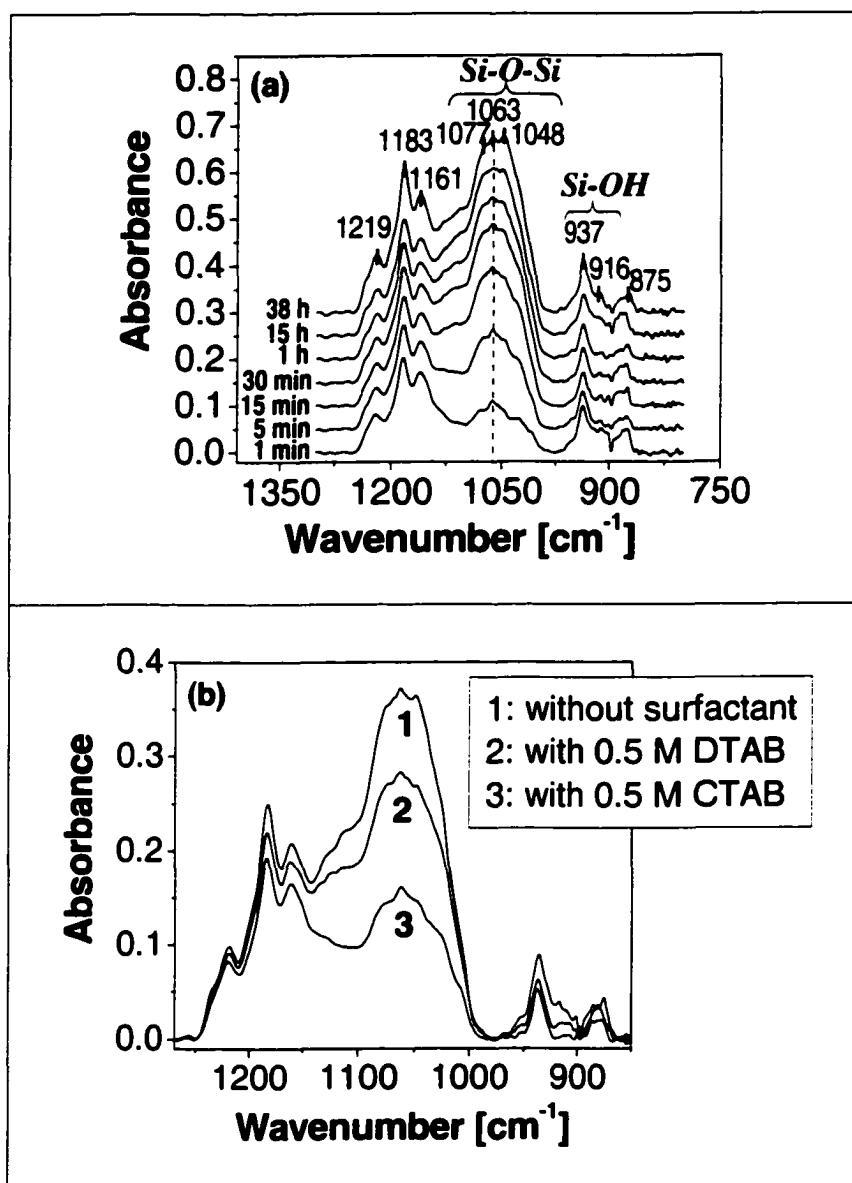


Figure 4.25: ATR-FTIR spectra of 3% reactive silane (a) without surfactant as a function of dispersion age and (b) with and without surfactant aged for 4 hours

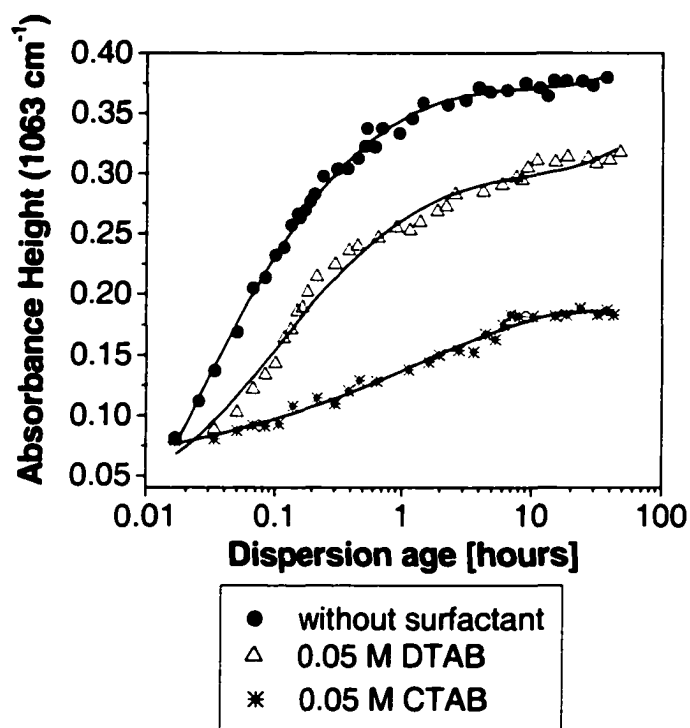
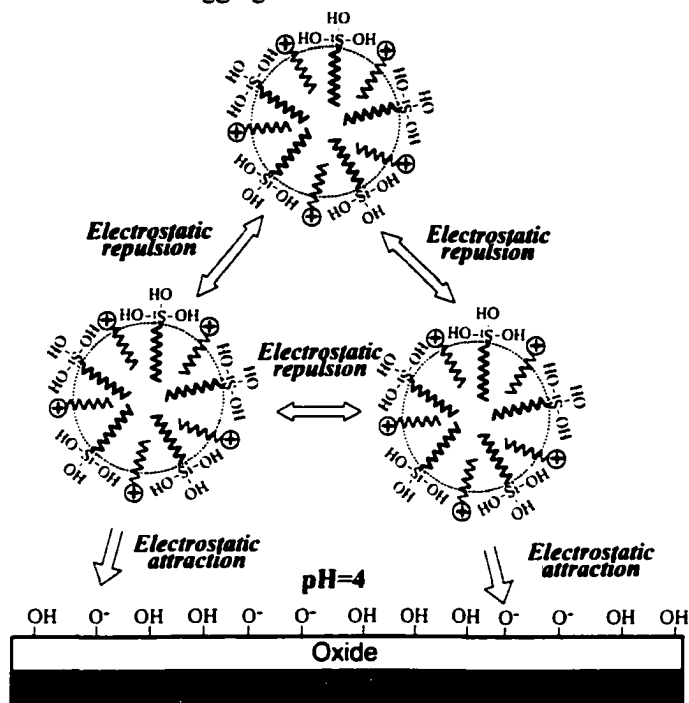


Figure 4.26: Kinetics of condensation for dispersions containing 3% reactive silane with and without surfactant

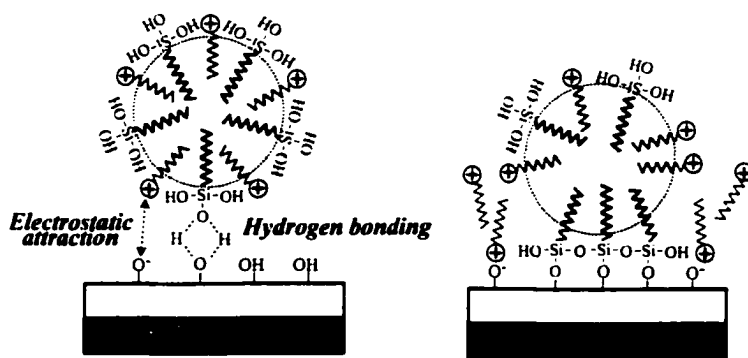
A plausible mechanism for the role played by the cationic surfactant molecules is schematically shown in Figure 4.27. The surfactant molecules serve two purposes: (i) prevent bulk condensation of hydrolyzed silanes by forming micelles containing surfactant and silane molecules and (ii) promote the transfer of silane molecules to the polysilicon surface by their electrostatic attraction to the oxidized polysilicon surface. The coating system is maintained at a pH value of 4, where the surface of pre-oxidized polysilicon would develop a net negative charge in the coating solution. The micelles of the cationic surfactant would be attracted to the negatively charged polysilicon surface and in that process they may be expected to transport the silane molecules to the surface. Once the hydrolyzed silane molecules are close to the surface they would react with the Si-OH sites to form a Si-O-Si linkage with the surface. Obviously, the extent of hydrophobicity of the surface will depend upon the tightness of packing of the hydrocarbon silanes after they chemisorb onto the surface. The removal of physisorbed surfacants and excess silane is completed by a deionized water rinse.

In order to confirm the proposed adsorption mechanism in a system containing cationic surfactants and organosilanes, zeta potential measurements were carried out on pre-oxidized polysilicon in 0.01 M KNO_3 solutions maintained at different pH values (Figure 4.28). The point of zero zeta potential or iso-electric point (IEP) was found to occur at a pH of approximately 2.5; this is in agreement with values reported in literature for silicon oxides on single crystal silicon.^(119,140)

(a) Surfactant/Silane aggregation and interaction



(b) Adsorption mechanism



(c) Rinsability with DI water

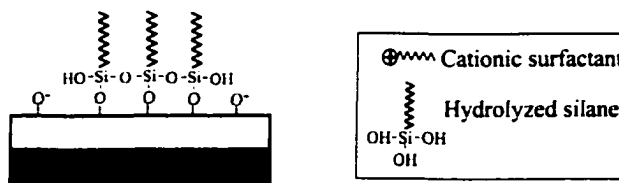


Figure 4.27: Mechanism model of surfactant/silane aggregation and adsorption onto pre-oxidized silicon at a pH of 4.

The zeta potential of pre-oxidized polysilicon as a function of DTAB concentration at pH value of 4 is also shown in Figure 4.28. The zeta potential reversed at a concentration of $\sim 2 \times 10^{-3}$ M which is below the critical micelle concentration value of DTAB. This sharp change, from negative to positive zeta potential, in cationic surfactant systems has been attributed to hemimicelle formation,^[14] where surface aggregates formed on the substrate reverse the overall zeta potential. The extent of adsorption of DTAB from a 16 mM solution as a function of pH onto pre-oxidized silicon is shown in Figure 4.29. The adsorption of DTAB was found to increase in the pH range of 2 to 5 and reached a plateau for pH values above 5. This shows that at pH value of 4 used in the coating experiments, DTAB molecules are likely to adsorb electrostatically onto pre-oxidized silicon but the adsorption density is not at its maximum.

The adsorption and zeta potential data lend credibility to the mixed micelle adsorption mechanism proposed in Figure 4.27. The addition of surfactants to silane dispersions provides stability against gelling of the dispersions. However, the amount of surfactant must be controlled to ensure that the hydrophobicity of the coating is not compromised. Based on the experimental conditions investigated, if the surfactant level is maintained below 0.05 M the stability of a 3% reactive silane dispersion can be significantly increased and the coatings formed from such co-dispersion can be made highly hydrophobic.

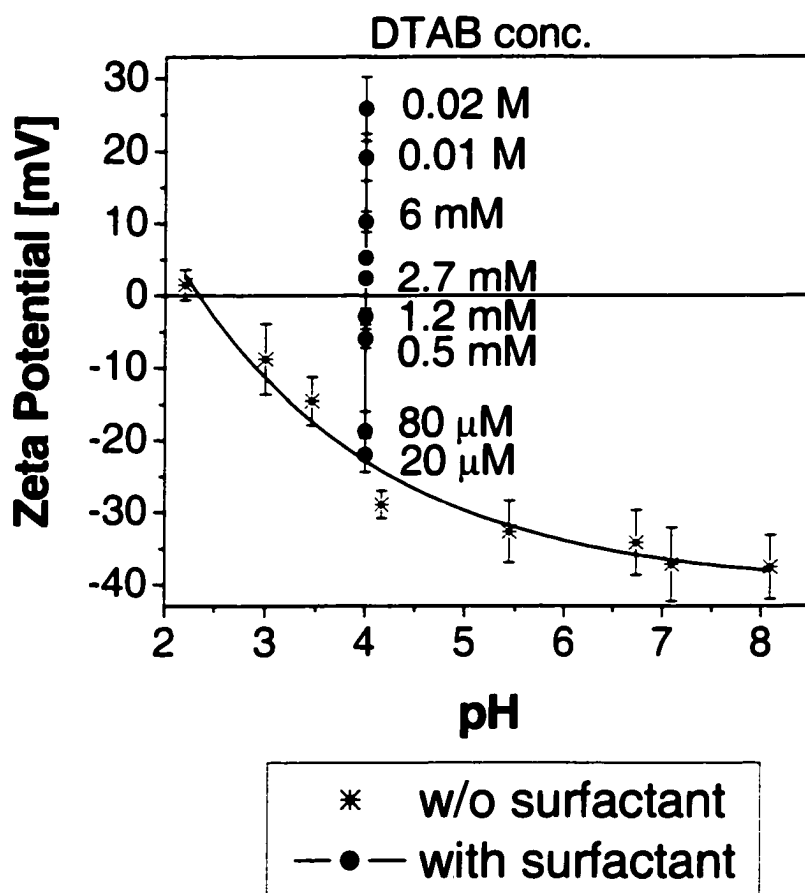


Figure 4.28: Zeta potential of pre-oxidized polysilicon as a function of pH and DTAB concentration

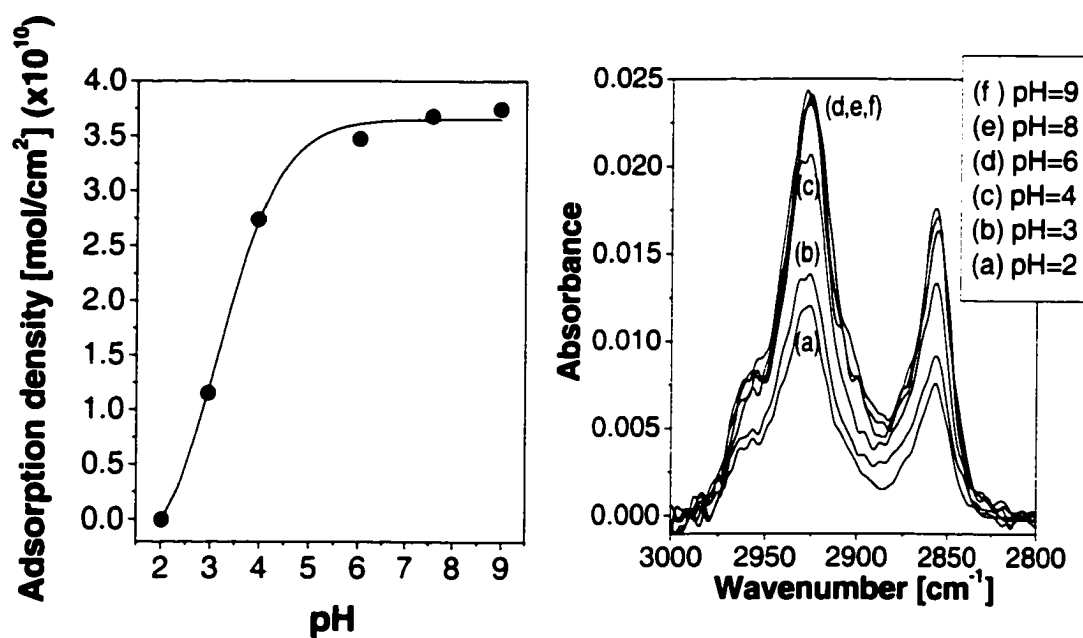


Figure 4.29: DTAB adsorption density as a function of pH

4.2.3 System 3: Glassclad[®]18

As may be seen from Figure 4.30, coatings formed with Siliclad[®] and OTS are more hydrophobic than the ones formed from Glassclad[®]18 silane dispersions. Curing of Glassclad[®]18 coatings at 125°C for 5 minutes resulted in advancing water contact angles as high as 105°. Maximum hydrophobicity was obtained when deposited from dispersions containing 10% reactive silane. Based on these results, Glassclad[®]18 was not chosen for further investigations.

4.2.4 System 4: Dupont TLF-8291

Coatings formed from Dupont TLF-8291 were slightly more hydrophobic than the coatings formed from Siliclad[®], especially after curing (Figure 4.31). However, the quality of the coatings was very sensitive to the extent of water rinsing that was used after the coating process. The effect of rinsing is shown in Figure 4.32 as a force-distance curve during immersion-withdrawal. The coated sample “squirt” rinsed for 30 seconds with DI water had contact angle <90° as evident by the increase in the force on the coated substrate during immersion into DI water. A sample rinsed for ~ 2.5 min on each side (high level of rinsing) was characterized by a decrease in force upon immersion indicating a hydrophobic coating. Measurements done for a coating formed with Siliclad[®], also displayed in the same plot, show no such increase in force during immersion. Coatings formed with Dupont TLF-829 also showed higher hysteresis in the contact angle than coatings formed with Siliclad[®].

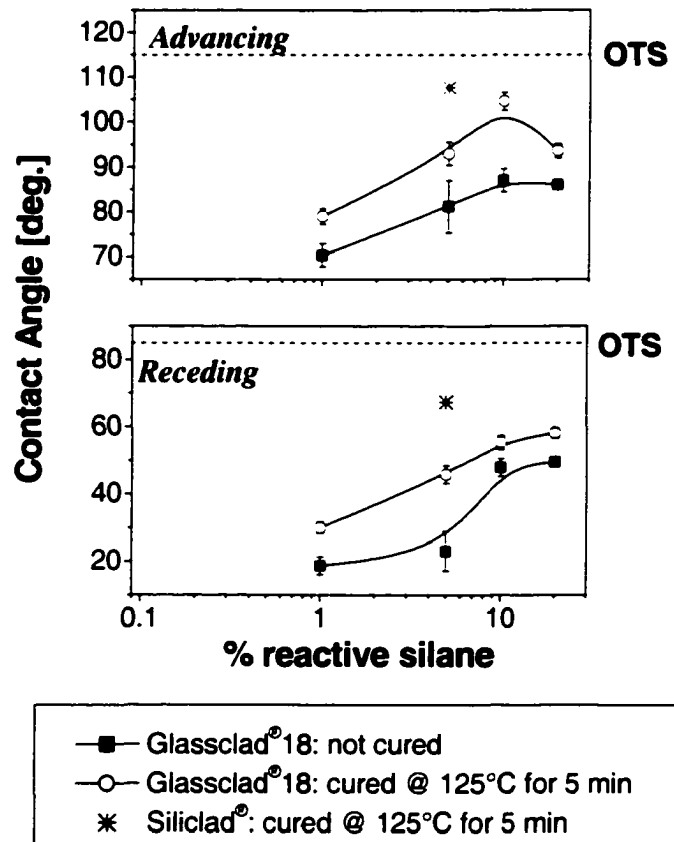


Figure 4.30: DI water contact angles on coatings deposited from Glassclad®18 dispersions containing different amounts of reactive silane

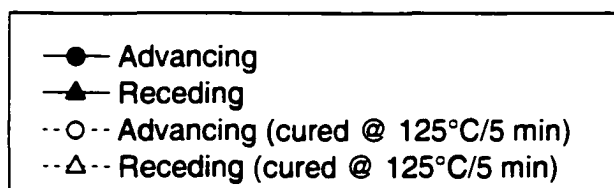
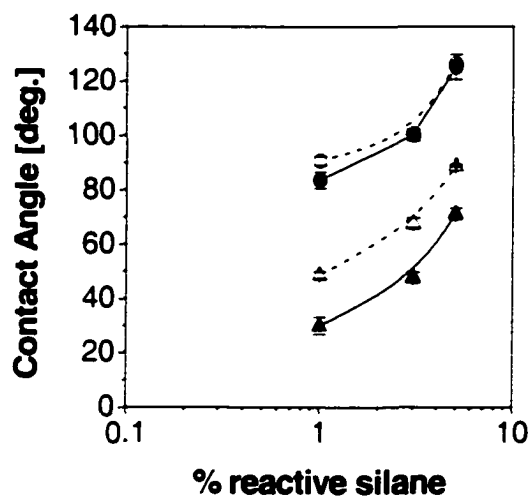


Figure 4.31: DI water contact angles on coatings deposited from Dupont TLF-8291 dispersions containing different amounts of reactive silane

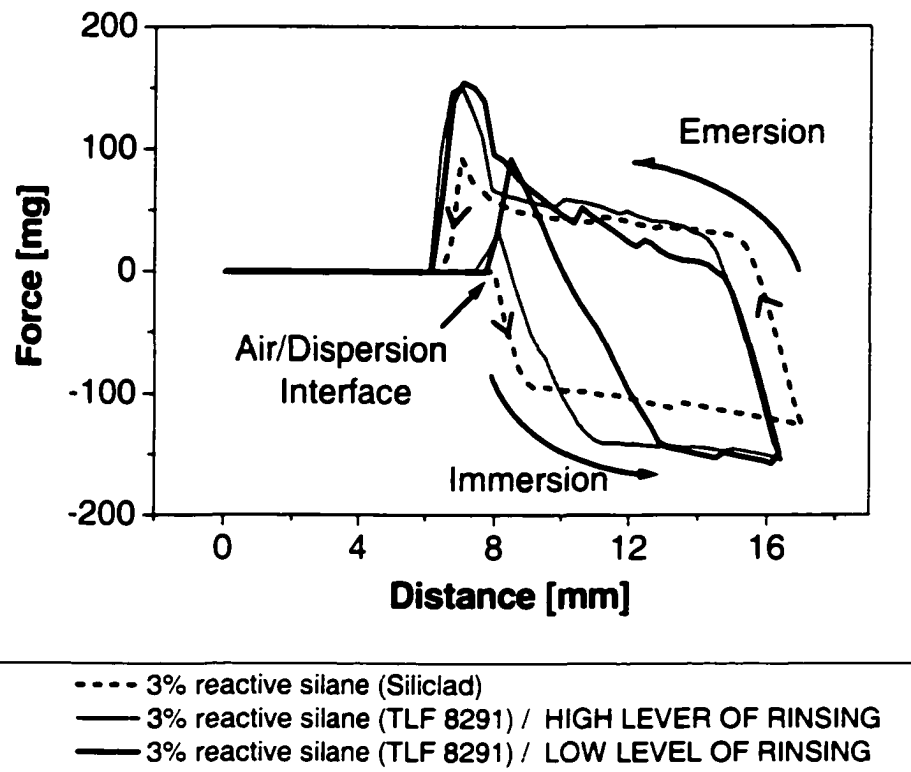


Figure 4.32: Force versus immersion depth curves for Dupont TLF-8291 and Siliclad[®] coated polysilicon samples

4.2.5 System 5: Cationic alkoxy silanes

Figure 4.33 depicts the surface tension of DMOAP and DIDAP as a function of concentration at $\sim 22^{\circ}\text{C}$. For both cationic alkoxy silanes the surface tension decreased with concentration, reached a minimum, increased again and reached a plateau value. The plateau values of surface tension were found to be at 46 and 29 dynes/cm for DMOAP and DIDAP, respectively. This indicates that DIDAP is more surface active than DMOAP. The minimum surface tension was $6 \times 10^{-4}\%$ for DIDAP and $9 \times 10^{-4}\%$ for DMOAP. For most pure surfactant systems a minimum on surface tension is never observed. In most cases, the existence of such minima has been explained as due to the presence of a minor component with a higher degree of surface activity. According to the manufacturer both DMOAP and DIDAP compounds contain very small amount of 3-chloropropyltrimethoxysilane ($\text{Cl}(\text{CH}_2)_3\text{Si}(\text{OMe})_3$): perhaps the minimum can be attributed to the presence of this impurity.

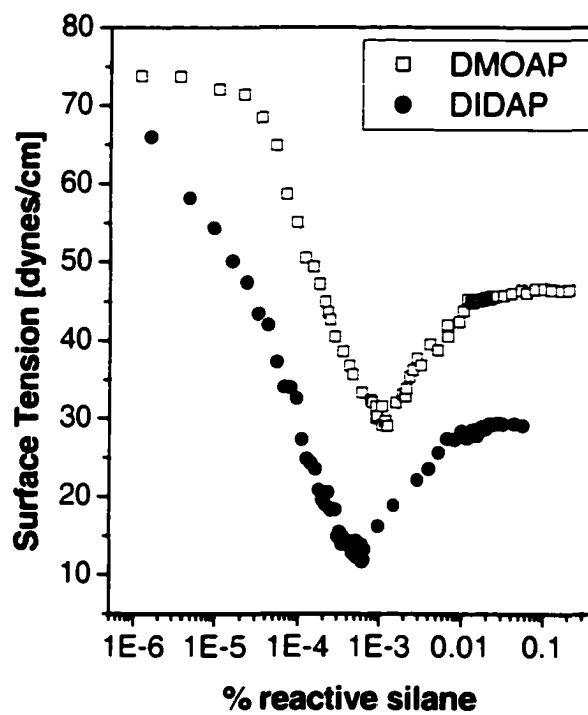


Figure 4.33: Surface Tension of DI water as a function of DMOAP and DIDAP concentration

4.2.5.1 Octadecyl cationic alkoxy silane (DMOAP)

In order to determine optimal conditions to deposit DMOAP coatings, DI water contact angle measurements were performed on polysilicon coated samples from DMOAP dispersions at different concentrations, pH and temperature (Figure 4.34). Initial experiments were focused on applying DMOAP coatings from aqueous dispersions containing different amounts of reactive silane without pH adjustment (pH~5.2) and at room temperature (~22°C). The hydrophobicity of these coatings is displayed in Figure 4.34(a). As may be seen from this figure, highly hydrophobic coatings, as determined by the value of advancing (θ_a) and receding (θ_r) contact angles, were formed from dispersions containing very low amounts of reactive silane (>0.01%). The advancing and receding contact angle values for coatings prepared from dispersions containing 0.01 % or more reactive silane were 100° and 55°, which are lower than those for coatings formed from an organic solvent containing octadecyltrichlorosilane (OTS) ($\theta_a=115^\circ$ and $\theta_r=85^\circ$).⁽¹²²⁾

The next set of experiments was focused on applying DMOAP coatings from dispersions containing 0.01% reactive silane at different pH values and room temperature. Because of the charged nature of the cationic alkoxy silane, the interaction of the silane headgroup with the anionic charged sites on the solid oxide is expected to be pH sensitive. Zeta potential measurements reported, in section 4.1.2, show that the point of zero zeta potential or iso-electric point (IEP) for chemical oxides formed on polysilicon and single crystal silicon is between 2 and 3. For the physical adsorption of the quaternary ammonium group it is desirable to have high concentration of negative

charges (Si-O⁻) and for siloxane chemisorption the presence of Si-OH surface groups is essential.⁽⁷³⁾ Figure 4.34(b) shows that at a pH below 4 the adsorption of the silanes was reduced due to electrostatic repulsion between the positively charged group in the silane molecule and the positively charged surface. Coatings with high hydrophobicity were obtained from dispersions at pH values above 4, where a combined electrostatic and covalent interaction between the silane molecule and pre-oxidized polysilicon surface is favorable. For maximum hydrophobicity and dispersion stability, it is desirable to have fast hydrolysis and low condensation of the -Si-O-CH₃ side groups, which for alkyltrialkoxysilanes is reported⁽¹³³⁾ to occur between pH 4 and 5.

The next step was to deposit films from DMOAP dispersions at different temperatures without pH adjustment. It may be seen in Figure 4.34(c) that the hydrophobicity of the coatings exhibited a maximum at temperatures above 35°C, which is contrary to n-alkyltrichlorosilanes that form well organized monolayers at temperatures below a transition temperature (T_c).^(60,64) The transition temperature for octadecyltrichlorosilane (OTS) monolayers has been reported to be ~28±4°C.

The first attempt to understand the effect of temperature on contact angles was made through surface pressure-area (π -A) isotherm measurements at different temperatures (Figure 4.35). The isotherms were recorded by spreading $\sim 1.7 \times 10^{17}$ DMOAP molecules (400 μ L of a ~0.039% reactive silane) onto 400 ml of DI water without pH adjustment. As the monolayer was compressed, the changes in slope on the pressure-area isotherm may be attributed to the transitions between gas (G), liquid-

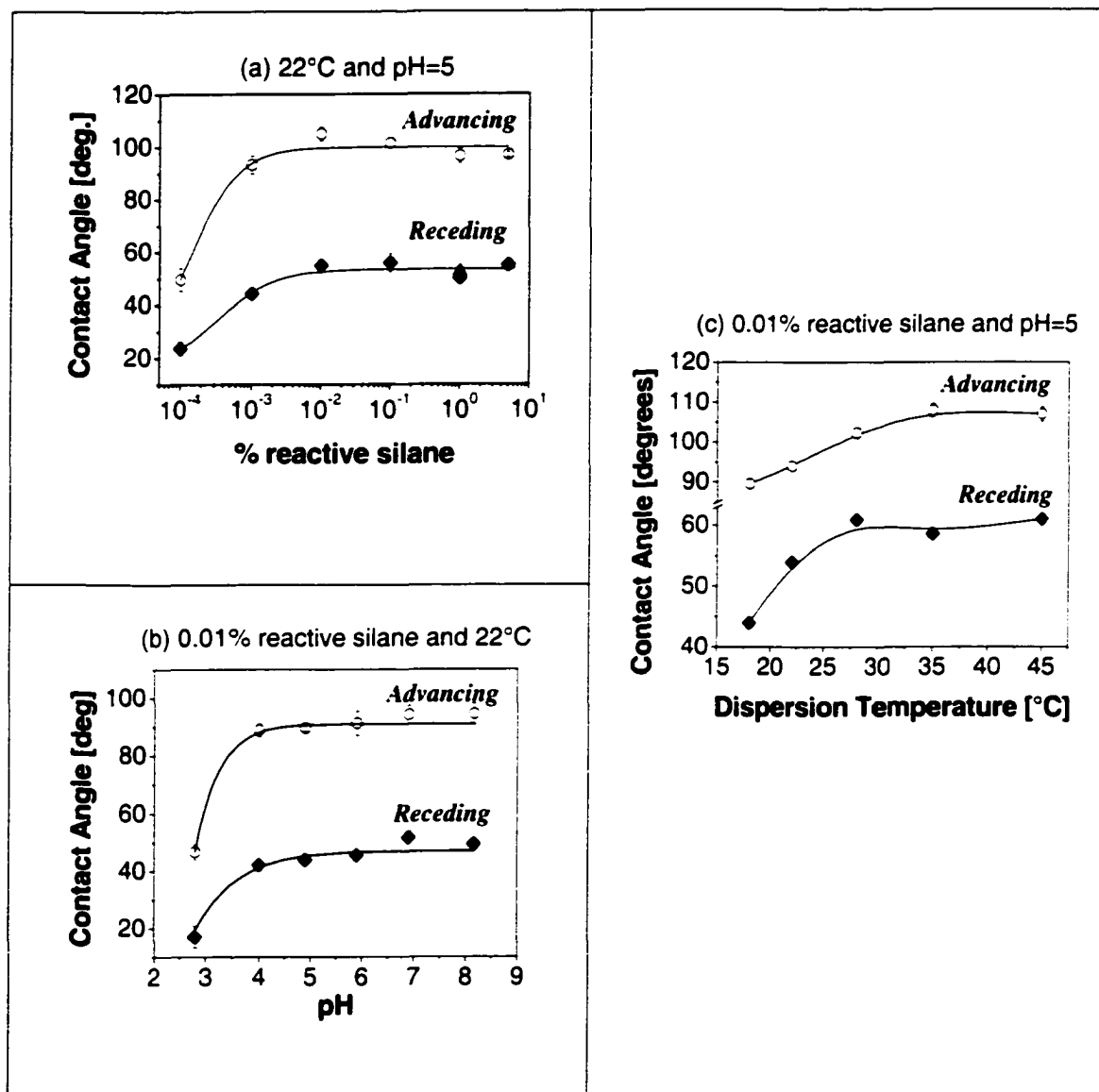


Figure 4.34: DI water contact angles on coatings deposited from DMOAP aqueous silane dispersions as a function of (a) reactive silane. (b) pH and (c) temperature

condensed (LC) and liquid-expanded (LE) phases. There was no coexistence of G/LE and LE/LC, which are identified as constant surface pressure regions on the isotherm. The solid phase (S) was not observed and could be as a result of less efficient packing due to the existence of the spacer between the quaternary ammonium group and siloxanes. The liquid-condensed phase was characterized by a sharp rise of the isotherms upon compression. Pressure-area isotherms of hydrolyzed octadecyltrichlorosilane (OTS)^(56,142) and octadecyltrimethoxysilane OTMS⁽¹⁴³⁾ have been reported to exhibit a transition from liquid-expanded to liquid-condensed phases and the coexistence of LE/LC.

The collapse pressures increased with decreasing the subphase temperature. The negative $\Delta\pi/\Delta T$ for the collapse pressures indicates that the collapse is kinetically and not thermodynamically controlled.⁽¹⁴⁴⁾ The area for the onset of surface pressure did not appear to be very sensitive to temperature. Usually, the collapse pressure provides valuable information on the stability of a monolayer; the higher the collapse pressure, the more stable the monolayer.⁽¹⁴⁵⁾ In the case of DMOAP less stable monolayers were formed by increasing temperature. It is puzzling that the increase of temperature which decreases the packing on DMOAP films is able to provide higher contact angles.

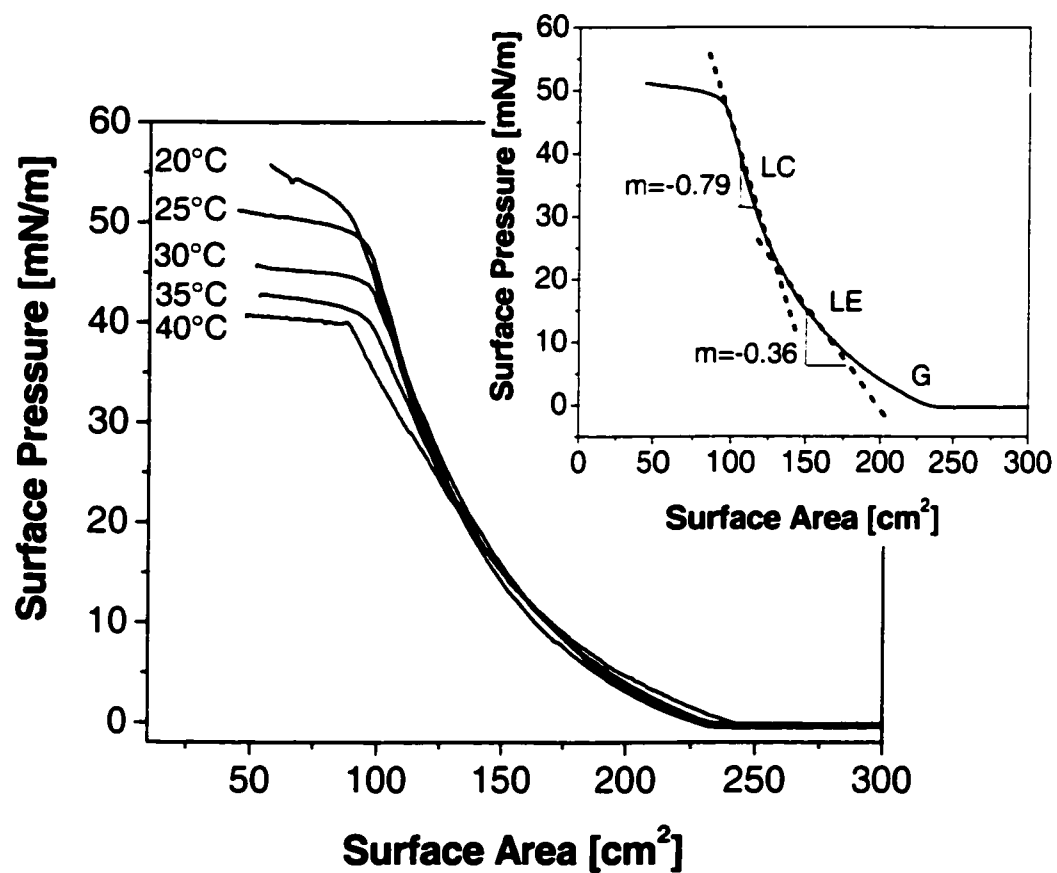


Figure 4.35: Π - A isotherms of DMOAP monolayers on DI water subphase at different temperatures

In this work, the wettability of DMOAP monolayers transferred at $\sim 22^\circ\text{C}$ onto pre-oxidized polysilicon at various surface pressures was studied. The quality and stability of LB films are mainly affected by the properties of monolayers on the subphase and by the transfer condition from liquid to the solid substrate. The surface pressure of the monolayer under which the transfer is carried out and the transfer rate are very important in controlling the arrangement and orientation of the molecules on a solid support. The DI water contact angles on the LB films are shown in Table 4.4. Because one layer of the LB films was obtained by withdrawing the hydrophilic pre-oxidized polysilicon from the subphase, DMOAP molecules were arranged with hydrophobic tails facing outward and thus hydrophobic surfaces were obtained. The coatings deposited at higher surface pressures showed an increase in advancing and receding contact angles. This indicates that as the surface pressure increases, the coatings have fewer defects as a result of less freedom for the molecules to tilt and rotate during LB film transfer. Water contact angles on DMOAP coatings deposited at 40 dynes/cm are very similar to the ones measured on coatings formed by dip coating at temperatures above 35°C .

Table 4.4: DI water contact angles on DMOAP LB films deposited at different surface pressures

SURFACE PRESSURE	Contact Angles	
	Advancing	Receding
20	101 ± 1	56 ± 2
30	105 ± 2	58 ± 1
40	109 ± 2	66 ± 1
Dip coating (0.01%, pH=4, 40°C)	108 ± 2	57 ± 3

The hydrophobicity of DMOAP coatings was found to be the highest at a deposition temperature of 35°C (Figure 4.34(c)). This can be explained by the existence of Krafft point for this ionic silane at a temperature in the vicinity of 35°C. For ionic surfactants, there is a temperature called the Krafft point below which the solubility is quite low and the solution contains surfactant ions but no micelles and behaves like a simple salt. Above the Krafft temperature, micelle formation becomes possible and there is a rapid increase in solubility of the surfactant.⁽¹⁴⁶⁾ For octadecyltrimethylammonium bromide (OTAB), the Krafft point is reported to be between 35 and 37°C⁽⁹⁹⁾ and is likely to be very similar for DMOAP. It appears that at a DMOAP concentration of 0.01% and temperatures below the Krafft point, the insoluble DMOAP molecules interfere with organization and packing of the molecules in the film. As temperature was raised, the solubility of DMOAP molecules increased and the hydrophobic character of the coatings increased until the Krafft temperature was reached.

The next step in this research was to check whether drying/curing under dry conditions would improve the coating hydrophobicity. It has been reported that curing or baking organosilane coatings between 100 and 200°C completes the lateral condensation reaction between adjacent silane molecules to form a more densely packed and stable 2-dimensional silane layer.⁽⁸⁴⁾ In the absence of lateral polymerization, the silane coating might be subject to attack by moisture or other reactive agents. The effect of curing under nitrogen conditions on the hydrophobic character of coatings deposited from an aqueous

dispersion containing 0.01% reactive silane dispersion of DMOAP at 40°C is shown in Figure 4.36. Both the advancing and receding contact angles increased with an increase in the curing temperature. For example, curing of the coatings at 250°C increased the advancing contact angle from 103° to 110° and the receding angle from 53° to 73°. The hydrophobicity reached a plateau when cured at temperatures above 200°C. Receding contact angles were more sensitive to curing temperature than advancing contact angles, which remained almost constant. Such phenomenon has also been observed on heterogeneous surfaces composed primarily of a hydrophobic material with a small area fraction of a hydrophilic component. For example, Lee *et al.*⁽¹⁴⁷⁾ found that when a hydrophilic glass substrate has a high fractional coverage (>0.6) of hydrophobic poly(α -methylstyrene), the receding contact angle increased from ~60° to 77° when the hydrophobic coverage increased, but the advancing contact angle remained constant (~100°).

The advancing contact angle obtained by curing DMOAP coatings was similar to the reported for OTS⁽⁸⁹⁾ coatings ($\theta_{adv.OTS}=115^\circ$). However, the receding contact angle was smaller ($\theta_{rec.OTS}=85^\circ$), this could be as a result of less efficient packing due to the existence of the spacer between the quaternary ammonium group and siloxanes

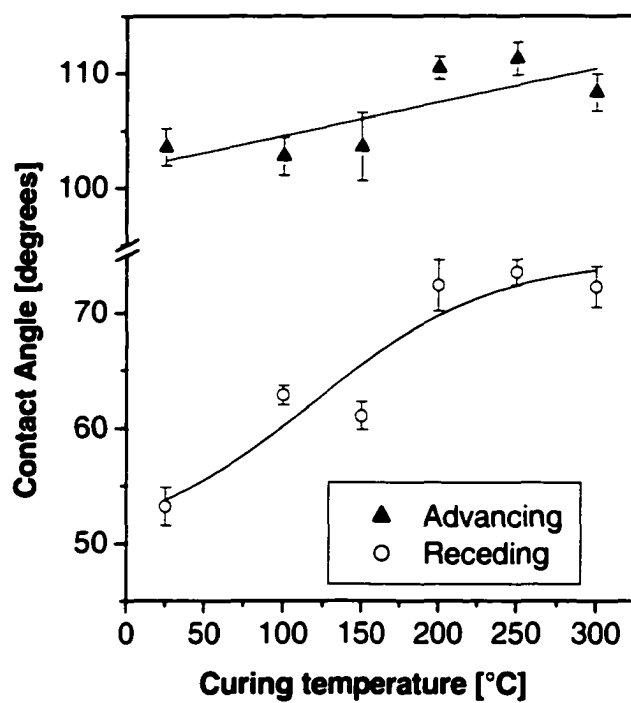


Figure 4.36: Effect of curing under nitrogen environment on hydrophobicity of DMOAP coatings (coatings deposited from 0.01% reactive silane dispersions at 40°C)

The stability of a DMOAP aqueous dispersion containing 3% reactive silane at a pH value of 4 was evaluated by measuring the viscosity at 30°C as a function of aging time (Figure 4.37). The viscosity did not increase even after 10 days. This indicates that DMOAP aqueous dispersions are very stable as a result of repulsion interactions between quaternary ammonium groups present on the surface of the micelles in solution that protect the silanol groups from reacting with each other. The hydrophobicity of coatings deposited from this DMOAP dispersion at room temperature as a function of dispersion age is also shown in Figure 4.37. The films formed from freshly prepared baths yield slightly higher hydrophobic films with respect to films deposited from dispersions 18 days old. The small decrease on contact angles ($\sim 7^\circ$) indicates the formation of silane networks with small molecular weight during the condensation process in the aqueous phase. Leyden *et al.*,⁽¹¹¹⁾ using ATR-FTIR spectroscopic measurements, determined that after 5 days, 78% of DMOAP was found to be in the condensed form and the solution was clear indicating that condensation occurred with low conversion.

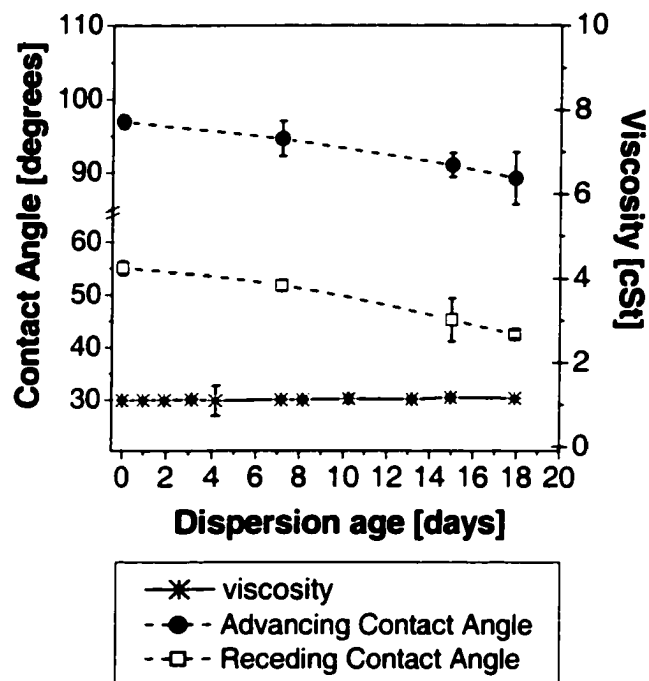


Figure 4.37: Viscosity of a DMOAP dispersion containing 3% reactive silane and water contact angles on coated surfaces deposited at room temperature ($\sim 22^{\circ}\text{C}$) as a function of dispersion age

4.2.5.1.1 Effect of temperature and humidity on coating hydrophobicity

Table 4.5 shows the water contact angles on polysilicon samples coated with DMOAP exposed to different conditions. Receding contact angles were more sensitive to changes in annealing temperature and environment.

When the coating was heated to 100°C in dry nitrogen for short time, the advancing contact angle did not to change, but the receding contact angle increased by 10°. However, if wet nitrogen was used (RH~99%) the receding angle was only 55°, which is the same as that for a coating which was not subjected to any heat treatment.

The next series of tests were carried out at curing temperature of 250°C. In these tests the environment was dry nitrogen, wet nitrogen or dry compressed air. At this high temperature, when the coating was cured under dry nitrogen, both the advancing and receding contact angles increased significantly from 104° to 111° and 53° to 74°, respectively. However, if the nitrogen ambient contained moisture, the humidity in the nitrogen stream reduced both advancing and receding contact angles. It should be noticed that even with water present in nitrogen, high temperature curing gives slightly higher receding contact angles than for the sample without any heat treatment. Extending the curing time in very humid nitrogen (RH~99%) did not improve the hydrophobic character of the coatings.

It appears that annealing DOMAP coatings under dry nitrogen mainly increases the receding contact angles of the coatings. This increase may be attributed to water removal from the coating that allows rearrangement of the molecules and lateral cross-linking. The fact that a humid nitrogen stream (RH~99%) did not increase the water contact angles on coatings cured at 100°C, as compared to the coating without heat treatment, perhaps indicates that the humidity in the stream did not allow the water to be removed from the coating.

Two tests were conducted to see if the addition of oxygen would have an influence on the wettability of the coatings. In these tests compressed air was used instead of nitrogen. The dry compressed air stream is not as effective as dry nitrogen stream in increasing the hydrophobicity of the samples.

Table 4.5: Thermal stability of DMOAP coatings under different conditions

Environmental chamber input conditions			Heating ramp time from room temperature	Holding time	Cooling ramp time to room temperature	Contact Angle [degrees]	
Temperature	Gas	Relative Humidity				Advancing	Receding
without heat treatment	-----	-----	-----	-----	-----	104 ± 2	53 ± 2
100°C	Nitrogen	<1%	1.5 min	5 min	3 min	103 ± 2	63 ± 1
		99%				99 ± 4	55 ± 2
250°C	Nitrogen	<1%	10 min	5 min	20 min	111 ± 1	74 ± 2
		50-60%				108 ± 1	71 ± 1
		99%				100 ± 2	66 ± 1
		99%		105 ± 3		67 ± 1	
	Compressed air	<1%	10 min	5 min	20 min	101 ± 3	60 ± 1
		<1%		1 hour		105 ± 2	66 ± 1

4.2.5.2 Didecyl cationic alkoxy silane (DIDAP)

Figure 4.38 shows the hydrophobicity of coatings deposited from a DIDAP dispersion containing 0.1% reactive silane as a function of deposition temperature. DIDAP coatings showed lower advancing contact angles but higher receding contact angles as compared to DMOAP coatings ($\theta_a=108^\circ$, $\theta_r=57^\circ$) when deposited at 35°C. This could be because DIDAP molecules have two hydrocarbon tails that allow better packing of the molecules and the hydrocarbon segments are more extended.

The Π -A isotherms of DIDAP monolayers at different temperatures (Figure 4.39), were recorded by spreading $\sim 2.6 \times 10^{17}$ DIDAP molecules (400 μL of $\sim 0.064\%$ reactive silane) onto 400 ml of DI water without pH adjustment. Similar to the pressure-area isotherm for DMOAP, three slope changes were observed and may be attributed to the transitions between gas (G), liquid-condensed (LC) and liquid-expanded (LE) phases. There was no coexistence of G/LE, LE/LC and solid (S) phases. Collapse pressures for DIDAP were slightly lower than for DMOAP monolayers. For example, at 35°C the collapse pressure for DIDAP monolayers was 37 mN/m and for DMOAP monolayers was 42 mN/m.

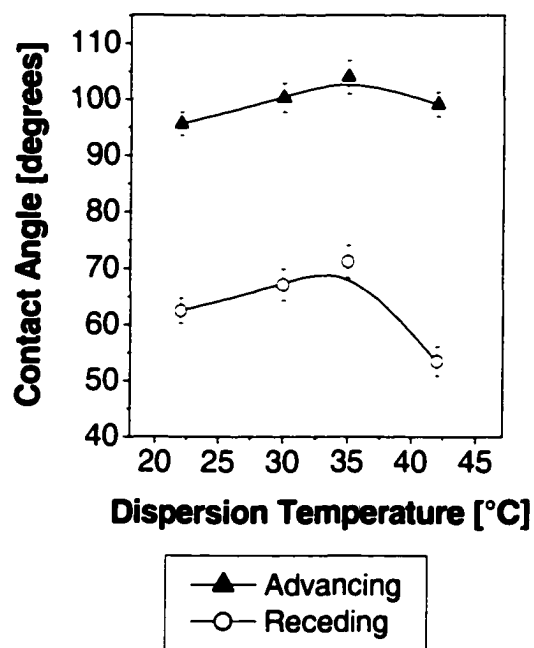


Figure 4.38: DI water contact angles on coatings deposited from DIDAP aqueous dispersions containing 0.1% reactive silane at pH value of ~5.2 as a function of deposition temperature

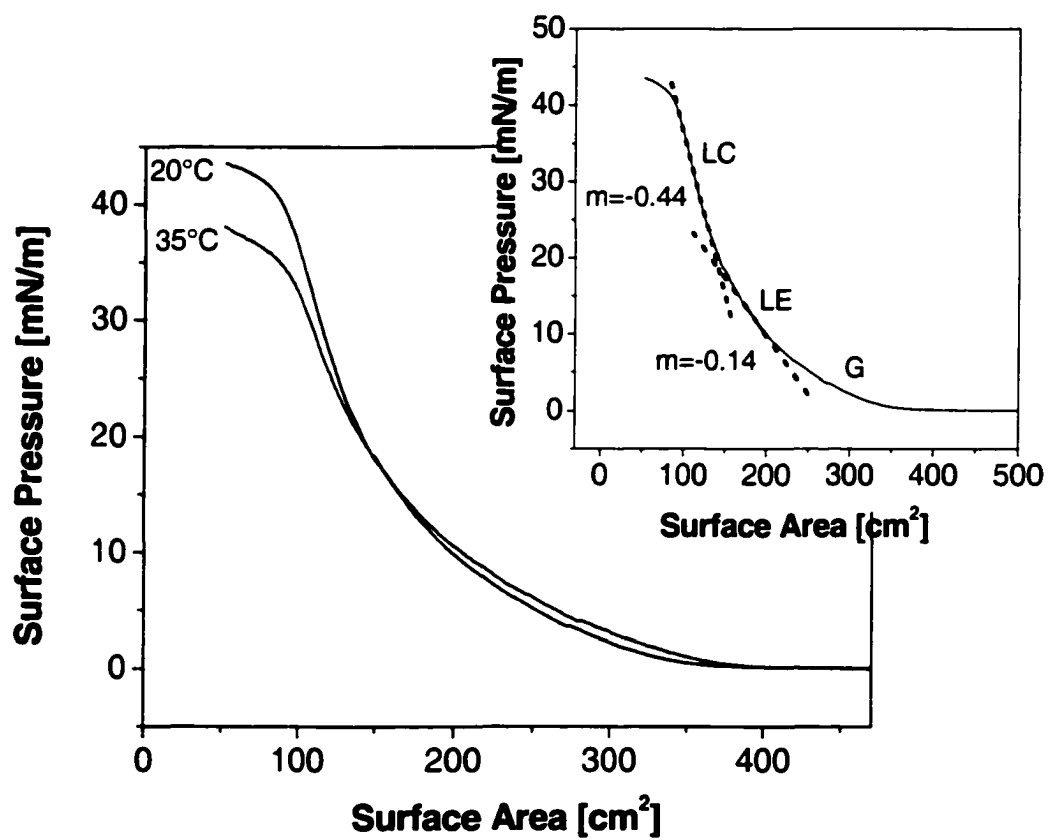


Figure 4.39: Π -A isotherms of DIDAP monolayers on DI water subphase at different temperatures

The wettability of DIDAP monolayers transferred at $\sim 22^{\circ}\text{C}$ onto pre-oxidized polysilicon at various surface pressures was also studied. The DI water contact angles on DIDAP LB films are shown in Table 4.4. The hydrophobicity of DIDAP coatings deposited at surface pressure of 40 dynes/cm was lower than coatings formed by dip coating. From Figure 4.35 it may be noticed that the collapse pressure for DIDAP at room temperature is almost 40 dynes/cm, which could indicate that a disorder and irregular LB film may be formed.

Table 4.6: DI water contact angles on DIDAP LB films deposited at different surface pressures

SURFACE PRESSURE	Contact Angles	
	Advancing	Receding
20	82.6 ± 1.6	42.0 ± 1.1
30	92.1 ± 4.3	46.4 ± 1.3
40	97.1 ± 1.3	51.8 ± 1.7
Dip coating (0.01%, pH=4, 40°C)	103.9 ± 3.2	71.2 ± 2.9

4.3 Coatings deposited onto single crystal silicon

Coatings were deposited onto single crystal silicon to avoid the negative impact that roughness can have on the accuracy and precision of film thickness measurements using ellipsometry. Additionally, smooth and flat surfaces, where surface corrugation is less than the length of the organosilane molecule, are required to image the structure of the coatings using atomic force microscopy.

Five coating systems were studied: Siliclad[®], DMOAP, DIDAP, DMOAP/Siliclad[®] and DIDAP/Siliclad[®]. These last two were double coating systems, in

which the first coating was deposited from either of the two cationic alkoxysilanes and the second one from Siliclad[®] dispersions containing 0.5% reactive silane. No delay time was imposed between immersion and withdrawal of the sample from the dispersion. This was done to improve the hydrophobicity and coverage of cationic alkoxysilanes coatings.

4.3.1 Layer thickness

4.3.1.1 Nulling ellipsometry

The first set of coating thickness measurements were carried out using a nulling ellipsometer. Measurements were taken at 5 points randomly selected across the surface and averaged. The thickness values obtained as a function of substrate contact time in a Siliclad[®] dispersion containing 3% reactive silane are shown in Table 4.7. The thickness of the films increased with coating time. The variability on thickness also increased with exposure time indicating the formation of non-uniform coatings.

Table 4.7: Ellipsometric thicknesses of Siliclad coatings deposited at different exposure times in a dispersion containing 3% reactive silane

Coating time	Thickness [Å]
2.5 min	28.6 ±4.2
7.5 min	37.8 ±2.9
12.5 min	35.1 ±1.0
32.5 min	44.4 ±10.2
62.5 min	59.9 ±16.2

For vertically oriented molecules, the thickness of octadecyltrichlorosilane (OTS) monolayers is reported in literature⁽⁸⁹⁾ to be 28.1 Å. The Siliclad[®] coating formed at a

very short dip time of 2.5 minutes appears to be roughly a monolayer. However, with time the layer thickness builds up.

Table 4.8 shows the thickness of coatings prepared from fresh dispersions containing different amounts of reactive silane for a fixed contact time of 2.5 min. The thickness of coatings deposited from dispersions containing 0.5% and 1% reactive silane were below the reported values for vertically oriented monolayers of octadecyltrichlorosilane (28.1 Å), whereas, the coatings prepared from 3 and 10% reactive silane dispersions were on the order of single molecule size.

Table 4.8: Ellipsometric thicknesses of Siliclad coatings deposited from dispersions containing different amounts of silanes

Concentration [% reactive silane]	Thickness from a 2.5 min deposition process [Å]
0.5	NA
1	1.8±1.2
3	28.6 ±4.2
10	28.9 ±1.3

The layer thicknesses for coatings deposited from dispersions containing 0.1% reactive silane of DMOAP and DIDAP were 23.4 Å ±0.6 and 10.3 Å ±1.1, respectively. These values are remarkably close to the molecular lengths (in vacuum) of this two cationic alkoxy silanes calculated by molecular modeling using HyperChem v.3.0 software (Figure 4.40). For comparison purposes, it may be stated that the thickness of decyltrichlorosilane (10 carbons) monolayers has been reported⁽⁸⁹⁾ to be 13.5 Å. Hence, it appears DMOAP and DIDAP coatings deposited on pre-oxidized silicon are roughly monolayer coatings.

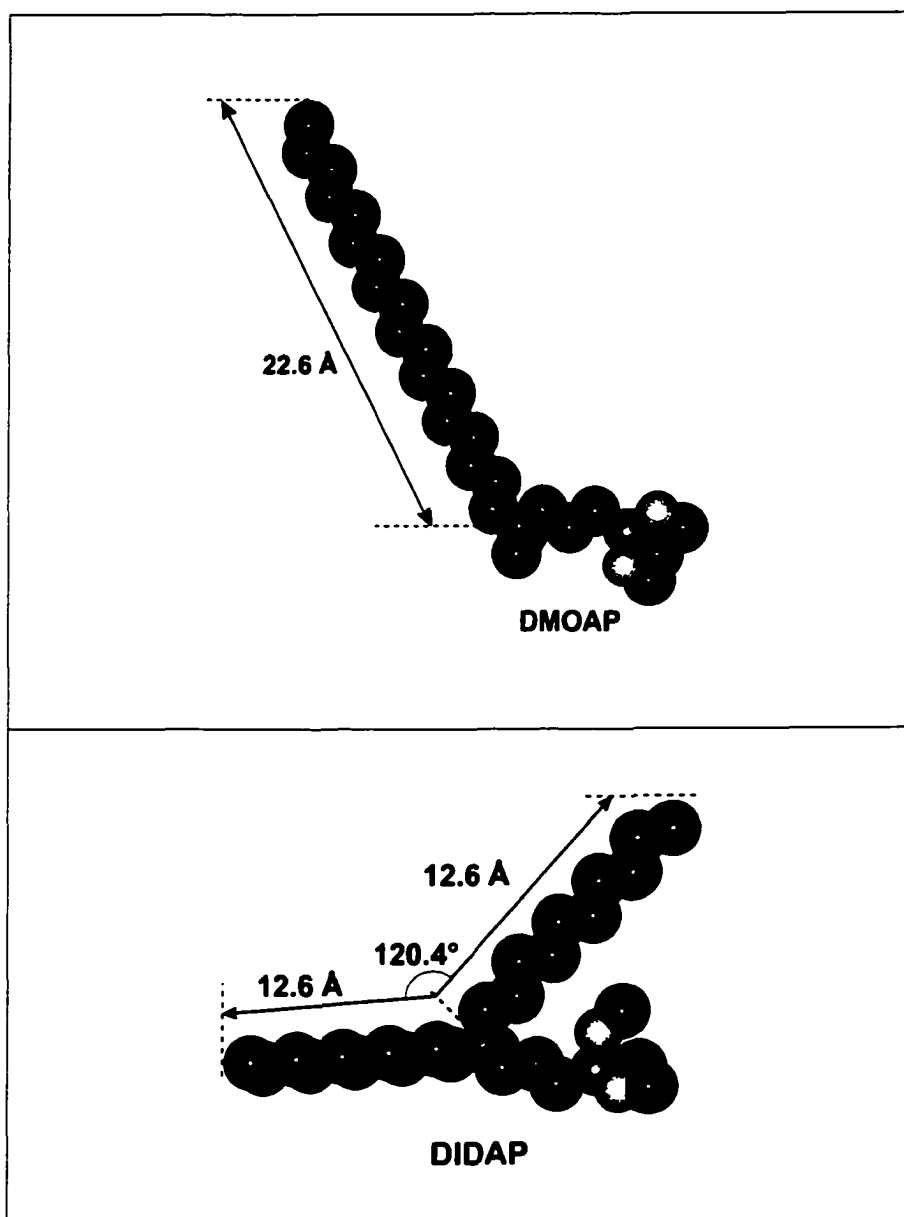


Figure 4.40: Molecular modeling of cationic alkoxy silanes using HyperChem v.3.0 software

4.3.1.2 Spectroscopic ellipsometry

Ellipsometric measurements in the spectral range 2000-6000 Å were first made on uncoated pre-oxidized silicon substrates; the delta (Δ) and psi (Ψ) data are shown in Figure 4.41. The samples were then coated in DIDAP or DMOAP dispersions, and the resultant profiles are also shown in Figure 4.41. The difference between the uncoated and coated sets of data indicates the thickness of the silane coating, which depends on the size of the molecules. It may be seen that mainly the values of Δ decrease and Ψ increase with an increase on film thickness. This change in Δ and Ψ as a function of thickness can be explained based on the following equations:⁽¹⁴⁸⁾

$$\Delta = \Delta' - \alpha t \quad (4.2)$$

$$\Psi = \Psi' + \beta t \quad (4.3)$$

where Δ' and Ψ' refer to the clean surface, Δ and Ψ refer to the film-covered surface, and α and β are constants dependent upon the angle of incidence, the refractive index of the film, the complex refractive index of the substrate and the wavelength of the incident light.

The ellipsometric values of Ψ and Δ were gathered at two angles (70° and 80°) near to, but on either side of, the Brewster's angle for Silicon (74°) in order to obtain higher sensitivity and to avoid measuring values of Ψ near 0° and Δ near 180°. ⁽¹⁴⁹⁾ Δ and Ψ were then converted into film thickness using the instrument software. The spectral range for the measurements was chosen in accordance to electronic transitions of silicon, which appear as peaks on the plots. ⁽¹⁵⁰⁾

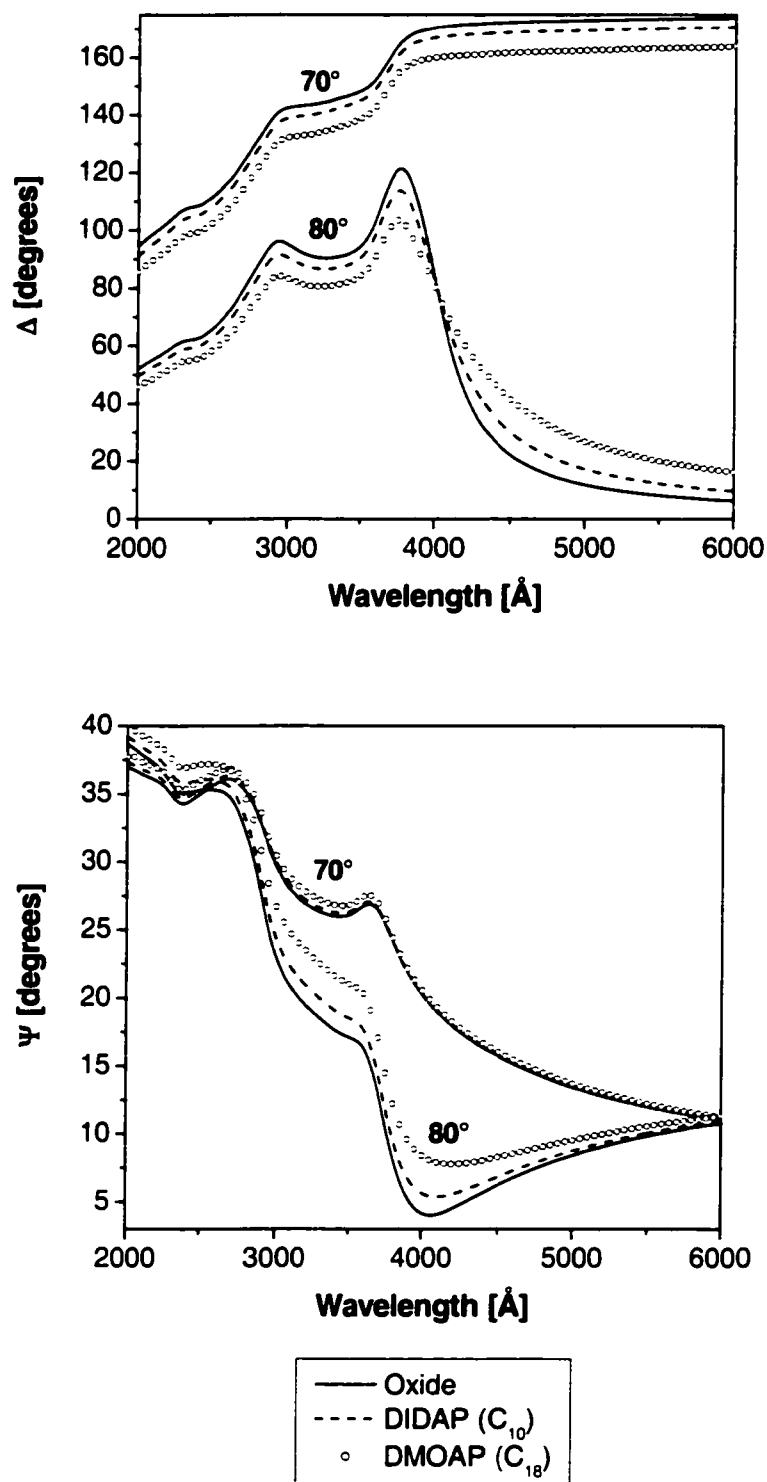


Figure 4.41: Delta and Psi values for uncoated and coated samples

The average film thickness values measured on five random regions on the coated samples are presented in Table 4.9. The calculations of film thickness from ellipsometry data are based on the assumption that all of the films have the same refractive index. The exact value of the refractive index cannot be derived with an acceptable degree of accuracy from Δ and Ψ data for such thin layers. It has been reported⁽⁸⁹⁾ that refractive index depends on the size of alkylsilane and the structure of the layer, but its impact on the thickness values is roughly 10% or less.

Table 4.9: Film thicknesses determined by Ellipsometry

COATING**	Thickness [Å]	
	Expected	Spectroscopic Ellipsometer
0.5% Siliclad®	N/A	5.2 ± 0.3
1% Siliclad®	N/A	8.9 ± 0.4
3% Siliclad®	N/A	44.5 ± 15.8
0.1% DMOAP	22.6*	20.7 ± 8.5
0.1% DIDAP	12.6*	7.6 ± 0.7
0.1% DMOAP/ 0.05% Siliclad®	-----	20.9 ± 4.5
0.1% DIDAP/ 0.5% Siliclad®	-----	6.4 ± 0.3
OTS (low humidity) ⁽⁸⁹⁾	28.1	-----
OTS (50% RH) ^(32,53)	26.5	-----

N/A: Not available due to proprietary information from Gelest

*From molecular modeling in vacuum using HyperChem v3.0

**The percentage indicated refers to the percent of reactive silane in the aqueous dispersion

The thickness of Siliclad[®] coatings was found to depend on reactive silane concentration. The thickness of coatings deposited from dispersions containing 0.5% and 1% reactive silanes was below the reported values for vertically oriented coatings of octadecyltrichlorosilane (28.1 Å). The reason for this is the presence of a large number of “lying-down” molecule defects. The coatings deposited from a dispersion containing 1% reactive silane showed higher thickness values as a result of increased silane coverage on the surface and/or decrease in defects. The thickness values of Siliclad[®] coatings deposited from dispersions containing 3% of reactive silane concentration were higher than the length of fully stretched alkylsilanes. This is most likely due to the deposition of particulates formed as a result of rapid oligomerization of the alkylsilanes in the aqueous phase prior to covalent bonding to the silicon surface⁽⁸⁹⁾ (Figure 2.23). The lower concentration of organosilane retards oligomerization in the bulk but the hydrophobic character of the coatings decreases as described in the next section.

The thickness values of coatings prepared from dispersions containing cationic alkoxysilanes (DMOAP and DIDAP) were similar to their molecular lengths and the thickness increased with alkyl chain length. The thickness of DMOAP coating was less than the length of the fully stretched octadecylsilane molecule, which could indicate a slightly disordered monolayer structure. Similar trends were observed for DIDAP coatings. The thickness of DMOAP/Siliclad[®] and DIDAP/Siliclad[®] double coating systems did not change after the first coating, likely due to the fact that these coatings are predominantly composed of cationic alkoxysilanes.

All previous thickness measurements were done on coatings formed on 1.5 cm x 1.5 cm samples. It is important to determine whether dip-coating process would deposit uniform coatings on bigger samples. For this purpose, 4-inch wafers were coated using another type of dip coater at speeds of 40 $\mu\text{m}/\text{sec}$ and 400 $\mu\text{m}/\text{sec}$. The regions where thickness measurements were conducted on the surface of the wafers are shown in Figure 4.42.

The thickness for DMOAP coatings deposited at withdrawal speeds of 40 and 400 $\mu\text{m}/\text{sec}$ (

Figure 4.43) corresponded to monomolecular films; however when the coating was deposited at slow withdrawal speed the sample had to be rinsed for longer time to remove excess silane.

Figure 4.44 shows the thickness values obtained on DIDAP coatings deposited at withdrawal speed of 40 $\mu\text{m}/\text{sec}$ with and without a delay time between immersion and withdrawal steps during coating deposition. Both coatings had the same thickness of ~ 8 Å, which is smaller than the value obtained by HyperChem modeling (12.6 Å). This could be attributed that the molecules are not normal to the substrate. If the molecules were lying down on the substrate, the coatings would have thickness of ~ 4 Å. The coating deposited on the wafer with a delay time of 10 minutes showed the presence of excess silane deposited on the surface which was removed after a 20 min rinse.

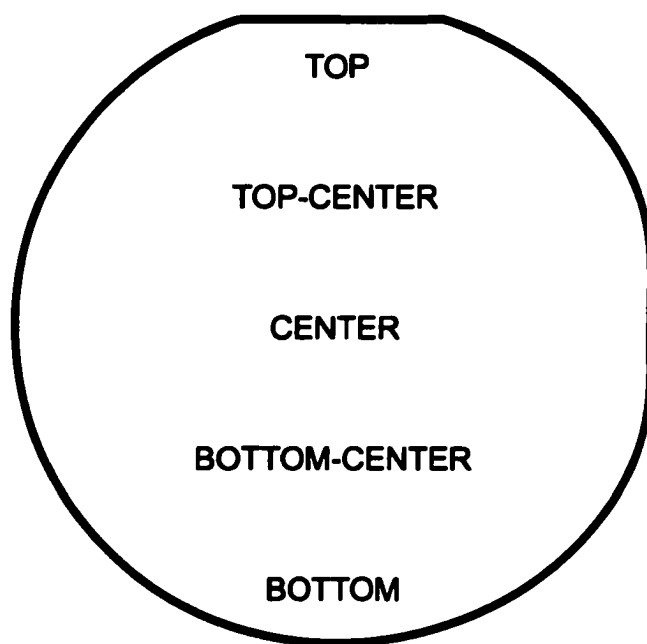


Figure 4.42: Regions on a wafer used to determine thickness uniformity by a dip coating process

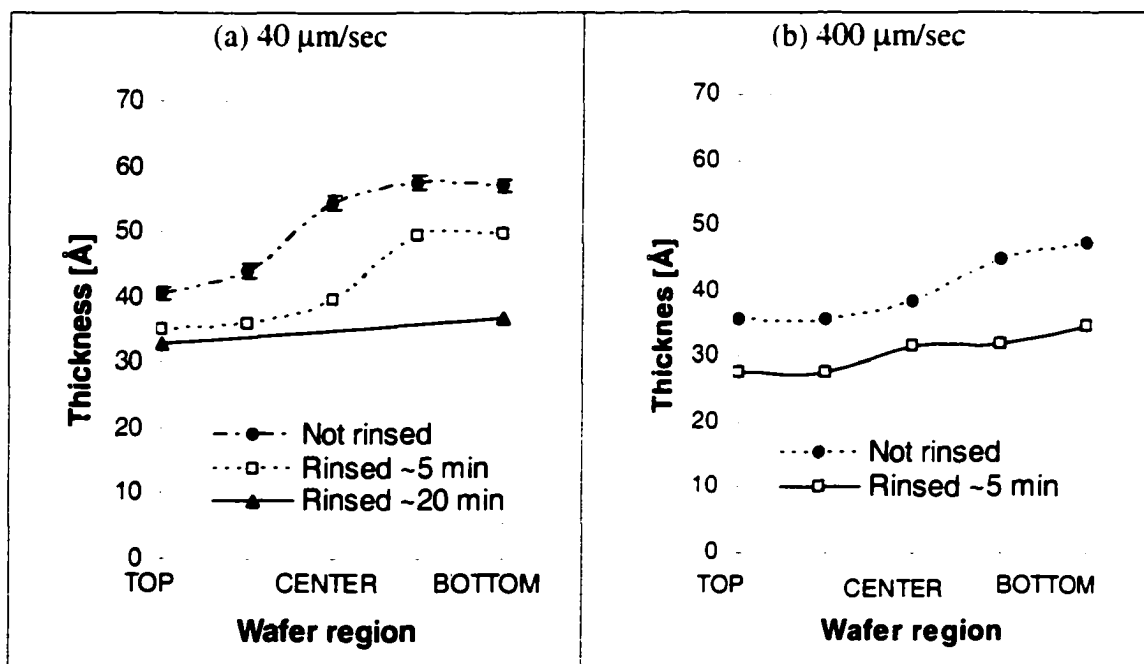


Figure 4.43: Thickness uniformity of coatings deposited from dispersions containing 0.1% DMOAP at withdrawal speed of (a) 40 $\mu\text{m}/\text{sec}$ and (b) 400 $\mu\text{m}/\text{sec}$

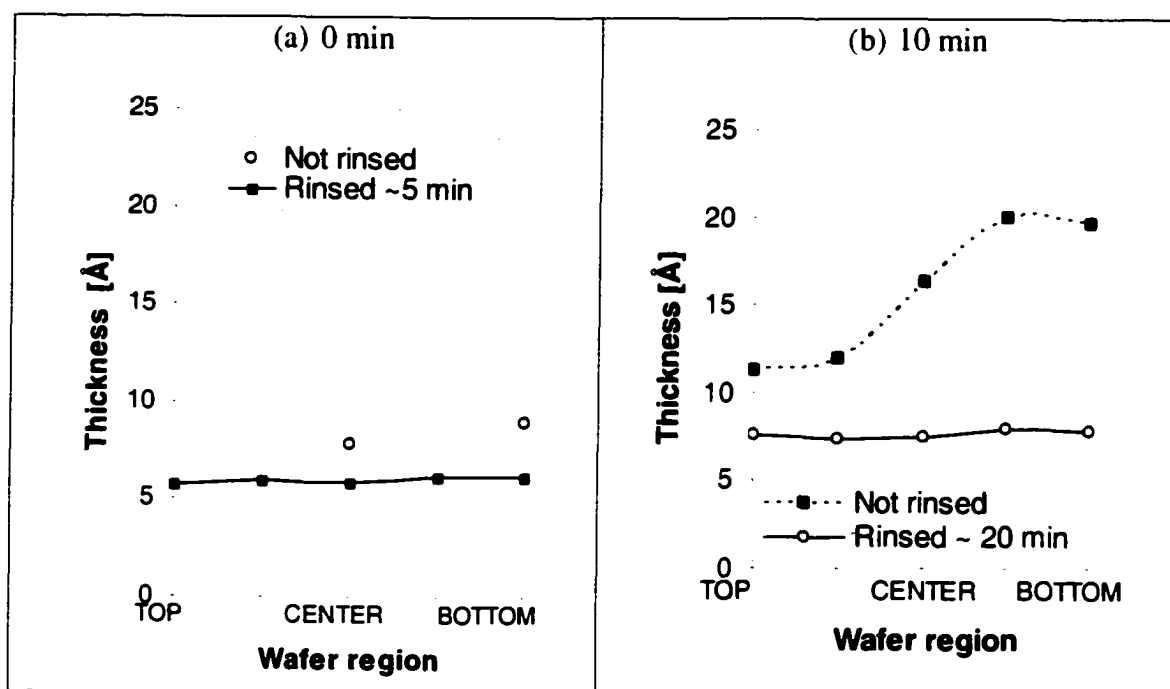


Figure 4.44: Thickness uniformity of coatings deposited from a dispersion containing 0.1% DIDAP at withdrawal speed of $40 \mu\text{m}/\text{sec}$ and different delay times

Figure 4.45 shows thickness of coatings deposited from dispersions containing 0.5% and 1% reactive Siliclad[®]. It may be seen that these values are below the reported thickness for monolayers of octadecyltrichlorosilane (28.1 Å), which can be explained by the presence of lying down molecules. The coating deposited from a dispersion containing 1% reactive silane showed higher thickness values as a result of increase silane coverage on the surface and/or packing of the monolayer. The deposition of coatings from dispersions with and without surfactant was characterized to determine if the presence of surfactant would interfere with the adsorption of silane onto the surface. The thickness for both cases was the same, indicating that the same quality of coatings can be obtained with and without the presence of surfactant in the silane dispersion. The addition of surfactant was necessary to improve the bath life of the dispersion. Coatings deposited from dispersions containing 3% reactive silane were not carried out due to the large amount of chemicals required for 4-inch wafers.

For the deposition of a DMOAP coating followed by a Siliclad[®] coating from a dispersion containing 0.5% reactive silane (

Figure 4.46(a)), a decrease in thickness after the deposition of the second coating was observed, which could be as the result of changes in optical properties of the composite coating or desorption of electrostatically adsorbed DMOAP by further rinsing.

DIDAP/Siliclad[®] double-coating system (

Figure 4.46(b)) showed no change in thickness after the deposition of the second coating. This could indicate that Siliclad[®] molecules did not deposit on DIDAP coated surfaces.

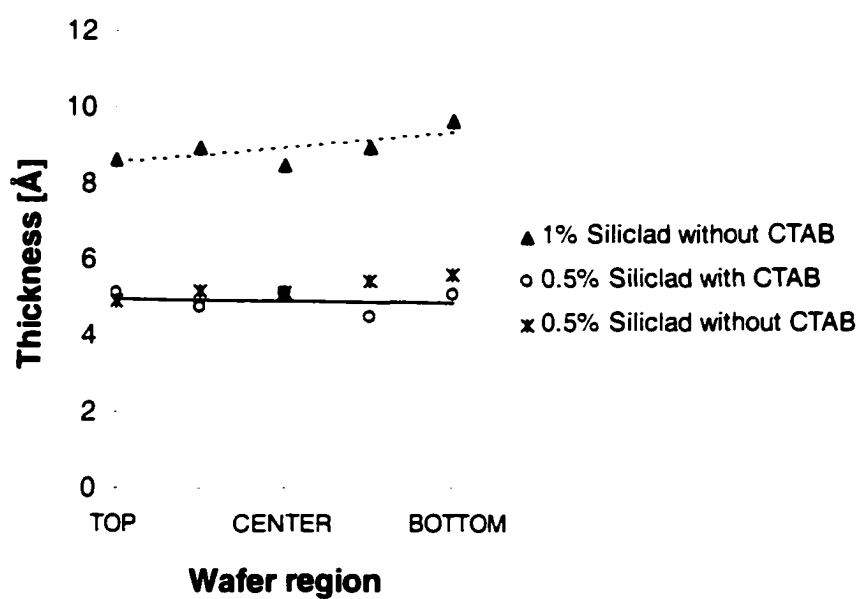


Figure 4.45: Thickness uniformity of coatings deposited from Siliclad[®] dispersions

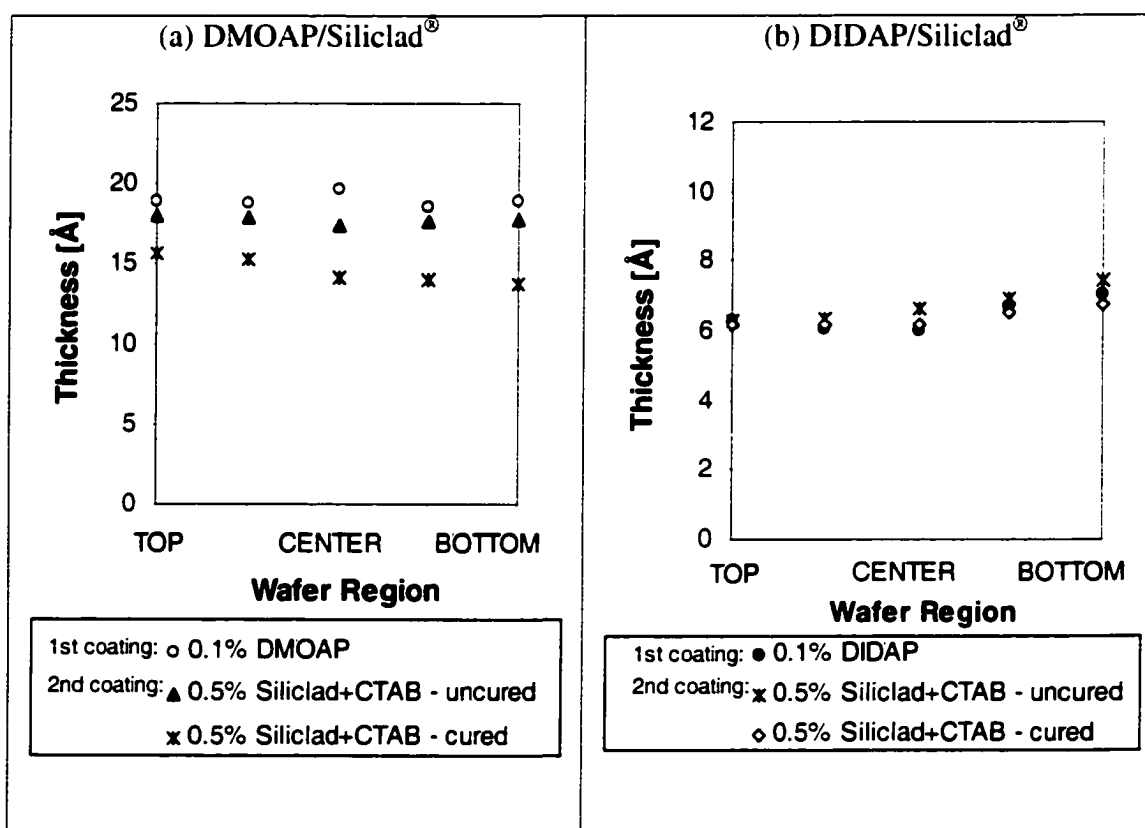


Figure 4.46: Thickness uniformity of (a) DMOAP/Siliclad[®] and (b) DIDAP/ Siliclad[®] double coating systems

4.3.2 Wettability

The dynamic DI water contact angles on the different organosilane coatings formed on single crystal silicon are listed in Table 4.10. The advancing contact angles on these coatings were between 94° and 109° and the receding contact angles varied from 60° to 90°. The hysteresis between advancing and receding contact angle was higher for DMOAP surfaces than for Siliclad[®] and DIDAP surfaces. This may be attributed to a difference in molecular scale roughness and porosity of the coatings.

Table 4.10: DI water contact angles on coated single crystal silicon

COATING	Contact Angle [degrees]		
	Advancing	Receding	f _{CH3}
0.5% Siliclad [®]	94.3 ± 0.7	72.1 ± 1.0	0.02
1% Siliclad [®]	96.4 ± 2.7	74.3 ± 1.4	0.05
3% Siliclad [®]	109.1 ± 1.2	91.3 ± 0.8	0.95
0.1% DMOAP	99.1 ± 1.6	59.8 ± 1.8	0.36
0.1% DIDAP	98.9 ± 1.2	77.2 ± 2.4	0.35
0.1% DMOAP/ 0.05% Siliclad [®]	101.2 ± 1.1	67.0 ± 0.4	0.50
0.1% DIDAP/ 0.5% Siliclad [®]	94.5 ± 2.0	73.8 ± 0.6	0.04
OTS (low humidity) ⁽⁸⁹⁾	110 ± 2	97 ± 2	1.0
OTS (50% RH) ^(32,53)	106 ± 2	80 ± 2	0.79

The advancing and receding contact angles reported in literature for coatings deposited from alkytrichlorosilanes onto pre-oxidized silicon with disordered monolayer structure are 103-105° and 91-92° respectively.⁽⁸⁹⁾ These contact angles are independent of the chain length. Highly ordered coatings of octadecyltrichlorosilane have shown advancing and receding contact angles of 110° and 98°, respectively. Self-assembled monolayers show higher contact angles because of the exposure of the highly

hydrophobic alkyl groups to the aqueous phase. Disordered monolayers were obtained for our coatings in most cases except for 3% reactive silane of Siliclad[®]. The increase in hydrophobicity of double coating systems could be an indication of improvement in coverage, assembly and/or orientation.

As a first evaluation of the degree of disorder, an approach developed by Israelachvili-Gee^(89,151) was used. In this method, the wettability of an alkyl-coated surface is determined using relative contributions to wettability by methyl or methylene according to the following equation:

$$(1 + \cos \theta_{\text{exp}})^2 = f_{\text{CH}_2}(1 + \cos \theta_{\text{CH}_2})^2 + f_{\text{CH}_3}(1 + \cos \theta_{\text{CH}_3})^2 \quad (4.4)$$

where θ_{exp} is the experimental advancing contact angle, θ_{CH_2} is the contact angle for pure surfaces of methylene groups (94°), θ_{CH_3} is the contact angle for pure surfaces of methyl groups (110°) and f is the fraction of methyl or methylene groups

Using this equation, the fraction of the surface that is composed of methyl groups (f_{CH_3}) was calculated from the contact angle data as shown in Table 4.9. For highly ordered coatings, the surface is composed primarily of methyl groups. Methylene groups start to be exposed as the degree of disorder increases. The high values of f_{CH_3} and thickness for coatings prepared from dispersions containing 3% reactive Siliclad[®] could indicate the deposition of highly oriented films. On the other hand, coatings deposited from dispersions containing 0.5% and 1% reactive silane showed low fraction of methyl groups and low thickness values as a result of low packing and predominantly “lying down” molecules that form a liquid expanded phase. DMOAP and DIDAP coatings

showed methyl fractions of ~ 0.35 and by recoating with Siliclad[®] the methyl fraction was improved to 0.5 for DMOAP coatings, but for DIDAP coatings a reverse effect was observed ($f_{\text{CH}_3} \sim 0.04$).

4.3.3 Uniformity

Figure 4.47 shows a set of AFM images of coatings prepared from Siliclad[®] dispersions on pre-oxidized silicon as a function of reactive silane concentration. These images provide evidence that Siliclad[®] coatings prepared from dispersions containing 0.5% reactive silane (Figure 4.47(a)) are composed of a continuous film with some particulate features which are 4-6 Å in height. Black spots in the image maybe identified as pores in the continuous film and their relative depth is roughly 5 Å. An increase in reactive silane concentration from 0.5% to 1% caused the particulates to grow laterally and vertically to a size of 11-13 Å in height and the relative pores depth to 6.5 Å (Figure 4.47(b)). The film deposited from a 3% reactive silane dispersion (Figure 4.47(c)) is characterized by large particles with vertical dimensions of 30-120 Å and lateral dimensions of hundreds of Å. These particulates are most likely formed as a result of silane cross-linking in the bulk. The advancing and receding contact angles for this coating are higher than for coatings prepared from lower silane concentration dispersions. The presence of particulates in the bulk of deposited films does not seem to be detrimental to the hydrophobic character of the films. The formation of these particulates has also been observed on OTS and DDMS coatings when deposited under humid conditions.⁽³²⁾

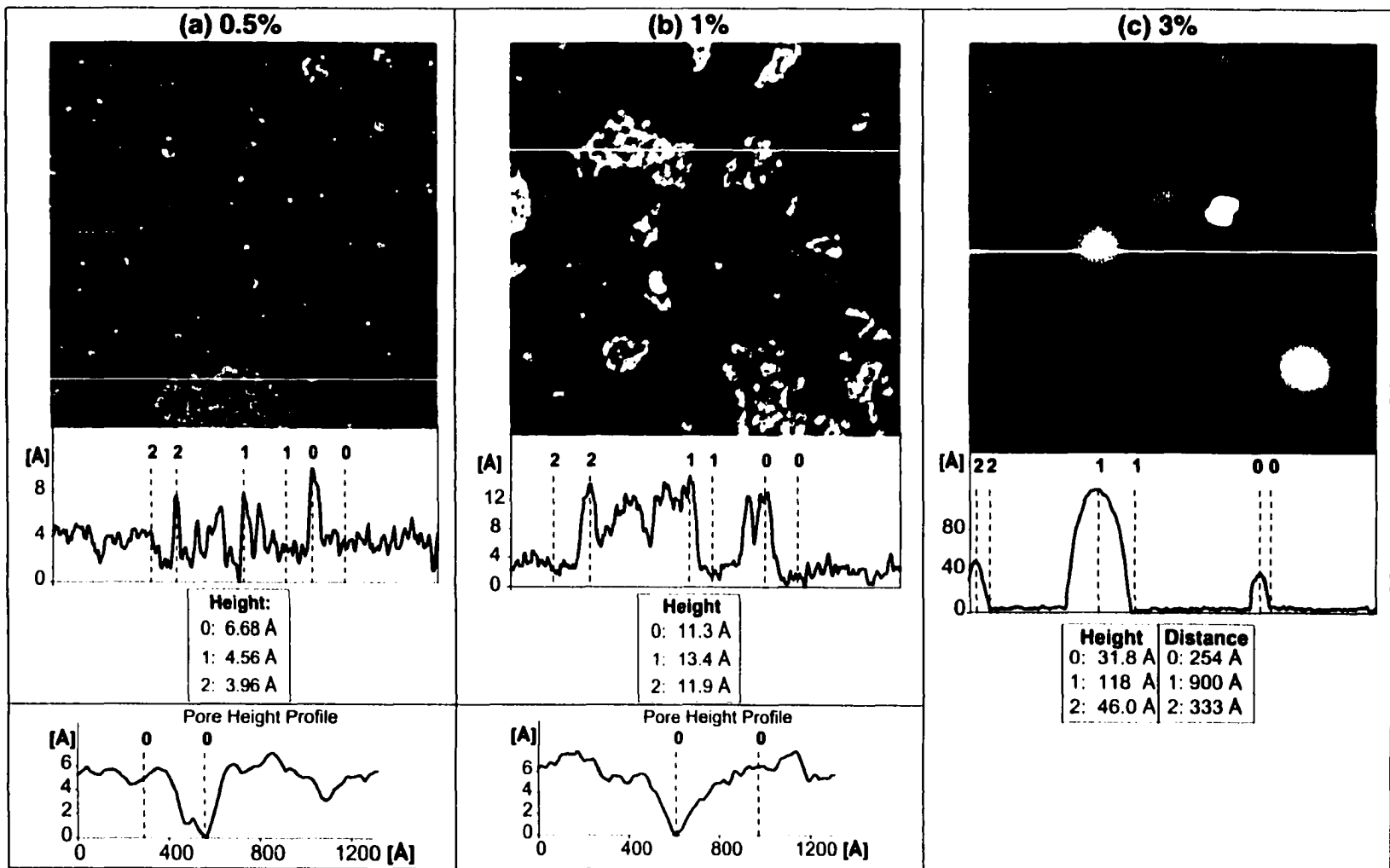


Figure 4.47: AFM images, of a $1\mu\text{m} \times 1\mu\text{m}$ region, showing Siliclad[®] coatings on single crystal silicon substrates (Height profiles in the lower part of the image were measured along the horizontal white lines. The pore height profiles were measured along the dotted lines)

Figure 4.48 shows an AFM image of a DMOAP film with the corresponding height profiles of particulates and pores. The particulates consist mainly of aggregates with uniform height of 40 Å and some with small features of 58 Å in height. These values correspond to bilayers and trilayers of DMOAP molecules. The pore depth was found to be 4.5 Å.

The amount of particulates on the top of the double coating system DMOAP/Siliclad[®] (Figure 4.49) appears to be lower than that observed for DMOAP (Figure 4.48) and Siliclad[®] (Figure 4.47(a)) coatings. This could be as a result of additional rinsing steps that were used to remove excess silane from the surface. The height of particulates was 35-42 Å, which is similar to DMOAP particulates. The pore depth was found to be 7.0 Å.

The pore depths in DMOAP and DMOAP/Siliclad[®] coatings were smaller than their respective film thicknesses measured using spectroscopic ellipsometry (Table 1). This could be due to the tip not reaching the substrate at the bottom of the pores.

Imaging of DIDAP and DIDAP/Siliclad[®] coatings was extremely difficult. An experiment was conducted in which one half portion of a pre-oxidized silicon sample was rapidly etched in HF and the unetched area was then coated with DIDAP. AFM analysis showed a gradual change in surface roughness at the expected boundary but no evidence of characteristic features or particulates. It is possible that these films were free of pores and particles. Further work will be necessary to elucidate these findings.

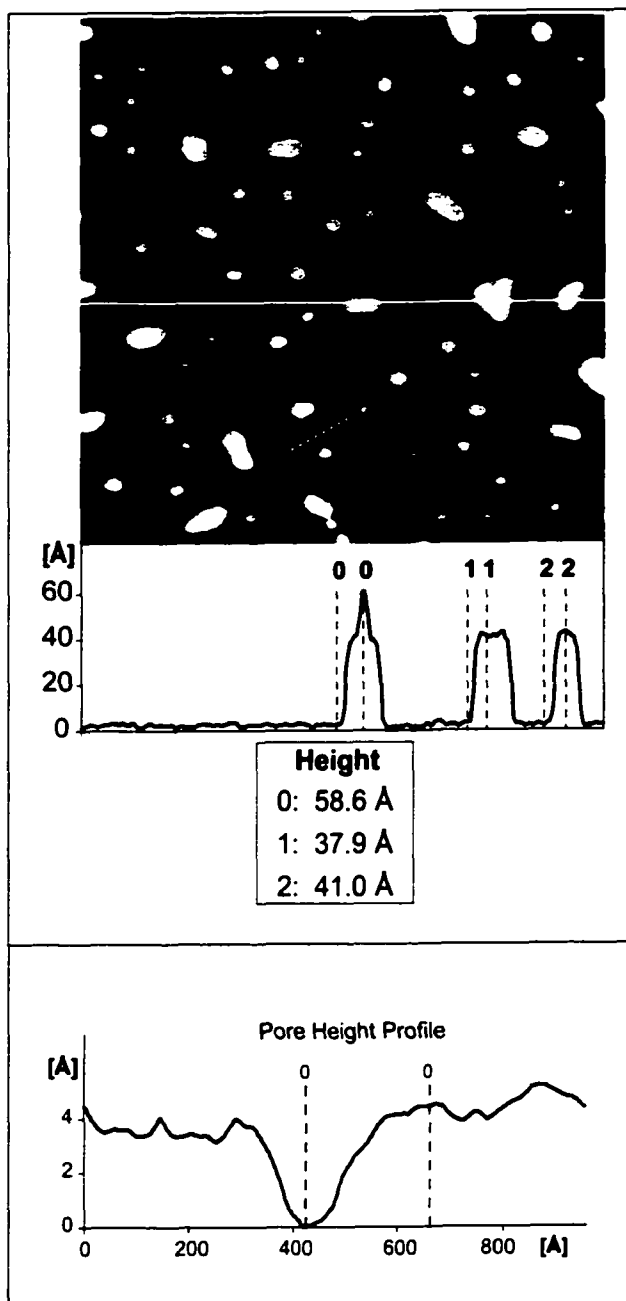


Figure 4.48: AFM image ($1\mu\text{m} \times 1\mu\text{m}$) of DMOAP coating. (Height profiles in the lower part of the image were measured along the horizontal white lines. Pore height profiles were measured along the dotted lines)

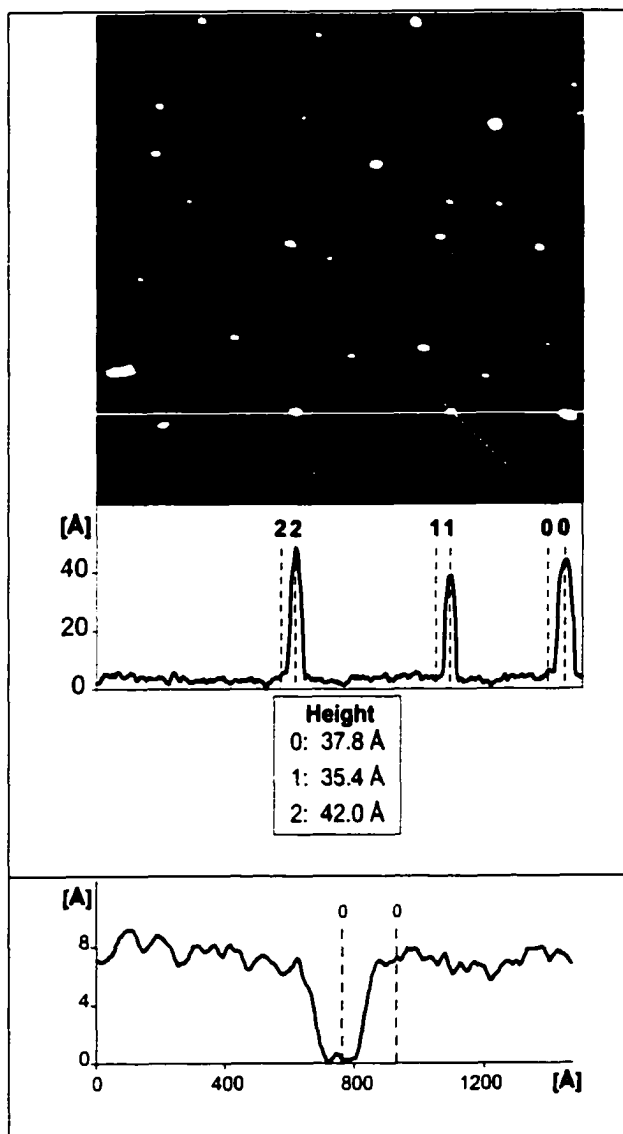


Figure 4.49: AFM image ($1\mu\text{m} \times 1\mu\text{m}$) of a DMOAP/Siliclad[®] coating. (Height profiles in the lower part of the image were measured along the horizontal white lines. Pore height profiles were measured along the dotted lines)

4.3.3.1 Removal of excess DMOAP

Kushmerick *et al.*⁽¹⁵²⁾ reported that film morphology dictates the anti-stiction properties of organosilane coatings used to release micromachined parts. Release stiction is reduced when an ideal monolayer film is present, but the formation of thick aggregate structures is a major source of irreproducible adhesion between microstructures. Polymerized clusters of alkyltrichlorosilane precursor molecules in the micron size range can mechanically interfere with the device operation.⁽³¹⁾ For these reasons, it is important to evaluate the possibility of excess silane removal that is deposited onto uncured cationic alkoxy silane coatings.

The topography of uncured DMOAP coatings formed on pre-oxidized silicon samples after different rinsing processes are shown in Figure 4.50. For these studies, DMOAP coatings were prepared by dip coating into dispersions containing 0.1% reactive silane at 40°C. The unrinsed sample exhibited inhomogeneous distribution of irregularly multilayer shaped islands. The sample soaked for 20 minutes in DI water showed fewer particles than the sample rinsed for 5 minutes using a squirt bottle. Most of the particles were removed by rinsing for 5 minutes with acetic acid at pH value of 2. Although no coating is visible on some areas; contact angle measurements indicate that a monolayer of hydrophobic DMOAP remained on the surface after the different rinsing processes.

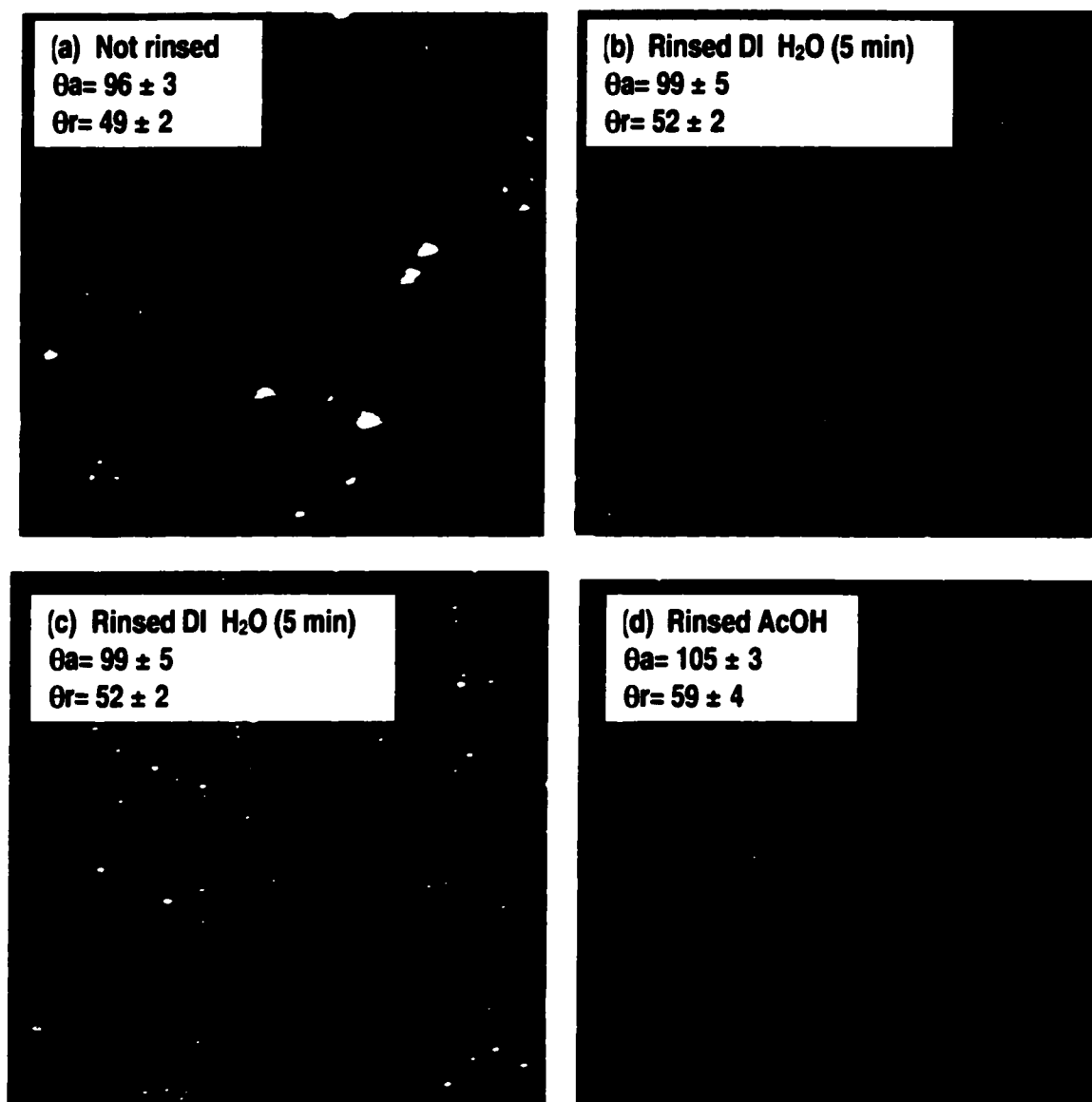


Figure 4.50: Tapping-mode AFM height images, of a 5 μm x 5 μm area, showing DMOAP coatings on single crystal silicon substrates: (a) without rinsing, (b) rinsed with DI water for 5 min, (c) immersed in DI water for 20 min and (d) rinsed with 0.1 M acetic acid (z range = 5 nm)

4.3.4 Porosity

Electrochemical Impedance spectroscopy (EIS) is a useful technique to characterize thin insulating films at electrode surfaces and can be particularly sensitive to the presence of pores or pinholes in films. In this work, the impedance of silicon/HF solution and silicon/coating/HF solution interfaces was analyzed using equivalent circuits. It was possible in this way to calculate interfacial resistance and capacitance that can be related to the quality of the films. The relative magnitude of these components provides an estimation of the protection provided by the coating against HF attack.

The equivalent circuits used to analyze the experimental data of uncoated and coated silicon samples are shown in

Figure 4.51. Because the experiments were carried out in HF solutions, no effects of oxide film were considered. In these circuits, R_{sample} is the sample bulk resistance and R_{sol} is the solution resistance. The sum of R_{sample} and R_{sol} will be referred to as R_o . The pore resistance (R_{pore}) that represents the resistance of pinhole type defect or chemical heterogeneity depends on the length of the pores and cross section. The capacitance $C_{\text{SC+DL}}$ consists of the space-charge capacitance (C_{SC}) and the double layer capacitance (C_{DL}) in series; and has been commonly used for interpreting interfacial phenomena that occur at the silicon/HF solution interface.^(153,154) The corresponding capacitance for a coated sample is $C'_{\text{SC+DL}}$. The interfacial charge-transfer resistance of uncoated and coated samples is R_t and R'_t , respectively.

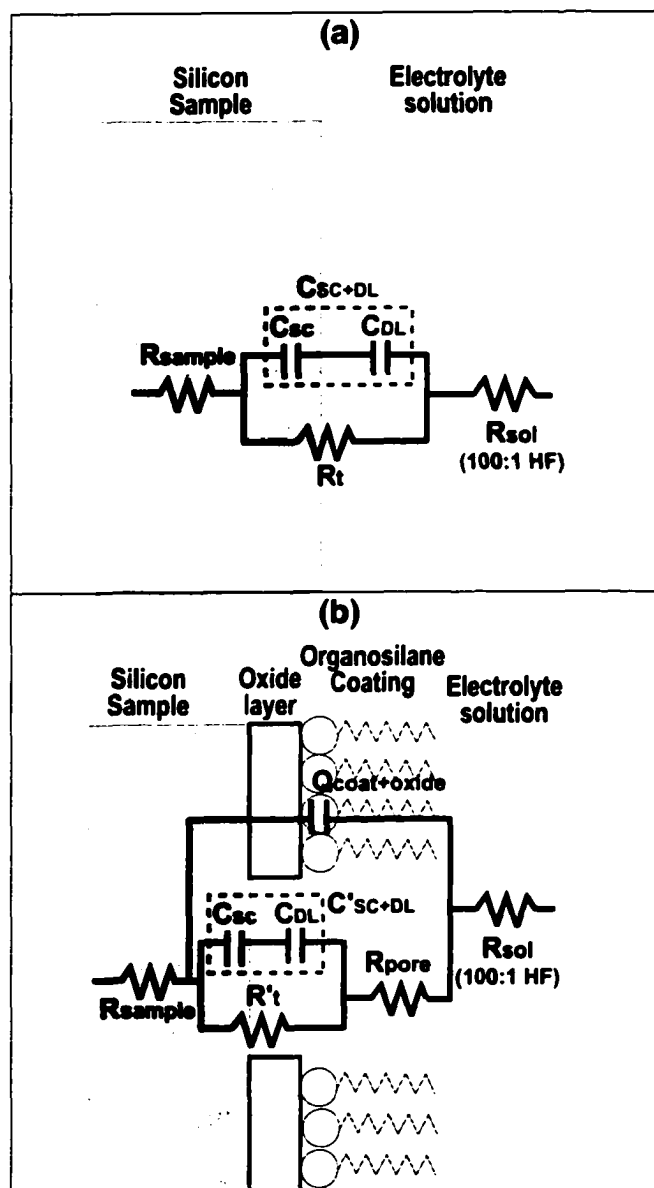


Figure 4.51: Equivalent circuit used for the interpretation of impedance spectra obtained for (a) uncoated and (b) coated silicon/solution interface in 100:1 HF

The values of R_t , C_{SC+DL} and R_{pore} for both coated and uncoated surfaces can be correlated to the area fraction of pore sites (θ) where silicon is in direct contact with HF: ⁽¹⁵⁵⁾

$$R'_t = \frac{R_t}{\theta}, \quad \theta C_{SC+DL} = C'_{SC+DL} \quad \text{and} \quad R_{pore} = \frac{R_{sol}}{\theta} \quad (4.5)$$

The coating and oxide capacitance is expressed in terms of a constant phase element (CPE). This is a "power law-dependent" interfacial capacity, which accounts for the topography of imperfections and roughness of the substrate and coating. The impedance of CPE is given as:

$$Z_{CPE} = \frac{1}{Y_0(j\omega)^n} \quad (4.6)$$

where Y_0 is the admittance and $n=1$ for an ideal capacitor. ⁽¹⁵⁶⁾

The EIS spectra for both uncoated and coated silicon in HF solutions under illumination are shown in Figure 4.52 to Figure 4.55 in the form of Nyquist plots. The points in the figures represent the experimental data, while the solid lines represent the best fits obtained by the NLLSF technique. In all cases, the spectra were characterized by one semicircle that represents a single time constant. Figure 4.52 shows the Nyquist plots for Siliclad[®] coatings formed from solutions containing different levels of reactive silane. The diameter of the semicircles increased with silane concentration indicating that the coating was able to provide a much higher degree of resistance to charge transfer. The spectra for DMOAP and DIDAP coated surfaces are shown in Figure 4.53. They appear quite similar to that for Siliclad[®] coated surfaces.

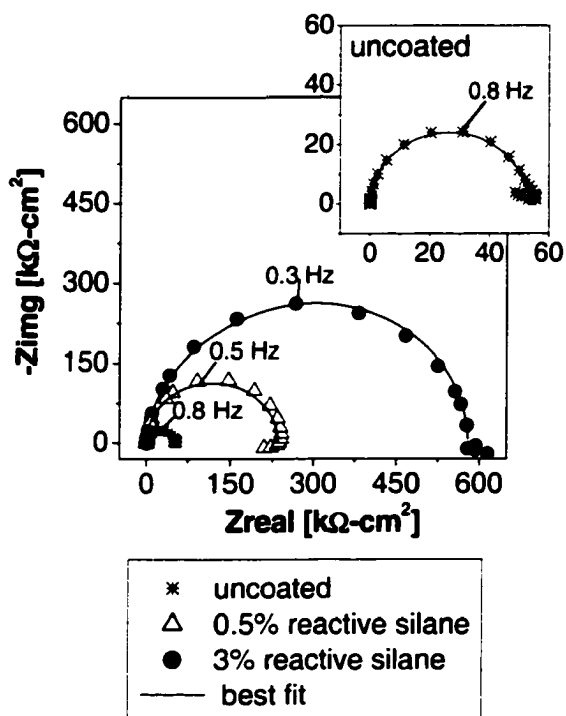


Figure 4.52: Nyquist plots for Siliclad[®] coated silicon samples in 100:1 HF

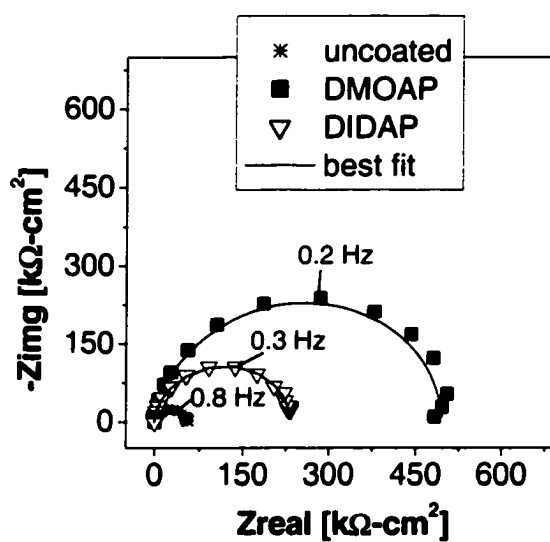


Figure 4.53: Nyquist plots for DMOAP and DIDAP coated silicon samples in 100:1 HF

The parameters evaluated by fitting the experimental data to the equivalent circuits are summarized in Table 4.11. At least three newly prepared samples for each type of coating were analyzed to determine the reproducibility of EIS measurements.

It is clear from the table that the R_t value for all coated surfaces is higher than that for uncoated surfaces. This implies that the electrochemical reactions proceed at lower rates when silane is deposited onto silicon. The very low value of charge transfer resistance for uncoated samples and the absence of Warburg component suggest that the electrochemical reaction at the silicon/HF solution interface is kinetically favorable and accelerated. The impedance in the low-frequency limit, R_t , significantly increased for all coated samples, especially for samples prepared from DMOAP and Siliclad[®] (3% reactive silane). The R_t value of Siliclad[®] coatings was dependent on the reactive silane concentration. The values of R_o ($2-6 \Omega\text{-cm}^2$) and R_{pore} ($4-15 \Omega\text{-cm}^2$) were found to be very small. This was expected because a highly doped sample and a high ionic strength solution (0.013 M) were used.

Analysis of the coating capacitance can be used to examine the structure of the monolayer assemblies. For all coatings, the deviation of the CPE from ideal behavior (i.e. capacitor) was very small ($n > 0.88$). Since the value of n does not depend on the length of the organosilane, Y_o was assumed to be approximately equal to C_{coat} throughout.⁶⁶⁾ According to Helmholtz model of the interface,¹⁵⁷⁾ the capacitance of the film is related to its thickness through the following equation:

$$Y_o \approx C_{\text{coat}} = \frac{\epsilon_{\text{SAM}} \epsilon_o}{d_{\text{SAM}}} \quad (4.7)$$

Table 4.11: Parameters obtained from the fitting of the EIS data to equivalent circuits

	Sample						
	Uncoated	Siliclad [®] (0.5%)	Siliclad [®] (3%)	DMOAP	DIDAP	DMOAP/ Siliclad [®]	DIDAP/ Siliclad [®]
Chi-Sqrd ($\times 10^{-3}$)	4.55 ± 0.55	3.38 ± 1.23	4.29 ± 0.44	2.03 ± 2.69	0.95 ± 0.05	3.64 ± 3.44	2.70 ± 1.96
R_o [$\Omega\text{-cm}^2$]	6.52 ± 3.76	2.29 ± 1.50	3.35 ± 0.37	5.11 ± 1.61	3.06 ± 2.10	6.66 ± 5.89	1.47 ± 1.07
Y_{oCOAT+O} x[$\mu\text{S/cm}^2$]	-----	0.47 ± 0.21	0.83 ± 0.09	0.90 ± 0.31	1.96 ± 0.41	0.66 ± 0.38	2.10 ± 0.48
n_{COAT+OX}	-----	0.97 ± 0.01	0.98 ± 0.3	0.92 ± 0.05	0.90 ± 0.03	0.89 ± 0.11	0.98 ± 0.02
R_{pore} [$\Omega\text{-cm}^2$]	-----	5.18 ± 1.47	11.31 ± 3.55	16.57 ± 12.09	3.73 ± 0.94	6.92 ± 2.29	2.68 ± 1.86
C_{sc+DL} [$\mu\text{F/cm}^2$]	2.67 ± 0.43	-----	-----	-----	-----	-----	-----
C'_{sc+DL} [$\mu\text{F/cm}^2$]	-----	0.69 ± 0.16	0.15 ± 0.05	0.53 ± 0.21	0.88 ± 0.55	0.35 ± 0.22	0.07 ± 0.04
R_t [$\text{k}\Omega\text{-cm}^2$]	59.39 ± 5.45	-----	-----	-----	-----	-----	-----
R'_t [$\text{k}\Omega\text{-cm}^2$]	-----	220.63 ± 37.00	553.55 ± 26.13	451.90 ± 49.59	236.71 ± 5.75	668.65 ± 62.68	369.48 ± 27.45
θ_R	1.0	0.28 ± 0.06	0.11 ± 0.01	0.13 ± 0.01	0.28 ± 0.07	0.09 ± 0.01	0.17 ± 0.01
θ_C	1.0	0.26 ± 0.06	0.07 ± 0.02	0.19 ± 0.08	0.32 ± 0.21	0.13 ± 0.09	0.03 ± 0.02

where d_{SAM} is the thickness of the monolayer, ϵ_{SAM} is the total permittivity of the film and ϵ_0 is the permittivity of vacuum. The value of Y_0 for DIDAP (10 carbon atoms) was larger than for DMOAP (18 carbon atoms) as expected from their thickness values. Siliclad[®] (3% reactive silane) and DMOAP coatings had very similar Y_0 values because both organosilane molecules are composed of 18 carbon atoms. The lower Y_0 value for coatings prepared from dispersions containing 0.5% reactive silane of Siliclad[®] is a result of less organized films. This confirmed by thickness value obtained using ellipsometry.

Figure 4.54 and Figure 4.55 show the EIS spectra for double coatings systems. The R_t values increased from 450 $\text{k}\Omega\text{-cm}^2$ and 200 $\text{k}\Omega\text{-cm}^2$ for DMOAP and Siliclad[®] single coating systems to 650 $\text{k}\Omega\text{-cm}^2$ for DMOAP/Siliclad[®] coatings and from 200 $\text{k}\Omega\text{-cm}^2$ for DIDAP to 350 $\text{k}\Omega\text{-cm}^2$ for DIDAP/Siliclad[®] coatings. This indicates that the defect levels in the film decreased by depositing a second silane layer. The charge transfer resistance for DIDAP coatings was lower than for DMOAP and Siliclad[®] coatings, leading to conclusion that DIDAP coating is a poor barrier for electron transfer.

The calculated values of area fraction of pore sites using R_t and $C_{\text{SC+DL}}$ are tabulated in Table 4.11 as θ_R and θ_C . These values show reasonable agreement. The most important observation that can be made from the table is that the area fractions are between 0.1 and 0.3 indicating that the coatings are fairly compact.

The capacitance associated with the Helmholtz double layer was lower than for a typical metal or semiconductor electrode ($>20 \mu\text{F/cm}^2$).⁽¹⁵⁴⁾ The same behavior has been observed by others⁽¹⁵³⁾ for n-type silicon exposed to 50:1 HF. From the equivalent circuit analysis, the value of the double layer capacitance was found to decrease for coated

samples and was the lowest for coatings prepared from Siliclad[®] dispersions containing 3% reactive silane and from the double coating system DIDAP/Siliclad[®]. This effect is due to a decrease in the effective surface area of silicon as a result of surface coverage. It has been reported previously^(153,158) that the surface coverage as a result of adsorption of organic molecules can reduce the double layer capacitance for semiconductor and metal electrodes from tens of microfarads to a few microfarads. The area fraction of pore sites (θ_c) calculated from the double layer capacitance is in agreement with the values obtained from charge transfer resistance.

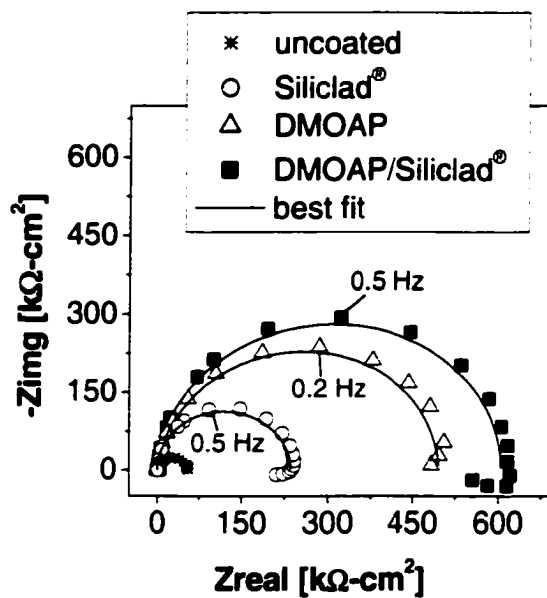


Figure 4.54: Nyquist plots for single and double DMOAP-Siliclad[®] coatings on silicon samples in 100:1 HF

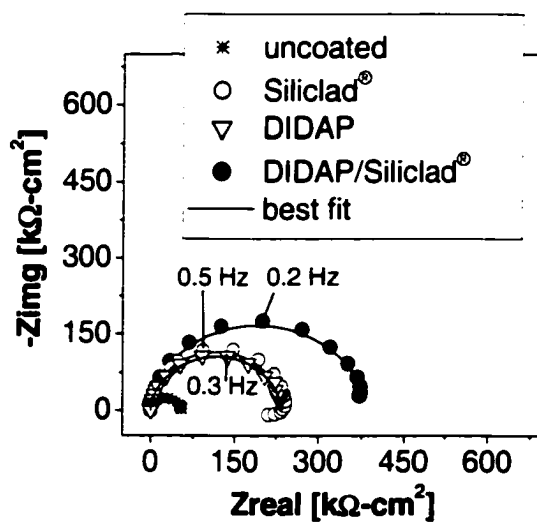


Figure 4.55: Nyquist plots for single and double DIDAP-Siliclad[®] coatings on silicon samples in 100:1 HF

4.4 DMOAP coatings deposited onto mica

A freshly cleaved mica surface was also chosen to characterize the morphology of the assembled DMOAP film formed *in-situ*. Mica was chosen because it is an atomically flat substrate, where surface corrugation is less than the organosilane molecule dimension, very easy to clean and negatively charged so that it interacts electrostatically with the positively charged headgroup of the cationic alkoxy silane. Mica possesses few, if any, surface hydroxyl groups⁽¹⁵⁹⁾ and is very likely that only physisorption of silane molecules occurs, resulting in a weak substrate-adsorbate bonding that allows surface mobility and molecular aggregation on the substrate.

Force profiles were obtained for DMOAP dispersions after their injection into the AFM liquid cell. Figure 4.56 shows tip displacement versus tip-sample (mica) separation profiles in DI water and in a DMOAP dispersion containing 0.0035% reactive silane. Formation of films containing areas with and without structures was observed (Figure 4.57) and the corresponding force curves are shown in Figure 4.56. Over areas of the sample where the AFM images did not show structures, the force curves showed a pre-contact breakthrough (indicated by "B" in the figure), indicating an adsorbed layer of DMOAP. Force curves over regions of the sample with visible structures showed two breakthroughs, indicating multilayer adsorption. DMOAP layers were imaged in soft contact mode by using applied forces lower than that necessary to break through the top most layer. The force was adjusted by changing the deflection set point of the cantilever. In the absence of DMOAP, approach of the tip to the surface produced an adhesive jump into contact with no pre-contact repulsion.

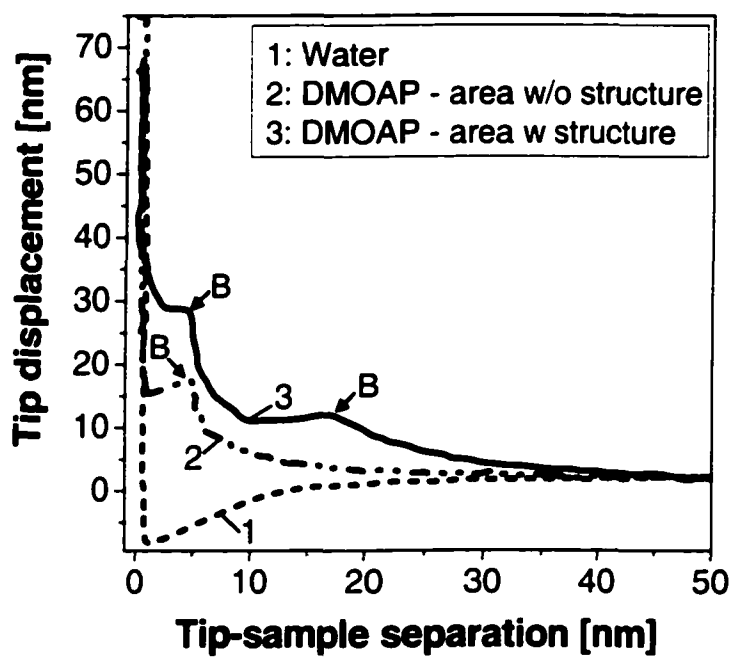


Figure 4.56: Tip displacement versus tip-mica sample separation curve for DI water and a 0.0035% reactive silane DMOAP dispersion

Figure 4.57 shows a series of *in-situ* AFM images on mica under no-flow deposition from a DMOAP dispersion containing 0.0035% reactive silane. These images do not show the mica surface, but rather the pattern of repulsive forces above it in solution. The dimensions of the DMOAP structures became larger with time until they reached equilibrium as a result of silane depletion from solution. These structures were not spherical, as might be expected for surface micelles, but rather irregularly shaped; this could be attributed to the precipitation of insoluble DMOAP molecules that exist at temperatures below the Krafft point. In section 4.2.5.1 of this dissertation the Krafft point of DMOAP was assumed to be similar to octadecyltrimethylammonium bromide (between 35 and 37°C).⁽⁹⁹⁾ After 90 minutes exposure the coverage of the second layer structures was ~15%. The advancing and receding contact angles measured on such sample were $92^\circ \pm 4$ and $43^\circ \pm 5$, respectively. The same type of flat structures has been observed by others⁽¹⁶⁰⁾ on FDTS-coated silicon wafers after heat treatment. After exposing to the stagnant solution for 90 minutes, a fresh silane solution was injected and ~45% of the surface was covered by these multilayered structures.

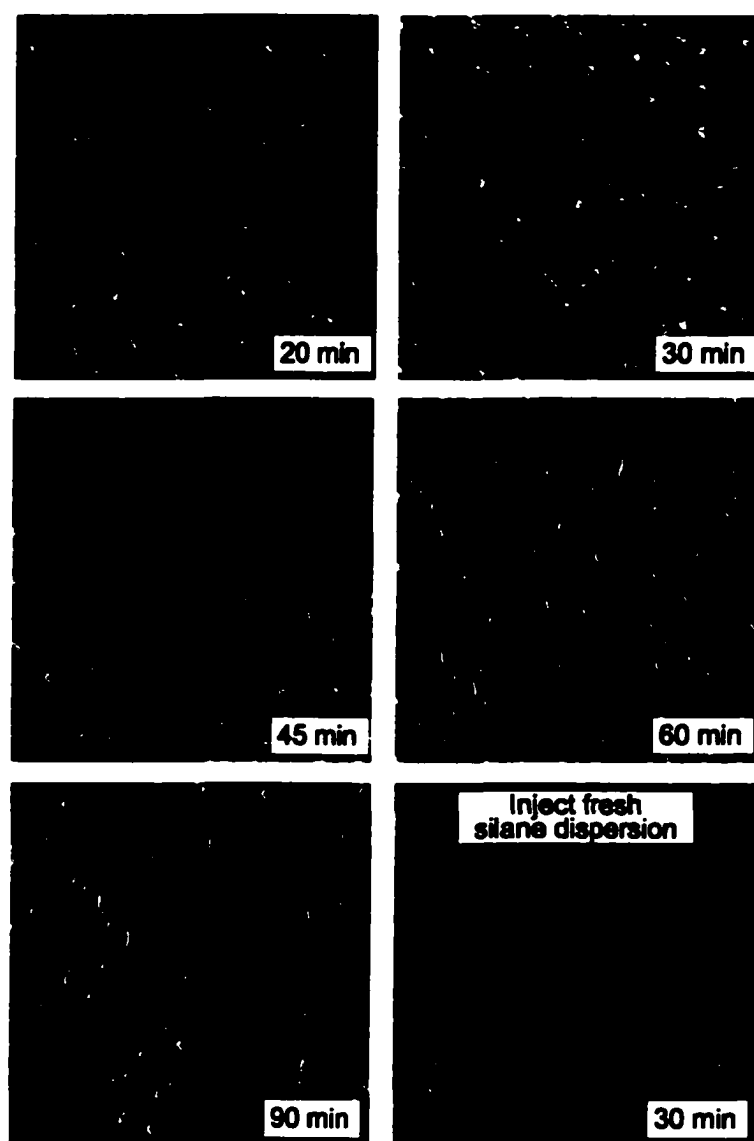


Figure 4.57: *In-situ* deflection-mode AFM images, of a $3.5\ \mu\text{m} \times 3.5\ \mu\text{m}$ region, showing DMOAP aggregates on mica as a function of exposure time at $\sim 22^\circ\text{C}$

Figure 4.58 shows force curves for DMOAP dispersions containing different amounts of reactive silane. The pre-contact repulsion region for dispersions containing 0.002-0.005% reactive silane had similar repulsive forces, whereas the dispersion containing very low reactive silane concentration (0.001%) showed very little pre-contact repulsive forces. The force curve obtained for a dispersion containing very high concentration of reactive silane (0.1%) showed multiple jumps that correspond to the rupture of successive DMOAP layers as the tip approaches the surface.¹⁶¹

Figure 4.59 shows AFM images of DMOAP structures on mica prepared from dispersions containing different amounts of reactive silane which were allowed to equilibrate for 1 hour. It is apparent from these images that the number of structures deposited on mica increased as reactive silane concentration increased due to the low solubility of DMOAP molecules below the Krafft point.

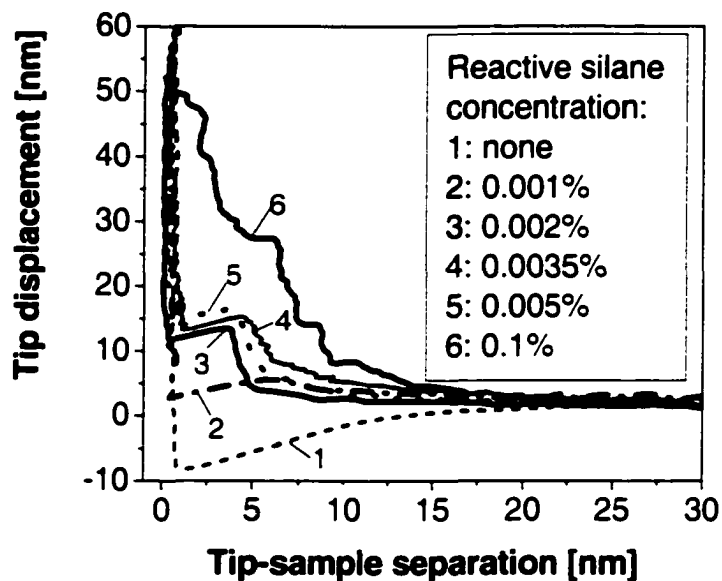


Figure 4.58: Tip displacement versus tip-sample separation profiles for DMOAP dispersions containing different amounts of reactive silane on mica

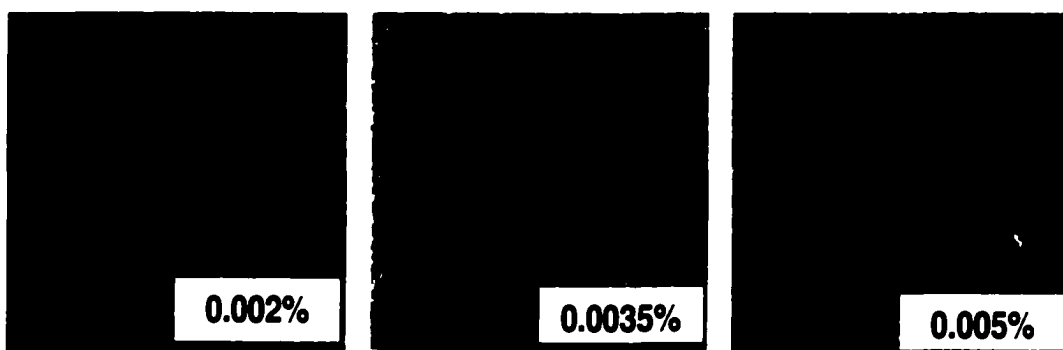


Figure 4.59: Deflection mode AFM images, of a $10\ \mu\text{m} \times 10\ \mu\text{m}$ region, showing DMOAP aggregates on mica as a function of reactive silane concentration

4.5 Optimization of dip coating conditions using design of experiments

In the experiments reported so far, the deposition of cationic alkoxy silanes was carried out by dip coating at immersion and withdrawal speeds of 140 $\mu\text{m}/\text{sec}$ without any extra holding time (delay time) between immersion and withdrawal steps. The factors or variables that may influence the hydrophobic character of the coatings are listed in Table 4.12.

Table 4.12: Important factors for dip coating of organosilanes

FACTOR	COATING EFFECT
Reactive silane concentration	Surface coverage
Dispersion pH	Organosilane hydrolysis and condensation
Deposition Temperature	Silane solubility
Immersion and Withdrawal Speed	Thickness and surface coverage
Delay time	Surface coverage and uniformity
Curing temperature and time	Organosilane cross-linking

The objective of the design of experiments was to determine the set of conditions that would maximize hydrophobicity with the smallest variability. This design was also useful to determine whether any change in dip coating conditions would affect the hydrophobic character of the coatings.

For the design, the values of pH (=4), temperature (=35°C) and reactive silane concentration (0.1%) were kept constant as predetermined by *one factor at a time* hydrophobicity maximization described in section 4.2.4 of this dissertation. A full and unreplicated 2^k factorial experimental design⁽¹⁶²⁾ with 1 block and 4 center points per block was used to evaluate the importance and interactions between immersion speed,

withdrawal speed and delay time. A two-level factorial design was chosen for simplicity, as it restricts the design to high and low values of the factors. The design is shown geometrically in Figure 4.60. The high and low values were chosen according to coating conditions that could be used in the manufacturing process of MEMS.

A table of 12 experiments (Table 4.13) was generated using Design Expert software version 6.0.7 (Stat-Ease Inc.) for the two cationic alkoxysilane systems, DMOAP and DIDAP. At each combination of these conditions, coatings were deposited on 1.5 cm x 1.5 cm polysilicon samples. Hydrophobicity of the coatings was determined by measuring advancing and receding contact angles immediately after film deposition using the Wilhelmy Plate Technique. The advancing and receding contact angle values were the response data considered for the design.

Table 4.13: Table of experiments generated by Design Expert software (ver. 6.0.7)

Run #	Factor A Withdrawal Speed [$\mu\text{m}/\text{sec}$]	Factor B Delay time [min]	Factor C Immersion Speed [$\mu\text{m}/\text{sec}$]
1	200	5	200
2	50	0	350
3	200	5	200
4	50	10	350
5	350	10	50
6	50	10	50
7	200	5	200
8	200	5	200
9	50	0	50
10	350	0	350
11	350	10	350
12	350	0	50

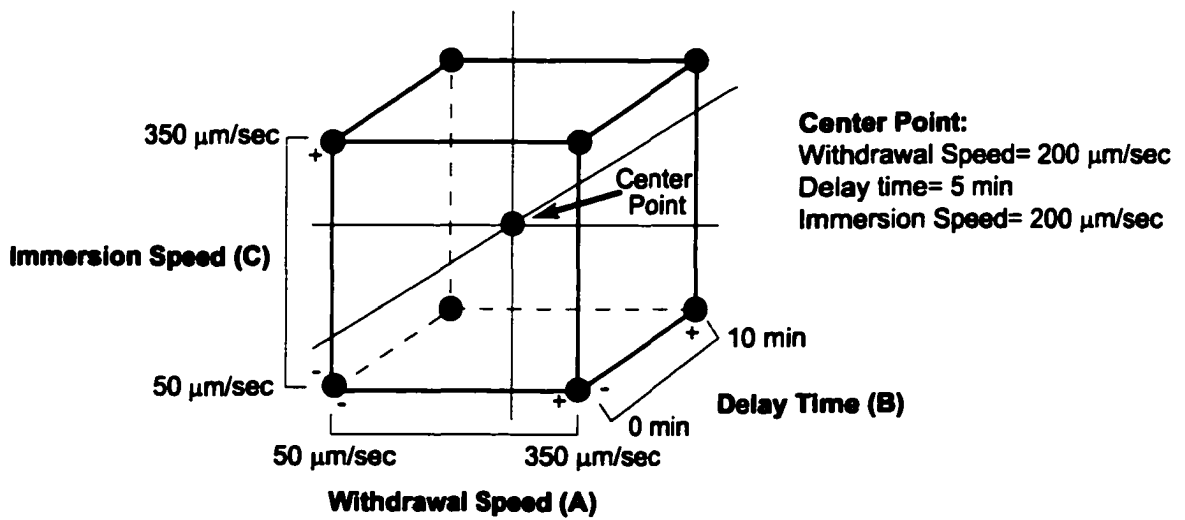


Figure 4.60: Factors and levels used for the optimization of coating deposition by the two-level factorial design

Figure 4.61 shows the general sequence used to analyze each response with Design-Expert software. First, the data was analyzed without any transformation. The significant factors were identified and separated from the insignificant factors by using half-normal probability plots. This plot offers the advantage that the straight line always passes through the origin and can only move in one dimension which makes it easy to select the significant factors. The outputs of the statistical analysis of variance (ANOVA) provided evidence for the validity of the model. Definitions of statistical terms^{162,163} used in the analysis are listed in Appendix A at the end of this dissertation. The important outputs on the effects were the F-value and associated probability (Prob>F). The values of adjusted R^2 , predicted R^2 , prediction error sum of squares (PRESS) and adequate precision (signal to noise ratio) were used to determine how well the model predicted and explained new data. Finally, the model was verified by diagnostic plots to determine if a run needed to be replicated and a 3D response surface was generated. The "Box Cox Plot" indicated that a power transformation ($y'=y^{\lambda}$) was the most appropriate transformation.

The half normal probability plots of the effect estimates and factor interactions for the power transformed advancing and receding contact angles for DMOAP and DIDAP coatings are shown in Figure 4.62. The effects are shown as square points and estimates of error are displayed as triangles. All the effects that lie along the line were insignificant, whereas the large effects were far from the line. The significant effects that emerge from this analysis were withdrawal speed (A) and delay time (B). The immersion speed (C)

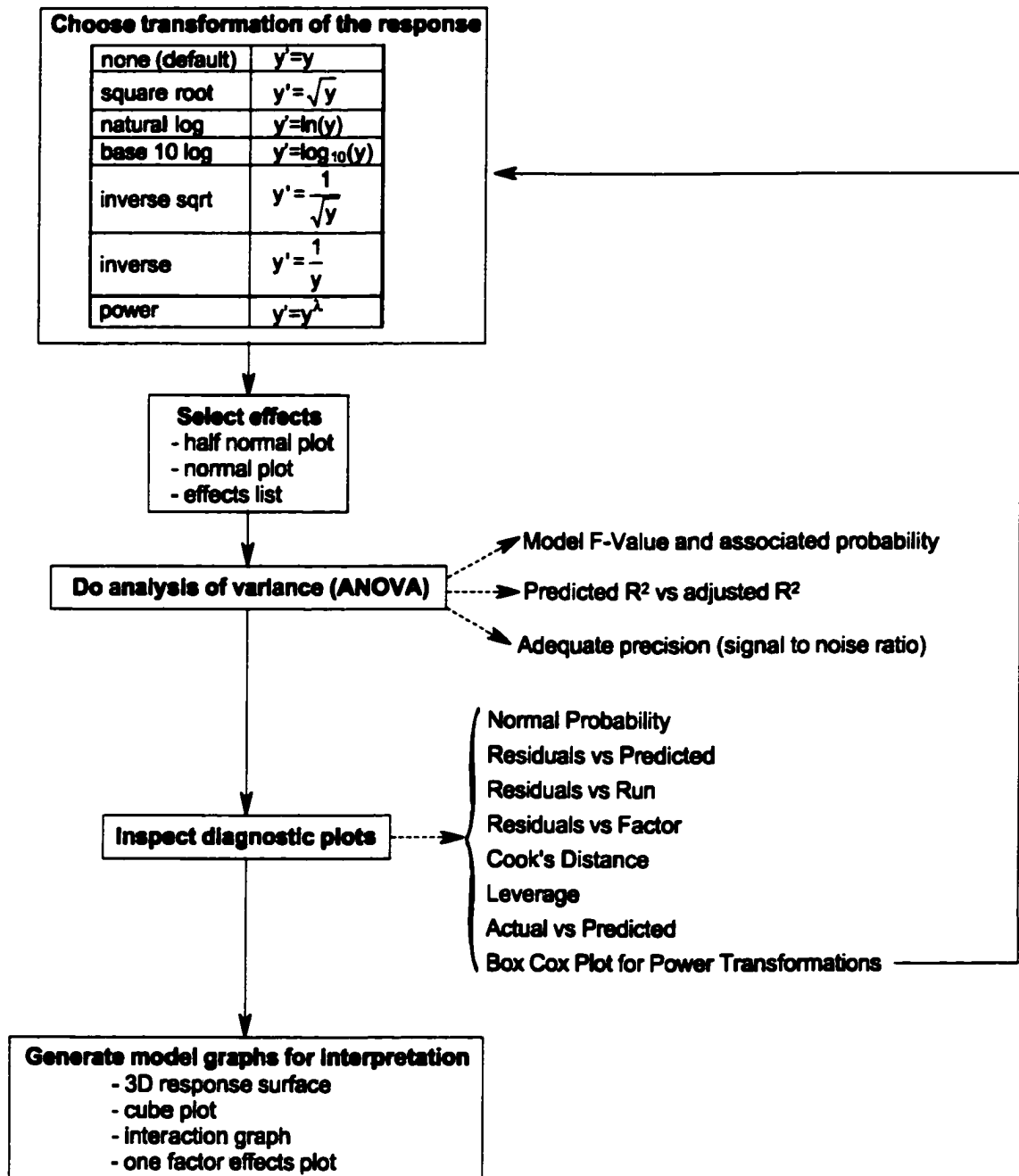


Figure 4.61: Design-Expert software general sequence of analysis

was found not significantly influence the hydrophobicity. No interactions between the factors were observed. Delay time (B) followed by withdrawal speed (A) were the largest effects for advancing and receding contact angles on DMOAP coatings and receding contact angles on DIDAP coatings, whereas the only significant effect for advancing contact angles on DIDAP coatings was withdrawal speed (A).

Analysis of variance (ANOVA) was carried out to test the accuracy of the models. Table 4.14 shows statistics obtained from ANOVA with and without data transformation. The following statistical conditions have to be followed to make a model valid: (i) *F-values* need to be large and *associated probability* ("Prob>F") less than 0.05 for effects to be significant; (ii) *predicted R²* needs to be in reasonable agreement with *adjusted R²* and within 0.2 of each other; (iii) the value of *adjusted and predicted R²* has to be close to 1; (iv) *adequate precision* has to be greater than 4; and (v) the *prediction error sum of squares (PRESS)* has to be as small as possible.

The model was statistically validated through the diagnostics plots. A "Box Cox" plot helped to determine the most appropriate power transformation to apply to response data. The statistics on the transformation are also shown in Table 4.14.

Better models were obtained for DMOAP coatings than for DIDAP coatings, as determined from the value of R^2 and PRESS. A replicate of DIDAP experiments was carried out to reduce the signal to noise ratio, but no improvement on the statistics was observed.

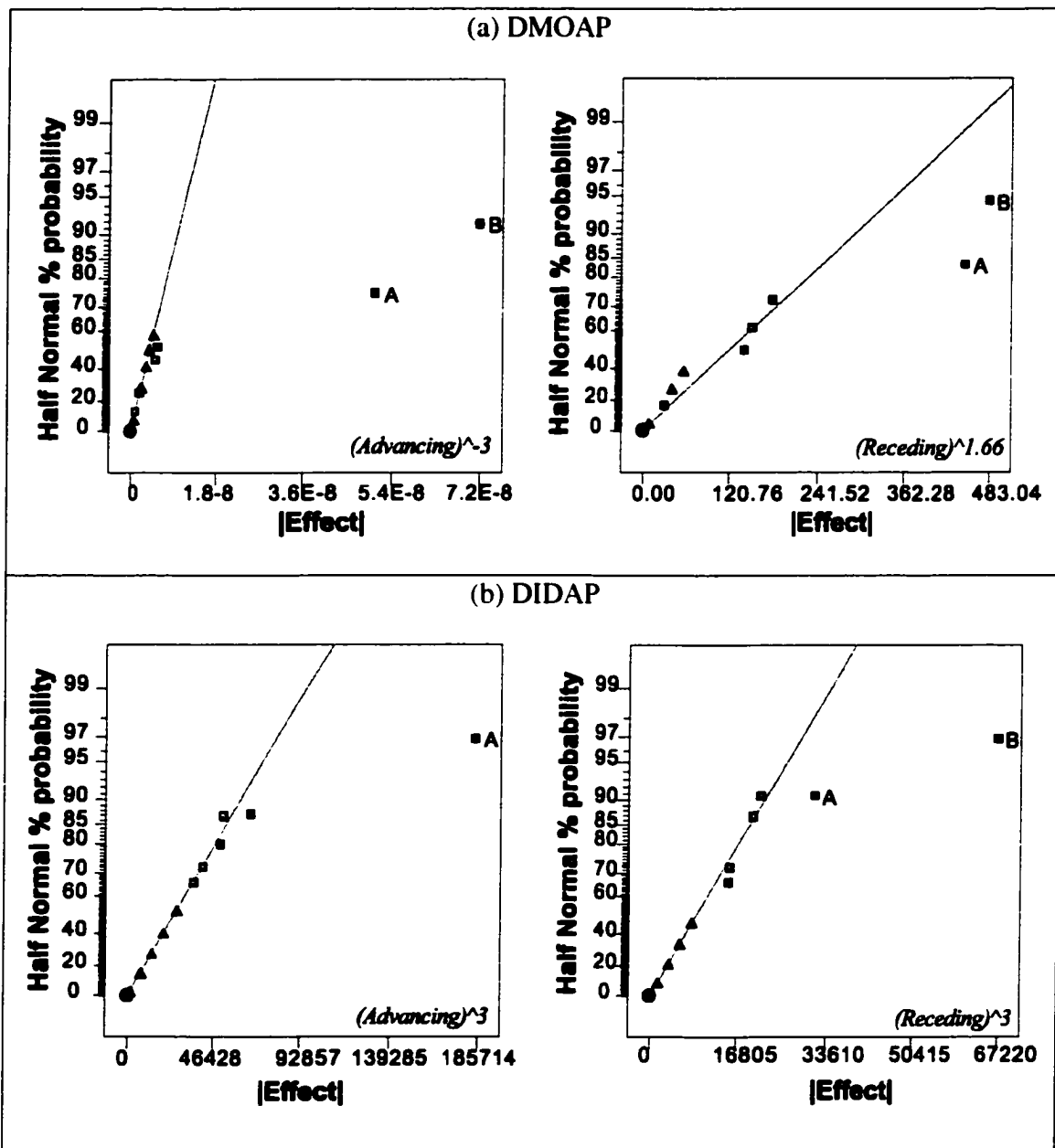


Figure 4.62: Half normal probability plot for the effects of advancing and receding contact angles of DMOAP and DIDAP coatings with power transformation (A: Withdrawal Speed and B: Delay time)

Table 4.14: Statistics from ANOVA analysis

	DMOAP			
	Advancing		Receding	
Transformation type	None	Power: -3	None	Power: 1.66
Effects	A, B	A, B	A, B	A, B
Model F value	A: 84.84 B: 167.38	A: 94.56 B: 191.54	A: 20.98 B: 22.93	A: 21.03 B: 22.55
Prob>F	A: 0.0008 B: 0.0002	A: 0.0006 B: 0.0002	A: 0.0025 B: 0.0020	A: 0.0025 B: 0.0021
Adjusted R²	0.9677	0.9716	0.7388	0.7680
Predicted R²	0.9324	0.9406	0.7193	0.7142
PRESS	1	5.67x10 ⁻¹⁶	128.90	5.98x10 ⁻⁴
Adeq. Precision	20.348	21.701	11.226	11.186
	DIDAP			
	Advancing		Receding	
Transformation type	None	Power: 3	None	Power: 3
Effects	B	B	A, B	A, B
Model F value	B: 23.72	B: 24.95	A: 21.33 B: 5.26	A: 25.85 B: 5.65
Prob>F	B: 0.0002	B: 0.0002	A: 0.0004 B: 0.0378	A: 0.0002 B: 0.0322
Adjusted R²	0.5868	0.6995	0.5795	0.7247
Prediction R²	0.5126	0.6323	0.4117	0.5868
PRESS	130.68	9.81x10 ⁻⁴	127.94	1.41x10 ⁻²
Adeq. Precision	6.376	6.539	7.919	8.548

The best mathematical models that fitted the experimental data for DMOAP and DIDAP coatings are:

DMOAP:

$$\frac{1}{\text{Advancing}^3} = 9.1 \times 10^{-7} + 2.4 \times 10^{-10} [\text{Withdrawal Speed}] - 7.6 \times 10^{-9} [\text{Delay time}] \quad (4.8)$$

$$\text{Receding}^{1.66} = 1488.3 - 2.2 [\text{Withdrawal Speed}] - 18.9 [\text{Delay time}] \quad (4.9)$$

DIDAP:

$$\text{Advancing}^3 = 1.0 \times 10^6 - 612.7 [\text{Withdrawal Speed}] \quad (4.10)$$

$$\text{Receding}^3 = 2.4 \times 10^5 - 104.8 (\text{Withdrawal Speed}) + 6722.1 (\text{Delay time}) \quad (4.11)$$

The 3D response curves for advancing and receding contact angles for DMOAP and DIDAP coatings are shown in Figure 4.63. The response plots for DMOAP coatings are given in Figure 4.63(a). The advancing and receding contact angles for DMOAP coatings varied from 101° to 106° and 54° to 58°. Even though statistical analysis indicated that withdrawal speed and delay time had significant effect on the value of advancing and receding contact angle, the range indicates that withdrawal speed and delay time have only a minor effect on hydrophobicity. In a processing point of view this offers the advantage of small variability on the hydrophobic character of the coatings when dip coating conditions are changed.

The response plots for DIDAP coatings are given in Figure 4.63(b). Withdrawal speed is the main effect that needs to be controlled to obtain high advancing and receding contact angles. The slower the withdrawal speed the higher the advancing and receding contact angles. Delay time has only a significant effect on receding contact angle. The longer the delay time the higher the receding contact angle. The advancing contact angle varied from 93° to 101° and receding from 59° to 67°.

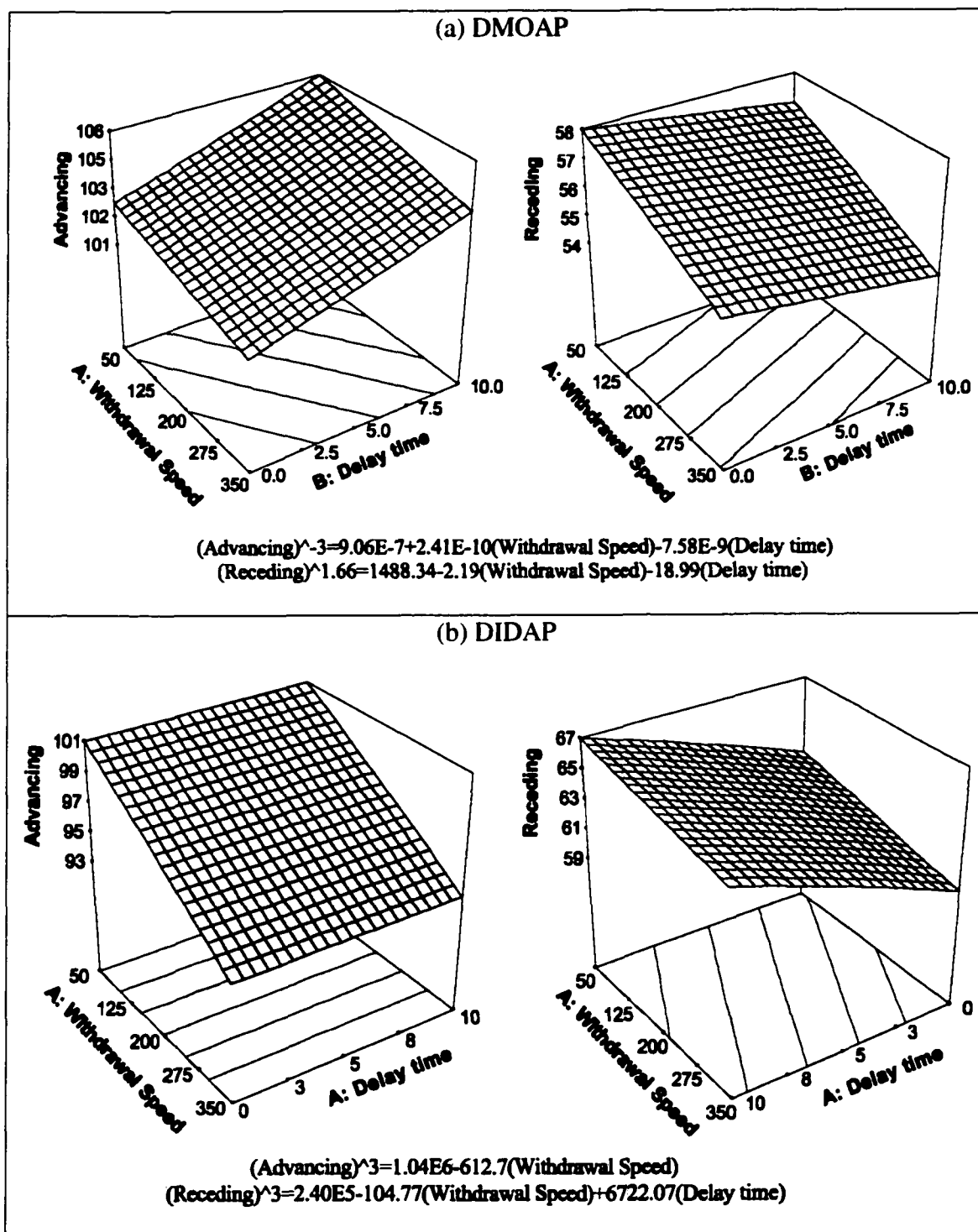


Figure 4.63: Effect of withdrawal speed and delay time on the hydrophobicity of DMOAP and DIDAP coatings

The optimum dip coating conditions obtained from the models generated by Design-Expert software are shown in Table 4.15 as run #1 and #2. Highly hydrophobic DMOAP coatings are obtained at immersion/withdrawal speeds of 350 $\mu\text{m}/\text{sec}$ and no delay time is required. DIDAP coatings need to be deposited with slow withdrawal speed and 10 min delay time. The conditions marked as run #3 and #4 also give highly hydrophobic DMOAP coatings but required longer processing time. Run #5 conditions require shorter processing coating time but the receding contact angle is slightly lower. A second set of experiments was conducted to verify point prediction and optimization. The model showed a good agreement of the experimental values with respect to the predicted advancing and receding contact angles.

Table 4.15: Optimum conditions to deposit hydrophobic coatings onto polysilicon

Dip coating conditions						Predicted angles (95% confidentiality)		Experimental results	
Run #	Type of Silane	Conc. [% Reactive silane]	Immersion Speed [$\mu\text{m}/\text{sec}$]	Delay time [min]	Withdrawal Speed [$\mu\text{m}/\text{sec}$]	θ_a	θ_r	θ_a	θ_r
1	DMOAP optimum	0.1 (35°C)	350	0	350	101-106	55-62	104 ± 4	55 ± 1
2	DIDAP optimum	0.1 (35°C)	350	10	50	99-102	65-69	101 ± 1	69 ± 5
3	DMOAP	0.1 (35°C)	350	0	50	103-107	52-57	103 ± 1	57 ± 2
4			350	10	50	103-107	55-60	106 ± 3	57 ± 3
5	DIDAP	0.1 (35°C)	350	0	50	99-102	60-64	100 ± 5	62 ± 1

4.6 Anti-stiction properties of DMOAP coatings

Micromachined structures used for preliminary studies on anti-stiction properties of DMOAP coatings were provided by Gary O'Brien (GOB), from the University of Michigan. These test structures consisted of three columns of comb-like single clamped beam arrays with single and double anchors (Figure 4.64). The 2 μm thick polysilicon beams were anchored 2 μm above the surface with widths of 2 μm , 4 μm and 6 μm , and lengths of 120 μm , 160 μm and 200 μm . A 2 μm annealed phosphosilicate glass (PSG) layer served as the sacrificial layer. The total number of beams per column was 100.

Unfortunately, polysilicon was over-etched during the processing of the wafer and the 2 μm wide beams were completely etched away. As a result of the disappearance of these beams, the real width of the 6 μm and 4 μm beams was determined to be 3.3 μm and 1.47 μm , respectively, using CD-SEM. The notation use in this dissertation to identify each array will be "length x real width" of the beams.

The arrays chosen for vertical stiction studies were 6 μm wide (real width: 3.3 μm) and 120 μm and 160 μm long. The 200 μm long beams, as well as the 1.45 μm wide beams showed a lot of lateral stiction that made very difficult to quantify vertical stiction.

An optical microscope, at 100 X, was used to evaluate the stiction on each sample. In an optical inspection, fully released beams and anchors would be in focus in contrast to beams with stiction which would appear fuzzy (out of focus), as indicated in Figure 4.65.

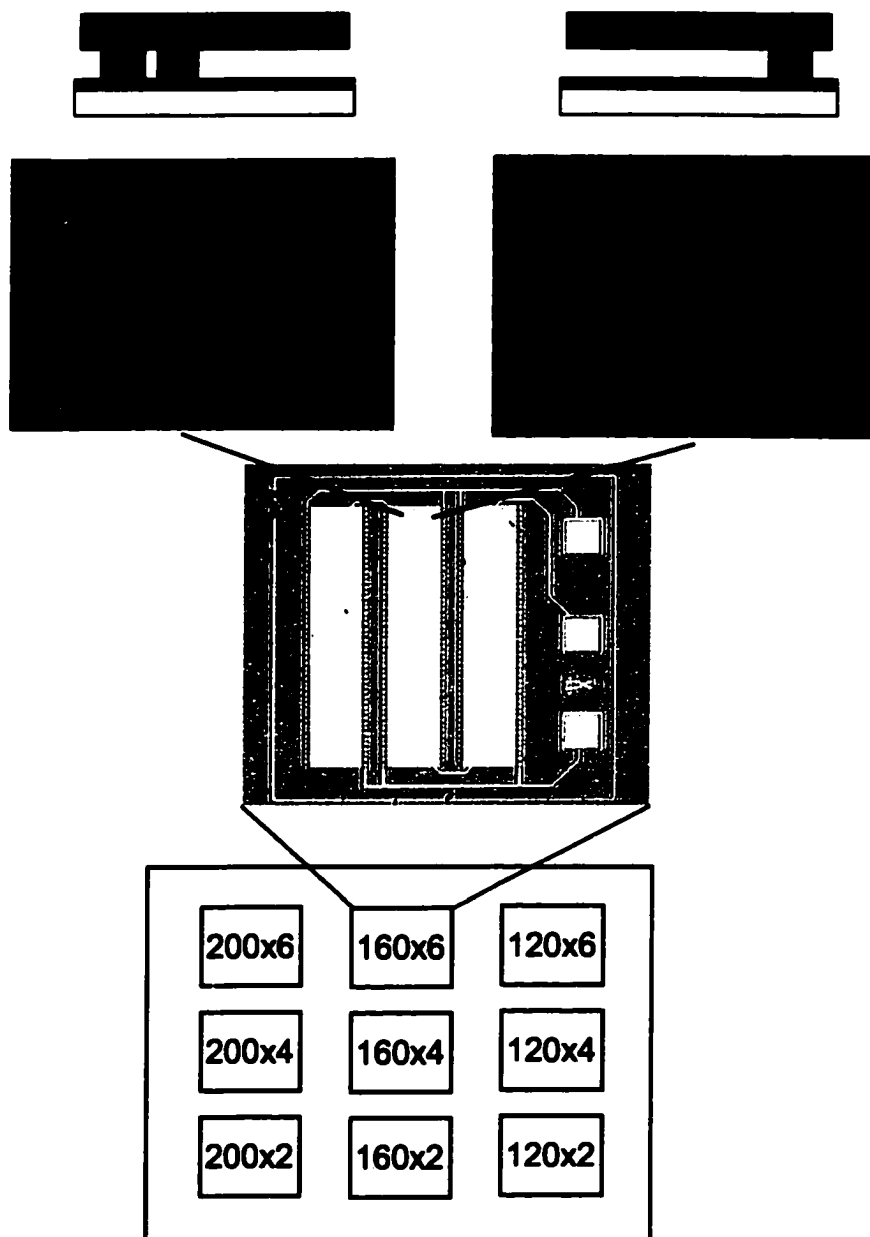


Figure 4.64: Schematic of GOB devices

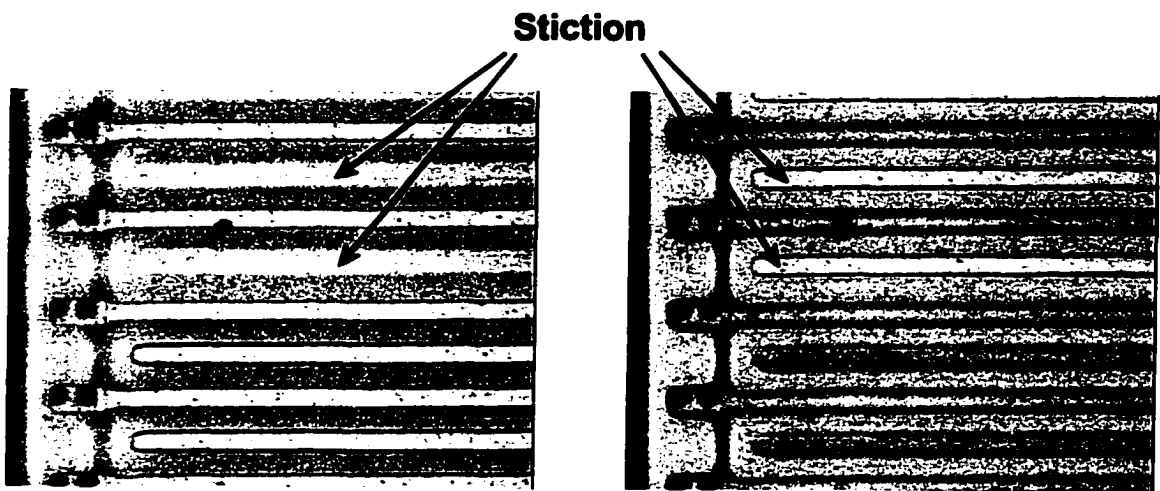


Figure 4.65: Optical microscopy stiction focal plane identification

The effects of various surface treatments on the stiction properties of GOB devices were investigated and are summarized in Table 4.16. As with any microstructure release procedure, the first step was the sacrificial layer etch. This was done with 49% HF. A DI water rinse after the sacrificial layer etch was done to pH neutrality to ensure that all HF was removed. Treatment I simply used HF etching solution to hydrogen-terminate the polysilicon microstructure surface. Treatment II was similar to I, except that an H₂O₂ oxidation step was inserted in order to produce surfaces with an oxide passivation instead of a hydrogen termination. Treatment III involved the formation of DMOAP coatings without curing. The deposition of the coating was done by immersing the sample in DMOAP dispersions at pH value of 4 and 35°C. The effect of reactive silane concentration and coating time on the extent of stiction was also investigated. The final rinse was done with methanol to displace any water under the beams and to reduce the surface tension at the liquid/solid interface. Additionally, the lower surface tension of methanol versus water decreases the collapse of structural layers as the solution dries. Finally, the samples were dried on a hot plate set up at 90°C.

The samples were kept horizontal in the liquid during the release and coating of the beams. Sample transfer, from one step to another, was done by keeping the sample wet at all times. This was done to avoid water draining from underneath the beams which could cause stiction.

Table 4.16: Sequence of processing steps used for release GOB devices

Step	Treatment		
	I (hydrophobic)	II (hydrophilic)	III (hydrophobic)
1	49% HF, 2.5 min	49% HF, 2.5 min	49% HF, 2.5 min
2	DI water rinse, 20 min	DI water rinse, 20 min	DI water rinse, 20 min
3	MeOH soak, 5 min	H ₂ O ₂ soak at 30°C, 20 min	H ₂ O ₂ soak at 30°C, 20 min
4	Dry on hot plate, 90°C	DI water rinse, 10 min	DI water rinse, 10 min
5		MeOH soak, 5 min	DMOAP coating formation
6		Dry on hot plate, 90°C	DI water rinse, 10 min
7			MeOH soak, 2 hours
8			Dry on hot plate, 90°C

The percentages of beams with stiction for each treatment shown in Figure 4.66(a) and (b) were calculated per column of each array and by the following equation:

$$\% \text{ stiction} = \frac{\text{number of beams adhered to the substrate}}{\text{total number of beams (=100)}} * 100 \quad (4.12)$$

Error bars in the same figures indicate the variability of stiction per column on each array.

Very high stiction values (~90%) were obtained on the hydrophilic samples (treatment II). Upon drying, the water meniscus was concave underneath the structure, creating a capillary force sufficiently strong to pull these surfaces into contact.

Alternatively, on HF- treated surfaces, low stiction (20-30%) was observed because the water meniscus had a convex curvature, thus lowering the attractive forces between the two surfaces. However, the adhesion reduction by hydrogen-terminated surfaces produced by HF is a temporary solution, because the surface quickly re-oxidizes in water and air.¹⁶⁴ Also, current packaging technologies require elevated temperatures (400-500°) that are too high for these surfaces to retain their hydrophobicity.

The next step was chemical modification of the surfaces with DMOAP coatings. The first set of experiments was carried out by exposing the samples for different periods of time to dispersions containing 0.1% reactive silane. Stiction was higher than for the HF-treated samples. This could be due to low silane coverage underneath the beams. The second attempt was to increase the silane concentration to 1% reactive silane. Samples exposed for 20 minutes showed lower stiction than samples treated with HF. This indicates that at optimized conditions silane-treated surfaces can have better anti-stiction properties than freshly HF treated surfaces. The high stiction values on samples coated for 60 minutes could be due to the formation of thick aggregate structures that affect the hydrophobic character of the coatings at those localized sites.

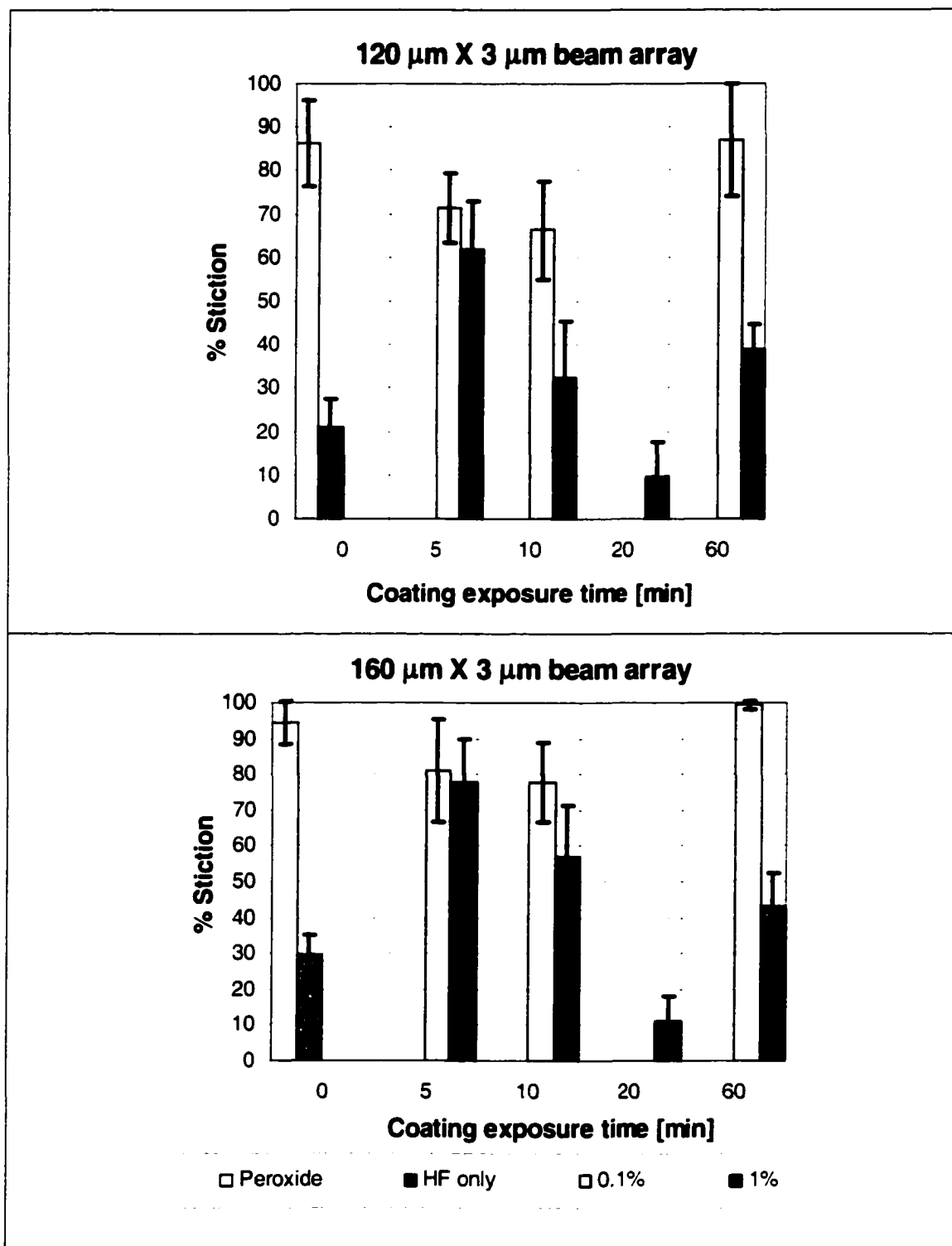


Figure 4.66: Effect of surface treatment on stiction

Optical microscopy images of uncoated and coated $120\ \mu\text{m} \times 3\ \mu\text{m}$ comb-like beam arrays are shown in Figure 4.67. The cantilever beam array in Figure 4.67(a) was released and oxidized using the standard hydrophilic process (treatment II). The array in Figure 4.67(b) was coated with a DMOAP dispersion containing 1% reactive silane for 20 minutes (treatment III). In Figure 4.67(a), most of the cantilever beams may be seen to be stuck to the substrate as a result of high capillary forces. In Figure 4.67(b), only one of the cantilever beams is stuck to the substrate.

The important conclusion that can be derived from these data is that silane-treated surfaces may be expected to exhibit varying anti-stiction behavior depending on the extent of coverage of molecules on the surface. Therefore, while contact angle may be sufficient to determine when surfaces are hydrophobic, a more quantitative study of coverage underneath the beams is required to produce coatings with good anti-stiction properties.

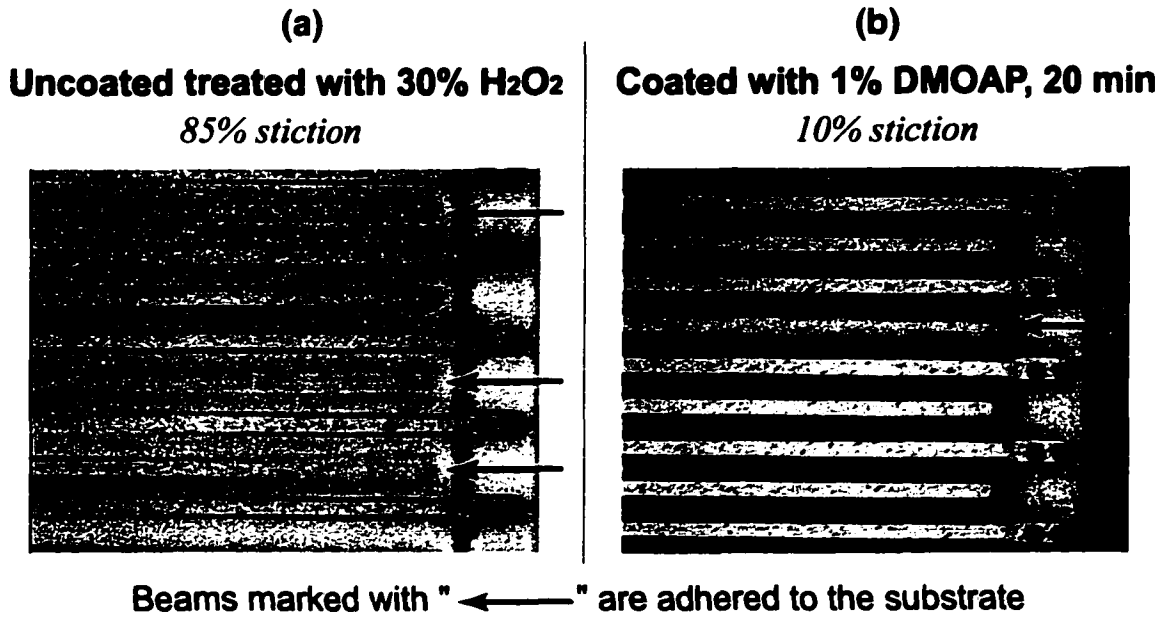


Figure 4.67: Stiction on 120 μm x 3 μm com-like beam arrays by different treatments

CHAPTER 5

CONCLUSIONS AND SUGGESTIONS FOR FUTURE RESEARCH

5.1 Conclusions

The following conclusions can be made from this study:

- Water dispersible silanes can be used to render pre-oxidized polysilicon highly hydrophobic
- Deposition temperature is a critical variable to obtain highly hydrophobic coatings from cationic alkoxy silane aqueous dispersions
- Curing of the coatings is an important step to improve the hydrophobicity of the coatings formed from Siliclad[®] and DMOAP dispersions.
- Siliclad[®] coatings have a high thermal stability.
- Addition of cationic surfactants, improves the stability of Siliclad[®] dispersions by retarding the formation of Si-O-Si linkages. The presence of surfactant is also beneficial in transporting the silane micelles to the surface due to their electrostatic attraction with the negatively charged surfaces. Suitable conditions can be found in which a cationic surfactant helps to stabilize the dispersion without being detrimental to the hydrophobicity of the coating.
- Cationic alkoxy silanes are very stable in aqueous media and the addition of a surfactant is not required.

- Ellipsometric analysis indicates that thickness of DMOAP and DIDAP coatings is roughly a (statistical) monolayer.
- Thickness of Siliclad[®] coatings increased with reactive silane concentration.
- Wettability data show that the hydrophobicity and methyl (CH₃) fraction of the coatings exposed to solutions can be improved by increasing Siliclad[®] concentration in the dispersions and by the deposition of a double coating such as DMOAP/Siliclad[®].
- AFM images show that the coatings deposited from dispersions containing low concentration of Siliclad[®] are thinner than the length of fully stretched alkyl chains in an octadecyl group. An increase in Siliclad[®] concentration increases the coating thickness, deposition and/or formation of particulates on the coating, as well as the contact angle. The DMOAP coatings consist of monolayers with small particulates and pores.
- Excess DMOAP can be removed by rinsing with acetic acid.
- EIS provides an effective method to determine the quality of the coatings by studying electron transfer reactions between a coated silicon surface and HF solutions. Analysis of the experimental results have shown that DMOAP and Siliclad[®] systems are capable of providing coatings with low porosity as well as high charge transfer resistance across the silicon/HF interface.
- Use of water-dispersible silanes can significantly reduce the use of organic solvents as well as the number of processing steps. The following table compares

a conventional SAM process using OTS with aqueous based processes developed in this research.

Table 5.1: Comparison of coating processes

	OTS <i>Organic Media</i>	SILICLAD® <i>Aqueous Media</i>	DMOAP <i>Aqueous Media</i>
A. Sacrificial Layer Etch		1. Dilute HF 2. H ₂ O rinse	
B. Surface Oxidation		3. H ₂ O ₂ soak 4. H ₂ O rinse	
C. Coating formation	5. IPA rinse 6. <i>Iso-octane</i> rinse 7. <u>OTS</u> solution in 4:1 <i>hexadecane</i> : <i>CCl₄</i> or <i>hexadecane</i> : <i>CHCl₃</i> 8. <i>Iso-octane</i> rinse	5. 3% <u>Modified octadecylsilane</u> dispersed in 1:1:8 <i>tertiary alcohol</i> : <i>diacetone alcohol</i> : <i>H₂O</i>	5. 0.01 % reactive silane at pH between 4 and 5 at 35°C (<i>Methanol:H₂O</i>)
D. Rinse and Dry	9. IPA rinse 10. H ₂ O rinse 11. Pull structures directly from water	6. H ₂ O rinse 7. Cure at 250°C	6. H ₂ O rinse 7. Cure at 250°C under dry nitrogen 8. Acetic acid rinse

- Preliminary studies on anti-stiction properties of DMOAP coatings, deposited onto comb-like beam arrays, have shown that adhesion of these beams to the substrate can be significantly reduced.

5.2 Suggestions for future research

For the future research, the following areas are suggested:

Anti-stiction coatings:

- Determine maximum length at which water dispersible silanes can eliminate stiction.
- Measure survivability of hydrophobic coatings to temperature, time, bias, contact and combinations of these conditions.

Wear resistant coatings:

- Develop the chemistries and techniques to deposit water-dispersible organosilane coatings onto wear resistant coatings, such as tungsten oxide deposited from a sol-gel process¹⁶⁵ or tungsten formed through WF_6 plasma at high temperatures.^{166,167}
- Investigate the effect of these duplex coatings on friction and wear on real MEMS devices that contain sliding and contacting surfaces.
- Measure the friction coefficient as a function of oscillatory cycles of the water-based silane coatings by using a sidewall tribometer developed by Sandia National Laboratories.¹⁶⁶
- Determine friction and wear properties of the organosilane coatings by using friction force microscopy (FFM).

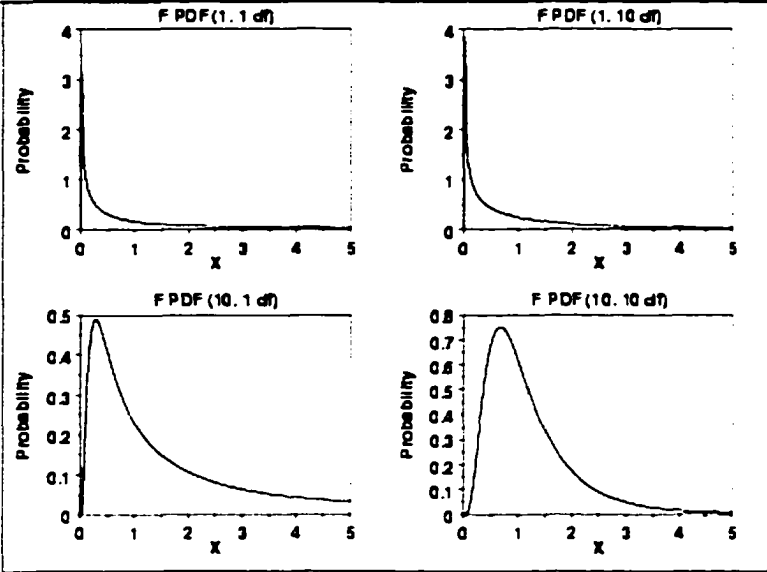
APPENDIX

GLOSSARY OF STATISTICAL TERMS

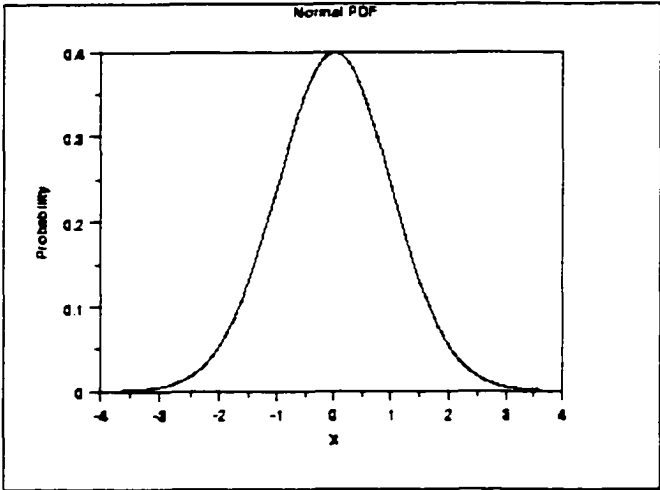
Actual value	The measured response data for a particular run.
Actual vs Predicted plot	A graph of the actual response values versus the predicted response values. It helps detect a value, or group of values, that are not easily predicted by the model.
Adequate precision	<p>This is a signal to noise ratio. It compares the range of the predicted values at the design point to the average prediction error. It is computed by dividing the difference between the maximum predicted response and the minimum predicted response by the average standard deviation of all predicted responses. Ratios greater than 4 indicate adequate model discrimination.</p> $\left[\frac{\max(y) - \min(y)}{\sqrt{\bar{V}(y)}} \right] > 4 \quad \text{where} \quad \bar{V}(y) = \frac{1}{n} \sum_{i=1}^n V(y) = \frac{p\sigma^2}{n},$ <p>p is the number of model parameters, σ^2 is the residual mean squares (MS) from ANOVA table and n is the number of experiments.</p>
Adjusted R ²	A measure of the amount of variation around the mean explained by the model, adjusted for the number of terms in the model. The adjusted R ² decreases as the number of terms in the model.

	$\text{Adj. } R^2 = 1 - \frac{\left(\frac{SS_{\text{residual}}}{DF_{\text{residual}}} \right)}{\left(\frac{SS_{\text{model}} + SS_{\text{residual}}}{DF_{\text{model}} + DF_{\text{residual}}} \right)}$
Analysis of Variance (ANOVA)	<ol style="list-style-type: none"> 1) A method based on the F-distribution, for testing the null hypothesis of no treatment effects. 2) A statistical technique which subdivides the total variation of a set of data into component parts associated with specific sources of variation for the purpose of testing a hypothesis on the parameters of a model.
Average effect of a factor	Is the change in response produced by a change in the level of the factor averaged over the levels of the other factor
Block	A group of trials based on a common factor
Box Cox plot	This plot provides a guideline for selecting the correct power law transformation. A recommended transformation is listed, based on the best lambda value, which is found at the minimum point of the curve generated by the natural log of the sum of squares of the residuals. If the 95% confidence interval around this lambda includes 1 then the software does not recommend a specific transformation.
Center Points	Experimental runs with all numerical factor levels set at the midpoint of their high and low settings. They are used to test curvature and, if replicated, as a test for lack of fit.

Cook's Distance plot	A measure of the effect each point has on the model. A point that has a very high distance value relative to the other points may be an outlier and should be investigated.
Degrees of freedom (DF)	The number of independent comparisons available to estimate a parameter. Usually the number of model parameters minus 1.
Effect	<p>The change in average response when a factor goes from its low level to its high level</p> $\text{estimated effect} = \bar{Y}(+) - \bar{Y}(-)$ <p>where $\bar{Y}(+)$ is the average of all response values for which the factor or interaction takes on its high level value and $\bar{Y}(-)$ is the average of all response values for which the factor or interaction takes on its low level value.</p>
F-distribution	<p>A probability distribution used in analysis of variance.</p> <p>If χ_u^2 and χ_v^2 are two independent chi-square random variables with u and v degrees of freedom, respectively, then the ratio</p> $F_{u,v} = \frac{\chi_u^2 / u}{\chi_v^2 / v}$ <p>follows the F distribution with u numerator degrees of freedom and v denominator degrees of freedom.</p> <p>The following is a plot of the F probability density function for 4 different values of the degrees of freedom.</p>

	
F-value	Large F-values indicate that the variance contributed by the model is significantly larger than the random error.
Factor	Independent variable to be manipulated in an experiment.
Half-normal probability plot	<p>This is a plot of the absolute value of the effects estimates against their cumulative normal probabilities. A straight line on the half-normal probability plot always passes through the origin and close to the fiftieth percentile data value.</p> <p>The outputs from the half-normal probability plot are:</p> <ol style="list-style-type: none"> 1. Primary: Grouping of factors and interactions into two categories: important and unimportant. For full factorial designs, interactions include the full complement of interactions of all orders; for fractional designs, interactions include only some, and occasionally none, of the actual interactions.

	2. Secondary: Ranked list of factors and interactions from most important down to least important.
Leverage plot	A measure of how each point influences the model fit. If a point has a leverage of 1, then the model must go through that point. That point controls the model. Leverages near one should be reduced by adding or replicating points.
Mean	<p>The mean of a probability distribution $f(y_i)$ is a measure of its central tendency or location. The mean or expected value of the discrete random variable y is:</p> $\mu = \sum_{i=1}^n y_i f(y_i)$ <p>The mean of "a" treatments or different levels of a single factor with "n" observations is:</p> $\mu = \frac{\sum_{i=1}^a \mu_i}{a}$
Mean Squares (MS)	$MS = \frac{SS}{a-1}$
Model	Is the empirical mathematical model that is fit to the data.
Normal distribution	<p>A random variable y with probability function $f(y) = \frac{1}{\sqrt{2\pi}\sigma} e^{-\frac{(y-\mu)^2}{2\sigma^2}}$ for $-\infty < y < \infty$ has a normal distribution; where μ is the mean of the</p>

	<p>distribution and σ^2 is the variance.</p> <p>The following is the plot of the standard normal distribution density function.</p> 
Normal probability	<p>The normal probability plot indicates whether the residuals follow a normal distribution, in which case the points will follow a straight line. An "S-shaped" curve indicates that a transformation of the response would provide a better analysis.</p>
Predicted R^2	<p>The predicted R^2 indicates how much the full model is expected to explain new data.</p> $\text{Pred. } R^2 = 1 - \frac{\text{PRESS}}{SS_{\text{total}} - SS_{\text{block}}}$
Predicted value	<p>The value predicted from the model, generated by using the prediction equation. Includes block and center point corrections, if present.</p>
Prediction error sum of squares (PRESS)	<p>The prediction error sum of squares (PRESS) statistic measures how well the model is likely to predict the responses in a new experiment. A</p>

	model with small value of PRESS indicates that the model is likely to be a good predictor.
R^2	<p>A measure of the amount of variation around the mean explained by the model</p> $R^2 = 1 - \frac{SS_{\text{residual}}}{SS_{\text{model}} + SS_{\text{residual}}}$
Replicate	An experimental run done again from start to finish. More replicates provide better estimates of error.
Residual	Difference between Actual and Predicted values for each point.
Residuals vs Factor plot	This is a plot of the residuals versus any factor. It checks whether the variance not accounted for by the model is different for different levels of a factor. If all is okay, the plot should exhibit a random scatter. Pronounced curvature may indicate a systematic contribution of the independent factor that is not accounted for by the model.
Residuals vs Predicted plot	This is a plot of the residuals versus the ascending predicted response values. It tests the assumption of constant variance. The plot should be a random scatter (constant range of residuals across the graph). Expanding variance in this plot indicates the need for a transformation.
Residuals vs Run plot	This is a plot of the residuals versus the experimental run order. It checks for lurking variables that may have influenced the response during the experiment. The plot should show a random scatter. Trends indicate a time-related variable lurking in the background. Blocking

	and randomization provide insurance against trends ruining the analysis.
Response	A measurable product or process characteristic to be affected by the experimental factors.
Sum of Squares (SS)	<p>The sum of squares of observations y_i is:</p> $SS = \sum_{i=1}^n (y_i - \bar{y})^2 \quad \text{where} \quad \bar{y} = \frac{\sum_{i=1}^n y_i}{n}$ <p>The sum of squares of "a" treatments or different levels of a single factor with "n" observations is:</p> $SS = \sum_{i=1}^a \sum_{j=1}^n (y_{ij} - \bar{y}_{..})^2 \quad \text{where} \quad \bar{y}_{..} = \frac{\sum_{i=1}^a \sum_{j=1}^n y_{ij}}{N}$
Variance (V)	<p>The variance of "y", denoted as σ^2 or V is</p> $\sigma^2 = V(y) = \sum_{i=1}^n (y_i - \mu)^2 f(y_i)$ <p>where μ is the mean and $f(y_i)$ is the probability function of y.</p>

REFERENCES

1. R. Maboudian, W. R. Ashurst and C. Carraro, "*Self-assembled monolayers as anti-stiction coatings for MEMS: characteristics and recent developments*", Sensors and Actuators, 82 219, (2000)
2. U. Srinivasan, M. R. Houston, R. T. Howe and R. Maboudian, "*Alkyltrichlorosilane-based self-assembled monolayer films for stiction reduction in silicon micromachines*", Journal of Microelectromechanical Systems, 7 (2), 252, (1998)
3. M. R. Houston, R. Maboudian and R. T. Howe, "*Self-assembled monolayer films as durable anti-stiction coatings for polysilicon microstructures*", in *Solid State Sensor and Actuator Workshop* p. 42, Hilton Head, South Carolina (1996)
4. T. Abe, W. C. Messner and M. L. Reed, "*Effects of Elevated-Temperature Treatments in Microstructure Release Procedures*", Journal of Microelectromechanical Systems, 4 (2), 66, (1995)
5. G. Mulhem, D. S. Soane and R. T. Howe, "*Supercritical carbon dioxide drying of microstructures*", in The 7th International Conference on Solid-State Sensors and Actuators, p. 296, Yokohama, Japan (1993)
6. C. W. Dyck, J. H. Smith, S. L. Miller, E. M. Russick and C. L. J. Adkins, "*Supercritical carbon dioxide solvent extraction from surface-micromachined micromechanical structures*", in Proceedings of the SPIE-International Society of Optical Engineering, p. 225, (1996)
7. A. Ulman, "*Formation and structure of self-assembled monolayers*", Chemical Reviews, 96 (4), 1533, (1996)
8. J. D. Legrange, J. L. Markham and C. R. Kurkjian, "*Effects of Surface Hydration on the Deposition of Silane Monolayers on Silica*", Langmuir, 9 (7), 1749, (1993)
9. C. P. Tripp and M. L. Hair, "*An Infrared Study of the Reaction of Octadecyltrichlorosilane with Silica*", Langmuir, 8 (4), 1120, (1992)
10. D. L. Angst and G. W. Simmons, "*Moisture Absorption Characteristics of Organosiloxane Self-Assembled Monolayers*", Langmuir, 7 (10), 2236, (1991)
11. S. Brandriss and S. Margel, "*Synthesis and Characterization of Self-Assembled Hydrophobic Monolayer Coatings on Silica Colloids*", Langmuir, 9 (5), 1232, (1993)

12. A. N. Parikh, D. L. Allara, I. B. Azouz and F. Rondelez, "An Intrinsic Relationship between Molecular-Structure in Self- Assembled N-Alkylsiloxane Monolayers and Deposition Temperature", Journal of Physical Chemistry, 98 (31), 7577, (1994)
13. R. Maboudian and R. T. Howe, "Stiction reduction processes for surface micromachines", Tribology Letters, 3 215, (1997)
14. R. L. Alley, G. J. Cuan, R. T. Howe and K. Komvopoulos, "The effect of release-etch processing on surface microstructure stiction", IEEE Solid-State Sensor and Actuators Workshop, 202, (1992)
15. N. Tas, T. Sonnenberg, H. Jansen, R. Legtenberg and M. Elwenspoek, "Stiction in surface micromachining". Journal of Micromechanics and Microengineering, 6 (4), 385, (1996)
16. S. T. Walsh, R. Boylan and S. F. Bart, "Overcoming stiction in MEMS manufacturing", Micro, 13 (3), 49, (1995)
17. B. P. Gogoi and C. H. Mastrangelo, "Post-processing release of microstructures by electromagnetic pulses", in The 8th International Conference on Solid State Sensors and Actuators, p. 214, Sweden (1995)
18. Y. Matsumoto, T. Shimada and M. Ishida, "Novel prevention method of stiction using silicon anodization for SOI structure". Sensors and Actuators A-Physical, 72 (2), 153, (1999)
19. K. Komvopoulos, "Surface engineering and microtribology for microelectromechanical systems", Wear, 200 (1-2), 305, (1996)
20. R. Legtenberg, H. A. C. Tilmans, J. Elders and M. Elwenspoek, "Stiction of Surface Micromachined Structures after Rinsing and Drying - Model and Investigation of Adhesion Mechanisms", Sensors and Actuators A-Physical, 43 (1-3), 230, (1994)
21. J. N. Israelachvili, *Intermolecular and surface forces*, (2nd ed.), pp. 480, Academic Press London, London, (1991)
22. R. Maboudian and R. T. Howe, "Critical review: Adhesion in surface micromechanical structures", Journal of Vacuum Science & Technology B, 15 (1), 1, (1997)
23. R. L. Alley, P. Mai and K. Komvopoulos, "Surface roughness modification of interfacial contact in polysilicon microstructures", in 7th International

- Conference in Solid-State Sensors and Actuators - Transducers '93, p. 288, Yokohama, Japan (1993)
24. Y. Yee, K. Chun, J. D. Lee and C. J. Kim. "*Polysilicon surface modification technique to reduce sticking of microstructures*", in The 8th International Conference on Solid State Sensors and Actuators and Eurosensors IX, p. 206. (June 25-29 1995)
 25. G. Fedder and R. T. Howe. "*Thermal assembly of polysilicon microstructures*", in Proceedings of the 4th IEEE Micro-Electromechanical Systems Workshop (MEMS 91), p. 57, Nara, Japan (1991)
 26. J. Anguita and F. Briones. "*HF/H₂O vapor etching of SiO₂ sacrificial layer for large-area surface-micromachined membranes*", Sensors and Actuators A-Physical, 64 (3), 247, (1998)
 27. A. ben-Hamida, J. O'Dwyer, R. Hanestad and I. Gelmi, "*Anhydrous HF etching for stiction-free MEMS process*", R&D Magazine, 5 (6), (June 2000)
 28. Y. I. Lee, K. H. Park, J. Lee, C. Lee, H. Yoo, C. Kim and Y. Yoon, "*Dry Release for Surface Micromachining with HF Vapor-Phase Etching*", Journal of Microelectromechanical Systems, 6 (3), 226, (1997)
 29. P. R. Scheeper, J. A. Voorthuyzen, W. Olthuis and P. Bergveld, "*Investigation of Attractive Forces between Pecvd Silicon- Nitride Microstructures and an Oxidized Silicon Substrate*", Sensors and Actuators A-Physical, 30 (3), 231, (1992)
 30. R. Maboudian, "*Adhesion and friction issues associated with reliable operation of MEMS*", Materials Research Society Bulletin, (6), 47, (1998)
 31. R. Maboudian, W. R. Ashurst and C. Carraro, "*Tribological challenges in micromechanical systems*", Tribology Letters, 12 (2), 95, (2002)
 32. W. R. Ashurst, C. Yau, C. Carraro, R. Maboudian and M. T. Dugger, "*Dichlorodimethylsilane as an anti-stiction monolayer for MEMS: A comparison to the octadecyltrichlorosilane self-assembled monolayer*", Journal of Microelectromechanical Systems, 10 (1), 41, (2001)
 33. U. Srinivasan, M. R. Houston, R. T. Howe and R. Maboudian, "*Self-assembled fluorocarbon films for enhanced stiction reduction*", in Transducers 97, International Conference in Solid-State Sensors and Actuators, p. 1399, (1997)

34. W. R. Ashurst, C. Yau, C. Carraro, C. Lee, G. J. Kluth, R. T. Howe and R. Maboudian, "*Alkene based monolayer films as anti-stiction coatings for polysilicon MEMS*", Sensors and Actuators, A: Physical, A91 (3), 239, (2001)
35. M. P. De Boer, P. J. Clews, B. K. Smith and T. A. Michalske, "*Adhesion of polysilicon microbeams in controlled humidity ambients*", Materials Research Society Symposium Proceedings, 518 (Microelectromechanical Structures for Materials Research), 131, (1998)
36. M. R. Houston, R. Maboudian and R. T. Howe, "*Ammonium fluoride anti-stiction treatments for polysilicon microstructures*", in The 8th International Conference on Solid State Sensors and Actuators and Eurosensors IX, p. 210, (1995)
37. R. C. Stoupe, US, 5,662,771 (1994)
38. C. H. Mastrangelo and G. S. Saloka, "*A dry release based on polymer columns for microstructure fabrication*", in Micro-Electromechanical Systems Workshop, p. 77, Ft. Lauderdale, FL, USA (1993)
39. P. F. Man, B. P. Gogoi and C. H. Mastrangelo, "*Elimination of post-release adhesion in microstructures using conformal fluorocarbon coatings*", Journal of Microelectromechanical Systems, 6 (1), 25, (1997)
40. F. Schreiber, "*Structure and growth of self-assembling monolayers*", Progress in Surface Science, 65 151, (2000)
41. S. I. Stupp, S. Son, L. S. Li, H. C. Lin and M. Keser, "*Bulk Synthesis of 2-Dimensional Polymers - the Molecular Recognition Approach*", Journal of the American Chemical Society, 117 (19), 5212, (1995)
42. P. C. Hiemenz and R. Rajagopalan, *Principles of colloid and surface chemistry*, (3rd ed., rev. and expanded.), pp. 650, Marcel Dekker, New York, (1997)
43. D. F. Evans and H. Wennerstrom, *The colloidal domain : where physics, chemistry, biology, and technology meet*, (2nd ed.), pp. 632, Wiley-VCH., New York ; Chichester [England] :, (1999)
44. M. M. Lipp, K. Y. C. Lee, D. Y. Takamoto, J. A. Zasadzinski and A. J. Waring, "*Coexistence of buckled and flat monolayers*", Physical Review Letters, 81 (8), 1650, (1998)
45. K. S. Birdi and D. T. Vu, "*Structures of Collapsed Lipid Monolayers Investigated as Langmuir-Blodgett-Films by Atomic-Force Microscopy*", Langmuir, 10 (3), 623, (1994)

46. S. Siegel, D. Honig, D. Vollhardt and D. Mobius, "*Direct Observation of 3-Dimensional Transformation of Insoluble Monolayers*", Journal of Physical Chemistry, 96 (20), 8157, (1992)
47. H. E. Ries and H. Swift, "*Twisted Double-Layer Ribbons and the Mechanism for Monolayer Collapse*", Langmuir, 3 (5), 853, (1987)
48. K. Kojio, A. Takahara and T. Kajiyama, "*Formation mechanism of n-octadecyltrichlorosilane monolayer prepared at the air/water interface*". Colloids and Surfaces A-Physicochemical and Engineering Aspects, 169 (1-3), 295, (2000)
49. H. Hoffmann, U. Mayer and A. Krischanitz, "*Structure of Alkylsiloxane Monolayers on Silicon Surfaces Investigated by External Reflection Infrared-Spectroscopy*", Langmuir, 11 (4), 1304, (1995)
50. D. L. Allara, A. N. Parikh and F. Rondelez, "*Evidence for a Unique Chain Organization in Long-Chain Silane Monolayers Deposited on 2 Widely Different Solid Substrates*", Langmuir, 11 (7), 2357, (1995)
51. H. O. Finklea, L. R. Robinson, A. Blackburn, B. Richter, D. Allara and T. Bright, "*Formation of an organized monolayer by solution adsorption of octadecyltrichlorosilane on gold: electrochemical properties and structural characterization*", Langmuir, 2 (2), 239, (1986)
52. J. Sagiv, "*Organized Monolayers by Adsorption .I. Formation and Structure of Oleophobic Mixed Monolayers on Solid-Surfaces*", Journal of the American Chemical Society, 102 (1), 92, (1980)
53. S. Semal, M. Voue, M. J. De Ruijter, J. Dehuit and J. De Coninck, "*Dynamics of Spontaneous Spreading on Heterogeneous Surfaces in a Partial Wetting Regime*", Journal of Physical Chemistry B, 103 (23), 4854, (1999)
54. T. Vallant, H. Brunner, U. Mayer, H. Hoffmann, T. Leitner, R. Resch and G. Friedbacher, "*Formation of Self-Assembled Octadecylsiloxane Monolayers on Mica and Silicon Surfaces Studied by Atomic Force Microscopy and Infrared Spectroscopy*", Journal of Physical Chemistry B, 102 (37), 7190, (1998)
55. N. B. Sheller, S. Petrash, M. D. Foster and V. V. Tsukruk. "*Atomic force microscopy and X-ray reflectivity studies of albumin adsorbed onto self-assembled monolayers of hexadecyltrichlorosilane*", Langmuir, 14 (16), 4535, (1998)
56. C. Carraro, O. W. Yauw, M. M. Sung and R. Maboudian, "*Observation of three growth mechanisms in self-assembled monolayers*", Journal of Physical Chemistry B, 102 (23), 4441, (1998)

57. S. Gauthier, J. P. Aime, T. Bouhacina, A. J. Attias and B. Desbat, "*Study of grafted silane molecules on silica surface with an atomic force microscope*", Langmuir, 12 (21), 5126, (1996)
58. S. R. Ge, A. Takahara and T. Kajiyama, "*Phase-Separated Morphology of an Immobilized Organosilane Monolayer Studied by a Scanning Probe Microscope*", Langmuir, 11 (4), 1341, (1995)
59. J. B. Brzoska, I. Benazouz and F. Rondelez, "*Silanization of Solid Substrates - a Step toward Reproducibility*", Langmuir, 10 (11), 4367, (1994)
60. J. B. Brzoska, N. Shahidzadeh and F. Rondelez, "*Evidence of a Transition-Temperature for the Optimum Deposition of Grafted Monolayer Coatings*", Nature, 360 (6406), 719, (1992)
61. M. Goldmann, J. V. Davidovits and P. Silberzan, "*Kinetics of self-assembled silane monolayers at various temperatures: evidence of 2D foam*", Thin Solid Films, 327-329 166, (1998)
62. D. K. Schwartz, S. Steinberg, J. Israelachvili and J. A. N. Zasadzinski, "*Growth of a Self-Assembled Monolayer by Fractal Aggregation*", Physical Review Letters, 69 (23), 3354, (1992)
63. K. i. Iimura, Y. Nakajima and T. Kato, "*A study on structures and formation mechanisms of self-assembled monolayers of n-alkyltrichlorosilanes using infrared spectroscopy and atomic force microscopy*", Thin Solid Films, 379 (1.2), 230, (2000)
64. R. R. Rye, "*Transition Temperatures for n-Alkyltrichlorosilane Monolayers*", Langmuir, 13 (9), 2588, (1997)
65. B. M. J. Kellner, F. Muller-Landau and D. A. Cadenhead, "*Temperature-dependence characterization of insoluble films at air-water interface*", Journal of Colloid and Interface Science, 66 (3), 597, (1978)
66. L. V. Protsailo and W. R. Fawcett, "*Studies of electron transfer through self-assembled monolayers using impedance spectroscopy*", Electrochimica Acta, 45 (21), 3497, (2000)
67. P. Diao, D. L. Jiang, X. L. Cui, D. P. Gu, R. T. Tong and B. Zhong, "*Studies of structural disorder of self-assembled thiol monolayers on gold by cyclic voltammetry and ac impedance*", Journal of Electroanalytical Chemistry, 464 (1), 61, (1999)

68. H. O. Finklea, S. Avery, M. Lynch and T. Furtch, "*Blocking Oriented Monolayers of Alkyl Mercaptans on Gold Electrodes*", Langmuir, 3 (3), 409, (1987)
69. C. Boulas, J. V. Davidovits, F. Rondelez and D. Vuillaume, "*Suppression of charge carrier tunneling through organic self- assembled monolayers*", Physical Review Letters, 76 (25), 4797, (1996)
70. V. Bertagna, R. Erre, F. Rouelle and M. Chemla, "*Ionic components dependence of the charge transfer reactions at the silicon/HF solution interface*", Journal of Solid State Electrochemistry, 4 (1), 42, (1999)
71. V. Bertagna, C. Plougonven, F. Rouelle and M. Chemla. "*Kinetics of electrochemical corrosion of silicon wafers in dilute HF solutions*", Journal of Electroanalytical Chemistry, 422 (1-2), 115, (1997)
72. E. P. Plueddemann, *Silane coupling agents*, (2nd), pp. 253, Plenum Press, New York, (1991)
73. B. Arkles, J. R. Steinmetz, J. Zazyczny and P. Mehta. "*Factors contributing to the stability of alkoxy silanes in aqueous solution*", Journal of Adhesion Science and Technology, 6 (1), 193, (1992)
74. C. J. Brinker and G. W. Scherer, *Sol-gel science : the physics and chemistry of sol-gel processing*, pp. 908, Academic Press, Inc., New York, (1990)
75. B. Arkles, "*Tailoring Surfaces with Silanes*", Chemtech, 7 (12), 766, (1977)
76. E. R. Pohl and F. D. Osterholtz, "*Kinetics and mechanism of aqueous hydrolysis and condensation of alkytrialkoxysilanes*", Polymer Science and Technology, 27 157, (1985)
77. R. C. Chambers, W. E. Jones, Y. Haruvy, S. E. Webber and M. A. Fox, "*Influence of Steric Effects on the Kinetics of Ethyltrimethoxysilane Hydrolysis in a Fast Sol-Gel System*", Chemistry of Materials, 5 (10), 1481, (1993)
78. J. M. Zeigler and F. W. G. Fearon, *Silicon-based polymer science : a comprehensive resource*, pp. 801, American Chemical Society., Washington, DC, (1990)
79. L. W. Kelts, N. J. Effinger and S. M. Melpolder, "*Sol-Gel Chemistry Studied by H-1 and Si-29 Nuclear-Magnetic- Resonance*", Journal of Non-Crystalline Solids, 83 (3), 353, (1986)

80. R. K. Iler, *The chemistry of silica : solubility, polymerization, colloid and surface properties, and biochemistry*, pp. 866, Wiley., New York, (1979)
81. E. J. A. Pope and J. D. Mackenzie, "Sol-gel processing of silica II. The role of the catalyst." Journal of Non-Crystalline Solids, 87 185, (1986)
82. F. D. Osterholtz and E. R. Pohl, "Kinetics of the hydrolysis and condensation of organofunctional alkoxy silanes: a review", Journal of Adhesion Science and Technology, 6 (1), 127, (1992)
83. P. Silberzan, L. Leger, D. Ausserre and J. J. Benattar, "Silanation of Silica Surfaces - a New Method of Constructing Pure or Mixed Monolayers". Langmuir, 7 (8), 1647, (1991)
84. C. P. Tripp and M. L. Hair, "Reaction of Methylsilanols with Hydrated Silica Surfaces - the Hydrolysis of Trichloromethylsilanes, Dichloromethylsilanes, and Monochloromethylsilanes and the Effects of Curing", Langmuir, 11 (1), 149, (1995)
85. G. A. Carson and S. Granick, "Self-Assembly of Octadecyltrichlorosilane Monolayers on Mica", Journal of Materials Research, 5 (8), 1745, (1990)
86. G. S. Caravajal, D. E. Leyden, G. R. Quinting and G. E. Maciel, "Structural Characterization of (3-Aminopropyl)Triethoxysilane- Modified Silicas by Si-29 and C-13 Nuclear Magnetic-Resonance", Analytical Chemistry, 60 (17), 1776, (1988)
87. P. VanDerVoort and E. F. Vansant, "Silylation of the silica surface a review", Journal of Liquid Chromatography & Related Technologies, 19 (17-18), 2723, (1996)
88. C. P. Tripp and M. L. Hair, "Reaction of Alkylchlorosilanes with Silica at the Solid Gas and Solid Liquid Interface", Langmuir, 8 (8), 1961, (1992)
89. A. Y. Fadeev and T. J. McCarthy, "Self-Assembly Is Not the Only Reaction Possible between Alkyltrichlorosilanes and Surfaces: Monomolecular and Oligomeric Covalently Attached Layers of Dichloro- and Trichloroalkylsilanes on Silicon", Langmuir, 16 (18), 7268, (2000)
90. A. M. Almanza-Workman, S. Raghavan, S. Petrovic, B. Gogoi, P. Deymier, D. J. Monk and R. Roop, "Characterization of highly hydrophobic coatings deposited onto preoxidized silicon from water dispersible organosilanes", Thin Solid Films, 423 (1), 63, (2002)

91. D. W. Britt and V. Hlady, "An AFM study of the effects of silanization temperature, hydration, and annealing on the nucleation and aggregation of condensed OTS domains on mica", Journal of Colloid and Interface Science, 178 (2), 775, (1996)
92. J. R. Malek and J. L. Speier, "Development of an Organosilicone Antimicrobial Agent for the Treatment of Surfaces", Journal of Coated Fabrics, 12 (1), 38, (1982)
93. M. A. Markowitz, G. Deng, M. C. Burleigh, E. M. Wong and B. P. Gaber, "Influence of Quaternary Amine Organosilane Structure on the Formation and Adsorption Properties of Surface-Imprinted Silicates". Langmuir, 17 (22), 7085, (2001)
94. T. Moses, "Interfacial ordering in a liquid crystal near the nematic-isotropic transition", Molecular Crystals and Liquid Crystals Science and Technology Section A- Molecular Crystals and Liquid Crystals, 319 121, (1998)
95. W. Chen, L. J. Martinez-Miranda, H. Hsiung and Y. R. Shen, "Orientational wetting behavior of a liquid-crystal homologous series", Physical Review Letters, 62 (16), 1860, (1989)
96. F. J. Kahn, "Orientation of liquid crystals by surface coupling agents", Applied Physics Letters, 22 (8), 386, (1973)
97. H. B. Klevens, "Critical micelle concentrations as determined by refraction", Journal of Physical and Colloid Chemistry, 52 130, (1948)
98. S. P. Moulik, M. E. Haque, P. K. Jana and A. R. Das, "Micellar Properties of Cationic Surfactants in Pure and Mixed States", Journal of Physical Chemistry, 100 (2), 701, (1996)
99. T. W. Davey, W. A. Ducker, A. R. Hayman and J. Simpson, "Krafft temperature depression in quaternary ammonium bromide surfactants", Langmuir, 14 (12), 3210, (1998)
100. R. L. Venable and R. V. Nauman, "Micellar weights of and solubilization of benzene by a series of tetradecylammonium bromides. The effect of the size of the charged head", Journal of Physical Chemistry, 68 (12), 3498, (1964)
101. R. G. Alargova, I. I. Kochijashky, M. L. Sierra and R. Zana, "Micelle Aggregation Numbers of Surfactants in Aqueous Solutions: A Comparison between the Results from Steady-State and Time-Resolved Fluorescence Quenching", Langmuir, 14 (19), 5412, (1998)

102. M. Czerniawski, "The double layer structure of colloidal electrolytes. III. Electrolytic conductivity of aqueous cetyltrimethylammonium bromide solutions", Roczniki Chemii, 40 (11/12), 1935, (1966)
103. P. Dynarowicz, W. Jawien, J. M. Trillo, N. V. Romeu and O. C. Mouzo, "Surface-Properties of Didodecyldimethylammonium Bromide Adsorbed and Spread at the Water/Air Interface", Journal of Colloid and Interface Science, 174 (2), 518, (1995)
104. A. M. Feltham and M. Spiro, "Platinized platinum electrodes", Chemical Reviews, 71 (2), 177, (1971)
105. P. J. Scales, F. Grieser, T. W. Healy, L. R. White and D. Y. C. Chan, "Electrokinetics of the silica-solution interface: a flat plate streaming potential study", Langmuir, 8 (3), 965, (1992)
106. R. A. Van Wagenen and J. D. Andrade, "Flat plate streaming potential investigations: hydrodynamics and electrokinetic equivalency", Journal of Colloid and Interface Science, 76 (2), 305, (1980)
107. H. J. Jacobasch and J. Schurz, "Characterization of polymer surfaces by means of electrokinetic measurements", Progress in Colloid and Polymer Science, 77 (Dispersed Syst.), 40, (1988)
108. S. Manne, "Visualizing self-assembly. Force microscopy of ionic surfactant aggregates at solid-liquid interfaces", Progress in Colloid and Polymer Science, 103 (Amphiphiles at Interfaces), 226, (1997)
109. S. Manne and H. E. Gaub, "Molecular-Organization of Surfactants at Solid-Liquid Interfaces", Science, 270 (5241), 1480, (1995)
110. M. Wright and I. Revenko, "Tapping Mode Atomic Force Microscopy Operation in Fluid", Application Note, Digital Instruments, (AN49), www.veeco.com/appnotes/AN49_FluidTapping.pdf,
111. D. E. Leyden, R. S. S. Murthy, J. B. Atwater and J. P. Blitz, "Studies of alkoxysilane hydrolysis and condensation by Fourier-transform infrared spectroscopy with a cylindrical internal-reflection cell", Analytica Chimica Acta, 200 (1), 459, (1987)
112. M. I. Tejedor-Tejedor, L. Paredes and M. A. Anderson, "Evaluation of ATR-FTIR Spectroscopy as an "in Situ" Tool for Following the Hydrolysis and Condensation of Alkoxysilanes under Rich H₂O Conditions", Chemistry of Materials, 10 (11), 3410, (1998)

113. D. E. Leyden and J. B. Atwater, "*Hydrolysis and condensation of alkoxysilanes investigated by internal reflection FTIR spectroscopy*", Journal of Adhesion Science and Technology, 5 (10), 815, (1991)
114. N. J. Harrick, *Internal Reflection Spectroscopy*, (2nd edition), Harrick Scientific Corp., New York, (1979)
115. J. S. Jeon, R. P. Sperline, S. Raghavan and J. B. Hiskey, "*In situ analysis of alkyl phosphate surfactant adsorption at the alumina/aqueous solution interface*", Colloids and Surfaces A-Physicochemical and Engineering Aspects, 111 (1-2), 29, (1996)
116. P. K. Singh, J. J. Adler, Y. I. Rabinovich and B. M. Moudgil, "*Investigation of self-assembled surfactant structures at the solid-liquid interface using FT-IR/ATR*", Langmuir, 17 (2), 468, (2001)
117. J. D. Miller and J. J. Kellar, "*Quantitative in-situ analysis of Collector adsorption reactions by FTIR internal reflection spectroscopy*", in Proceedings of Challenges in Mineral Processing, p. 109, Berkeley, CA (1989)
118. C. Raghunath, "*Fundamental aspects of particulate contamination of Tungsten and thermal oxide wafers during Chemical-Mechanical Polishing*", Ph.D. Dissertation, University of Arizona, (1997)
119. Y. Duval, J. A. Mielczarski, O. S. Pokrovsky, E. Mielczarski and J. J. Ehrhardt, "*Evidence of the Existence of Three Types of Species at the Quartz-Aqueous Solution Interface at pH 0-10: XPS Surface Group Quantification and Surface Complexation Modeling*", Journal of Physical Chemistry B, 106 (11), 2937, (2002)
120. N. Sahai and D. A. Sverjensky, "*Evaluation of internally consistent parameters for the triple-layer model by the systematic analysis of oxide surface titration data*", Geochimica Et Cosmochimica Acta, 61 (14), 2801, (1997)
121. E. J. A. Pope and J. D. Mackenzie, "*Sol-gel processing of silica. II. The role of the catalyst*", Journal of Non-Crystalline Solids, 87 (1-2), 185, (1986)
122. S. Ge, A. Takahara and T. Kajiyama, "*Aggregation Structure and Surface-Properties of Immobilized Organosilane Monolayers Prepared by the Upward Drawing Method*", Journal of Vacuum Science & Technology a-Vacuum Surfaces and Films, 12 (4), 2530, (1994)
123. R. N. Wenzel, "*Resistance of Solid Surfaces to Wetting of water*", Industrial and Engineering Chemistry, 28 988, (1936)

124. J. N. Chazalviel, "Surface methoxylation as the key factor for the good performance of n-silicon/methanol photoelectrochemical cells", Journal of Electroanalytical Chemistry and Interfacial Electrochemistry, 233 (1-2), 37, (1987)
125. N. Y. Kim and P. E. Laibinis, "Thermal Derivatization of Porous Silicon with Alcohols", Journal of the American Chemical Society, 119 (9), 2297, (1997)
126. J. E. Bateman, B. R. Horrocks and A. Houlton, "Reactions of water and methanol at hydrogen-terminated silicon surfaces studied by transmission FTIR", Journal of the Chemical Society-Faraday Transactions, 93 (14), 2427, (1997)
127. G. Cleland, B. R. Horrocks and A. Houlton, "Direct functionalization of silicon via the self-assembly of alcohols", Journal of the Chemical Society-Faraday Transactions, 91 (21), 4001, (1995)
128. R. P. Sperline, "Infrared spectroscopic study of the crystalline phases of sodium dodecyl sulfate", Langmuir, 13 (14), 3715, (1997)
129. R. G. Nuzzo, L. H. Dubois and D. L. Allara, "Fundamental-Studies of Microscopic Wetting on Organic-Surfaces .1. Formation and Structural Characterization of a Self- Consistent Series of Polyfunctional Organic Monolayers", Journal of the American Chemical Society, 112 (2), 558, (1990)
130. D. L. Allara and R. G. Nuzzo, "Spontaneously Organized Molecular Assemblies .2. Quantitative Infrared Spectroscopic Determination of Equilibrium Structures of Solution-Adsorbed Normal-Alkanoic Acids on an Oxidized Aluminum Surface", Langmuir, 1 (1), 52, (1985)
131. K. Bierbaum, M. Kinzler, C. Woll, M. Grunze, G. Hahner, S. Heid and F. Effenberger, "A near-Edge X-Ray-Absorption Fine Structure Spectroscopy and X-Ray Photoelectron-Spectroscopy Study of the Film Properties of Self-Assembled Monolayers of Organosilanes on Oxidized Si(100)", Langmuir, 11 (2), 512, (1995)
132. A. Hozumi, H. Sugimura, Y. Yokogawa, T. Kameyama and O. Takai, "Zeta-Potentials of planar silicon plates covered with alkyl- and fluoroalkylsilane self-assembled monolayers", Colloids and Surfaces, A: Physicochemical and Engineering Aspects, 182 (1-3), 257, (2001)
133. E. R. Pohl and F. D. Osterholtz, "Kinetics and mechanism of aqueous hydrolysis and condensation of alkyltrialkoxysilanes", Polymer Preparations (American Chemical Society, Division Polymer Chemistry), 24 (1), 200, (1983)

134. S. R. Wasserman, Y. T. Tao and G. M. Whitesides, "*Structure and Reactivity of Alkylsiloxane Monolayers Formed by Reaction of Alkyltrichlorosilanes on Silicon Substrates*", Langmuir, 5 (4), 1074, (1989)
135. R. Banga, J. Yarwood, A. M. Morgan, B. Evans and J. Kells, "*In-situ FTIR studies of the kinetics and self assembly of alkyl and perfluoroalkyl trichlorosilanes on silicon*". Thin Solid Films, 284-285 261, (1996)
136. A. N. Parikh, M. A. Schivley, E. Koo, K. Seshadri, D. Aurentz, K. Mueller and D. L. Allara, "*n-alkylsiloxanes: From single monolayers to layered crystals. The formation of crystalline polymers from the hydrolysis of n-octadecyltrichlorosilane*". Journal of the American Chemical Society, 119 (13), 3135, (1997)
137. D. G. Kurth and T. Bein, "*Optical Effects in Reflection-Absorption Ir Spectroscopy of Thin-Films of Silane Coupling Agents on Metallic Surfaces*", Langmuir, 11 (2), 578, (1995)
138. K. I. Iimura and T. Kato, "*Robustness of monolayers on the solids; comparative studies on thermal, solvent, pH, and mechanical resistance among 1-layer LB films of cadmium arachidate and alkylchlorosilanes*", Colloids and Surfaces A-Physicochemical and Engineering Aspects, 171 (1-3), 249, (2000)
139. R. Maoz, J. Sagiv, D. Degenhardt, H. Moehwald and P. Quint, "*Hydrogen-bonded multilayers of self-assembling silanes: structure elucidation by combined Fourier transform infra-red spectroscopy and x-ray scattering techniques*", Supramolecular Science, 2 (1), 9, (1995)
140. W. Rudzinski, R. Charmas, W. Piasecki, B. Prelot, F. Thomas, F. Villieras and J. M. Cases, "*Calorimetric effects of simple ion adsorption at the silica/electrolyte interface: Quantitative analysis of surface energetic heterogeneity*", Langmuir, 15 (18), 5977, (1999)
141. R. W. Smith, "*Effect of amine structure in cationic flotation of quartz*", Transactions of the Society of Mining Engineers of AIME, 254 (4), 353, (1973)
142. J. Y. Fang and C. M. Knobler, "*Control of Density in Self-Assembled Organosilane Monolayers by Langmuir-Blodgett Deposition*", Journal of Physical Chemistry, 99 (26), 10425, (1995)
143. D. W. Britt and V. Hlady, "*Protonation, hydrolysis, and condensation of mono- and trifunctional silanes at the air/water interface*", Langmuir, 15 (5), 1770, (1999)

144. J. Mu, H. Okamoto, T. Yanai, S. Takenaka and X. Feng, "Synthesis and monolayer formation of liquid crystal polysiloxanes having a lateral side chain with a perfluoroalkyl chain", Colloids and Surfaces A-Physicochemical and Engineering Aspects, 181 (1-3), 303, (2001)
145. P. Dynarowicz, N. V. Romeu and J. M. Trillo, "Stability of dialkyldimethylammonium bromides monolayers spread at the water/air interface", Colloids and Surfaces A-Physicochemical and Engineering Aspects, 131 (1-3), 249, (1998)
146. R. J. Hunter, *Foundations of colloid science*, (Repr. 1992 (with corrections)), pp. 671. Clarendon Press, Oxford University Press, Oxford [England] : New York, (1992)
147. Y. L. Lee, C. H. Chen and Y. M. Yang, "Surface morphology and wetting behavior of poly(alpha- methylstyrene) thin films prepared by vacuum deposition", Langmuir, 14 (24), 6980, (1998)
148. T. Smith, "Ellipsometry for Measurements at and Below Monolayer Coverage", Journal of the Optical Society of America, 58 (8), 1069, (1968)
149. R. M. A. Azzam and N. M. Bashara, *Ellipsometry and polarized light*, pp. 529. North-Holland Publishing Company, Amsterdam : New York, (1977)
150. C. Bungary and J. Hilfiker, "Measuring multilayer thin film structures with spectroscopic ellipsometry", Vacuum Technology and Coatings, 32, (December 2001)
151. J. N. Israelachvili and M. L. Gee, "Contact Angles on Chemically Heterogeneous Surfaces", Langmuir, 5 (1), 288, (1989)
152. J. G. Kushmerick, M. G. Hankins, M. P. de Boer, P. J. Clews, R. W. Carpick and B. C. Bunker, "The influence of coating structure on micromachine stiction", Tribology Letters, 10 (1-2), 103, (2001)
153. X. Cheng, G. Li, E. A. Kneer, B. Vermeire, H. G. Parks, S. Raghavan and J. S. Jeon, "Electrochemical impedance spectroscopy of copper deposition on silicon from dilute hydrofluoric acid solutions", Journal of the Electrochemical Society, 145 (1), 352, (1998)
154. J. N. Chazalviel, "Impedance Studies at Semiconductor Electrodes - Classical and More Exotic Techniques", Electrochimica Acta, 35 (10), 1545, (1990)
155. J. R. Scully, R. P. Frankenthal, K. J. Hanson, D. J. Siconolfi and J. D. Sinclair, "Localized corrosion of sputtered aluminum and aluminum-0.5% copper alloy

- thin films in aqueous hydrofluoric acid solution. I. Corrosion phenomena*", Journal of the Electrochemical Society, 137 (5), 1365, (1990)
156. J. R. Macdonald, *Impedance spectroscopy : emphasizing solid materials and systems*, pp. xvi, Wiley, New York, (1987)
157. G. K. Jennings, J. C. Munro, T. H. Yong and P. E. Laibinis, "Effect of chain length on the protection of copper by n-alkanethiols", Langmuir, 14 (21), 6130, (1998)
158. M. Saakes, P. J. van Duin, A. C. P. Ligtoet and D. Schmal, "Investigations of the negative plate of lead/acid cells. 2. Verification with 2 V cells", Journal of Power Sources, 47 (1-2), 149, (1994)
159. H. Brunner, T. Vallant, U. Mayer, H. Hoffmann, B. Basnar, M. Vallant and G. Friedbacher, "Substrate Effects on the Formation of Alkylsiloxane Monolayers", Langmuir, 15 (6), 1899, (1999)
160. B. C. Bunker, R. W. Carpick, R. A. Assink, M. L. Thomas, M. G. Hankins, J. A. Voigt, D. Sipola, M. P. de Boer and G. L. Gulley, "The Impact of Solution Agglomeration on the Deposition of Self-Assembled Monolayers", Langmuir, 16 (20), 7742, (2000)
161. H. N. Patrick, G. G. Warr, S. Manne and I. A. Aksay, "Self-assembly structures of nonionic surfactants at graphite/solution interfaces", Langmuir, 13 (16), 4349, (1997)
162. D. C. Montgomery, *Design and analysis of experiments*, (5th ed.), pp. 684, John Wiley & Sons, Inc., New York, (1997)
163. D. C. Montgomery, G. C. Runger and N. F. Hubele, *Engineering Statistics*, (2nd ed.), pp. 494, John Wiley & Sons, Inc., New York, (2001)
164. D. Graf, M. Grundner, R. Schulz and L. Muhlhoff, "Oxidation of Hf-Treated Si Wafer Surfaces in Air", Journal of Applied Physics, 68 (10), 5155, (1990)
165. J. P. Cronin, D. J. Tarico, J. C. L. Tonazzi, A. Agrawal and S. R. Kennedy, "Microstructure and properties of tungsten trioxide films made by sol-gel process for large area electrochromic windows", Proceedings of the SPIE-International Society of Optical Engineering, 1758 (Sol-Gel Opt. II), 343, (1992)
166. S. S. Mani, J. G. Fleming, J. J. Sniegowski, M. P. De Boer, L. W. Irwin, J. A. Walraven, D. M. Tanner and M. T. Dugger, "Chemical Vapor Deposition coating for micromachines", in Materials Research Society Symposium Proceedings, Methods, Mechanisms and Models of Vapor Deposition p. 21, (2000)

167. S. S. Mani, J. G. Fleming, J. J. Sniegowski, M. P. De Boer, L. W. Irwin, J. A. Walraven, D. M. Tanner and D. A. La Van, "*Selective W for coating and releasing MEMS devices*", in Materials Research Society Symposium Proceedings, Materials Science of Microelectromechanical Systems (MEMS) Devices II p. 135, (2000)